

EXPERIMENTAL INVESTIGATIONS RELATED TO IONOSPHERIC PROBING

by

M. Katzin
W. P. Markey
D. L. Ringwalt
R. E. Skinner

GPO PRICE \$ _____

CFSTI PRICE(S) \$ 41.60

Hard copy (HC)

Microfiche (MF)

653 July 65

Final Report, Part 1
on
Contract NASw-835

Prepared for

National Aeronautics and Space Administration
Goddard Space Flight Center
Greenbelt, Maryland.

Report No. NAS 835-4
31 January 1966

ELECTROMAGNETIC RESEARCH CORPORATION

5001 COLLEGE AVENUE
COLLEGE PARK, MD.



EXPERIMENTAL INVESTIGATIONS RELATED TO IONOSPHERIC PROBING

by

M. Katzin
W. P. Markey
D. L. Ringwalt
R. E. Skinner

Final Report, Part 1
on
Contract NASw-835

Prepared for
National Aeronautics and Space Administration
Goddard Space Flight Center
Greenbelt, Maryland.

ELECTROMAGNETIC RESEARCH CORPORATION

5001 COLLEGE AVENUE
COLLEGE PARK, MD.

Report No. NAS 835-4
31 January 1966

ABSTRACT

An experimental investigation of the behavior of an r-f capacitance probe has shown that the expected decrease in capacitance upon immersion in a plasma may not always be found. Due to the formation of ion sheaths around the electrodes and the effective conductivity due to collisions at higher pressures, the effective separation between the plates may decrease in a plasma, with a resulting increase in capacitance. Consequently, in the use of this type of probe, compensation or allowance for the effects of sheath formation is required.

A program for D-region simulation by ultraviolet photoionization of nitric oxide was studied both theoretically and experimentally. First a theoretical study was carried out, in which the required photon flux was calculated, taking into account the various loss processes which are operative. This showed that a photon flux of 10^{14} to 10^{15} photons-cm⁻²-sec⁻¹ is sufficient to generate electron densities suitable for D-region simulation, and that the electron temperature should be that of the gas for pressures of 10^{-1} Torr or greater. Furthermore, it was shown that a somewhat lower electron temperature should be obtainable with a krypton UV-tube than with a hydrogen tube.

To demonstrate feasibility experimentally, several tubes of new design were built and the effects of tube geometry and gas filling were investigated. Krypton was found to yield a higher efficiency and output than hydrogen or hydrogen-neon combinations for the gas filling. UV outputs one to two orders of magnitude higher than the output of a commercially available UV tube were obtained. Output and efficiency were well above the minimum values determined from the theoretical study.

Finally, a plasma of approximately the desired characteristics was generated by photoionization of NO in a bell jar, and ionization densities and electron

temperatures of the expected order were obtained, using double probes to measure the plasma characteristics. Electron densities around 10^7 cm^{-3} and electron temperatures around 1800° K were obtained.

For the development of a large-volume low-temperature plasma, a UV-tube design was chosen which would allow a number of tubes to be packed fairly closely in a bank mounted on the vacuum chamber. A number of these tubes were constructed and their characteristics measured. This program resulted in UV-tubes which adequately meet the requirements for producing a large-volume plasma, yielding flux levels up to $10^{15} \text{ photons sec}^{-1}$ per tube. The tubes were proved by life tests and subsequent operation to have exceptional stability and reliability, and long life. In addition, large photon detectors for these tubes were constructed.

The final part of the program was devoted to the development of a large-volume plasma in the chamber, using the tubes developed under the program. Unexpectedly, the probe curves obtained were of unusual shape, being wholly unlike those obtained in the bell jar during the feasibility study program. A repeat of the measurements in the bell jar also gave anomalous probe curves. This was finally traced to the fact that in the later measurements a different sample of NO was used, which was manufactured by a completely different process from the first sample, although obtained from the same manufacturer. Mass analysis of the second sample in the chamber showed N_2O as an impurity, with a concentration of 0.5%. Analysis shows that N_2O acts as a very effective electron attaching agent, producing negative ions, as well as distorting the electron energy distribution. As a result, positive ion and electron densities obtained are two to three orders of magnitude below those expected, and obtained in the bell jar measurements with the first (uncontaminated) sample of NO. Thus this type of impurity must be kept to a very low level.

Recommendations for further improvements in experimental techniques are made.

PREFACE

Contract NASw-835 comprises theoretical and experimental studies related to ionospheric probing. The theoretical studies are supported by the Office of Space Sciences of NASA Headquarters, while the experimental studies are funded by NASA Goddard Space Flight Center (GSFC). Consequently, the final report on the contract is being divided into corresponding separate parts. The present report presents the results of the experimental program.

Work under the contract commenced 1 October 1963. The results of the work during the first 12 months of the contract have already been reported in detail*.

The experimental program itself comprised two broad tasks. One was the study of plasma generation techniques for ionospheric simulation, especially of the D-region by UV photoionization of nitric oxide. The other task was the development of techniques for in-flight measurement of antennas aboard a spacecraft (rocket or satellite). Work on the latter task has been continued under Contract NAS5-9170, so that it will not be reported here. Consequently, the present report is devoted principally to a presentation of the results of the ionospheric simulation program and related activities.

* "Experimental Investigations Related to Ionospheric Probing," Scientific Report No. 2, ERC Report No. NAS 835-2, 30 September 1964.

TABLE OF CONTENTS

	<u>Page</u>
ABSTRACT	ii
PREFACE	iv
1. INTRODUCTION	1
2. R.F. CAPACITANCE PROBE	4
3. DEVELOPMENT OF A LARGE-VOLUME, LOW-TEMPERATURE PLASMA BY PHOTOIONIZATION OF NO	16
3.1 Introduction	16
3.2 Feasibility Study Program	17
3.2.1 Theoretical Feasibility Study	17
3.2.1.1 Introduction	17
3.2.1.2 Electron Source	18
3.2.1.3 Loss Processes	20
3.2.1.3.1 Recombination	20
3.2.1.3.2 Attachment	20
3.2.1.3.3 Diffusion	22
3.2.1.4 Plasma Densities	26
3.2.1.4.1 Infinite Plasma	26
3.2.1.4.2 Finite Plasma	27
3.2.1.5 Mean Free Paths and Sheath Size	32
3.2.1.6 Thermalization	34
3.2.1.7 Conclusions	39
3.2.2 Experimental Feasibility Study	40
3.2.2.1 UV Sources	40
3.2.2.1.1 Introduction	40

	<u>Page</u>
3.2.2.1.2 Tube Design Considerations	41
3.2.2.1.3 Window Seal	42
3.2.2.1.4 Experimental Tubes	43
3.2.2.1.5 Gas Handling System	47
3.2.2.1.6 Performance Tests	48
3.2.2.1.6.1 Introduction	48
3.2.2.1.6.2 Standard Tube Measurements	51
3.2.2.1.6.3 New Designs	54
3.2.2.1.6.4 Gas Mixture Effects	66
3.2.2.1.6.5 Conclusions	68
3.2.2.2 Small Volume Plasma Generation	70
3.2.2.2.1 Objectives	70
3.2.2.2.2 Experimental Setups and Results	70
3.2.3 Summary and Conclusions of Feasibility Study Program	78
3.3 Program to Develop a Large-Volume Low-Temperature Plasma	79
3.3.1 Scope and Plans	79
3.3.2 Mod-D Tube Design and Fabrication Program	80
3.3.2.1 Introduction	80
3.3.2.2 Window Sealing Tests	81
3.3.2.3 Beam Angle Measurements	83
3.3.2.4 Large Detectors	86
3.3.2.5 Mod-D Design	91
3.3.2.5.1 Construction	91
3.3.2.5.2 LiF Window Transmission	91
3.3.2.5.3 Gas Filling Performance Tests	93

	<u>Page</u>
3.3.2.5.4 Performance of Mod-D and D-Tube Geometries and Effect of Capillary Window Spacing	97
3.3.2.5.5 Beam Angle Measurements	97
3.3.2.6 Mod-D Tube Fabrication Program	100
3.3.2.6.1 Bakeable Gas-Handling System	100
3.3.2.6.2 Tube Processing	100
3.3.2.6.3 Performance Tests	103
3.3.2.6.4 Life Tests	106
3.3.2.6.5 Spectrums	109
3.3.2.7 Conclusions	111
3.3.3 Large-Volume Plasma Production	111
3.3.3.1 Objectives	111
3.3.3.2 Tube Bank Mount	112
3.3.3.3 Tube Bank Power Supply	114
3.3.3.4 ND Gas-Handling System	114
3.3.3.5 Differential Pumping System for the Mass Spectrometer	118
3.3.3.5.1 Differential Pumping System	119
3.3.3.5.2 Modifications to Mass Spectrometer	119
3.3.3.6 Film Build-Up on Windows of UV-Tubes	122
3.3.3.7 Probe Measurements	125
3.3.3.7.1 Introduction	125
3.3.3.7.2 Probes for Measurement of Plasma Characteristics	126
3.3.3.7.3 Probe Data	128
3.3.3.7.3.1 Chamber Measurements (Series II)	128

	<u>Page</u>
3.3.3.7.3.1.1 Small Double Probe	128
3.3.3.7.3.1.2 Gerdian Condenser	133
3.3.3.7.3.1.3 Large Double Probe Results	139
3.3.3.7.3.1.4 Langmuir Probe Results	141
3.3.3.7.3.1.5 Summary of Series II Measurements	145
3.3.3.7.3.2 Repeat of Ball Jar Measurements (Series III)	145
3.3.3.7.3.3 Final Chamber Measurements (Series IV)	148
3.3.3.7.3.3.1 Langmuir Probe	149
3.3.3.7.3.3.2 Double Probe	149
3.3.3.7.3.4 Summary and Conclusions	158
3.3.3.8 Mass Analysis	159
3.3.3.8.1 Cracking Pattern Measurements	159
3.3.3.8.1.1 Preliminary Studies of NO	160
3.3.3.8.1.2 Improved Accuracy of Mass Determination	163
3.3.3.8.2 Chamber Mass Spectrums	165
3.3.3.8.3 Chemical Analysis of NO	169
3.3.3.8.4 Summary and Conclusions	171
3.3.3.9 Summary and Conclusions	173
4. MISCELLANEOUS VACUUM SERVICES	175
4.1 Portable 4-Inch Vacuum System	175
4.2 Vac-Ion System	175
4.3 Portable 2- and 4-Inch Vacuum Systems	177
4.4 Outgassing Rate of a Fiberglass Rocket Body	178

	<u>Page</u>
4.5 Ion Trap Test	183
4.6 Bell Jar Life System	185
4.7 Tube Fabrication Services	185
5. SUMMARY, CONCLUSIONS AND RECOMMENDATIONS	186
5.1 Summary and Conclusions	186
5.2 Recommendations	188
APPENDIX A - PROBE THEORY	190
A1. INTRODUCTION	190
A2. DOUBLE PROBE THEORY	191
A2.1 Maxwellian Velocity Distribution and NO Negative Ions	191
A2.1.1 No Collisions in the Sheath ($\lambda_p \gg a$)	195
A2.1.1.1 (r/a) Independent of η	197
A2.1.1.2 $(r/a) \propto \eta^{-1}$	199
A2.1.1.3 $(r/a) \propto \eta^{-\frac{1}{2}}$	200
A2.1.1.4 Dependence of Sheath Size on Potential	201
A2.1.1.5 Comparison with Experimental Data	203
A2.1.2 The Effect of Collisions in the Sheath	203
A2.1.2.1 The Sheath Edge and the Effect of a Net Field	203
A2.1.2.2 Many Collisions ($\lambda_p \ll a$)	204
A2.1.2.3 A Few Collisions ($\lambda_p \sim a$)	206
A2.1.3 Determination of Electron Temperature	207
A2.2 Negative Ions	208
A2.3 Non-Maxwellian Electron Energy Distribution	210
A2.3.1 Monoenergetic Isotropic Distribution	211
A2.3.2 Rectangular Isotropic Energy Distribution	213

	<u>Page</u>
A2.3.3 Two-Peak Distribution	215
A2.4 Highly Asymmetrical Double Probes	216
A3. SUMMARY AND CONCLUSIONS	218
APPENDIX B - THE EFFECT OF ELECTRON ATTACHMENT	220
B1. ENERGY DEPENDENCE OF ELECTRON REMOVAL CROSS SECTIONS	220
B2. ATTACHMENT AND DETACHMENT	222
B2.1 General	222
B2.2 Attachment with N_2O Present	222
B3. SUMMARY AND CONCLUSIONS	225
BIBILIIOGRAPHY	226
FIGURES 1 - 108	

1. INTRODUCTION

Ionospheric parameters may be measured with a variety of rocket-borne probes or sensors. One type of probe which has been flown on several rockets is a simple capacitor. Its philosophy is based on the reduction in the effective dielectric constant of the medium below its free-space value by the free electrons in the ionosphere. Thus, if a resonant LC-circuit, using a capacitor open to the atmosphere, is carried into the ionosphere on a rocket, the ionosphere will cause changes in the resonance frequency of the LC-circuit. The resonance frequency in the ionosphere should be higher than when the capacitor is outside the ionosphere. Laboratory measurements at ERC on such a probe have shown that this idealized situation is not always found. Due to the buildup of sheaths and the effective conductivity due to collisions, the effective separation between the plates may decrease in a plasma, with a resulting increase in capacitance. This may help to explain difficulties which have been experienced with such probes in rocket experiments. This work is described in Sec. 2 of this report.

Laboratory simulation of the D-region of the ionosphere would allow experimental studies of the characteristics of various instruments used to determine ionospheric parameters. One of the important processes in D-region formation is considered to be photoionization of nitric oxide (NO), a trace constituent of the upper atmosphere, by solar Lyman- α radiation. Because of the high absorption coefficient of NO in the ultraviolet around the Lyman- α line, the use of this process to produce a low temperature plasma in the laboratory has been advanced. This process, therefore, has been studied both theoretically and experimentally under this contract, with the goal of producing a low-temperature plasma in the large-volume high-vacuum chamber installed at ERC (which will be referred to hereafter as "the chamber", for brevity). This problem, which received the major part of the effort reported here, is discussed in Sec. 3. Accordingly, Sec. 3 comprises the bulk of this report.

Before proceeding with the simulation program on a large scale, a feasibility study program was carried out. This is reported in Sec. 3.2. It consisted first of a theoretical study, in which the required photon flux was calculated, taking into account the various loss processes which are operative. This was followed by an experimental feasibility study to demonstrate that UV sources with large enough efficiency and photon flux to meet the requirements could be produced. Several tubes of new design were built and the effects of tube geometry and gas filling were investigated. Krypton was found to yield a higher efficiency and output than hydrogen or hydrogen-neon combinations for the gas filling. UV outputs one to two orders of magnitude higher than the output of a commercially available UV tube were obtained. Output and efficiency were well above the minimum values determined from the theoretical study. The final step was to generate a plasma of approximately the desired characteristics by photoionization of NO on a small scale. This was accomplished in a bell jar, and ionization densities and electron temperatures of the expected order were obtained, using double probes to measure the plasma characteristics.

Following the successful demonstration that UV-tubes of the requisite output and efficiency could be built, a program to develop a large-volume low-temperature plasma in the chamber was undertaken. This is described in Sec. 3.3. From the various basic tube designs investigated in the feasibility study program, it remained to choose a design which would allow a number of tubes to be packed fairly closely in a bank mounted on the chamber. Tubes of the design which was developed are designated as Mod-D. It was then necessary to fabricate a sufficient quantity of these tubes and to demonstrate that adequate output could be achieved and maintained for a reasonable life span. The Mod-D tube fabrication and test program is described in Sec. 3.3.2. This program resulted in highly reliable UV-tubes which adequately meet the requirements for producing a large-volume plasma,

yielding flux levels up to 10^{15} photons-sec⁻¹. The tube geometry is compact, lending itself to close packing in a bank of tubes to increase the UV beam area. The tubes were proved by life tests and subsequent operation to have exceptional stability and reliability, and long life.

The final part of the program was devoted to the development of a large-volume plasma in the chamber, using the Mod-D tubes developed under the program. This is discussed in Sec. 3.3.3. Unexpectedly, the probe curves obtained were of unusual shape, being wholly unlike those obtained in the bell jar during the feasibility study program. A repeat of the measurements in the bell jar also gave anomalous probe curves. This was finally traced to the fact that in the later measurements a different sample of NO was used, which was manufactured by a completely different process from the first sample. Mass analysis of the second sample in the chamber showed N₂O as an impurity, with a concentration of 0.5%. Theoretical work (presented in Appendices A and B) shows that N₂O acts as a very effective electron attaching agent, producing negative ions, as well as distorting the electron energy distribution. From the measurement program, electron temperatures in the uncontaminated sample of NO used in the first bell jar plasma of around 1800°K are deduced. Thus the photoionization process does result in a rather cool plasma, as predicted theoretically.

Conclusions and recommendations for improvements in techniques are presented in Sec. 3.3.4.

A brief summary of miscellaneous services allied to the plasma simulation activities is presented in Sec. 4. Finally, an overall summary and conclusions regarding the entire experimental program are given in Sec. 5, together with recommendations for future work of this type.

2. R.F. CAPACITANCE PROBE

As is well known, the free electrons in a plasma reduce the effective dielectric constant of the medium below the free-space value. Consequently, if a parallel-plate capacitor is immersed in the plasma and made part of a tuned circuit, the resonance frequency of the tuned circuit will vary as the capacitance is affected by the plasma. This effect has often been proposed as a plasma measurement technique.

The complex dielectric constant of a lossy plasma in the absence of a steady magnetic field is

$$\epsilon'/\epsilon_0 = 1 - \frac{x}{1+z^2} - i \frac{xz}{1+z^2} \quad (1)$$

where

$$x = (\omega_p/\omega)^2 = (f_p/f)^2 = \text{normalized (plasma frequency)}^2 \quad (2)$$

and

$$\omega_p^2 = Ne^2/(\epsilon_0 m)$$
$$N = 1.24 \cdot 10^{-3} f_p^2 \text{ cm}^{-3} \quad (3)$$

$$z = \nu/\omega = \text{normalized collision frequency} \quad (4)$$

The imaginary part of (1) is equivalent to a conductivity.

From (1), under suitable conditions of plasma parameters and frequency, a measurable change in resonance should result. Consequently, this effect is a potentially useful diagnostic technique. In fact, GSFC has flown several embodiments of this idea in attempts at measuring the lower levels of the ionosphere, but no successful results were obtained.

Another such flight instrument, designed and built by GSFC, was delivered to ERC for evaluation in the high-vacuum chamber. This instrument contained an oscillator, which was swept in frequency between approximately 1 and 5 Mc, and fed a tuned circuit. The capacitor of this tuned circuit was constructed of two planar screens of coarse mesh to allow the surrounding medium to penetrate between the

plates. The resonance frequency of the tuned circuit was about 3 Mc in free space.

This unit was placed in the high-vacuum chamber between two 1-foot diameter electrodes which were used to develop a d-c discharge plasma. It was expected that as the plasma was developed, the resonance frequency of the tuned circuit would increase, due to the lower dielectric constant of the plasma. However, the opposite effect was noted. The 3-Mc resonance frequency (in free space) shifted to a lower frequency, corresponding to an increase in dielectric constant, when the plasma was developed. In addition, a large decrease in the height of the resonance peak was observed, indicating a severe loading of the tuned circuit by the plasma. These effects were realized for various values of pressure between 20 and 5 microns and discharge currents up to 10 ma. At still lower pressures it was not possible to start the discharge with the voltage (15 kv) available.

In order to explore a wider range of frequency than that available in the instrument, the following changes were made. The tuned circuit of the instrument was left in its original position in the chamber and fed from a Jerrold model 900A sweep-frequency oscillator mounted outside the chamber. The resonance indicator consisted of an oscilloscope connected across a 50-ohm resistor in series with the tuned circuit. With this arrangement the following observations were made:

(a) Two resonances, one at about 3 Mc and one at about 5 Mc, were noted.

(b) In free space, only the 3-Mc resonance was affected by changing the condenser plate separation or by placing dielectric material between the condenser plates. Thus the 5-Mc resonance appeared to be associated with the feed system to the tuned circuit.

(c) When the plasma was developed, both the 3- and 5-Mc resonances were lowered in frequency. Again this condition pertained to all values of pressure between 20 and 5 microns and to discharge currents up to 10 ma.

The observations that the plasma produced a heavy loading of the tuned circuit indicated that the imaginary part of (1) was large. This, in turn, suggested a large value of the normalized collision frequency, z . A calculation of collision frequency, using values of electron temperature measured with a Langmuir probe under similar discharge conditions, gave a value of ν of about 60 Mc at a pressure of 10μ . Consequently a value of $x = 1$ would be obtained at a frequency of about 10 Mc.

Several other measurements were made with a simple planar condenser consisting of two metal discs about 6" in diameter which was resonated at various frequencies with a suitable inductance. At 15 Mc, a small increase in resonance frequency (to 15.2 Mc) was measured at a pressure of 10μ and a discharge current of 5 ma. Using (1), (2), and (3), this indicated an electron density of about 10^5 cm^{-3} . Further experimentation showed that about 7 Mc was a transition frequency, below which the resonance frequency decreased and above which it increased when the plasma was produced.

In an effort to understand fully the preceding observations, some experiments were conducted with a cylindrical discharge tube (about 20 mm in diameter and 45 cm long) with disc discharge electrodes at each end. Brass foil electrodes were taped outside the central portion of this tube to form a condenser whose free-space capacitance was measured to be 22 pf. A small coil was connected across this condenser and fed from the Jerrold sweep-frequency generator. An oscilloscope was connected to a tap on the coil to observe resonance. Measurements in the vicinity of 170 Mc showed measurable increases in resonance frequency and decreases in height of the resonance peak when the plasma was generated.

With no discharge, the resonance frequency was measured with a marker generator, and the height of the resonance peak was noted. Then, at a given gas pressure, the discharge was started and the voltage adjusted until the height of

the resonance peak dropped by a factor of 2. The discharge current, I , change in resonance frequency, Δf , and the gas pressure, p , were recorded. Measurements were made over a range of gas pressures. The data obtained are given in the first three columns of Table I.

Table I

<u>p (microns)</u>	<u>Δf (Mc)</u>	<u>I (ma)</u>	<u>$p\Delta f$</u>
70	4.0	0.75	280
150	2.0	0.85	300
220	1.5	1.00	330
350	1.0	1.30	350
700	0.5	2.22	350
2000	0.25	5.10	500

Since each measurement was made with the same reduction in Q of the resonant circuit, the imaginary part, β , of (1) was held constant. Thus we have

$$\beta \equiv \frac{xz}{1+z^2} = \text{const.} \quad (5)$$

Then, from (1), the real part, α , is

$$\alpha = 1 - \frac{x}{1+z^2} = 1 - \frac{\beta}{z}.$$

If we denote the resonance frequency with no plasma by f_0 , and that with the plasma by f_1 , we have

$$\frac{1}{\omega_0^2} = LC_0$$

and

$$\frac{1}{\omega_1^2} = LC^1 = LC_0 \left(1 - \frac{x}{1+z^2}\right) = \frac{1}{\omega_0^2} \left(1 - \frac{x}{1+z^2}\right).$$

Hence

$$\frac{x}{1+z^2} = \frac{\omega_0^2 - \omega_1^2}{\omega_1^2} \approx \frac{2\Delta f}{f_1} \approx \frac{2\Delta f}{f_0} \quad (6)$$

or, from (5),

$$\frac{\beta}{z} = \frac{2\Delta f}{I_0} \quad (7)$$

If we assume that the electron density in the discharge is proportional to the discharge current, I , then we see from (3) and (2) that

$$\propto I. \quad (8)$$

Further, if we assume that collision frequency is proportional to pressure, then we have from (7) that

$$p\Delta f = \text{const.} \quad (9)$$

The fourth column in Table I gives values of $p\Delta f$, and it is seen that this product is rather constant, except for the last value (the value of Δf here is not very accurate, since it was read as the difference of two settings in a region where successive dial marks corresponded to a difference of 1 Mc).

Taking note of (8), we may write (5) as

$$\beta = \text{const} \propto \frac{I_p}{1 + (ap)^2}, \quad ap = z = v/w$$

or

$$I = \text{const} \frac{1 + (ap)^2}{p}. \quad (10)$$

This relation has the two asymptotes

$$\propto \frac{1}{p}, \quad (ap)^2 \ll 1$$

$$\propto p, \quad (ap)^2 \gg 1.$$

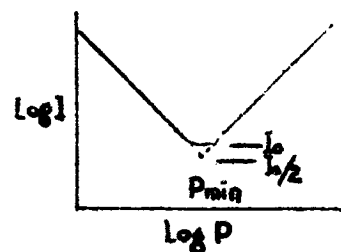


Fig. 1

Thus on a log-log plot of I vs. p , the curve should have a shape as illustrated in Fig. 1 at the right. At the pressure p_{\min} corresponding to the minimum value of I , we have

$$ap_{\min} = 1, \quad \text{or} \quad p_{\min} = 1/a.$$

At p_{\min} , $z = 1$, so that

$$v|_{p_{\min}} = \omega.$$

To determine N , we can use (6) and (3) once the value of z has been determined.

A plot of I vs. p is shown in Fig. 2, the measured values being indicated by the circled points. These points suggest a minimum at a pressure of $p = 70 \mu$. Accordingly a curve in accordance with (10) was calculated on the basis of $p_{\min} = 70 \mu$. This is the solid line in Fig. 2.

Since $z = 1$ at 70μ , we have

$$v|_{p=70\mu} = 2\pi f = 2\pi \cdot 170 \approx 1000 \text{ Mc.}$$

Then from (6)

$$x = \frac{2\Delta f}{f_0} (1 + z^2) = \frac{4 \times 4}{170} = 0.094$$

Hence from (3)

$$\begin{aligned} N &= 1.24 \times 10^{-8} f_p^2 = 1.24 \times 10^{-8} \times 0.094 \times (170)^2 \times 10^{12} \\ &= 3.4 \times 10^7 \text{ cm}^{-3}. \end{aligned}$$

This value of N corresponds to a current $I = 0.75 \text{ ma.}$ For other values of I , N will vary proportionately.

A straight line fitted empirically to the higher pressure points in Fig. 2 (the dashed line) varies as $p^{0.79}$, instead of the unity exponent assumed. This discrepancy may be due to a variation of collision frequency with voltage across the discharge tube.

If we convert the value $z = 1$ at 170 Mc and 70μ to a frequency of 3 Mc , assuming a linear relation between pressure and collision frequency, then we find that a pressure of about 1μ is required for $z = 1$ at the lower frequency, and 0.1μ or 10^{-4} Torr for $z = 0.1$. This is a suitable range of values that should be used to check the proba.

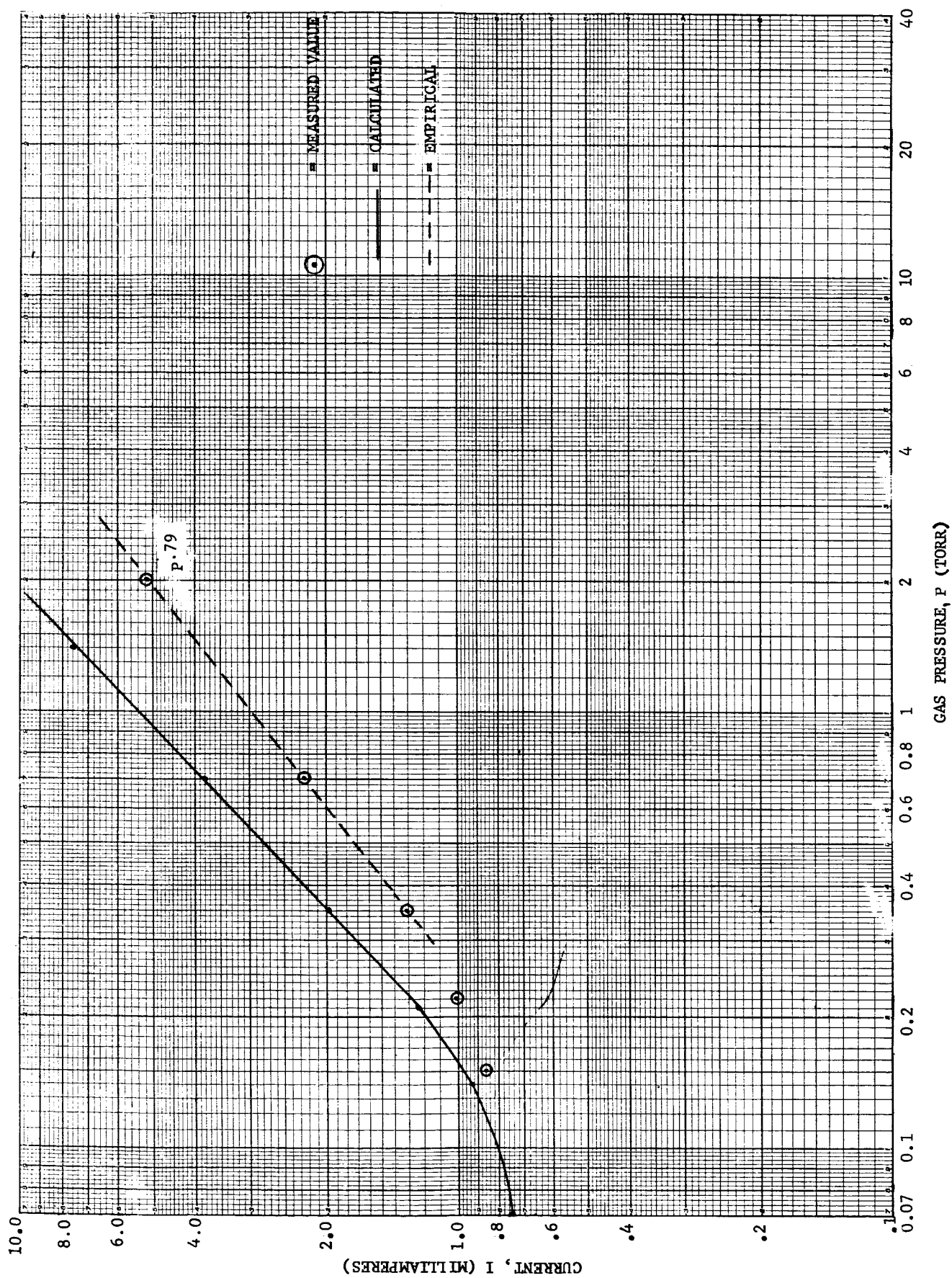


FIG. 2 CURRENT VS. PRESSURE FOR CONSTANT LOADING OF TUNED CIRCUIT, FIRST SET OF DATA

It was found later that the thermocouple gauge used to measure p had become defective. Hence a second set of data was taken, and is given in Table II. The error in the measurement of p did not affect the previous results appreciably. The data of Table II, however, extend over a greater range of p .

Table II

$$f_0 = 182.5 \text{ Mc}$$

<u>p (microns)</u>	<u>Δf (Mc)</u>	<u>I (ma)</u>
20	4.5	2.3
25	5.5	2.2
30	7.5	3.8
35	7.5	3.5
40	7.5	3.3
45	7.0	3.4
50	6.0	3.2
60	6.0	3.0
70	5.5	2.9
80	5.6	2.7
90	4.5	2.6
100	4.5	2.6
110	4.6	2.5
120	4.0	2.6
130	3.5	2.4
140	3.5	2.4
156	3.5	2.5
175	2.5	2.7
200	2.5	2.9
300	2.0	3.6
400	1.5	4.4
500	1.0	5.7

The logarithmic plot of I vs. p , shown in Fig. 3, illustrates more clearly the behavior predicted by (10). The plot does not appear to be entirely symmetric about p_{\min} as predicted. The appearance of the discharge at the lower pressures was fluctuating indicating that the discharge was prone to oscillations, which was not taken into account in the idealized theory used here. It was found, however, that the data were entirely reproducible, so that the deviation from symmetry appears to be a genuine departure from that predicted by the idealized theory.

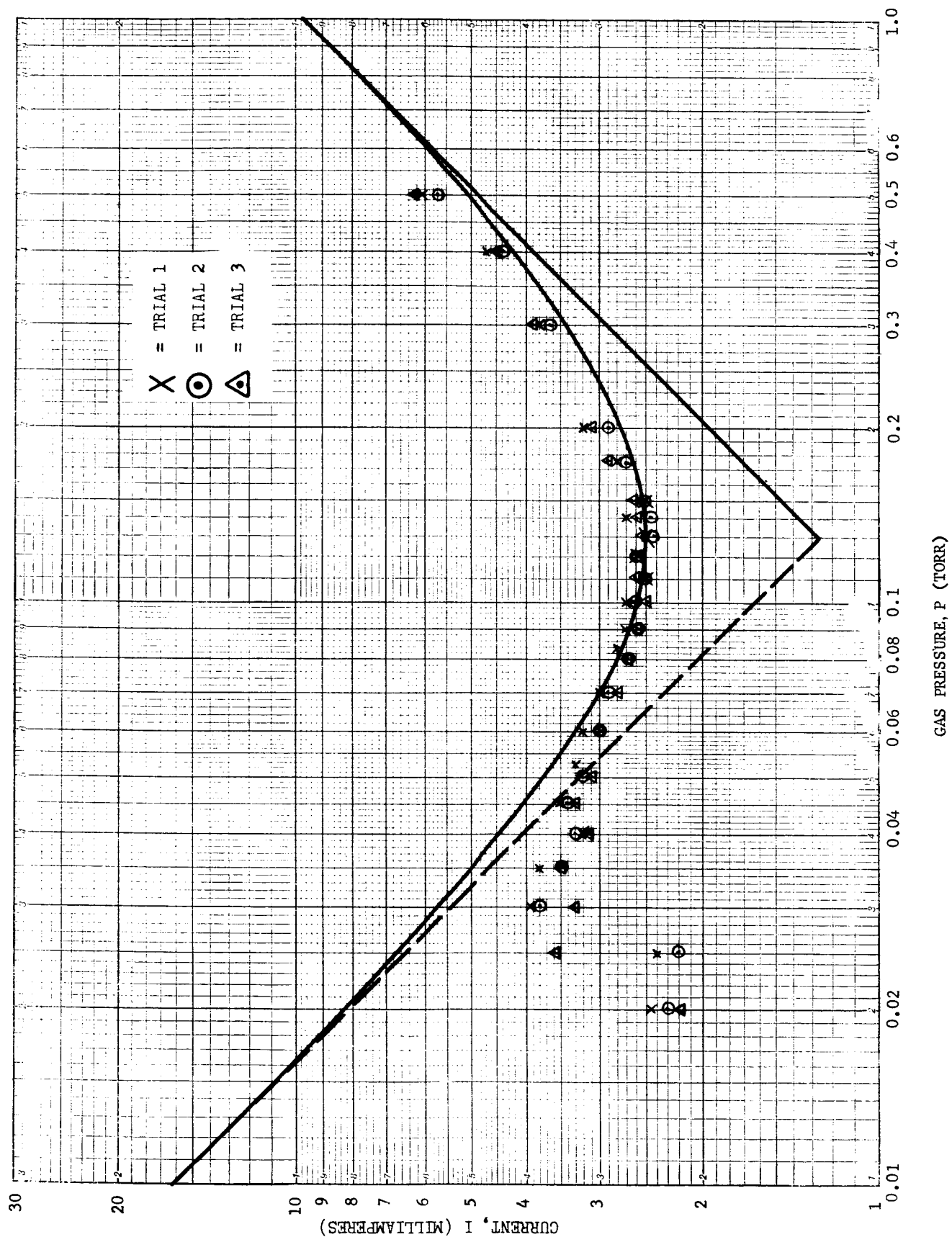


FIG. 3 CURRENT VS. PRESSURE FOR CONSTANT LOADING OF TUNED CIRCUIT, SECOND SET OF DATA

From (7) we have

$$z = v/\omega = \beta E_0 / 2\Delta f \quad (11)$$

or

$$v = \pi \beta f f_0 / \Delta f \approx \pi \beta E_0^2 / \Delta f. \quad (12)$$

The collision frequency in its simplest form is given by

$$v = P_c \bar{v} \quad (13)$$

where P_c is the collision probability for electrons and \bar{v} is the mean electron velocity. From (13) and (12)

$$p = (\pi \beta / P_c \bar{v}) (E_0^2 / \Delta f). \quad (14)$$

Thus, if N is proportional to p , then $P_c \bar{v}$ should be a constant, and since β is held constant in the experiment, the term $\pi \beta / P_c \bar{v}$ should be a constant.

A plot of p vs. $E_0^2 / \Delta f$ is shown in Fig. 4. The straight line appears to be a good fit to the points. This implies that the assumption that $v \propto p$ is valid for the range of parameters used in the experiment.

In analyzing the data in Tables I and II it was implicitly assumed that the plasma fills the entire inter-electrode space of the condenser. Since the electrodes were placed outside the glass envelope of the discharge tube, the plasma fills only part of the inter-electrode space. The equivalent circuit of this condenser thus consists of two capacitances in series, as sketched below in Fig. 5.

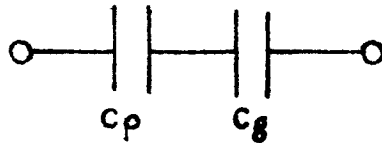


Fig. 5 Equivalent Circuit of Plasma Condenser

C_p is the capacitance between the inside walls and C_g the capacitance through the glass envelope. An estimate of C_g showed that C_g was large compared to C_p , so

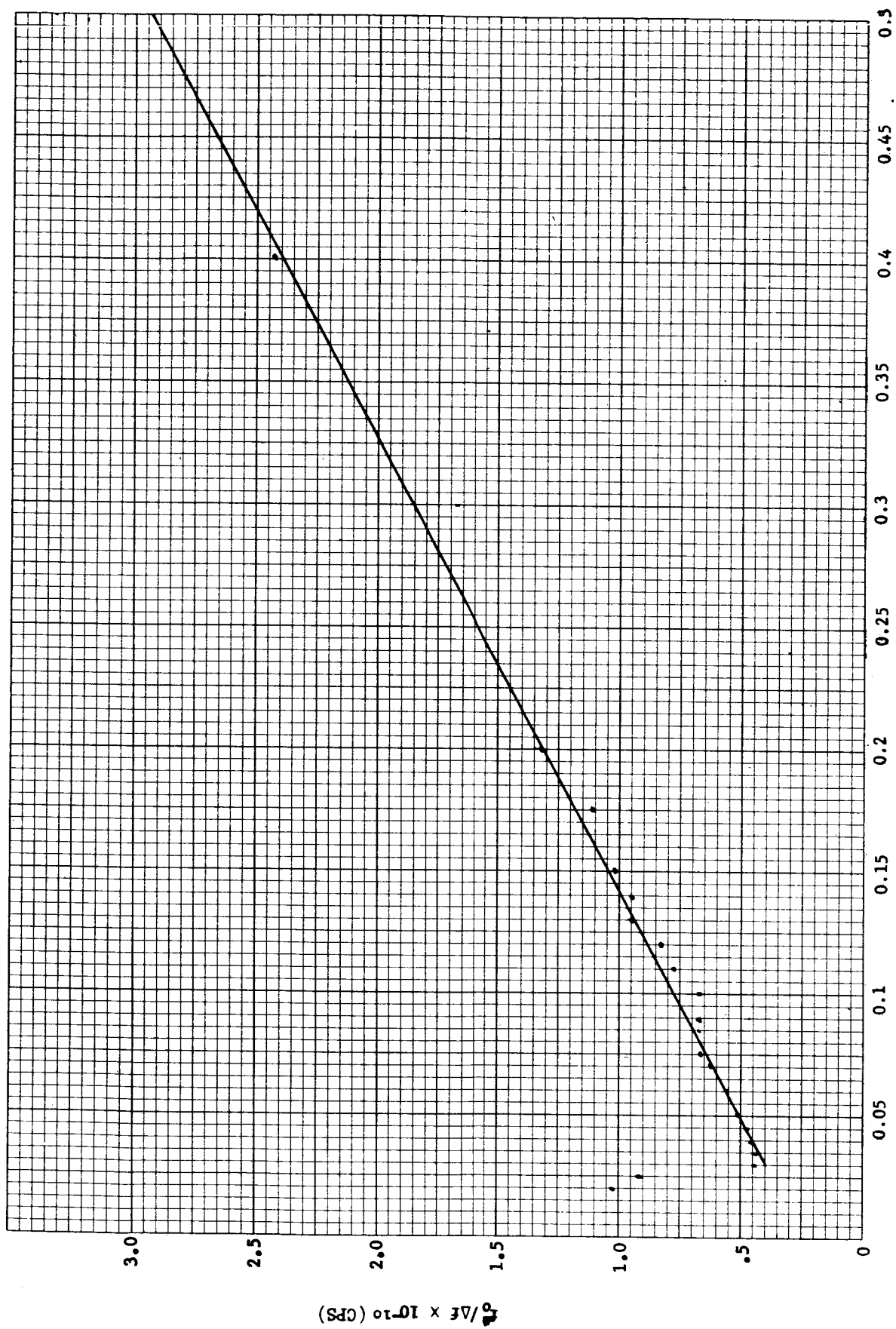


FIG. 4 $\Delta f / \Delta t$ AS A FUNCTION OF GAS PRESSURE

that only a small correction to C_p would result.

For a high-pressure plasma (and hence large value of z), where the plasma has the properties of a conductor between the plates of C_p , C_p will be effectively shorted out, leaving only C_g as the effective capacitance of the arrangement. Thus, since C_g is larger than C_p , the effective capacitance will increase when the plasma is formed under such conditions. This was actually observed at lower frequencies in the glass discharge tube.

The same type of effect can be produced if an ion sheath forms around the electrodes of the condenser when the plasma is generated. The sheath, being devoid of electrons, will behave like a layer of vacuum at the r-f excitation frequency, resulting in an equivalent capacitance C_g that depends on the sheath thickness. Thus the formation of an ion sheath will result in a condition represented by the equivalent circuit shown above. This suggests an explanation for the increase in capacitance (decrease in resonant frequency) that was observed in the large vacuum chamber. Since the lowest pressure used was about 5×10^{-3} Torr, the value of z at 3 Mc was 5 or more. Consequently the plasma acted essentially like a conductor, so that the capacitor C_p was effectively shorted out, as discussed above, leaving only C_g in the circuit. For a thin ion sheath, therefore, the effective capacitance would increase when the plasma is generated.

The above discussion indicates that careful attention is required in the design of a condenser type probe to compensate for the effects of sheath formation.

3. DEVELOPMENT OF A LARGE-VOLUME, LOW-TEMPERATURE PLASMA BY PHOTOIONIZATION OF NO

3.1 Introduction

One of the tasks under the contract was to determine the feasibility of producing a low electron temperature plasma through ultraviolet irradiation of an atmosphere containing nitric oxide. The ionization of nitric oxide by solar Lyman- α radiation ($\lambda = 1215.6\text{\AA}$) is considered to be one of the basic reactions giving rise to the daytime D-layer of the ionosphere [1]*.

The germane properties of the atmosphere in the region of the D-layer are summarized in Table III, taken from [2]. The electron density ranges from 10 to 10^4 cm^{-3} , with electron and ion temperatures believed to be fairly close to those of the gas.

Table III

Properties of the Atmosphere in the Region of the D-Layer

<u>Height (km)</u>	<u>Temp. °K</u>	<u>Number Density cm^{-3}</u>	<u>p Torr</u>	<u>\bar{M}</u>
50	283	2.25×10^{16}	.659	26.97
60	254	7.26×10^{15}	.192	28.97
70	210	2.08×10^{15}	.0452	28.97
80	166	4.48×10^{14}	.00756	28.97
90	166	5.90×10^{13}	.00102	28.97

A good simulation of the D-region would be produced by a plasma having the following properties: (a) electron densities in the range of 10 to 10^4 cm^{-3} , (b) electron and ion temperatures in the order of 300° K , and (c) total gas pressures ranging from about 0.6 to 0.001 Torr .

*

Numbers in brackets refer to the correspondingly numbered references in the Bibliography on p. 226.

The work on this problem was divided into the following tasks, or goals:

- 1) To demonstrate feasibility theoretically.
- 2) To demonstrate experimental feasibility by showing that UV sources with large enough efficiency and photon flux can be produced.

The degree to which these goals have been met are described in detail in the following sections. Section 3.1.1 is a theoretical feasibility study of the photoionization of nitric oxide (NO), in which it is shown that a photon flux at the Lyman- α line of hydrogen of 10^{14} to 10^{15} photons-cm⁻²-sec⁻¹ is required. Section 3.1.2 describes an experimental feasibility study of UV sources (which will be called UV-tubes hereafter), through which it was demonstrated that tubes with the requisite characteristics can be made. Experiments are described which led to the generation of a small scale plasma by photoionization of NO with electron densities of 10^7 to 10^8 cm⁻³ and electron temperatures less than 6000° K. From these, it appears feasible to produce a larger scale plasma in the chamber.

3.2 Feasibility Study Program

3.2.1 Theoretical Feasibility Study

3.2.1.1 Introduction

The photoionization of NO may be accomplished by irradiating a volume containing NO with a beam of ultraviolet radiation from a hydrogen discharge. In the calculations to follow, it is assumed that all of the UV output of the hydrogen discharge is concentrated in the Lyman- α line of hydrogen. The UV beam photoionizes the NO, generating electrons with initial birth energies equal to the difference between the photon energy and the ionization energy of NO. The electrons and ions so generated are then thermalized by collisions with the gas atoms and eventually disappear through loss processes such as recombination, attachment, and diffusion to the walls. The production and loss processes will now be discussed in turn.

3.2.1.2 Electron Source

From [3], the photoionization cross section of NO for Lyman- α radiation is

$$\sigma_1 = 2.02 \times 10^{-18} \text{ cm}^2$$

and the total absorption cross section is

$$\sigma_t = 2.4 \times 10^{-18} \text{ cm}^2$$

These cross sections lead to the values of the UV beam e-folding distances given in Table IV. The electron volume source strength, S, is defined by

$$S = \bar{\phi} \Sigma_1 = \bar{\phi} N \tau_1 \quad (15)$$

where N is the particle density per cm^3 . Fig. 6 is a plot of S as a function of Lyman- α photon flux, $\bar{\phi}$, for various pressures.

Table IV

Lyman- α e-Folding Distance in NO as a Function of Pressure

<u>P</u> <u>(Torr)</u>	<u>e-Folding</u> <u>Distance (cm)</u>
1.0	1.3×10^1
0.1	1.3×10^2
0.01	1.3×10^3
0.001	1.3×10^4

The excess Lyman- α photon energy over the ionization energy is 0.95 eV, which is equivalent to a temperature of 11000° K*. Therefore, the electron temperature cannot exceed this value, and no doubt should be considerably less.

The measurements of UV-tube performance, described later in Sec. 3.2.2 indicate that the maximum feasible photon flux obtainable lies between 10^{14} and 10^{16} photons $\text{cm}^{-2} \text{ sec}^{-1}$. Therefore, the rest of the considerations

*

Here the temperature is defined so that the energy = kT.

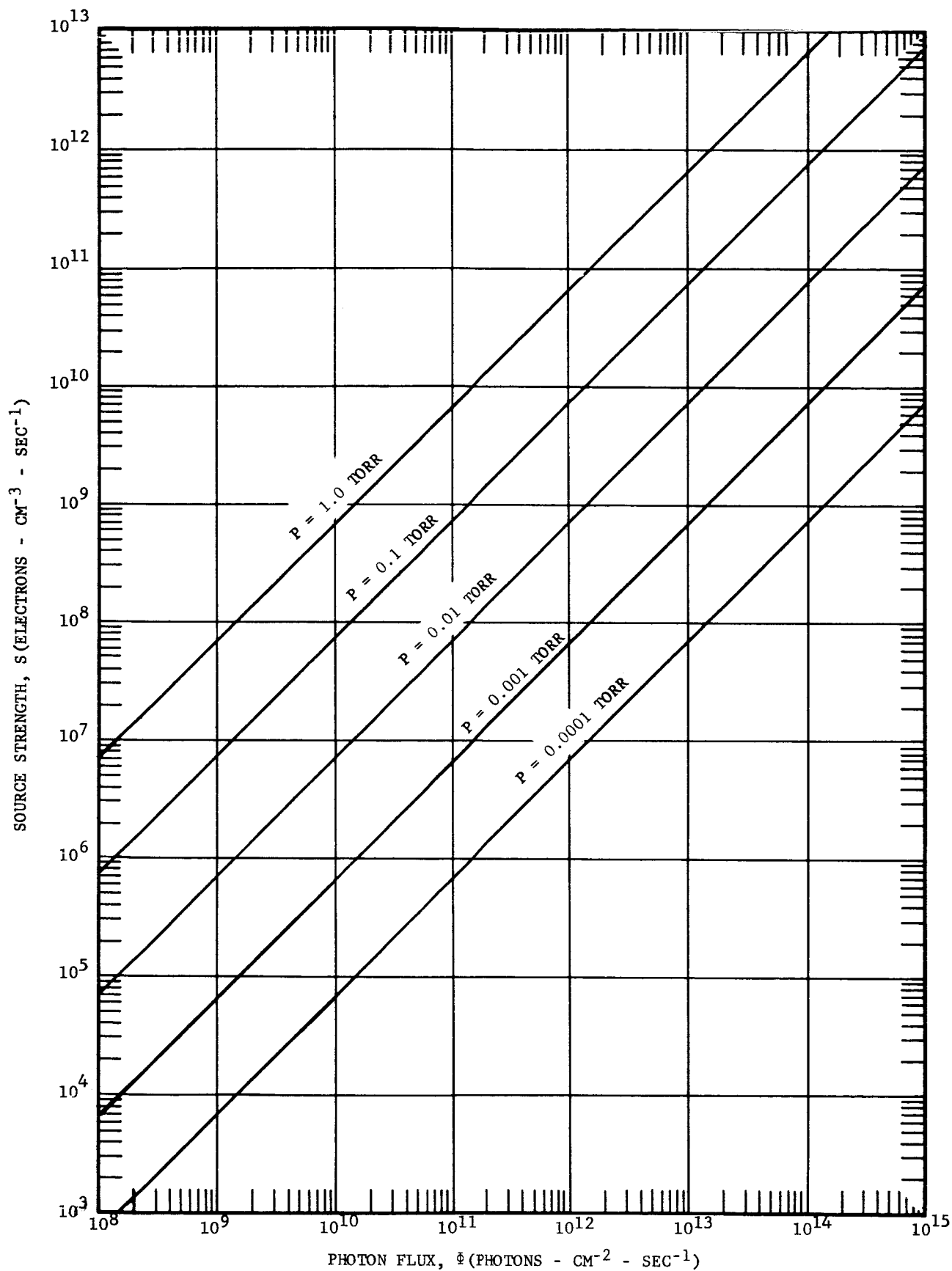


FIG. 6 ELECTRON SOURCE STRENGTH FOR LYMAN- α PHOTOIONIZATION OF NO AS A FUNCTION OF PHOTON FLUX

will pertain to photon fluxes less than 10^{15} photons-cm⁻²-sec⁻¹.

3.2.1.3 Loss Processes

3.2.1.3.1 Recombination

There are three recombination mechanisms. These are radiative recombination ($\text{NO}^+ + e \rightarrow \text{NO} + h\nu$), dissociative recombination ($\text{NO}^+ + e \rightarrow \text{N} + \text{O}$), and three-body recombination ($\text{NO}^+ + \text{NO} + e \rightarrow 2 \text{NO}$). Values of the corresponding recombination rates α_R , α_D , α_B , as given by various referenced authors are given in Table V. The total recombination loss rate L_{α} , is given by

$$L_{\alpha} = \bar{\alpha} n^2 = (\alpha_R + \alpha_D + \alpha_B n^2) \quad (16)$$

where n is the electron density. The electron loss rate for the various recombination mechanisms, as a function of electron density, are plotted in Fig. 7

Table V

Recombination Rate Coefficients for Nitric Oxide

<u>Reference</u>	<u>α_R (cm³-sec⁻¹)</u>	<u>α_D (cm³-sec⁻¹)</u>	<u>α_B (cm³-sec⁻¹)</u>
[2]	3×10^{-12}	3×10^{-6}	10^{-26}
[4]		1.3×10^{-6}	
[5]		$\leq 2 \times 10^{-6}$	
[6]		1×10^{-6}	

for several pressures. In the subsequent calculations, a value of $\alpha_D = 10^{-6}$ cm³-sec⁻¹ is used.

3.2.1.3.2 Attachment

Data on the attachment cross section and rates in NO are almost non-existent. A rough order-of-magnitude guess as to their values can, however, be made by examining the data for oxygen and nitrogen.

There are three processes whereby electrons may be lost from the plasma by attachment. These are radiative ($\text{NO} + e \rightarrow \text{NO}^- + h\nu$), dissociative ($\text{NO} + e \rightarrow \text{N} + \text{O}^-$), and three-body attachment ($\text{NO} + \text{NO} + e \rightarrow \text{NO}^- + \text{NO}$). Making use of data for the

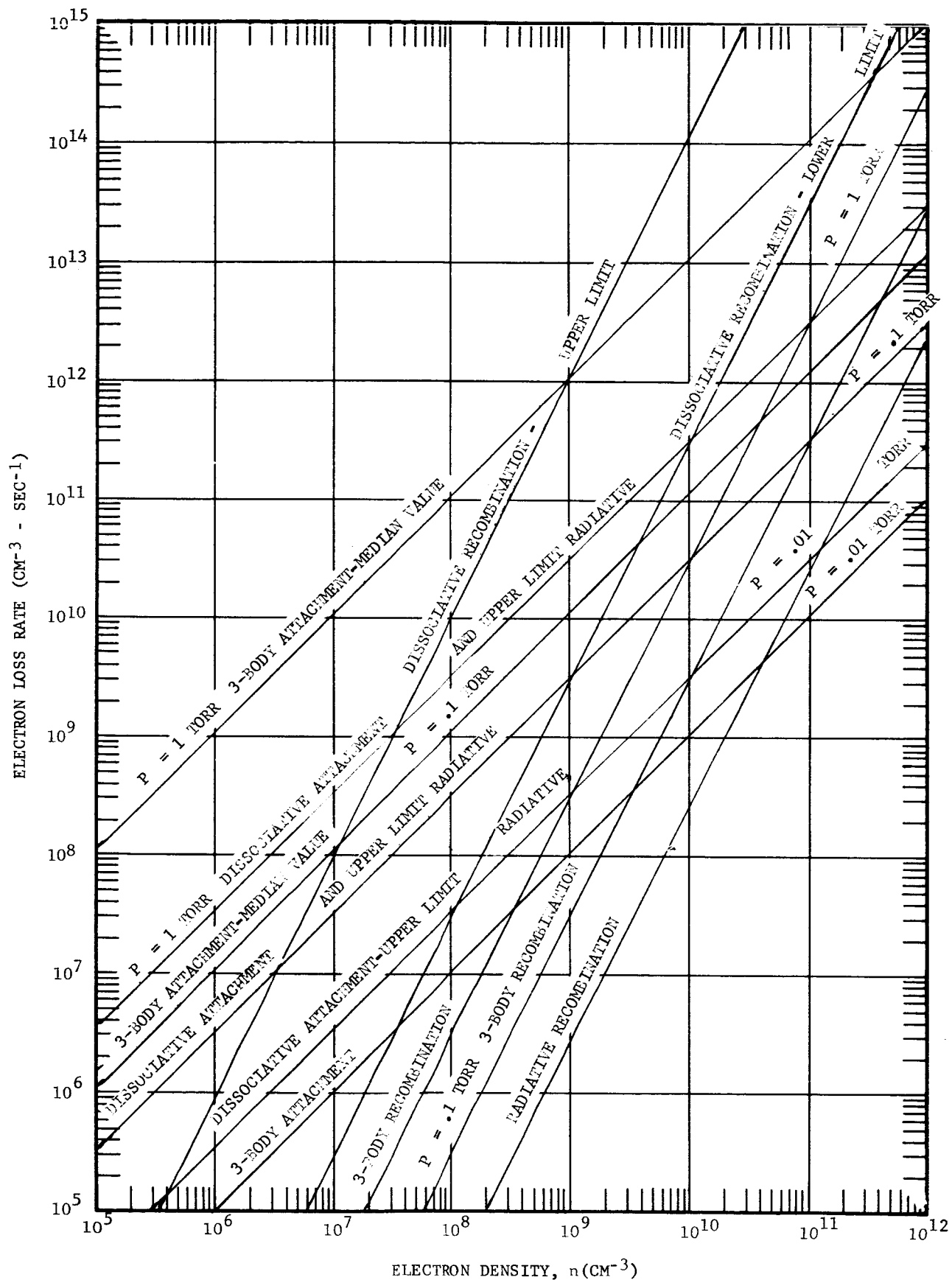


FIG. 7 ELECTRON LOSS RATE IN NO FOR VARIOUS PROCESSES AS A FUNCTION OF ELECTRON DENSITY

analogous processes for nitrogen and oxygen, we find the following estimates for the reaction rate coefficients:

$$\beta_R \sim 10^{-15} \text{ to } 10^{-19} \text{ cm}^3\text{-sec}^{-1}$$

$$\beta_D \sim 10^{-15} \text{ cm}^3\text{-sec}^{-1}$$

$$\beta_B \sim 10^{-30 \pm 2} \text{ cm}^6\text{-sec}^{-1}$$

In [4], we find $\beta_B = 4 \times 10^{-31} \text{ cm}^6\text{-sec}^{-1}$. Thus $\beta_B = 10^{-30} \text{ cm}^6\text{-sec}^{-1}$ is taken as being a reasonable value for the following calculations. The loss rates for the various recombination processes, as a function of electron density, are also shown in Fig. 7 for various pressures. For pressures ≤ 1 Torr, dissociative recombination is the dominant loss process at the higher electron densities ($> 10^{10}$). Three-body attachment is the dominant process for lower densities ($< 10^9$) at 1 Torr. Three-body attachment is comparable to dissociative attachment between 0.1 and 0.01 Torr. At lower pressures, dissociative attachment becomes the dominant loss process at lower electron densities. In Fig. 8 the total loss rate is plotted as a function of electron density with gas pressure as parameter. The total loss rate, L , due to non-diffusive processes is given by

$$L = L_\alpha + L_\beta = (\alpha_R + \alpha_D + \alpha_B N)n^2 + (\beta_R + \beta_D + \beta_B N)nm. \quad (17)$$

3.2.1.3.3 Diffusion

The free diffusion coefficient of a single species is given by

$$D_{\pm} = \bar{c}\lambda_{\pm}/3 \quad (18)$$

where $\bar{c} = (8kT/m)^{1/2}$ is the mean velocity, λ is the mean free path, and + and - denote ions and electrons, respectively. However, when both ions and electrons are present, and the electron and ion densities are sufficiently large, the ions and electrons do not diffuse independently, and the diffusion coefficient is the

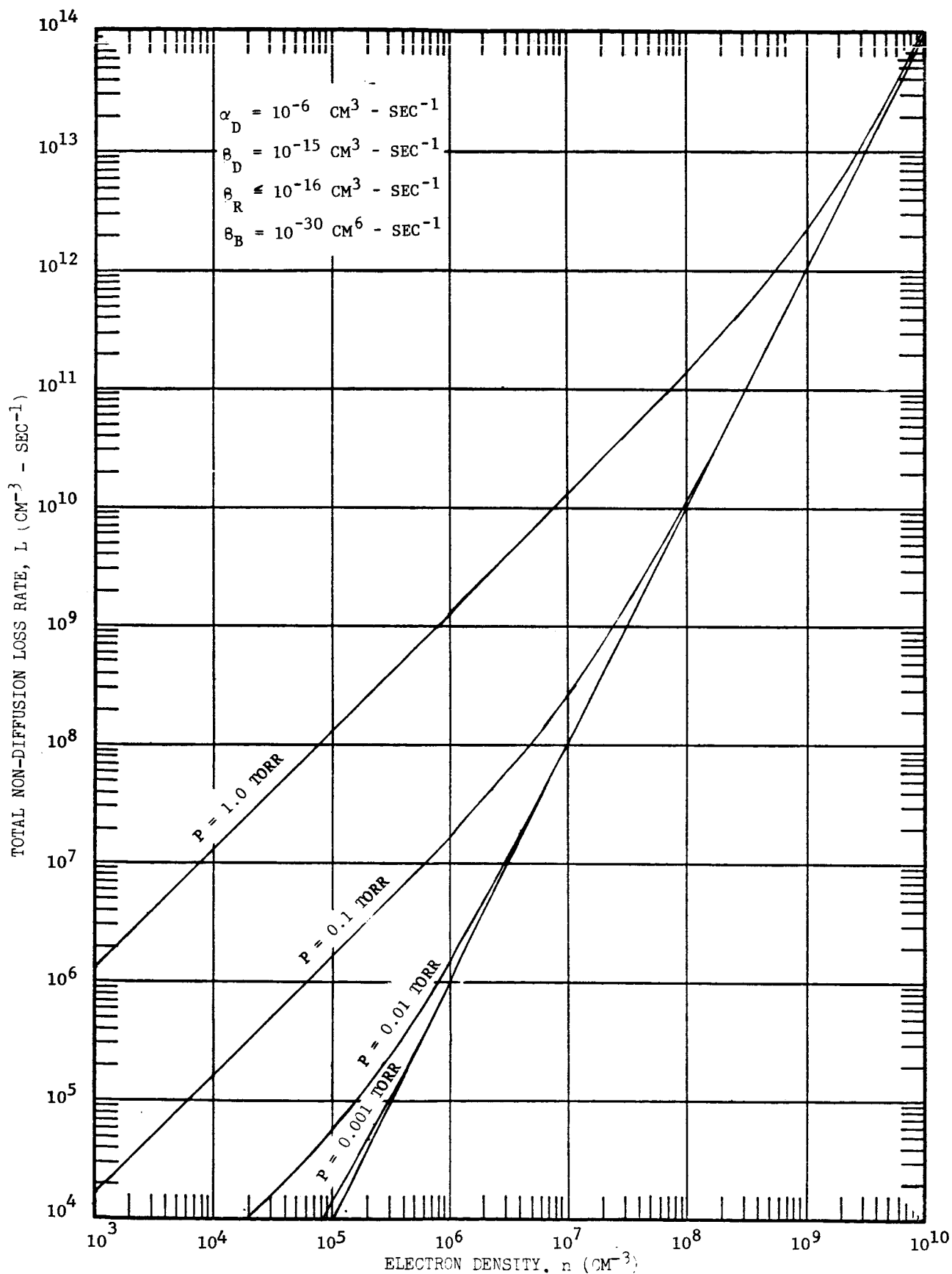


FIG. 8 TOTAL NON-DIFFUSION LOSS RATE IN NO AS A FUNCTION OF ELECTRON DENSITY FOR SEVERAL GAS PRESSURES

Thus at $r = 0$,

$$n = n_0 = (S/4D) a^2 . \quad (25)$$

If $a \neq b$, (22a) and (22b) must be solved simultaneously, subject to the boundary conditions

- 1) at $r = b$, $n_2 = 0$
- 2) at $r = a$, $n_1 = n_2$ and $dn_1/dr = dn_2/dr$

The general solutions of (22) in the two regions are found to be:

$$\text{Region 1: } n_1 = (-S/4D) r^2 + A_2, \quad r \leq a . \quad (26a)$$

$$\text{Region 2: } n_2 = A_3 \ln(r) + A_4, \quad a \leq r \leq b. \quad (26b)$$

Then from the above boundary conditions,

$$n_1 = n_0 \left\{ [2 \ln(b/a) + 1] - (r/a)^2 \right\} \quad (27a)$$

and

$$n_2 = 2n_0 \ln(b/r) . \quad (27b)$$

Thus at $r = 0$,

$$n = n_0 [2 \ln(b/a) + 1] \quad (28)$$

where n_0 is the density that would be obtained if $b = a$.

It is thus seen that the density obtained on axis with the walls located at $r = b$ is equivalent to a bare system with radius a_1 , where

$$a_1 = aC^{-1} \quad (29a)$$

where

$$C^2 = [2 \ln(b/a) + 1]^{-1} . \quad (29b)$$

A plot of C vs. b/a is given in Fig. 9.

(b) For the case $\bar{\alpha} n^2 \ll \beta n$, (21) may be solved for $a = b$.

This is the case of a plasma of sufficiently low density that recombination is not important, but attachment losses are the same order of magnitude as diffusion losses. In this case (22a) may be written

$$r^2 \frac{d^2 n}{dr^2} + r \frac{dn}{dr} = (\beta/D) r^2 n = (-S/D) r^2 \quad (30)$$

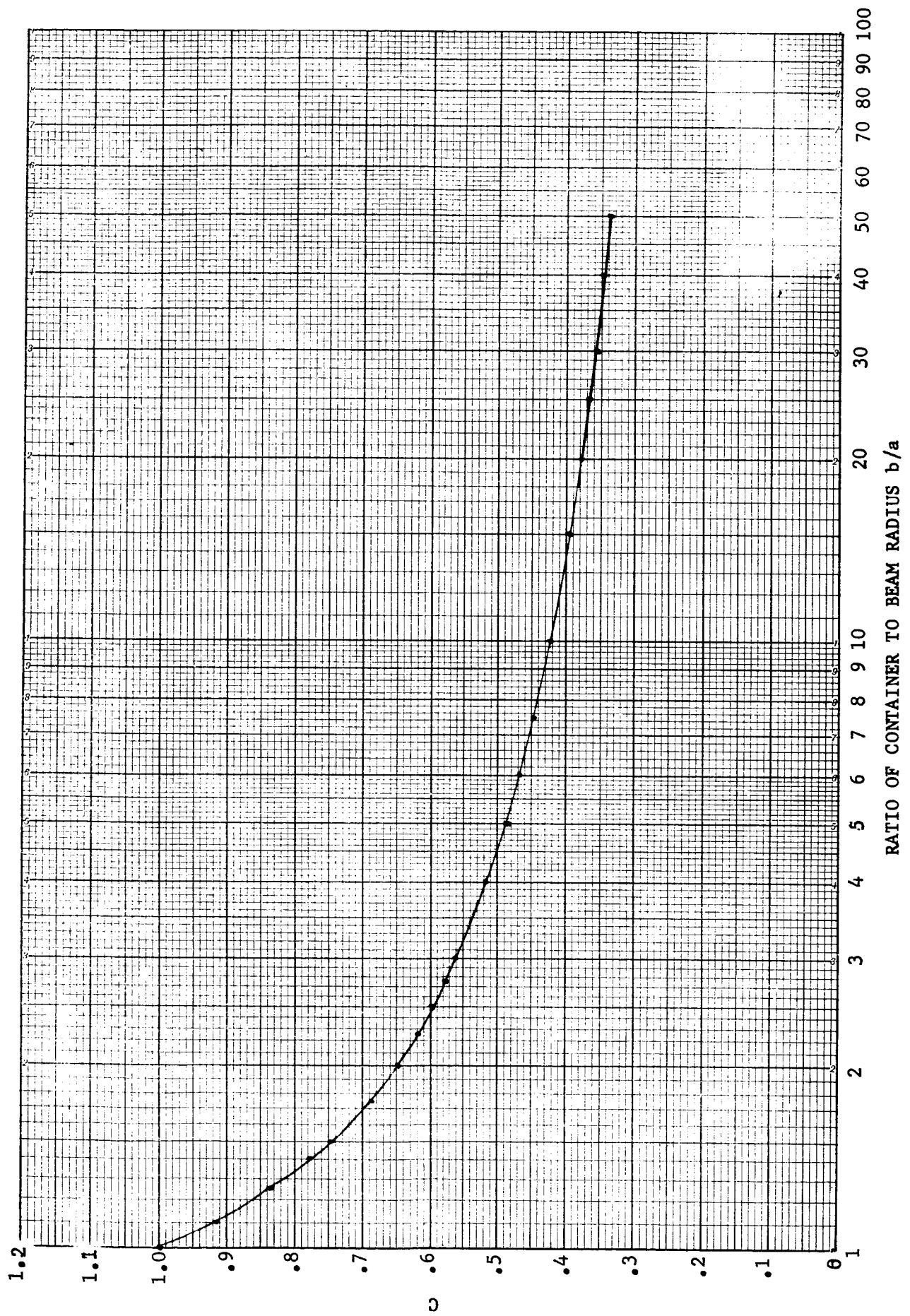


FIG. 9 EQUIVALENT BARE RADIUS FACTOR AS A FUNCTION OF b/a

Clearly, the inhomogeneous equation has the special solution

$$n = S/\bar{\beta} . \quad (31)$$

The homogeneous equation can be transformed into a modified Bessel equation of order zero. Thus a solution of (30) which is finite at $r = 0$ is

$$n = aI_0(\alpha r) + (S/\bar{\beta}) \quad (32)$$

where $\alpha^2 = \bar{\beta}/D$. With the boundary condition $n = 0$ at $r = a$, (32) becomes

$$n = (S/\bar{\beta}) \left\{ 1 - [I_0(\alpha r)/I_0(\alpha a)] \right\} \quad (33)$$

Hence, at $r = 0$,

$$n = n_\beta \left\{ 1 - [I_0(\alpha a)] \right\} \quad (34)$$

where

$$n_\beta = S/\bar{\beta} .$$

For $(\alpha a)^2 \ll 1$, it is easy to show that $n = n_\beta \alpha^2 a^2/4 = n_0$, as it should.

(c) The validity of (22b) is now considered. Clearly (22b) will not be valid throughout the entire region $a \leq r \leq b$. It will be valid, however, in some more restricted region $a \leq r \leq c < b$ when

$$2D n_0/r^2 \gg \alpha n^2 + \bar{\beta} n . \quad (35)$$

At some value of $r = c < b$, the two sides of (35) will approach equality. At this point, the boundary effectively has been reached. This means that there exists some value of b where increasing b no longer decreases the diffusion losses. The mathematics beyond this point becomes quite involved, and no good method of presenting the results is known. However, this will present no major obstacle to the present goal of obtaining a reasonable estimate of the photon flux required to obtain a specified electron density at a specified NO pressure.

3.2.1.4 Plasma Densities

3.2.1.4.1 Infinite Plasma

For an infinite plasma there are no diffusion losses, so that the electron densities, as a function of photon flux, are limited

by recombination and attachment. The electron density can be obtained by setting

$$L = S . \quad (36)$$

Since this is the minimum loss situation, the electron densities so obtained represent upper limits. The result of (36) is plotted in Fig. 10 for various pressures. Fig. 10 illustrates the strange fact that, at sufficiently low photon fluxes, lowering the gas pressure can increase the electron density.

The next question is how large does the plasma have to be in order to be essentially infinite when sitting at the center? When $b = a$, from (24) the losses due to diffusion, L_D , are given by

$$L_D = 4 D n/a^2 . \quad (37)$$

Defining the critical radius a_c to be the radius for which $L_D = 0.1L$, then from (37)

$$a_c = [4Dn_\infty/0.1L]^{1/2} \quad (38)$$

where n_∞ is the electron density for an infinite plasma. The value of a_c as a function of a photon flux obtained from (36) and (38) combined is plotted in Fig. 11 for various pressures. The curves have been smoothed slightly in the transition regions.

If $b \neq a$, then a lower limit on the critical radius can be obtained by multiplying a_c by the factor C^{-1} of (29b) and Fig. 9. The length of the plasma column should be roughly $10 a_c$.

3.2.1.4.2 Finite Plasma

For a finite plasma, we consider as a typical case one which can be generated in the chamber. In this chamber, 8-inch diameter ports are available at each end for bringing in the UV beam. Thus, $a \approx 10$ cm. The chamber is approximately one meter in diameter and approximately two meters long. On the basis of the preceding discussion, in order to estimate the electron density that can be produced in this chamber as a function of photon flux, n has

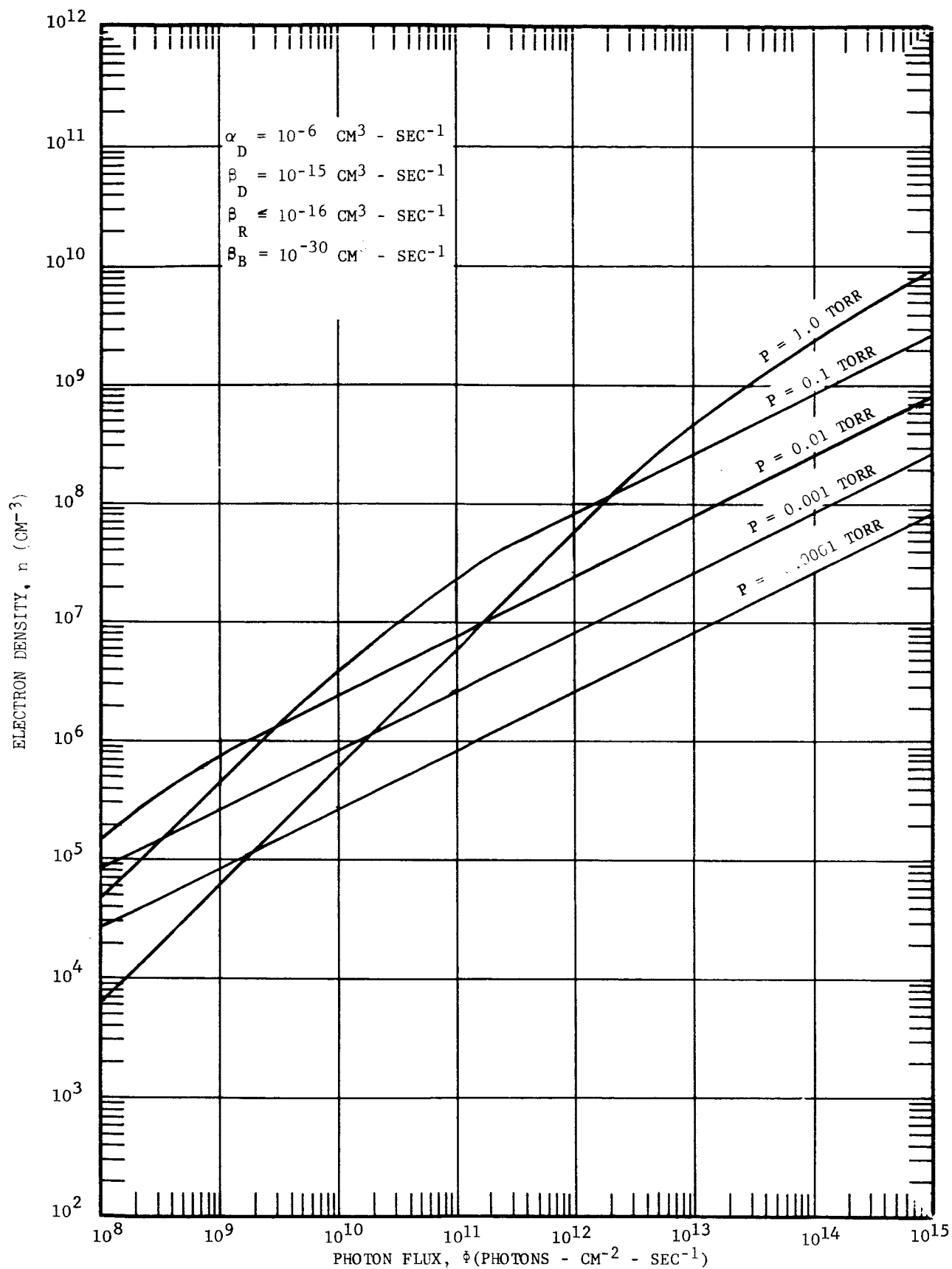


FIG. 10 INFINITE PLASMA ELECTRON DENSITIES AS A FUNCTION OF PHOTON FLUX FOR VARIOUS PRESSURES

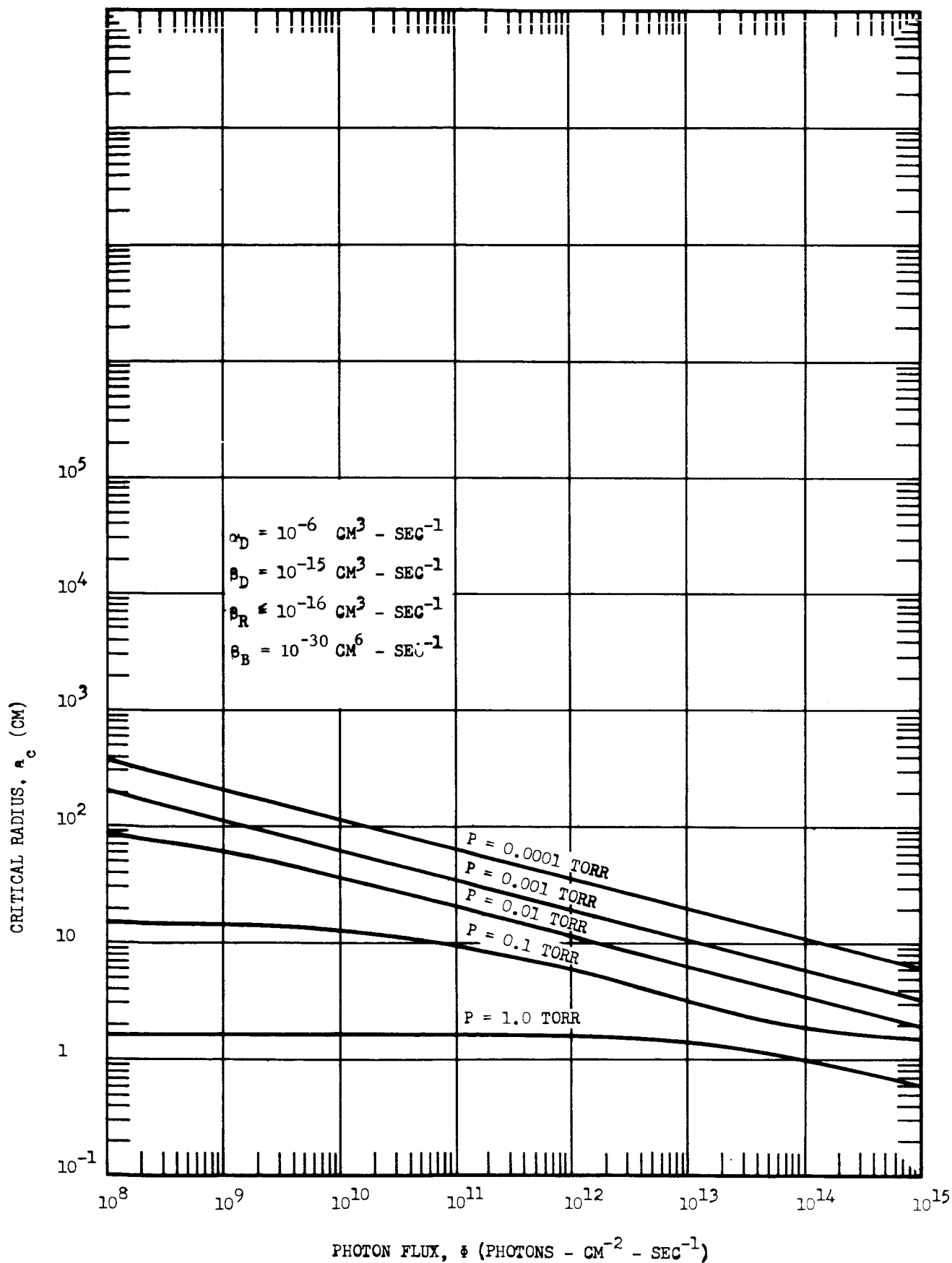


FIG. 11 CRITICAL RADIUS AS A FUNCTION OF PHOTON FLUX FOR VARIOUS PRESSURES

been calculated as a function of photon flux for $a = 10$ cm, $b/a = 1$ for pressures ranging from 10^{-4} to 1 Torr. The results are plotted in Fig. 12. At $p = 1$ Torr, the electron density on axis is essentially that for an infinite plasma. At $p = 0.1$ Torr, and for electron densities below the transition point between recombination- and attachment-limited loss, the losses are a mixture of attachment and diffusion, so that (35) was used in the calculation. For pressures $\leq 10^{-2}$ Torr, the losses are dissociative recombination limited for high fluxes, and diffusion limited for low fluxes. No attempt was made to calculate the transition regions between the attachment-limited and diffusion-limited regimes accurately. Densities in these portions of the curves are shown dashed.

Since it has been assumed that $b/a = 1$, the electron densities of Fig. 12 are on the low side. On the other hand, if sufficient thermalization does not take place, or if the assumed value of D_a is too small, or if at the lower electron densities the diffusion tends away from ambipolar to free diffusion (see [8], p. 91-95), the values in Fig. 12 may be several orders of magnitude too large. Assuming for the moment that the values of Fig. 12 are correct, it is seen that a flux of 10^{14} photons-cm $^{-2}$ -sec $^{-1}$ is sufficient to produce an electron density greater than 10^4 cm $^{-3}$ at a pressure of 10^{-4} Torr, and greater than 10^5 cm $^{-3}$ at 10^{-6} Torr. Even if the diffusion is completely free and the loss is actually given by D_{\perp} , which is about two orders of magnitude greater than D_a , a photon flux of 10^{14} cm $^{-2}$ would give an electron density greater than 10^4 cm $^{-3}$ at $p = 10^{-3}$ Torr. Thus photon fluxes greater than 10^{14} photon-cm $^{-2}$ -sec $^{-1}$, would produce sufficient densities for L-Region simulation in this size system, provided certain conditions to be discussed in the next two sections are met. These conditions involve ion and electron mean free paths, sheath thicknesses, and thermalization.

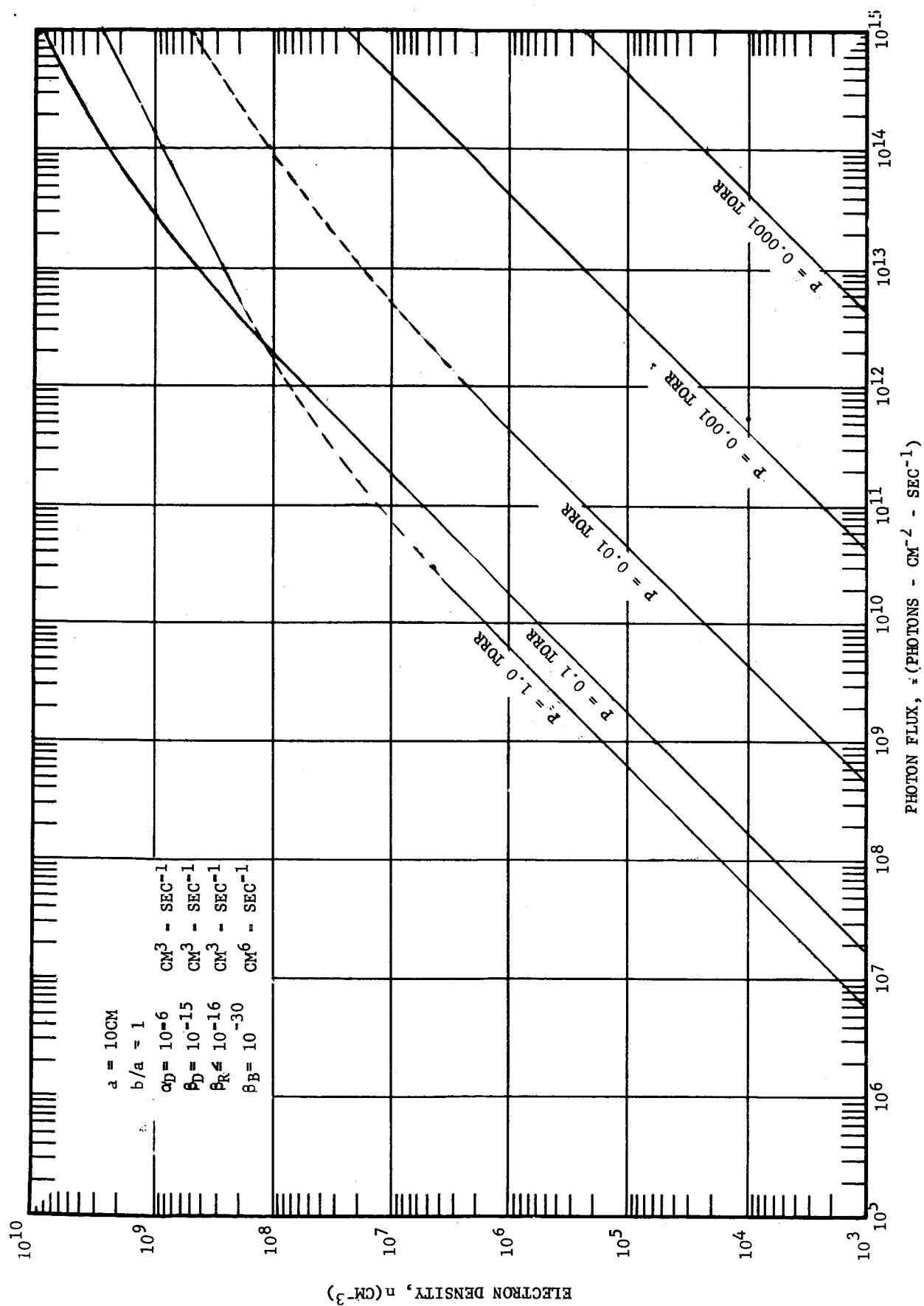


FIG. 12 THEORETICAL ELECTRON DENSITIES AS A FUNCTION OF PHOTON FLUX FOR THE LARGE HIGH VACUUM CHAMBER WITH PRESSURE AS A PARAMETER

3.2.1.5 Mean Free Paths and Sheath Size

For good D-Region simulation and to have a true plasma, it is required that the following conditions be met:

- (a) The ion mean free path $\lambda_i \ll a$.
- (b) If possible, the electron mean free path $\lambda_e \ll a$.
- (c) The Debye length $\lambda_D \ll a$.
- (d) Sheath size $x \ll a$.

These conditions must be met by any simulation system and really serve to establish a lower limit on the size of the simulation region.

So far, data on mean free paths of ions and electrons in NO have not been found. However, those for N_2 should be reasonably close. [7] gives the values for λ_i and λ_e shown in Table VI.

Table VI

Ion and Electron Mean Free Paths in N_2 as a Function of Pressure

<u>p (Torr)</u>	<u>λ_i (cm. at 0.03 ev)</u>	<u>λ_e (cm. at 0.03 ev)</u>	<u>λ_e (cm. at .5-1 ev)</u>
1	5×10^{-3}	0.62	5×10^{-2}
0.1	5×10^{-2}	6.2	5×10^{-1}
0.01	5×10^{-1}	62	5
0.001	5	620	50

From these values it is seen that condition (a) is met for all pressures $\geq 10^{-3}$ Torr and condition (b) on λ_e is not met for pressures much less than 1 Torr. If thermalization has taken place and $n \geq 10^4 \text{ cm}^{-3}$, $\lambda_D \leq 1.2 \text{ cm}$. Since the Debye length is governed by the ion temperature [9] and the ions are thermalized in a couple of collisions, the condition on λ_D will be met for all gas pressures $\geq 10^{-3}$ Torr.

To estimate the sheath size, it is possible to make use of the fact that the plasma will assume a potential such that the walls are at a potential V_f

ambipolar diffusion coefficient, which is given by

$$D_a = (D_- \mu_+ + D_+ \mu_-) / (\mu_+ + \mu_-) \quad (19)$$

where μ is the mobility. Furthermore [7, p. 123], if $\mu_- \gg \mu_+$ and $T_e \gg T_i$

$$D_a = k T_e \mu_+ / e = T_e \mu_+ / 11,606. \quad (20)$$

Gunton and Inn [4] find that $D_a = (80/p) \text{ cm}^2\text{-sec}^{-1}$, where p is expressed in Torr at an estimated temperature of 0.04 eV.

In the following calculation, the fact that electrons of higher energy diffuse faster will be neglected, and only the loss of thermal (i.e., approximately 3×10^4 K) Maxwellian-distributed electrons will be considered. A cylindrical photon beam of radius a , passing through a cylindrical column of NO of radius b , $b \geq a$, will be considered. Then

$$D \nabla^2 n - (\bar{\alpha} n^2 + \bar{\beta} n) = \begin{cases} -S, & r \leq a. \\ 0, & a \leq r \leq b. \end{cases} \quad (21)$$

Subject to the boundary condition that the plasma density goes to zero at the walls*, this equation may be solved for the case of an infinitely long cylinder under several sets of useful conditions:

(a) For a plasma where losses due to diffusion are dominant, i.e.

$L \ll S$, we have for $r \leq a$

$$D \nabla^2 n = -S. \quad (22a)$$

For $a \leq r \leq b$

$$D \nabla^2 n = 0. \quad (22b)$$

For an infinitely long cylindrical plasma column, (22a) reduces to

$$\frac{d^2 n}{dr^2} + \frac{1}{r} \frac{dn}{dr} = -S/D. \quad (23)$$

If $a = b$, i.e., the walls occur at the beam boundary,

$$n = \left\{ -S/4D \right\} (r^2 - a^2). \quad (24)$$

*

This boundary condition is only approximate. It leads to an overestimate of the losses and, hence, an underestimate of the electron density.

with respect to the plasma, where V_f is given by [10]

$$V_f = - (T_e/23,212) \ln(m_e T_e / m_e T_+) . \quad (39)$$

Then, for a planar geometry, the sheath size is given in turn by [11]

$$x^2 = 2.336 \times 10^{-8} V^{3/2} [1 + (2.66/\sqrt{\eta_+})] \sqrt{m_e/m_+} / j_+$$

where

$$\eta_+ = eV/kT_+ = 11,606V/T_+$$

and j_+ is the random ion current density given by

$$j_+ = (8kT_+/2\pi m_+)^{1/2} en .$$

Thus

$$x^2 = 5.04 \times 10^4 \sqrt{\phi_+} V^{3/2} [1 + (2.66/\sqrt{\eta_+})] / n \quad (40)$$

where $\phi_+ = 11,606/T_+$. x , for $T_+ = 300^\circ$ K, is shown in Fig. 13 as a function of electron density for several electron temperatures. It is seen that condition (d) is met, provided that the electron temperature is not much higher than 300° K.

3.2.1.6 Thermalization

Thermalization is the process whereby a group of particles (here electrons or ions) born at some energy higher than the mean thermal energy of the surrounding medium comes into thermal equilibrium with this medium. This occurs as a result of energy transfer from the particles to the medium by collisions, and thus is dependent on the details of the collision process.

Since an NO ion in NO can lose a large fraction of its energy excess in one elastic collision, it takes only a few collisions for the ion to reach equilibrium with the gas, so that the ion temperature will be substantially the same as the gas temperature if the beam size is greater than the ion mean free path. i.e., $a > \lambda_+$ (see Table VI). On the other hand, for an electron, because of the small ratio of electron to molecule or ion mass, it takes many elastic collisions (approximately 10^4 to 10^5) to come into equilibrium with the gas. Hence the slowing down of electrons is very dependent on the details of the

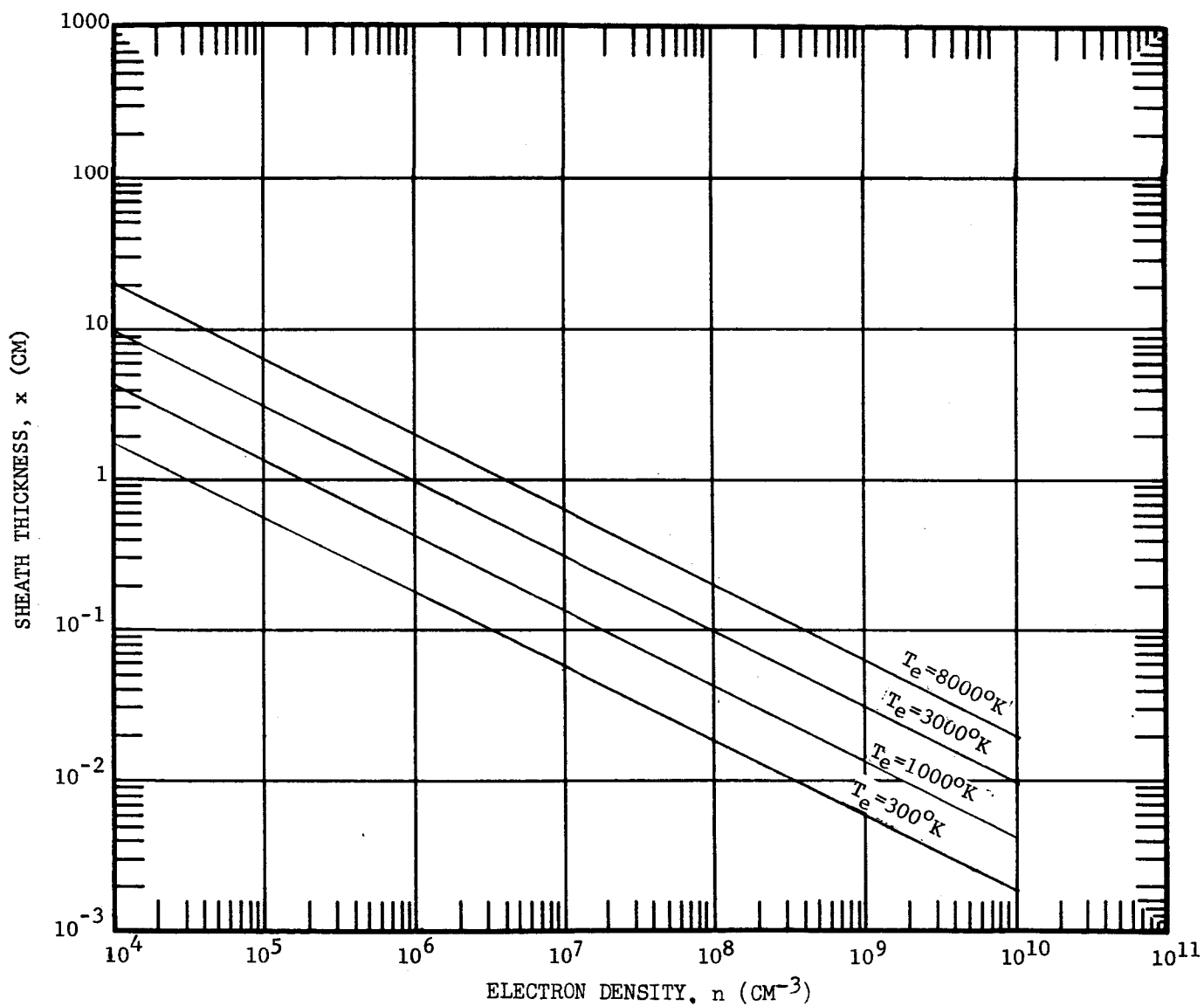


FIG. 13 PLANAR SHEATH THICKNESS AS A FUNCTION OF ELECTRON DENSITY FOR SEVERAL ELECTRON TEMPERATURES, $T_i = 300^\circ\text{K}$

energy loss during a collision, which, in turn, affects the energy dependence of the collision frequency. For the energy range of interest, 0.025 ev to 1 ev, these details are not known for NO. Consequently, this will lead to some uncertainty in the results of the calculations below.

While slowing down, the electron will travel some mean "crow flight" distance, R , from its point of birth. If the system dimensions are greater than R , then the electrons will come to equilibrium with the gas, resulting in a relatively cold plasma. If the dimensions are less than R , however, then thermalization will not occur. In this case, a result of the nature of the dependence of R on initial and final electron energy, the plasma will be warm (several 1000° K). Since the distance R obviously will decrease with increasing pressure, there will be some pressure around which the transition from a warm to a cold plasma takes place.

In the following, some calculations are made to determine this approximate transition pressure for a large volume plasma in the large high-vacuum chamber.

An estimate of R may be obtained by means of Fermi age theory. R is related to the age τ by $\tau = R^2/6$. In turn, the age for slowing down from energy E_0 to energy E is given by [12]

$$\tau(E) = \int_E^{E_0} [D_a/\xi \ N_s(E)v] dE/E \quad (41)$$

where $\sigma_s(E)$ is the electron scattering cross section at energy E , v is the electron velocity, and where ξ is the average logarithmic energy decrement. For the case at hand, ξ is given by

$$\xi = 2m_e/m = 3.63 \times 10^{-6} \quad (42)$$

Making use of (20), (41) becomes

$$\tau(T) = \int_T^{T_0} [\mu_+ k / (e\xi v_c(T))] dT \quad (43)$$

where

$$\nu_c(E) = N \bar{\nu}_s(E) v = p P_c(E) v \quad (44)$$

is the electron collision frequency at energy $E = kT$, $v = (2kT/m)^{1/2}$ is the thermal velocity, P_c is the collision probability at pressure $p = 1$ Torr, $T_0 = E_0/k$, and $T = E/k$. Since μ_+ and ξ are independent of electron energy, (43) reduces to

$$\tau(T) = [\mu_+ k / (e \xi)] \int_T^{T_0} dT / \nu_c(T) . \quad (45)$$

Clearly, to proceed further one must know something about the energy dependence of ν_c . Two cases are considered: In the first, ν_c is assumed constant. In the second, ν_c is assumed to vary linearly with energy.

(a) ν_c constant

If ν_c is constant, (45) becomes

$$\tau(T) = [\mu_+ k / (e \xi \nu_c)] (T_0 - T) . \quad (46)$$

To evaluate this, we need to find μ_+ and ν_c . For μ_+ we make use of the result from [7] that for $T_+ = T_-$

$$D_a = 2 T_0 \mu_+ k / e .$$

Using $D_a = 80/p \text{ cm}^2\text{-sec}^{-1}$, this gives, for $T_- = 300^\circ \text{ K}$,

$$D_a = (80/p) \text{ cm}^2\text{-sec}^{-1}, \mu_+ = (1.55 \times 10^3/p) \text{ cm}^2\text{-sec}^{-1}\text{-volt}^{-1} .$$

Since collision frequency data for ND are not available, we use the values for N_2 as a first approximation. Then from [7] we obtain $P_c \approx 1.6$ at 300° K ; from [8] we obtain $P_c \approx 20$ at 0.95 ev ($11,000^\circ \text{ K}$). Insertion of these values into (46) leads to

$$\nu_c = 1.525 \times 10^7 p \text{ sec}^{-1} \text{ at } 300^\circ \text{ K}$$

$$\nu_c = 1.155 \times 10^9 p \text{ sec}^{-1} \text{ at } 0.95 \text{ ev } (11,000^\circ \text{ K}) .$$

These two values are two orders of magnitude apart, and belie the assumption that ν_c is constant. Nevertheless, taking the arithmetic average of these two values for the value of ν_c to be used in (46), we find that for slowing down

from 0.95 ev to 300° K

$$\tau = 6.73 \times 10^{-2} / p^2 \text{ cm}^2$$

and thus, that

$$R = (0.635/p) \text{ cm} . \quad (47)$$

(b) ν_c a Linear Function of Energy

Assuming that the electron collision frequency varies with energy

as

$$\nu_c = a + bT, \quad (48)$$

(45) becomes

$$\tau(T) = [\mu_e k / (eE)] b^{-1} \ln[\nu_c(T_0) / \nu_c(T)] . \quad (49)$$

Fitting (48) to the two end points gives

$$a = -1.71 \times 10^7 \text{ sec}^{-1} \text{ and } b = 1.066 \times 10^5 \text{ } ^\circ\text{K}^{-1} \text{ sec}^{-1} .$$

Hence, from (49) we have for thermalization from .95 ev to 300° K :

$$\tau = (0.15/p^2) \text{ cm}^2$$

so that

$$R = (0.95/p) \text{ cm} . \quad (50)$$

The two estimates (47) and (50) differ by a factor of only 1.5, in spite of the different assumptions regarding ν_c .

If thermalization is to occur, then we should have $a > R$. Taking the larger of the estimates (47) and (50), we find $R = 0.95 \text{ cm}$ for $p = 1 \text{ Torr}$. Thus, thermalization definitely should occur for $p > 0.1 \text{ Torr}$ in the chamber.

We now have to examine closely the assumptions that the collisions are elastic and that ν_c varies linearly with energy, which lead to (48). No data, of course, are available on the detailed energy dependence of P_c for energies much below 1 ev. However, the NO molecule has many vibrational and rotational energy levels lying in this energy range. Thus, one would expect that the collision cross section would remain large until the electron energy has dropped

below the lowest level. Further, these collisions should be inelastic, with much greater energy degradation (perhaps by a factor of 10 or more) than implied by (42). Such behavior is exhibited by most diatomic molecules (see [7], p. 107) and accounts for the linear dependence of the electron drift velocity on E/p in diatomic gases. Thus (50) should represent an upper limit on R , and the actual value of R could be as much as a factor of 10 or more less than the value given by (50). An estimate of these effects may be obtained by taking P_e to be constant at its value for 1 ev ($P_e \approx 20$) and assumes ξ to be 10-times greater than the value in (42); then from (44) and (45) we find

$$R = 0.19/p \text{ cm}.$$

Thus, for $0.1 \text{ Torr} > p \geq 0.005 \text{ Torr}$ we have a transition region where the question of thermalization in the chamber is still open. Below approximately 0.005 Torr, thermalization clearly would not take place.

One way of reducing the electron temperature is to use lower energy photons, and thus impart a lower excess energy to the electrons at birth. Krypton has a resonance line at 1236A, which would result in an electron birth energy of 0.75 ev. Thus a krypton discharge, instead of hydrogen, should yield somewhat lower electron temperatures. In addition, the use of a buffer gas with high scattering cross section could give an additional improvement.

3.2.1.7 Conclusions

The results of the theoretical study lead to the following conclusions and recommendations:

- 1) A photon flux of 10^{14} to 10^{15} photons-cm⁻²-sec⁻¹ is sufficient to generate adequate electron densities for D-region simulation for total gas pressures down to 10^{-4} Torr in the chamber.
- 2) The electron temperature in the chamber will be that of the gas for pressures equal to or greater than 10^{-1} Torr. For $0.1 \text{ Torr} > p \geq 0.005 \text{ Torr}$ a transition region occurs where the degree of thermalization is still an open

question. For $p < 0.005$ Torr thermalization will not occur to any great extent and the electron temperature will be in the order of several thousand degrees.

3) A somewhat lower electron temperature should be obtainable with a krypton discharge.

4) The use of a buffer gas with large electron scattering cross section should further enhance thermalization and thus result in lower electron temperatures.

3.2.2 Experimental Feasibility Study

3.2.2.1 UV Sources

3.2.2.1.1 Introduction

The preceding theoretical study indicated that UV-tubes having hydrogen Lyman- α photon fluxes of 10^{14} to 10^{15} photons-cm⁻²-sec⁻¹ in a photon beam of 10-cm radius, would provide adequate D-Region simulation in the large high-vacuum chamber. If it is assumed, from practical considerations, that the upper limit on window size for a given tube is approximately 5-cm diameter, and that the upper limit on power dissipation for any one tube is approximately 100 watts (5 watts-cm⁻²) then, since one hydrogen Lyman- α photon has an energy of 1.6×10^{-11} erg, the values of maximum photon flux as a function of efficiency may be calculated. These calculations are given in Table VII, allowing for a lithium fluoride (LiF) window transmission of about 35%.

Table VII

Maximum Photon Flux as a Function of Source Efficiency (maximum dissipation 5 watts-cm ⁻² of window)	
<u>Efficiency (percent)</u>	<u>Maximum equivalent Hydrogen Lyman-α Photon Flux (photons-cm⁻²-sec⁻¹)</u>
1.0	10^{16}
0.1	10^{15}
0.01	10^{14}

Table VII indicates that UV sources having efficiencies of 0.01 to 0.1% are required. A part of the present program was to demonstrate that a UV source having the required efficiency could be made. In addition, some of the problems of large tube fabrication were investigated.

3.2.2.1.2 Tube Design Considerations

The only known commercially available sealed DC discharge UV source tube is manufactured by GBL Associates according to an NRL design. This tube type is not suitable for the present application. The discharge beam is produced in a capillary tube only 2-3 mm in diameter, and the tube has a low efficiency (in the order of 10^{-3} percent). Consequently, design improvements were necessary to raise the tube efficiency and beam cross section in order to obtain a much higher photon flux output.

From a consideration of the GBL tube geometry, it was surmized that the low efficiency may be due to two factors: First, only those photons in the area of the beam impinging upon the LiF window escape and are effective. From geometrical considerations, this area is only about 0.5 percent of the total surface area of the capillary tube. The second possible source of inefficiency may be absorption in the discharge tube, with consequent line reversal.

These were the primary reasons which lead to consideration of several approaches to improve the source tube efficiency in order to obtain the requisite size beam. These approaches were:

(a) Use of thin planar d-c discharge tube, one side of which is the LiF window. Under proper conditions this should place a large percentage of the total surface area of the discharge (approaching 50 percent) against the LiF window, minimizing absorption and geometrical losses.

(b) Addition of a hot tungsten filament to the GBL tube. It was thought that the hot tungsten filament would dissociate the hydrogen and decrease the total power consumption for a given UV output.

(c) A "scaled-up" GBL tube with or without dissociation filaments.

(d) Develop a low-voltage (20 to 40 volts), high-current-density sheet electron beam directly behind and parallel to the LiF window. In this tube the

pressure would be adjusted so that the distance between the accelerating grid and the anode would be about one mean free path for excitation. This would be a low voltage device in contrast to a DC discharge system, and should operate with high photon to DC power efficiency.

(e) Develop a DC discharge within a cylinder of LiF. This design places the maximum possible area of the source against the LiF.

(f) Use other gases, such as neon, helium, or krypton mixed with the hydrogen to decrease self-absorption and to improve discharge efficiency. This approach utilizes the Penning effect to decrease the energy for ionization and theoretically should lead to a considerable improvement in efficiency. This approach also contemplates the possible use of krypton alone, since it produces output in the usable wavelength range and can lead to very long-lived tubes [15].

3.2.2.1.3 Window Seal

The problem of sealing the LiF window to the glass body of the hydrogen discharge tube has been considered in some detail. The somewhat standard approach is to seal the LiF window to the tube with silver chloride (AgCl). Both the edge of the window and the glass are silvered and then the AgCl is melted into place. The full technique is described in [13] and [14]. This approach is reliable for windows having diameters less than about 7/16 inch (although windows up to 3/4 inch diameter have been successfully sealed, [13]). With larger windows, the following problems arise: After installation of the window, the tubes need to be baked* at about 450-500°C to outgas the glass envelope and discharge electrodes. The large difference in coefficients of expansion of the LiF and the glass body causes the glass body to crack during or after the baking process.

★

For non-baked tubes an epoxy resin with the trade name Torr-Seal works quite well, and Wikinson [15] now uses black sealing wax (Apiezon W).

LiF has a high coefficient of thermal expansion ($37 \times 10^{-6}/^{\circ}\text{C}$). Because of this, it appears that, if normal techniques are used, and a high temperature (400°C) bake after sealing is required, it will be impossible to seal a 2-inch LiF window directly to Pyrex, but that it might be possible to seal a 2-inch window directly to aluminum, and, possibly, to silver, copper, or stainless steel.

Several methods of avoiding the problem of differential thermal expansion between the window and the envelope appear to be possible:

(a) The baking can be carried out in vacuum before the window is sealed. After cooling down, the window is sealed on, the entire operation being performed under vacuum. The mechanical arrangements required for this procedure appear to be practicable.

(b) A bellows type of joint between the window and the envelope could be introduced to take up the differential expansion.

(c) For application to experiments in the chamber, thorough outgassing by a high temperature bake probably could be dispensed with. Instead, the UV-tubes could be filled just prior to an experiment. The useful life then probably would be one or more days, which should be adequate for any one experiment. The tubes then could be rejuvenated by flushing and refilling with a clean mixture, while the chamber was being prepared for the next set of experiments.

(d) As a further improvement over (c), a continuous flow system could be set up to maintain gas purity.

3.2.2.1.4 Experimental Tubes

After consideration of the factors discussed above, a number of experimental tubes were fabricated. Of the approaches (a)-(f) discussed in Sec. 3.2.2.1.2, (d) and (e) were rejected as being outside the scope of the present program. The remaining ideas were embodied in one or more experimental tubes.



FIG. 14 STANDARD DISCHARGE TUBE WITH DISSOCIATION FILAMENTS, TUBE A-5

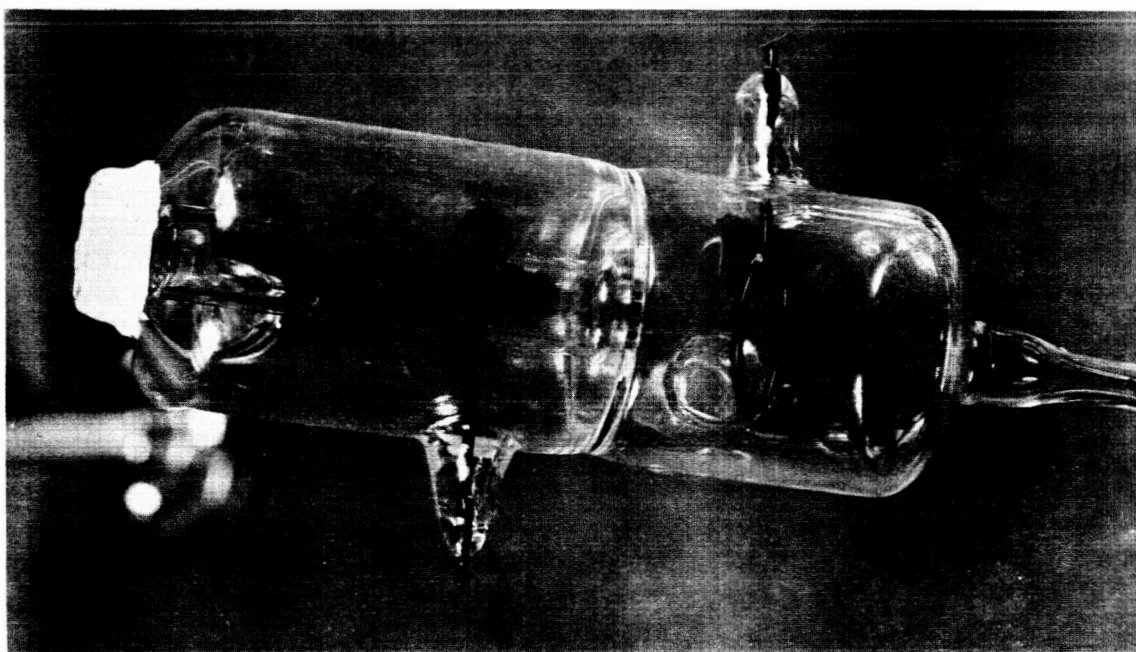


FIG. 15 "SCALED" STANDARD DC DISCHARGE TUBE WITH ONE
CENTIMETER DIAMETER BEAM, TUBE D-3

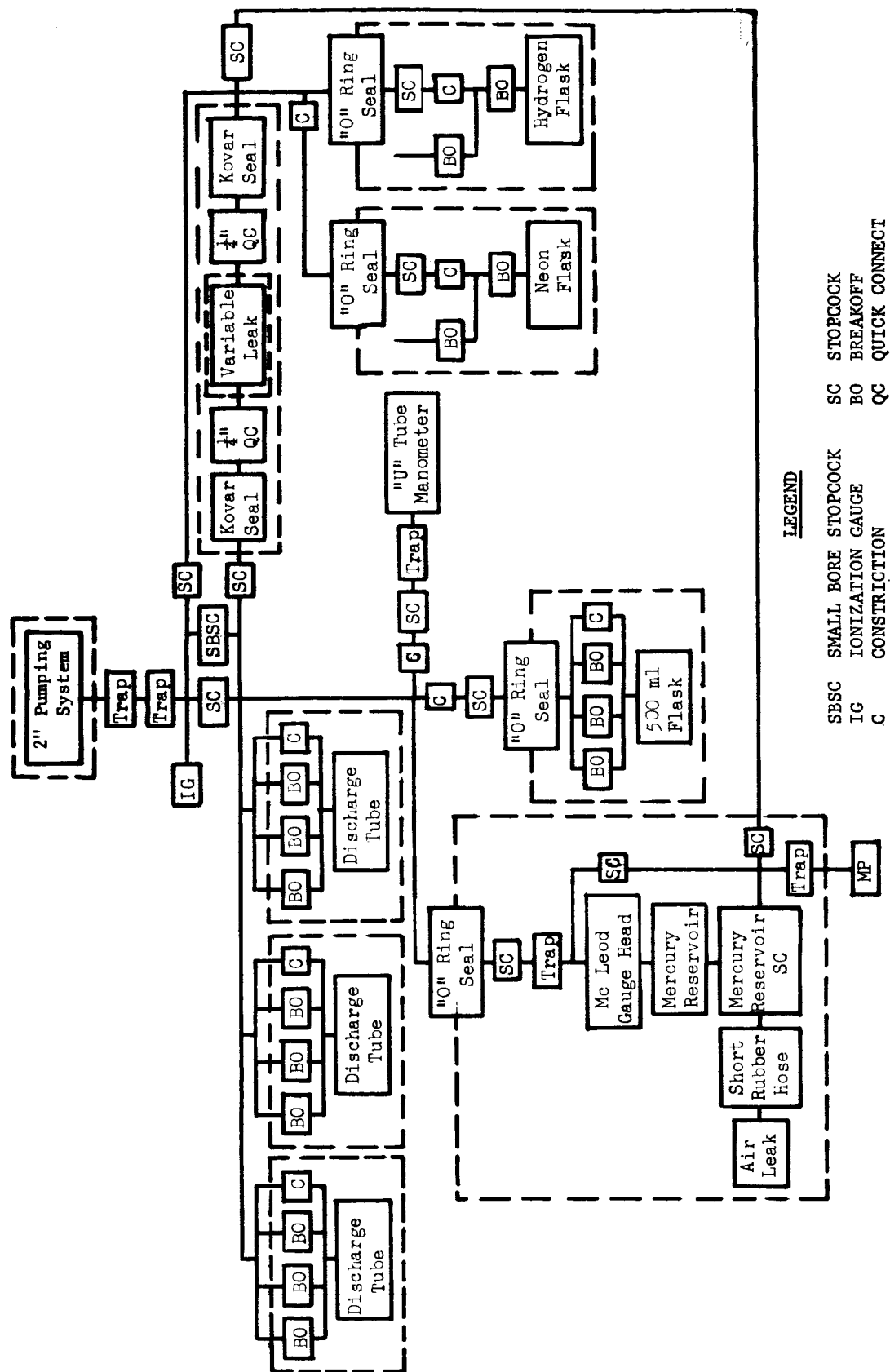


FIG. 16 GAS HANDLING SYSTEM FOR FILLING DISCHARGE TUBES: BLOCK DIAGRAM

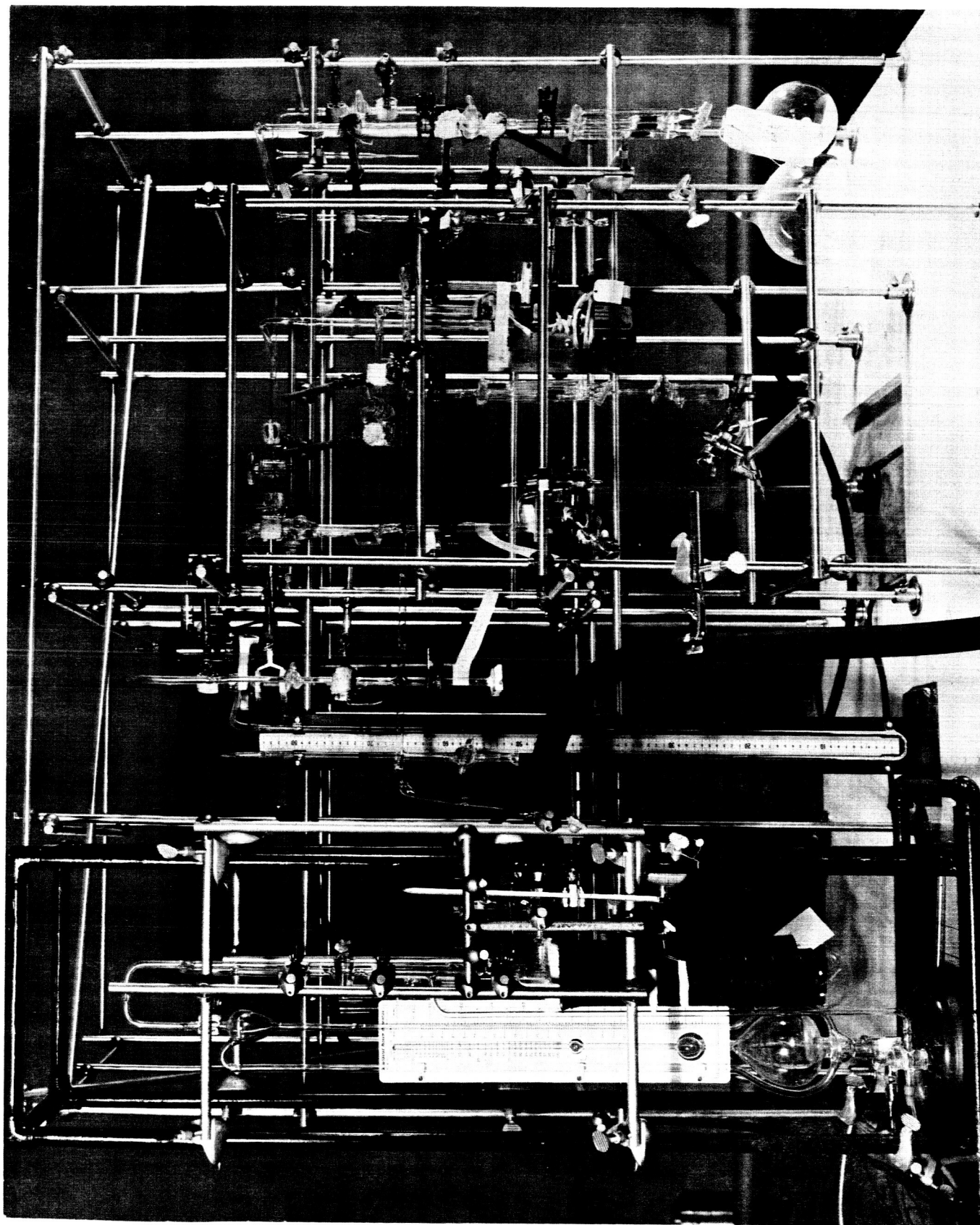


FIG. 17 GAS HANDLING SYSTEM

In order to have available a reference standard, several tubes were fabricated after the GBL design. These will be referred to as "standard" tubes, and will be designated as tubes A-1, A-2, or A-3. In addition, three tubes of this design, but with tungsten filaments added, were fabricated. This will be designated as A-4, A-5, or A-6. One of these is shown in Fig. 14.

Two types of planar discharge tubes were designed and constructed. The first type had a non-confined geometry where the electrodes were located next to the window with a large volume behind the window. These tubes will be referred to as B-1, B-2, B-3, or B-4. The second type had a confined geometry, where the discharge was physically confined between two closely spaced glass plates, one of which contained the LiF window. These tubes will be referred to as B-5 and B-6. In B-1, B-2, and B-3, the windows were sealed with AgCl, while B-4, B-5, and B-6 were sealed with Torr Seal.

Three scaled-up versions of the standard design were constructed; these will be designated as D-1, D-2, or D-3. In D-1, the window was sealed with AgCl, but cracked at the seal on cooling. D-2 and D-3 were sealed with Torr Seal. One of these tubes is shown in Fig. 15.

3.2.2.1.5 Gas Handling System

A gas handling system was constructed to fill the experimental discharge tubes with various mixtures of gases at varying pressures. The various gas mixtures were formulated at reduced pressure (~ 200 Torr), in 500 ml flasks, which were then sealed off and removed from the system. As the various mixtures were required, the 500 ml flasks were attached to the system and used to fill the tubes. A block diagram of the system is shown in Fig. 16 and a photograph of the assembled system is shown in Fig. 17. The system allowed filling of as many as four discharge tubes simultaneously. This ensured that the gas conditions in these tubes would be identical. The system could be evacuated

initially to a pressure of less than 8×10^{-6} Torr. Filling pressure measurements were made with a McCleod Gauge, except above 10 Torr, where a mercury U-Tube manometer was used. The pressure rise, as a function of time, due to outgassing of the walls in that portion of the system to which the tubes are attached, was measured. (This portion of the system is always trapped with liquid nitrogen.) A typical outgassing curve is shown in Fig. 18. For those mixtures where the minor constituent has a concentration of about 0.1 percent, and the filling pressure is about 1 Torr, the contamination of this constituent will run up to about one part per thousand. Contamination is greater, of course, for filling pressures below 1 Torr. This contamination could be reduced by adding baking facilities to the system. Because of this level of contamination, a bakeable gas handling system was used in connection with the follow-on program described in Sec. 3.3.2.6.

3.2.2.1.6 Performance Tests

3.2.2.1.6.1 Introduction

Tests were performed on several standard tubes (A-1, A-2, A-3) and on tubes A-5, B-3, B-4, B-5, D-2, and D-3 for several different gas mixtures over a wide range of pressures. In all cases the performance of Tube A-5 was used as a basis of comparison. Tube current, I_L , tube voltage, V_L , and UV output were measured. The circuitry for measurement of tube voltage and current is shown in Fig. 21.

The detectors which were used to measure the UV output were nitric oxide ionization chambers with lithium fluoride windows. Three different detectors having different efficiencies for Lyman- α were used. All results have been normalized to the most efficient detector. The detectors were operated at 45 volts, a value determined to be optimum by measuring the I-V characteristics of two of the detectors at varying UV flux levels. Typical curves of detector current, I_D , vs. detector voltage, V_D , for three flux (discharge tube current) levels for

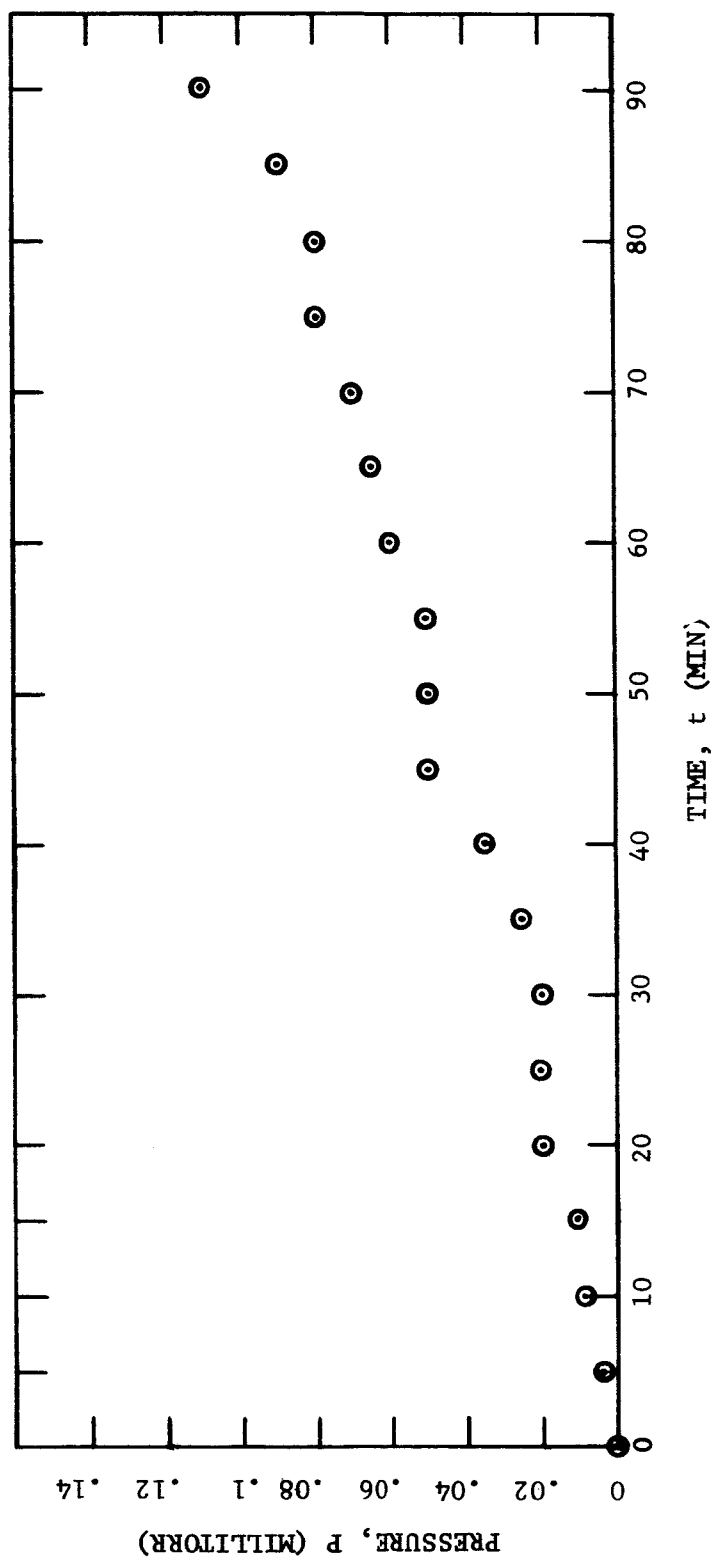


FIG. 18 OUTGASSING OF GAS HANDLING SYSTEM - PRESSURE IN
CLOSED OFF SYSTEM AS A FUNCTION OF TIME

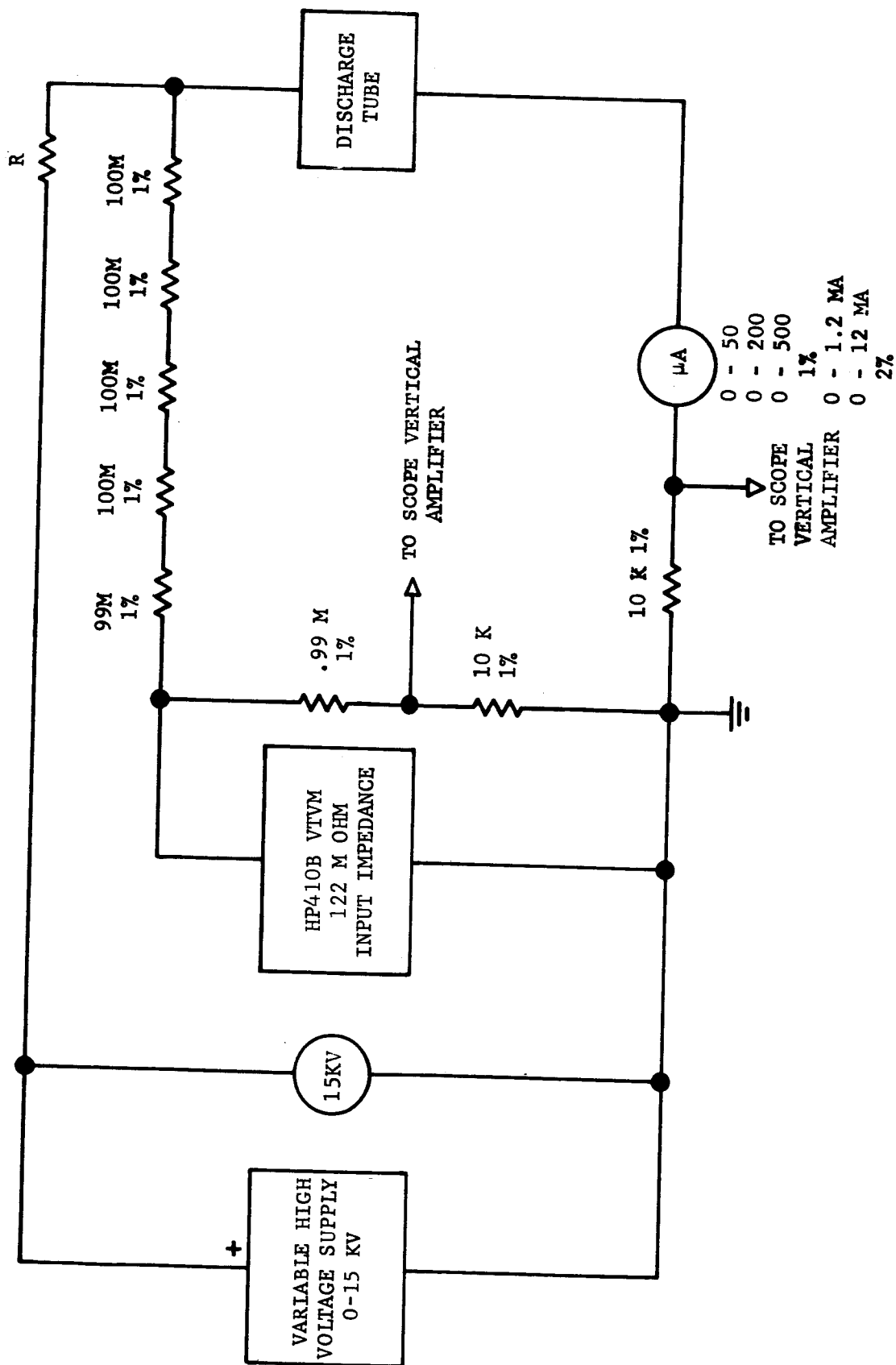


FIG. 19 DISCHARGE TUBE MEASURING CIRCUIT

detector No. 2 are shown in Fig. 20. The middle of the plateau occurs at 40 - 45 volts. With the detector operating in the plateau region, the photon flux is given by the detector current divided by e , the charge of an electron, multiplied by the detector efficiency, η_D . Thus $I_D = 1.6 \times 10^{-5} \text{ amp} = 10^{14} \times \eta_D \text{ photons-sec}^{-1}$.

From the measured quantities, the discharge tube I-V characteristics, UV output vs. DC power input, UV output vs. tube current, and efficiency vs. tube current were obtained.

3.2.2.1.6.2 Standard Tube Measurements

Some of the characteristics of three standard tubes A-1, A-2, A-3 were measured. Tubes A-1 and A-2 failed after a measurement of detector current vs. discharge tube current, I_L , so that no other measurements were obtained on these tubes.

A complete set of measurements was made on tube A-3 for $10 \mu\text{a} < I_L < 200 \mu\text{a}$. The results are shown in Figs. 21, 22, and 23. From Fig. 21, it is seen that subnormal glow occurs for $10 \mu\text{a} < I_L < 80 \mu\text{a}$ and normal glow for $80 \mu\text{a} < I_L < 200 \mu\text{a}$. From Fig. 22, tube UV output varies linearly with tube current. This is to be expected, since the UV output is from the positive column, which is confined radially by the capillary tube. Since the column does not change area, and the number of exciting collisions per unit volume should be proportional to current density, the UV output should be proportional to the total current. It follows that the efficiency should be constant in the normal glow region and should decrease in the subnormal region. This feature is shown in Fig. 23.

The voltage drop across the tube is rather large ($\sim 1 \text{ kv}$). This may be due to the constriction of the positive column by the capillary tube, resulting in high charge loss to the walls with a consequent increase in voltage drop. In spite of this, it will be seen that the efficiency is relatively high.

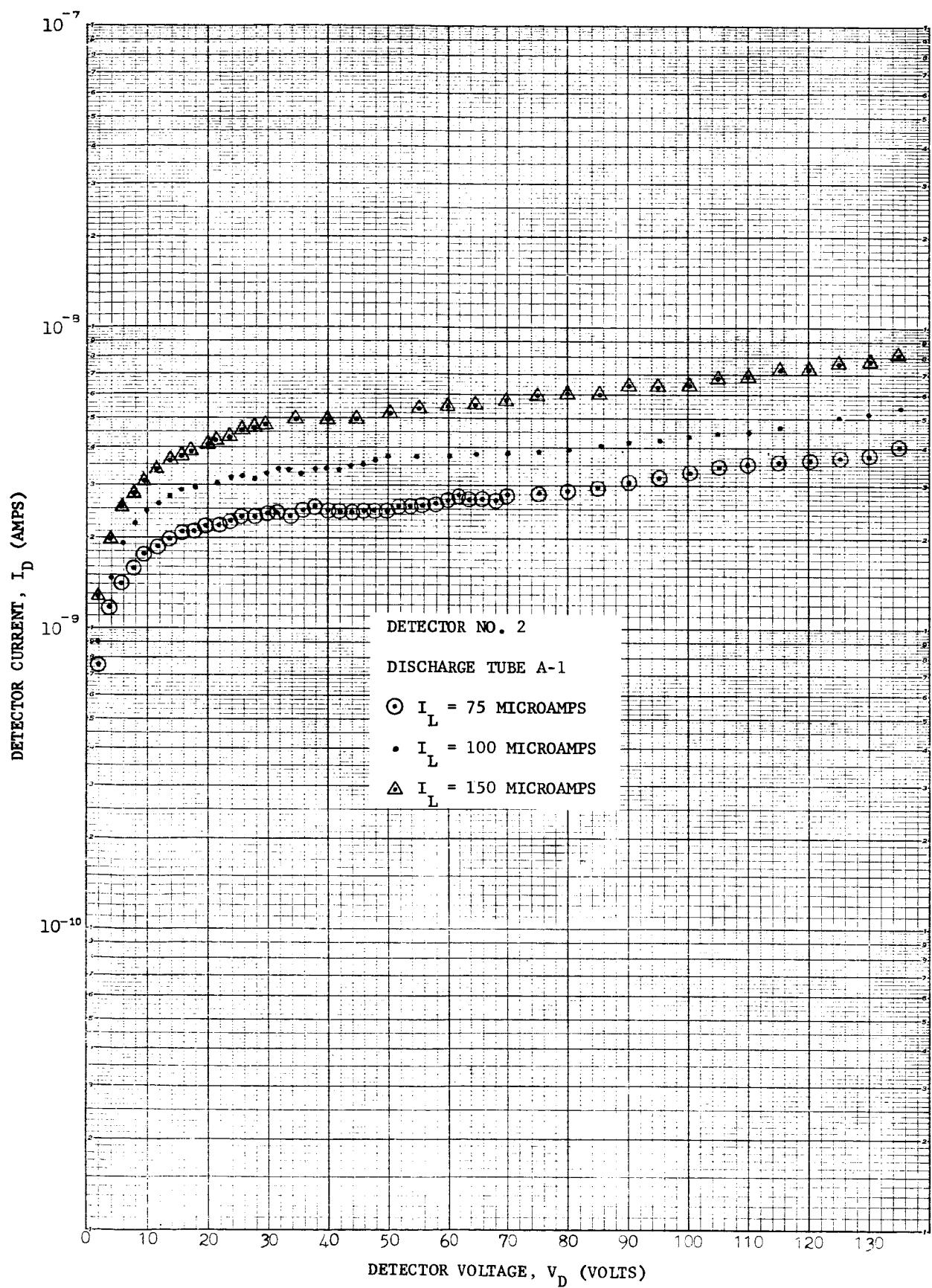


FIG. 20 NO DETECTOR TUBE I-V CHARACTERISTICS
WITH TUBE INTENSITY AS A PARAMETER

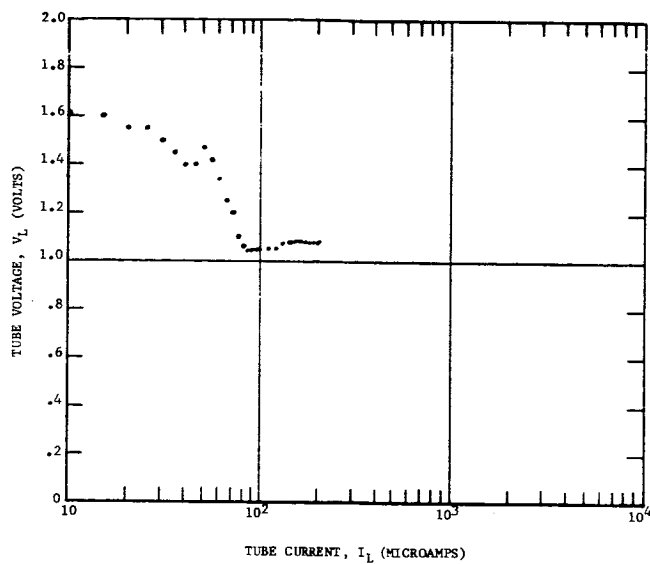


FIG. 21 MEASURED $V-I$ CHARACTERISTICS FOR STANDARD TUBE A-3

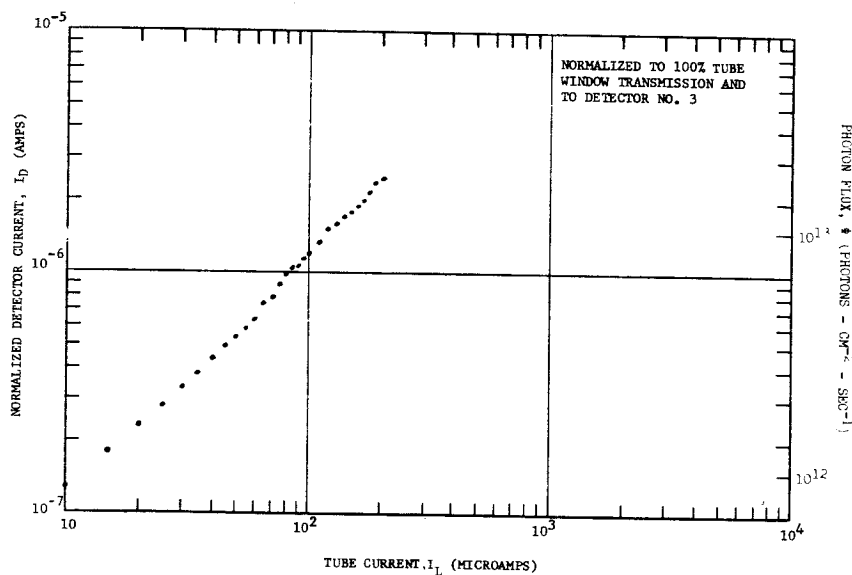


FIG. 22 DETECTOR CURRENT VS TUBE CURRENT FOR STANDARD TUBE A-3

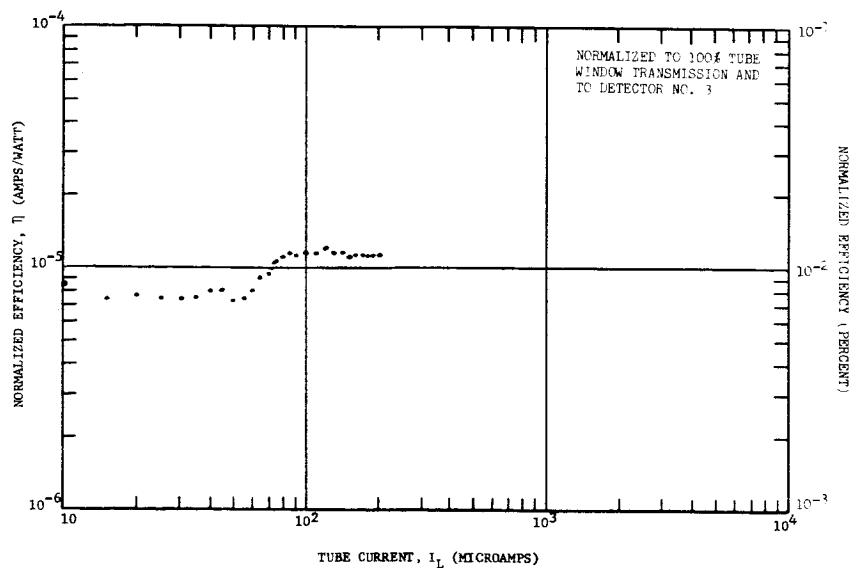


FIG. 23 NORMALIZED EFFICIENCY VS TUBE CURRENT FOR STANDARD TUBE A-3

The photon flux distribution across the LiF window was determined by measuring the flux transmitted through a 1-mm diameter hole centered on the detector axis, as a function of its position, x , relative to the discharge tube axis. The results are plotted in Fig. 24. The beam is seen to have a half-power aperture width of 3 mm. The capillary tube is 1.4 mm i.d.

3.2.2.1.6.3 New Designs

The performance of six tubes of four different geometries was measured with three gas mixtures during six data runs, with gas pressures ranging from 0.03 to 11 Torr. Tube A-5 was used as a standard of comparison. The measurement conditions are summarized in Table VIII, in which a cross indicates that measurements were made on a particular tube. The data for Run 5 is not reported on here since it was run with tube B-5 alone, and almost identical data were obtained on Run 6.

Table VIII

Summary of Conditions and Correction Factors for the Tube Performance Measurements

Window Transmission Correction Factors to 100% Transmission	Run Number				
	1	2	3	4	6
Mixture	0.17H ₂ +99.97%Ne	90%H ₂ +10%Ne	90%H ₂ +10%Ne	~100%H ₂	90%H ₂ +10%Ne
Gas Pressure (Torr)	0.105-1.15-11	0.0315 -0.196-2.18	1.12-2.15	1.70 -2.95	1.10-2.12 -5.05-7.01 -9.50
Mean Water Vapor Attenuation Correction Factor	3.98 ⁺³⁷ / _{-25%}	3.79 ⁺³² / _{-26%}	3.73 ⁺³⁵ / _{-27%}	3.78 ⁺³⁵ / _{-26%}	4 ± 10%
Tube					
A-5	3.17 ± 25%	X	X	X	X
B-3	9.71 ± 30%	X	X	X	
B-4	5.05 ± 30%	X			
B-5	5.05 ± 30%			X	X
D-2	4.05 ± 30%		X		X
D-3	5.05 ± 30%			X	

To allow meaningful comparison between the various tubes, it is necessary to correct for the differences in window transmission and for water vapor absorption of Lyman- α radiation between the UV source tube and the detector. The data for each tube were corrected to 100 percent window transmission, and were also corrected for water vapor absorption. These two correction factors are also shown in Table VIII. In later measurements, the path between the UV-tube and detector was evacuated in order to avoid water vapor attenuation.

The error in the corrections allows the cumulative error in the data for UV intensity and efficiency to range from about $\pm 35\%$ to about $\pm 60\%$. However, a comparison of the data for various runs indicates that the errors are probably less than is indicated. Comparisons between certain tubes which were measured side-by-side on the same day should exhibit little relative error.

The curves of voltage vs. current ($V-I$), and of the detector current, I_D , versus DC power input, P_L , for Run 1 are shown in Figs. 25 and 26, respectively. From these curves it follows that the output and efficiency of tube B-3 is nearly the same, or up to a factor of 8 better, than tube A-5. This fact was also found in subsequent measurements with other gas mixtures. From Figs. 25 and 26 it can be seen that the major part of the lower efficiency of tube A-5 can be accounted for by the higher voltage drop.

Figs. 27 and 28 show the $V-I$ characteristics and $I_D - P_L$ characteristics for Run 2. It can be seen that output and efficiency of tube B-3 increases with increasing pressure. This effect can be explained by the fact that, as the pressure is increased the discharge is more closely confined to the window. On the other hand, the efficiency of tube D-2 decreases with increasing pressure. It will be seen that this is characteristic of all tubes except B-3 and B-4.

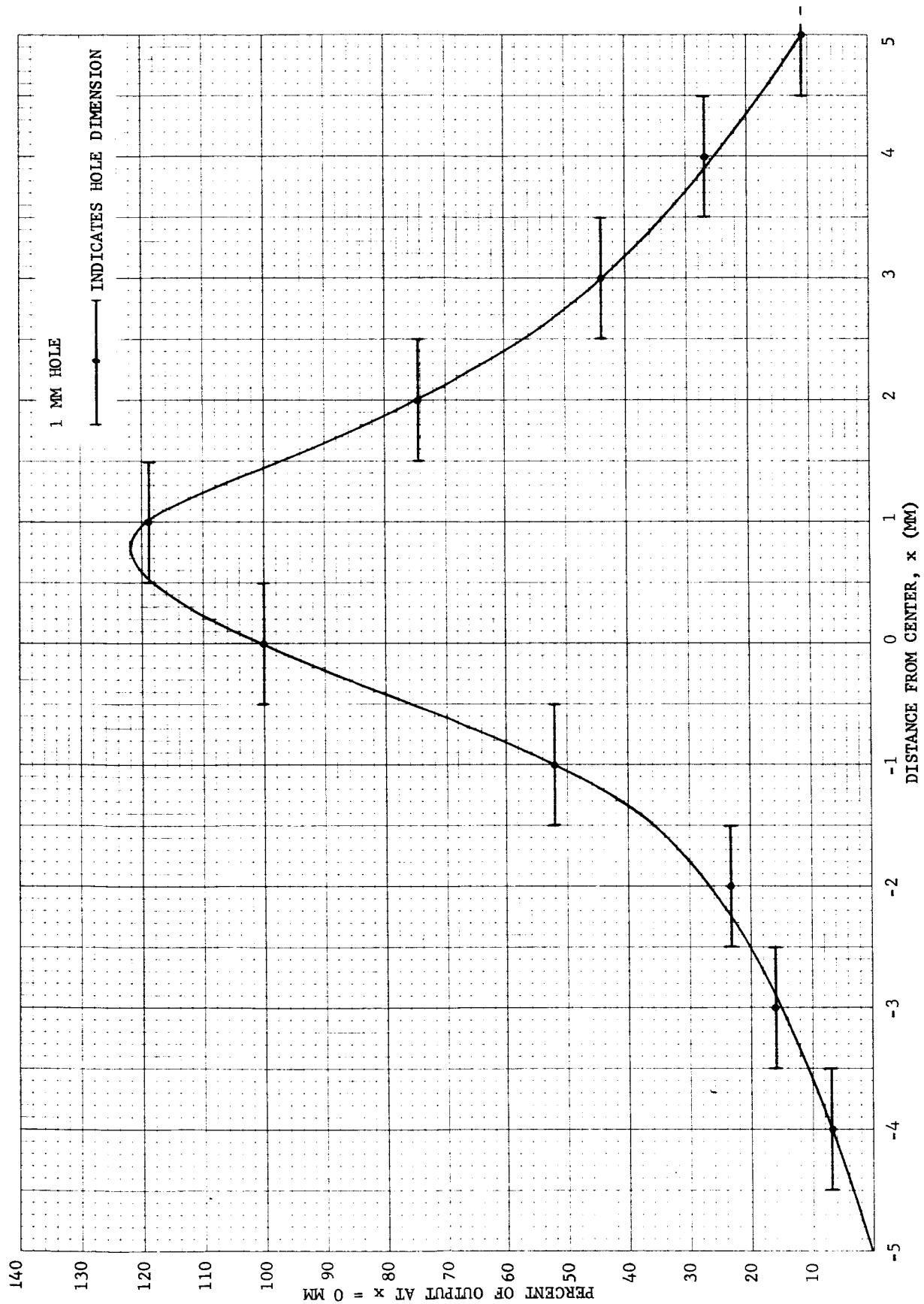


FIG. 24 PHOTON DISTRIBUTION ACROSS THE WINDOW OF TUBE A-3

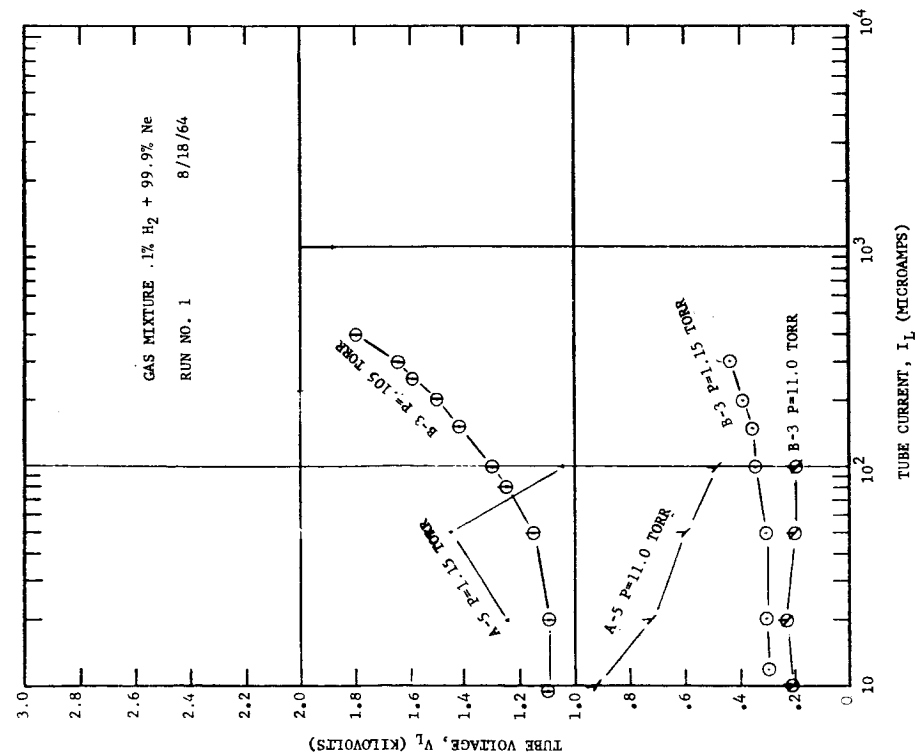


FIG. 25 RUN NO. 1 TUBE V-I CHARACTERISTICS

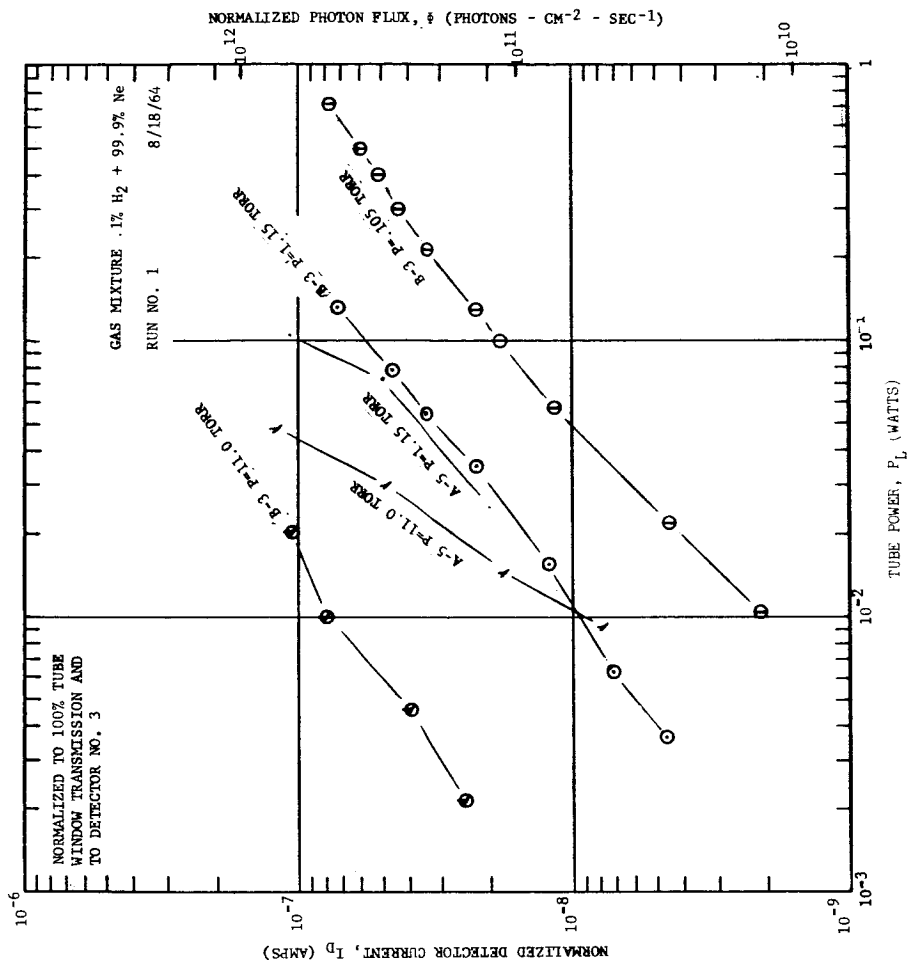


FIG. 26 RUN NO. 1 DETECTOR CURRENT VS TUBE POWER CHARACTERISTICS

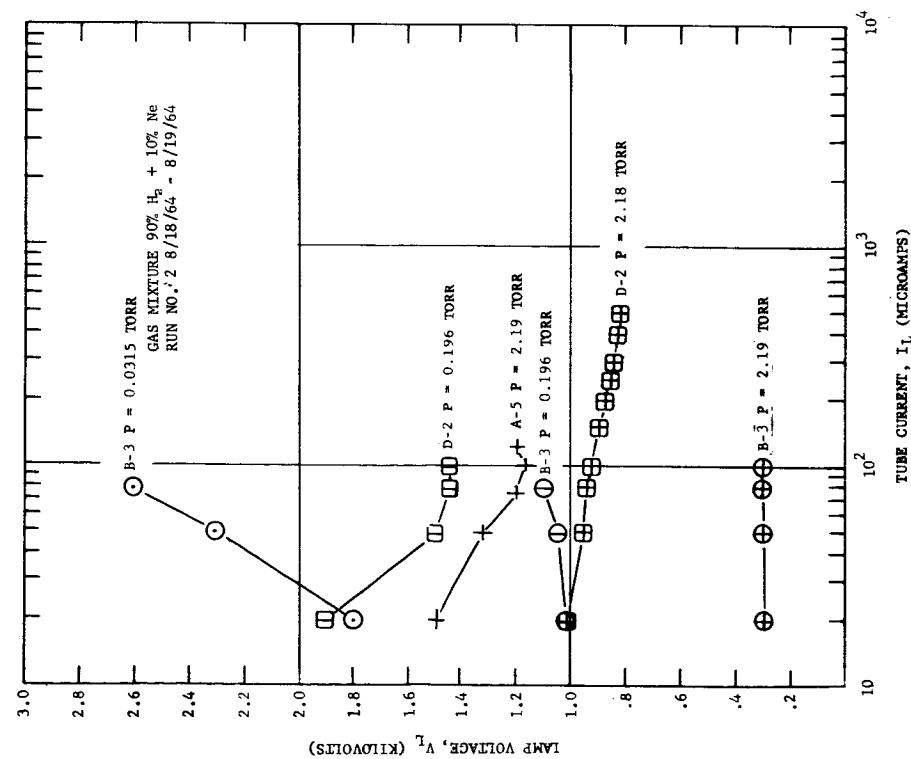


FIG. 27 RUN NO. 2 TUBE V-I CHARACTERISTICS

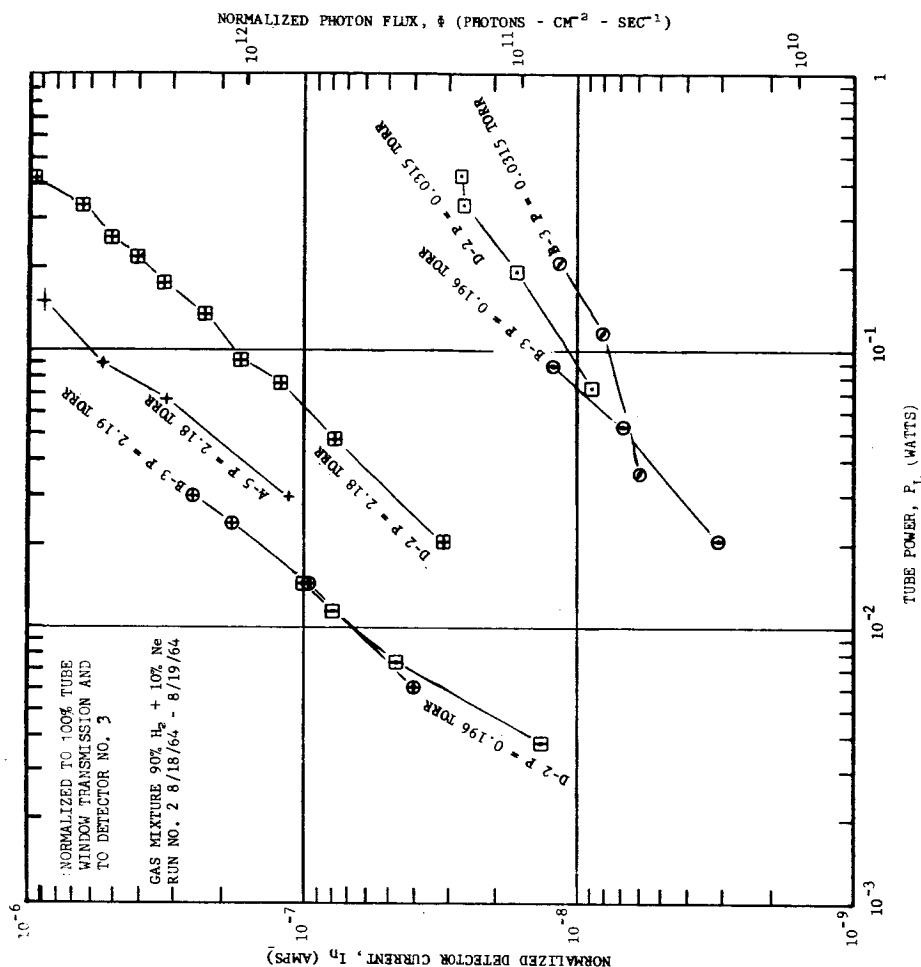


FIG. 28 RUN NO. 2 DETECTOR CURRENT VS TUBE POWER CHARACTERISTICS

The effect of gas mixture is shown by a comparison of Run 2 with Run 1. In going from the 0.1% H_2 + 99.9% Ne mixture to the 90% H_2 + 10% Ne mixture the efficiency and UV output increases by nearly a factor of ten.

The observed large increase in efficiency with increasing pressure for tube B-3, concurrent with the increasing confinement of the discharge to the window, led to the construction of the confined planar discharge geometry, tube B-5. Run 3 was made to compare the performance of tube B-5 with tube A-5. The results are shown in Figs. 29, 30, and 31. At low currents, and hence low power levels, the efficiency and UV light output of tube B-5 are considerably higher than those of tube A-5. The efficiencies and UV output of the two tubes are comparable at the higher currents. Examination of the V-I characteristic (Fig. 29) for a pressure of 1.12 Torr shows that the deterioration of efficiency of B-5 at the higher power levels occurs because of a movement of the discharge into the abnormal glow region. However, the V-I characteristic for the higher pressure (2.15 Torr) shows that the discharge is in the subnormal to normal glow region. It would be expected that the efficiency of B-5 at 2.15 Torr would remain high at currents higher than those for which data were taken. However, the measurements on B-5 at 2.15 Torr were terminated because of deterioration of the cathode and consequent change in the discharge characteristics.

Having determined that the confined geometry of tube B-5 produced a greater efficiency and higher output than tube A-5, Run 4 was made with an approximately 100 percent hydrogen mixture for tubes A-5, B-3, B-5, and D-3 at pressures of 1.7 and 2.95 Torr. The results are given in Figs. 32, 33, and 34.

Consistent with the earlier results, B-3 had about the same efficiency and UV output as A-5. Tube D-3 was less efficient than A-5. (This is also borne out in Run 6.) B-5 is more efficient and has a higher UV output than A-5, by up to a

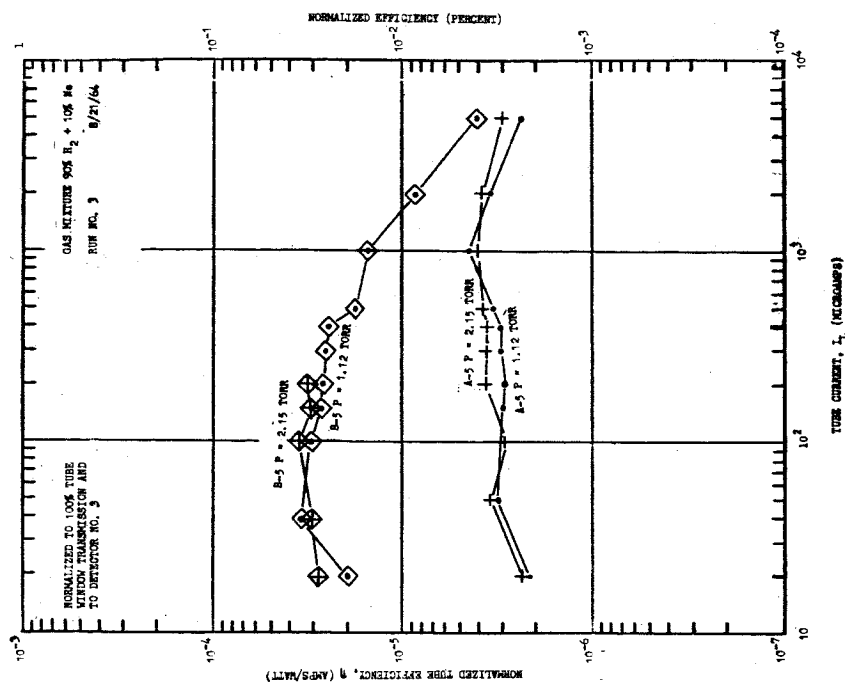


FIG. 31 RUN NO. 3 TUBE EFFICIENCY VS TUBE CURRENT CHARACTERISTICS

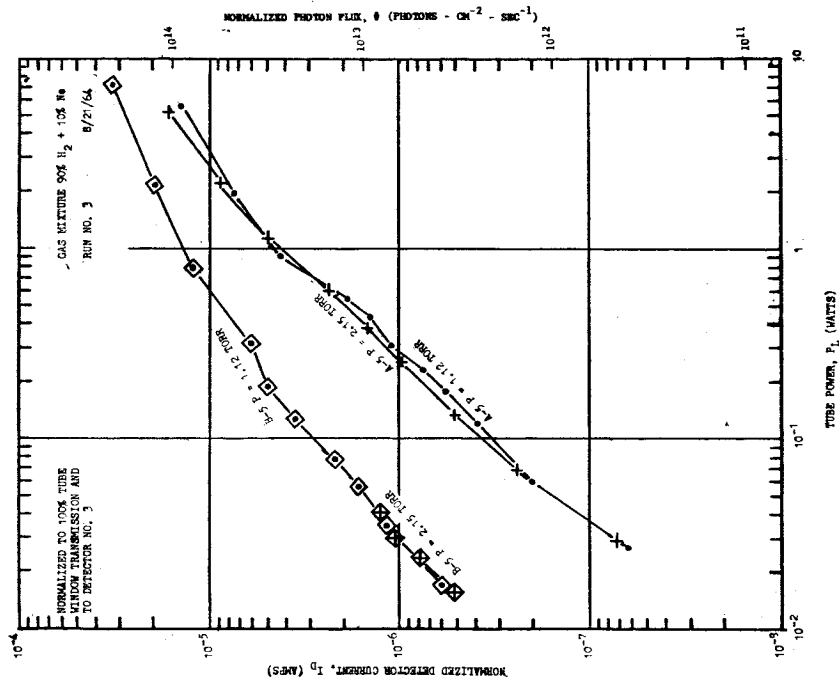


FIG. 30 RUN NO. 3 DETECTOR CURRENT VS TUBE POWER CHARACTERISTICS

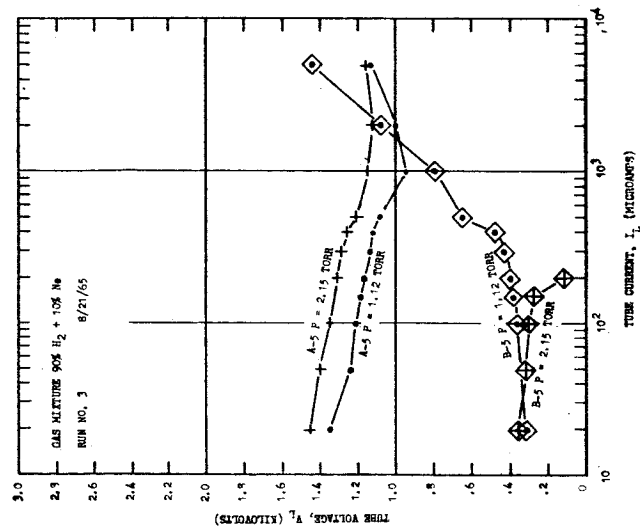


FIG. 29 RUN NO. 3 TUBE V-I CHARACTERISTICS

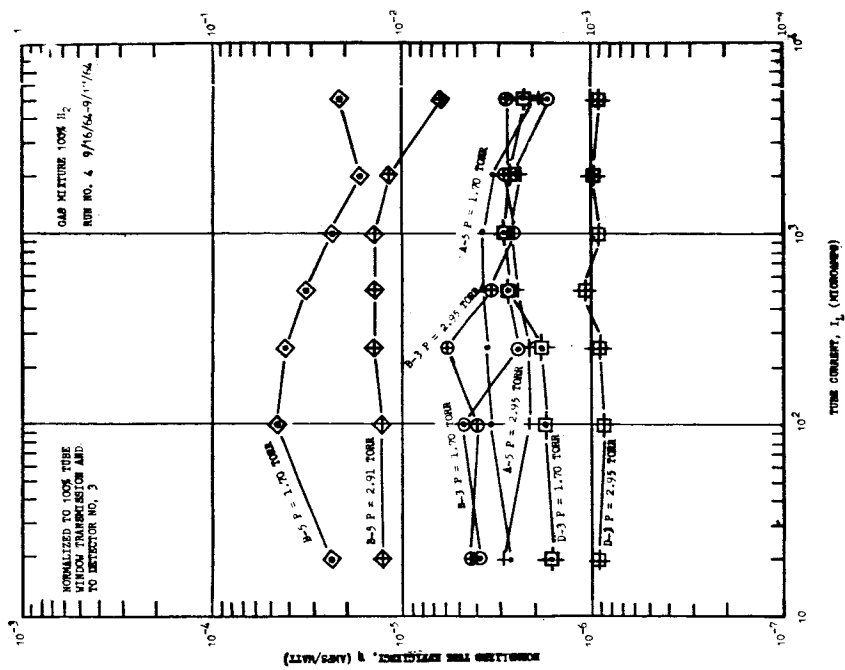


FIG. 32 RUN NO. 4 TUBE V-I CHARACTERISTICS

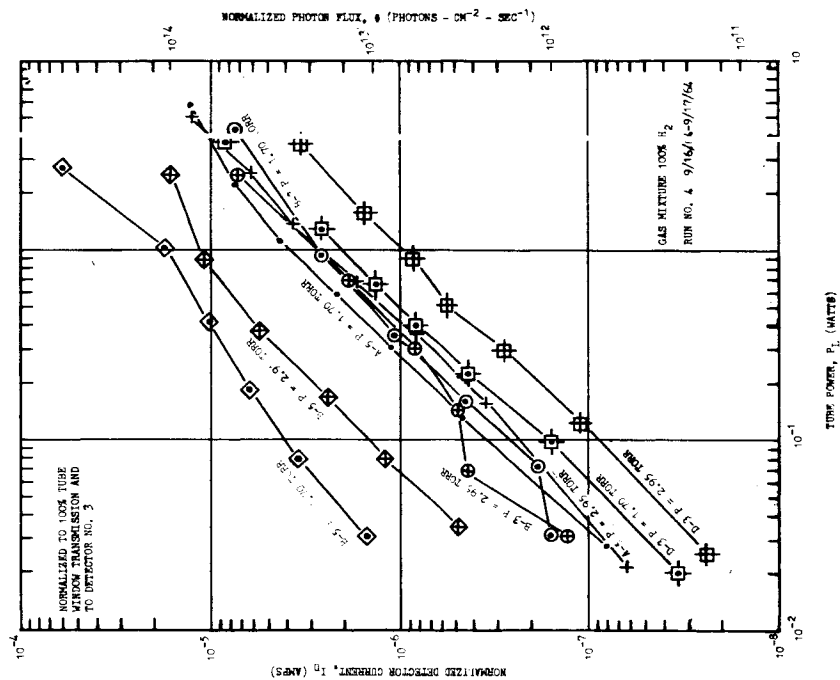


FIG. 33 RUN NO. 4 DETECTOR CURRENT VS TUBE POWER CHARACTERISTICS

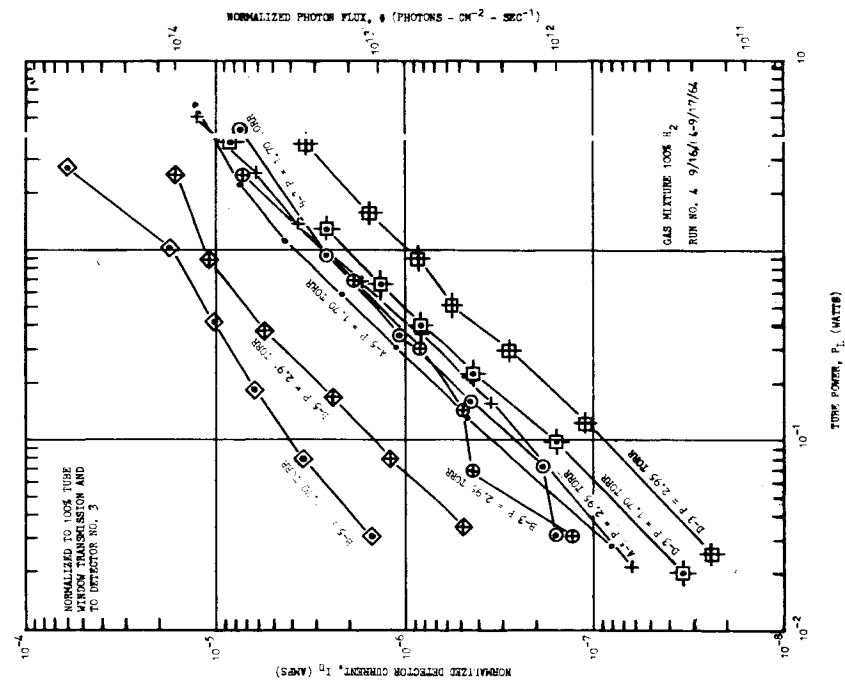


FIG. 34 RUN NO. 4 TUBE EFFICIENCY VS TUBE CURRENT CHARACTERISTICS

factor of about ten. Pressure is seen to have practically no affect on the UV output of A-5 and D-2. This is expected, since in the positive column the number of excitation collisions will be proportional to pressure, while the energy gained between collisions will be approximately inversely proportional to pressure, so that the UV output which, to terms of first order, should be proportional to the product of these two quantities, is independent of pressure. On the other hand, an increase in pressure in A-5 and D-3 results in a decrease in efficiency. This decrease can be directly correlated with the increase in voltage drop with pressure observed in the V-I characteristics.

The UV output and efficiency of tube B-5 changes rather markedly for a factor of less than two increase in pressure, while the V-I characteristic remains relatively unchanged. As will be seen, this feature can be correlated with changes in discharge characteristic.

To investigate further the pressure dependence of UV output for tubes B-5, A-5, and D-2, the data shown in Figs. 35, 36, 37 were obtained. The UV output of A-5, and to a lesser extent of D-2, is relatively independent of pressure, while the UV output of B-5 is quite dependent on pressure. The UV output of all tubes, at a given pressure, varies approximately linearly with lamp current, except where the tube is operating in the subnormal or abnormal glow regions. The efficiencies of these tubes have been plotted against lamp current, I_L , in Fig. 37 for various pressures. The efficiency of A-5 is relatively constant with I_L . The variation of efficiency of D-2 with I_L can be correlated with the fact that at the higher pressures it is operating in the subnormal glow region. The efficiency of B-5 is quite dependent upon pressure.

The following discussion will be concerned only with tube B-5. From the plots of detector current, I_D , vs. lamp current, I_L , it appears that the output of B-5 at the lower currents is roughly proportional to pressure. It is difficult

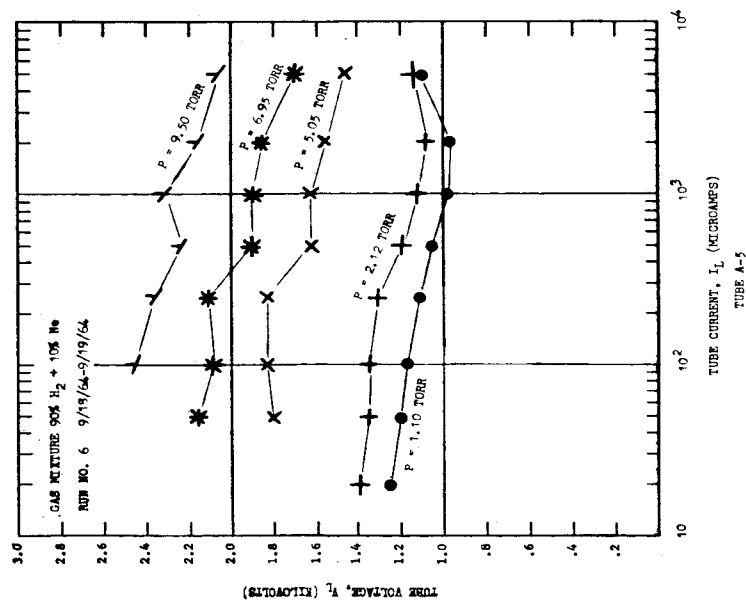
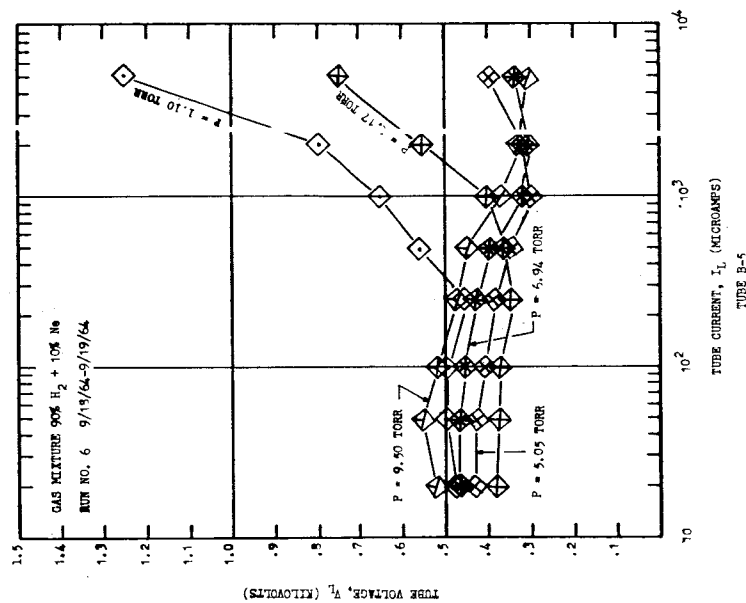
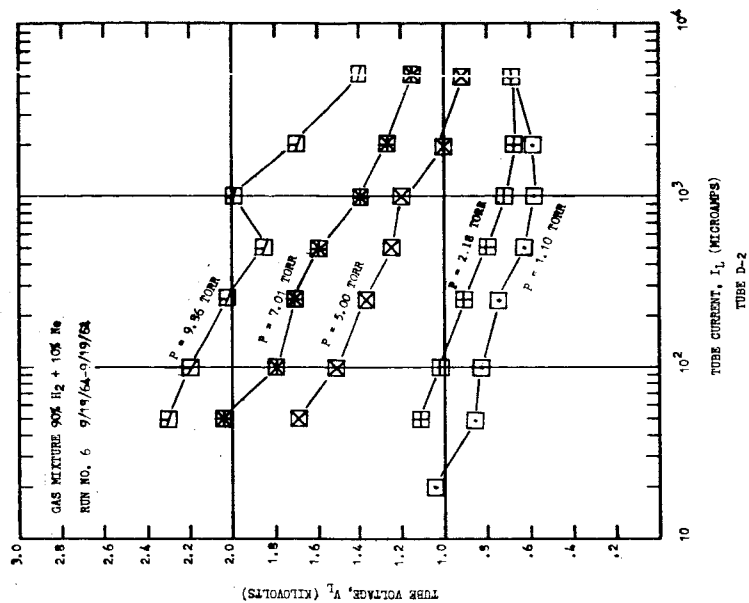


FIG. 35 RUN NO. 6 TUBE V-I CHARACTERISTICS

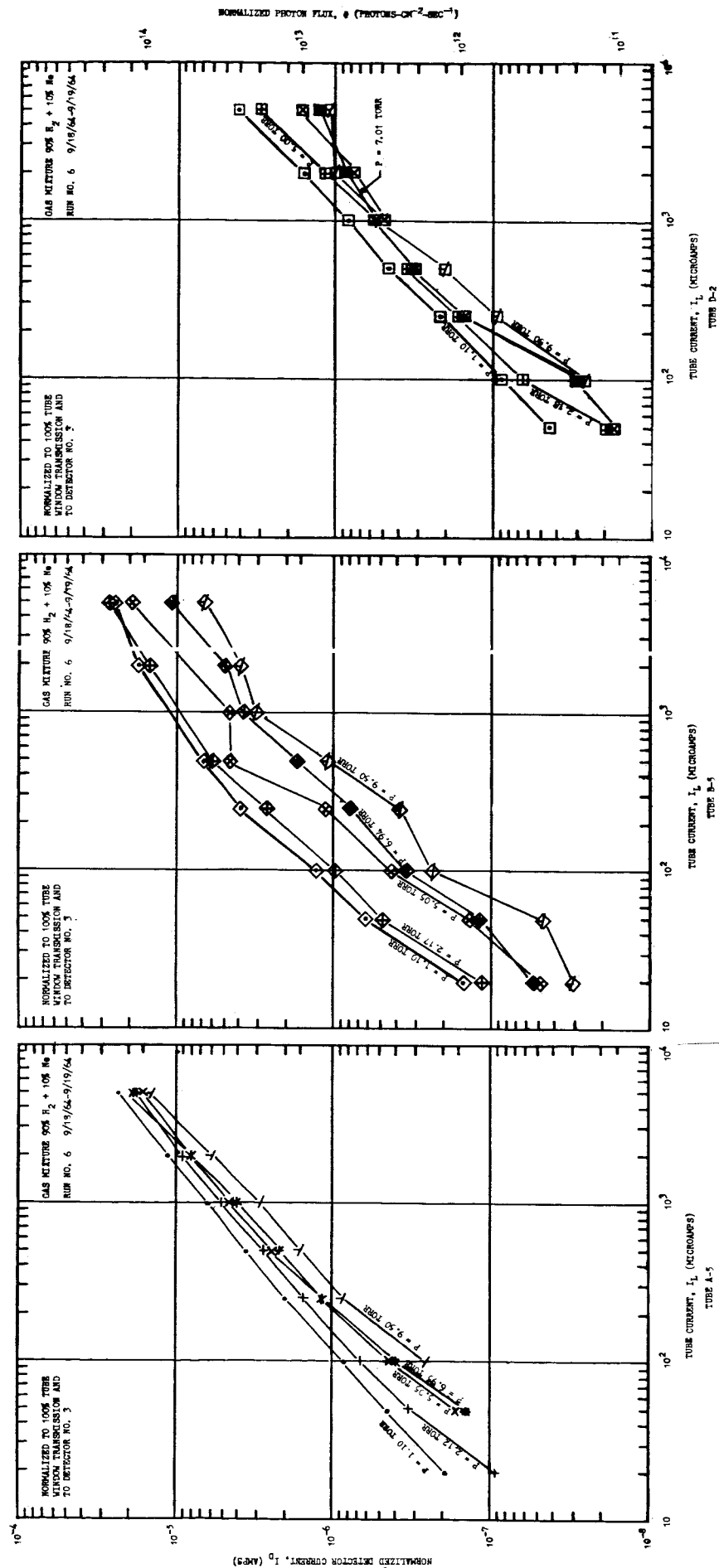


FIG. 36 RUN NO. 6 DETECTOR CURRENT VS TUBE CURRENT CHARACTERISTICS

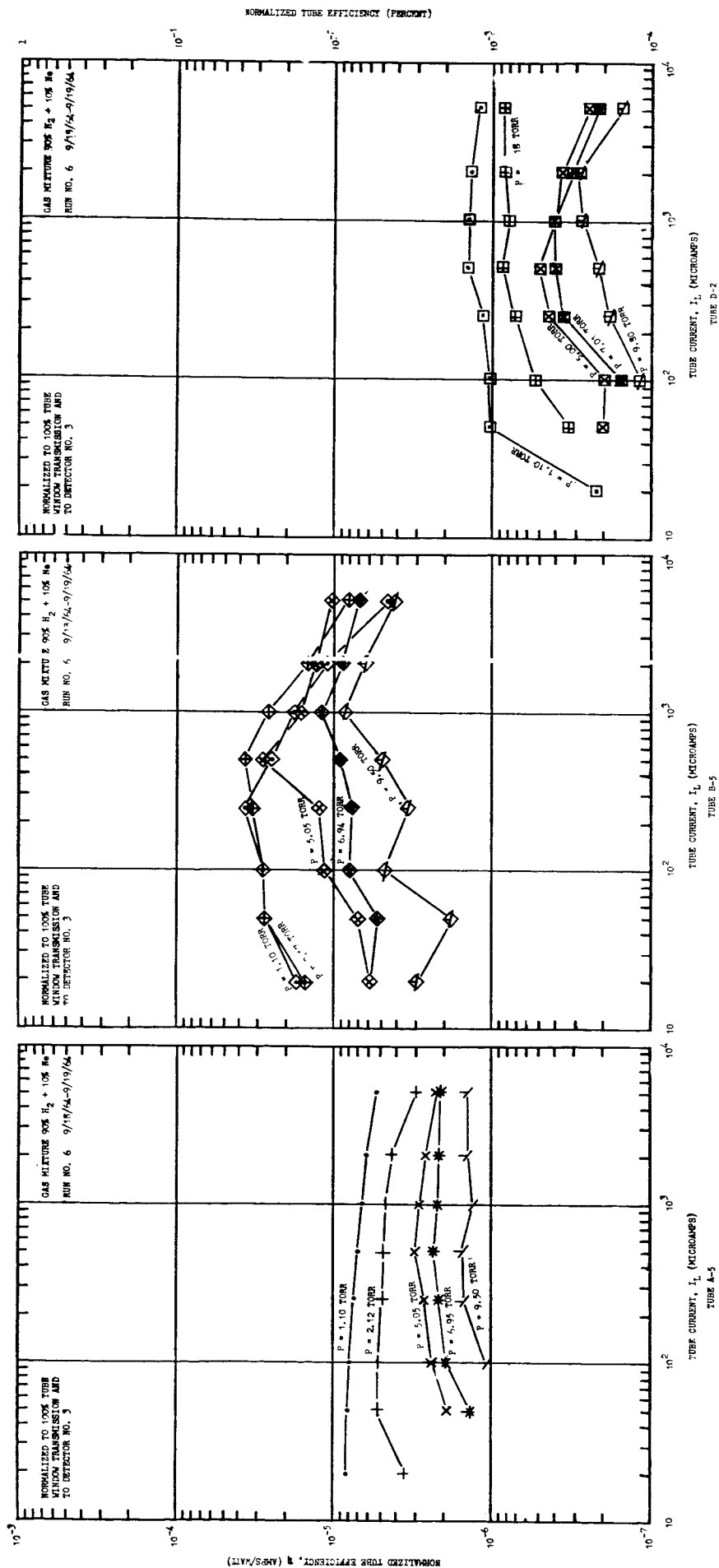


FIG. 37 RUN NO. 6 TUBE EFFICIENCY VS TUBE CURRENT CHARACTERISTICS

to fully justify this statement since the points are scattered. Visual examination of the discharge suggested that this feature is somewhat correlated with the area of the luminous zones, particularly that of the cathode glow. An examination of the efficiency, η , vs. I_L curves, shows that at low pressures the efficiency is high at lower currents, and then falls off above some critical current as the current is increased. This is correlated with the movement of the discharge into the abnormal glow region. Further, as pressure is increased, the efficiency becomes more nearly constant with changes in I_L , but at a lower efficiency. This is correlated, in turn, with the drop in UV output and increasing voltage drop across the tube with increasing pressure. The drop of efficiency with increasing I_L at the lower pressures might be eliminated by increasing the cathode surface area to shift the abnormal glow region to current levels above those at which the lamp is operated.

Tube B-7 was constructed to have an electrode spacing twice that of B-5. The electrodes were positioned to allow, by reversal of polarity, either the positive column or the negative glow region to be in front of the window. Preliminary measurements showed that the negative glow region had an output approximately ten times that of the positive column.

3.2.2.1.6.4 Gas Mixture Effects

As already seen, performance measurements were made with three gas mixtures. These were 0.1% H_2 + 99.9% Ne, 90% H_2 + 10% Ne, and 100% H_2 . A study of Figs. 26, 28, and 33 shows that the outputs at a given power level, and hence the efficiencies, for the three mixtures are in the ratio 1:6:3.5 for pressures in the 1 - 2 Torr range. This result suggests that there exists an optimum mixture.

The variation in output with mixture is a result of two competing processes. First, the normal cathode fall for neon is less than for hydrogen. This implies

that increasing neon concentration should give increasing efficiency. This effect can be seen to some extent in Figs. 25, 27, and 32. On the other hand, the more neon the less hydrogen present and the smaller the probability of an electron-hydrogen collision, so that the light output for fixed current should ultimately decrease with increasing neon concentration. That this does occur can be extracted from Figs. 25 to 28, 32, and 33. In practice the detailed behavior is complicated by the existence of the Penning effect for neon-hydrogen mixtures, and possibly strong effects of gas impurities.

To compare krypton vs. hydrogen as the active filling gas, tests were made with several tube types. When krypton is used, getters may be used to insure purity of the krypton. Getters cannot be used in hydrogen-filled tubes, since any known getter absorbs hydrogen as well as the impurities. Before krypton could be used, however, it was necessary to determine whether the output from a krypton-filled tube would be at least as great as that from a hydrogen-filled tube.

Comparisons were made between the outputs of tubes filled with several pressures of a 90/10 mixture of hydrogen and neon, and with several pressures of krypton. The comparisons between the tubes were made with an evacuated (< 0.2 Torr) adaptor between the UV-tube and an NO ion-chamber detector. This adaptor insured that the measurements were all taken with the same source-to-detector distance, and that the measurements would not require a correction for water vapor in the measuring path. The results of these tests are shown in Figs. 38, 39, and 40 where the detector current, I_D , (a measure of the UV output) has been plotted against source tube current, I_L , for three different tube types. These plots show that:

- 1) The type-A tube had about the same output when filled with either krypton or a 90/10 mixture of hydrogen and neon.

2) The type-B tube had a slightly greater output when filled with krypton than when filled with a 90/10 mixture of hydrogen and neon, except for the pressure of 5.05 Torr. The cathode of this tube was deteriorating during the test, so the data are questionable.

3) The type-D tube had greater output when filled with krypton than when filled with a 90/10 mixture of hydrogen and neon.

The data shown in Figs. 38, 39 and 40 indicate that krypton is at least as good as hydrogen for filling the UV-tubes. For the type-D tube, krypton gives appreciably greater output.

Another tube characteristic of interest is the tube efficiency, here defined as the ratio of the UV output to the DC power input to the tube. The efficiency (η), has been plotted against tube current (I_L) for the three tube types, in Figs. 41, 42, and 43. There is a definite trend for the krypton filling to give significantly greater efficiencies. This trend is more marked for the type-D tube and less marked for the type-A tube. As mentioned earlier, the data for the type-B tube are questionable.

3.2.2.1.6.5 Conclusions

The results reported above lead to the following conclusions:

- 1) The scaled-up standard geometry can give useful outputs.
- 2) Tube output varies linearly with current in the normal glow region.
- 3) A planar discharge tube can be made which is at least ten times as efficient, and which gives considerably more UV output, than the standard tube. This type of tube should have efficiencies of 10^{-2} to 10^{-1} percent and photon fluxes of 10^{14} to 10^{15} photons-cm⁻²-sec⁻¹. In the design of this tube, particular attention must be paid to cathode material and cathode surface area. This tube should be operated with the negative glow over the window.

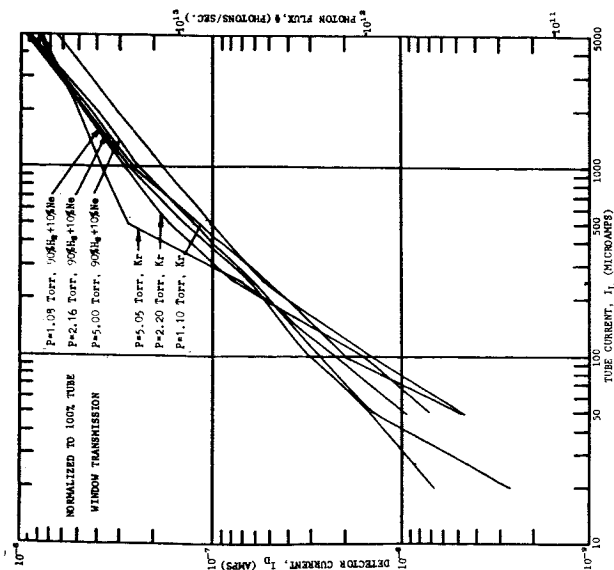


FIG. 38 TUBE A-6
OUTPUT VS TUBE CURRENT: COMPARISON
OF KRYPTON TO H_2-N_2 MIXTURE

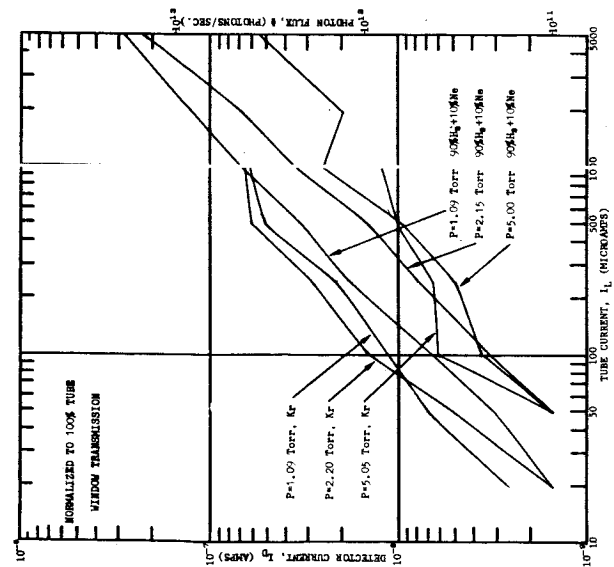


FIG. 39 TUBE B-5
OUTPUT VS TUBE CURRENT: COMPARISON
OF KRYPTON TO H_2-N_2 MIXTURE

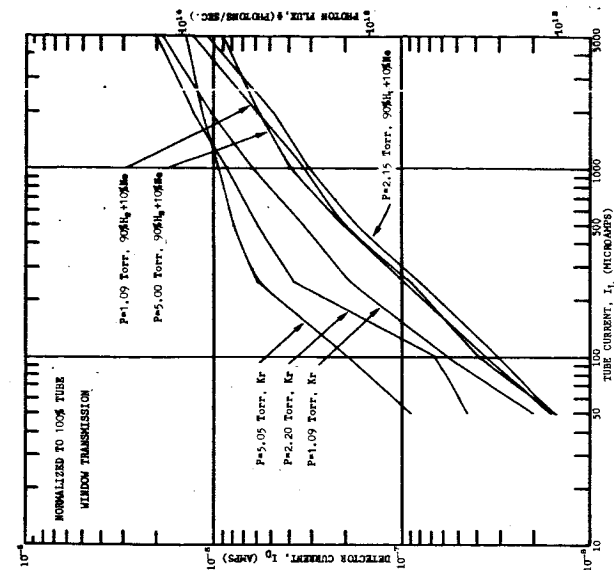


FIG. 40 TUBE D-3
OUTPUT VS TUBE CURRENT: COMPARISON
OF KRYPTON TO H_2-N_2 MIXTURE

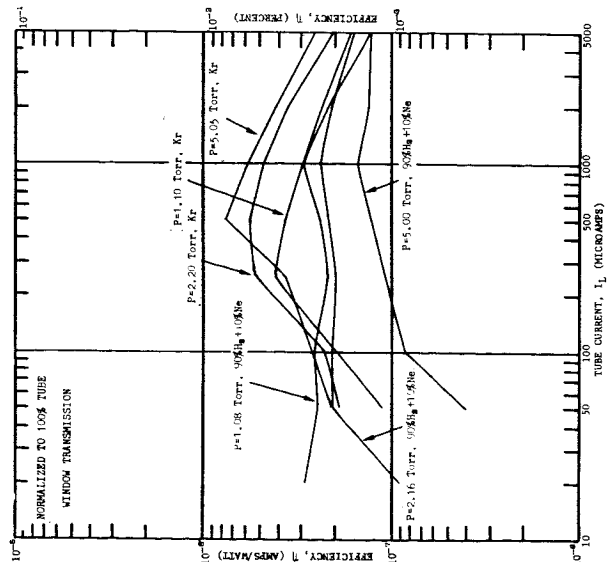


FIG. 41 TUBE A-6
EFFICIENCY VS TUBE CURRENT: COMPARISON
OF KRYPTON TO H_2-N_2 MIXTURE

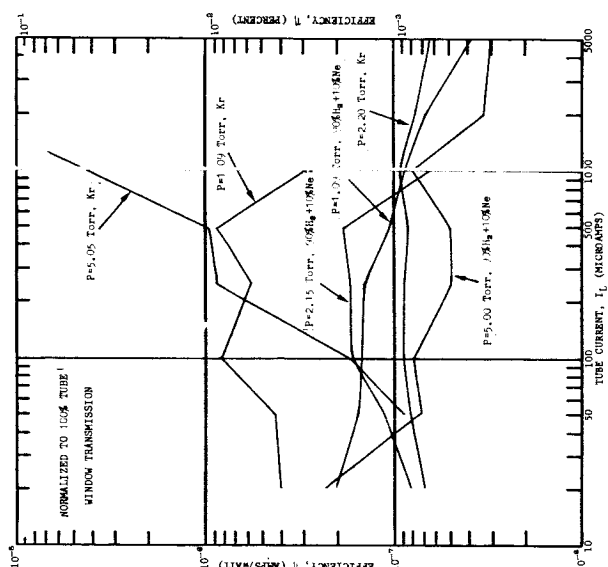


FIG. 42 TUBE B-5
EFFICIENCY VS TUBE CURRENT: COMPARISON
OF KRYPTON TO H_2-N_2 MIXTURE

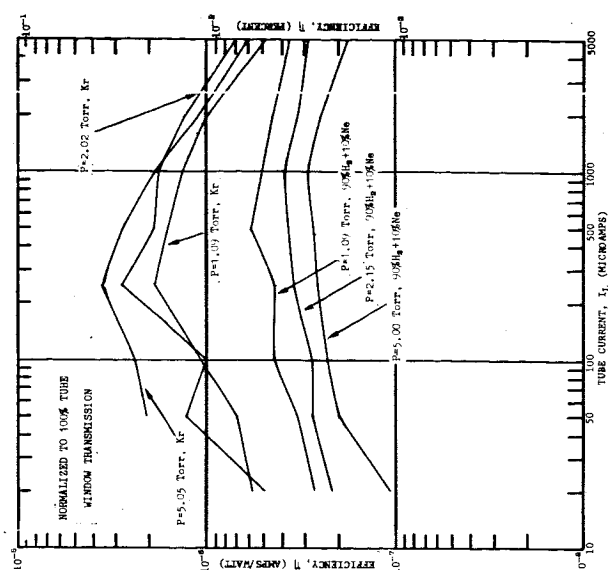


FIG. 43 TUBE D-3
EFFICIENCY VS TUBE CURRENT: COMPARISON
OF KRYPTON TO H_2-N_2 MIXTURE

4) The sealing of large (2-inch diameter) windows to the discharge tube body is a problem which needs consideration, but which should not hold up the development of a large vacuum plasma, since suggested techniques appear to be feasible.

5) The effect of gas mixture on efficiency is considerable. The experimental efficiency ratios for 0.1% H_2 + 99.9% Ne, 90% H_2 + 10% Ne, and 100% H_2 are 1:6:3.5.

6) Krypton is at least as good, and probably better, than a 90/10 mixture of hydrogen and neon for filling the UV tubes. In particular, krypton appears to increase the output of the type-D tube more than the other types. This is important (even if unexplained), since this tube type was selected to develop the large-volume plasma in the chamber.

3.2.2.2 Small Volume Plasma Generation

3.2.2.2.1 Objectives

The objectives of this part of the experimental investigation were to generate a plasma of approximately the desired characteristics by photoionization of nitric oxide, to measure the properties of this plasma, and to correlate the experimental results with the theory. If this could be achieved, then the feasibility of the method would be demonstrated.

3.2.2.2.2 Experimental Setups and Results

The experimental approach was to mount a UV-tube (Tube D-2 or D-3 described in Sec. 3.2.2.1.4) in a bell jar filled with NO and to measure the characteristics of the resulting plasma with a floating double-probe system.

Two different double-probe arrangements were used. The experimental setups within the bell jar for these two probe arrangements are shown in Figs. 44 and 45. The UV-tube was mounted vertically with its beam directed downward. Aluminum

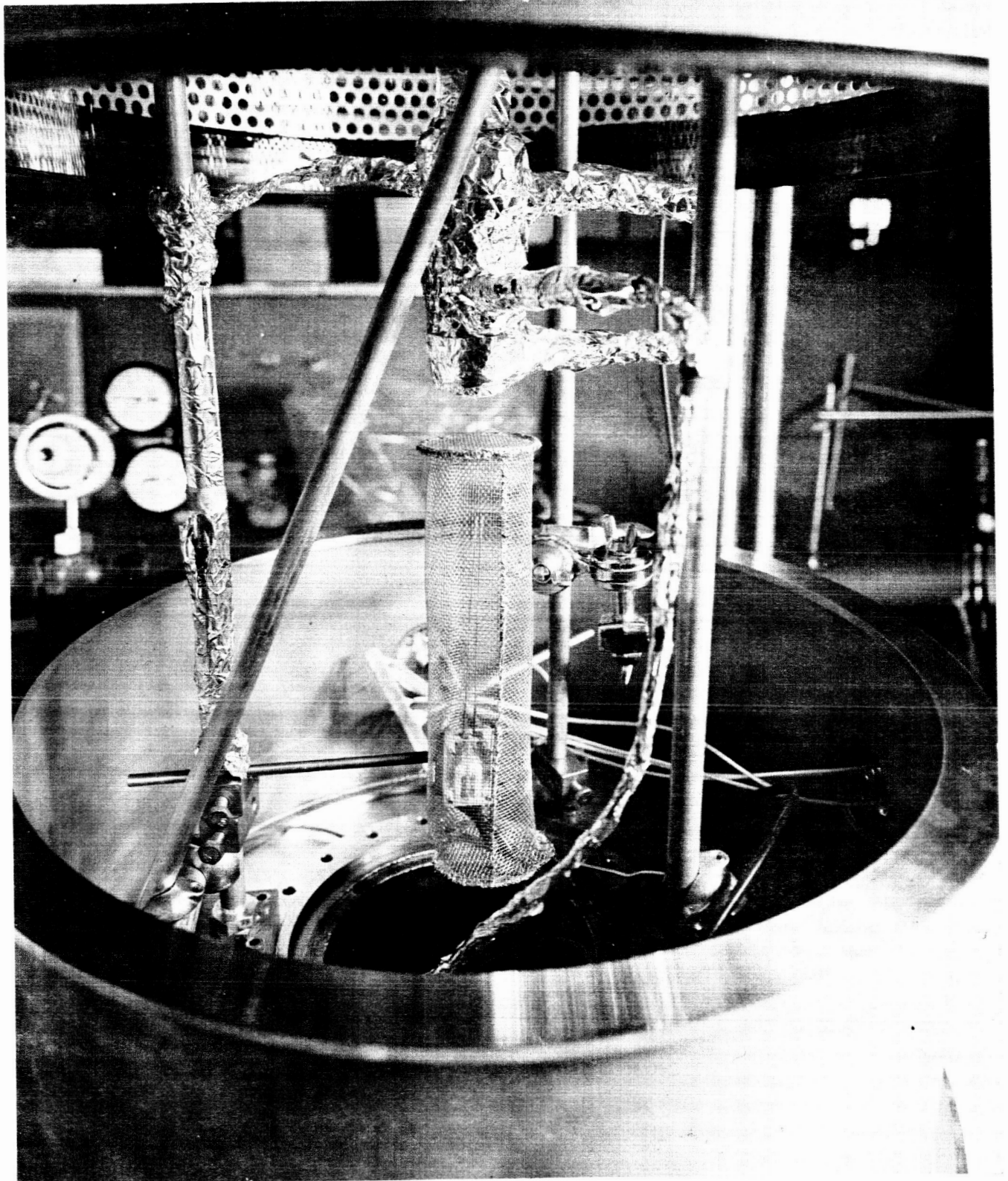


FIG. 44 PLASMA EXPERIMENTAL SETUP ONE

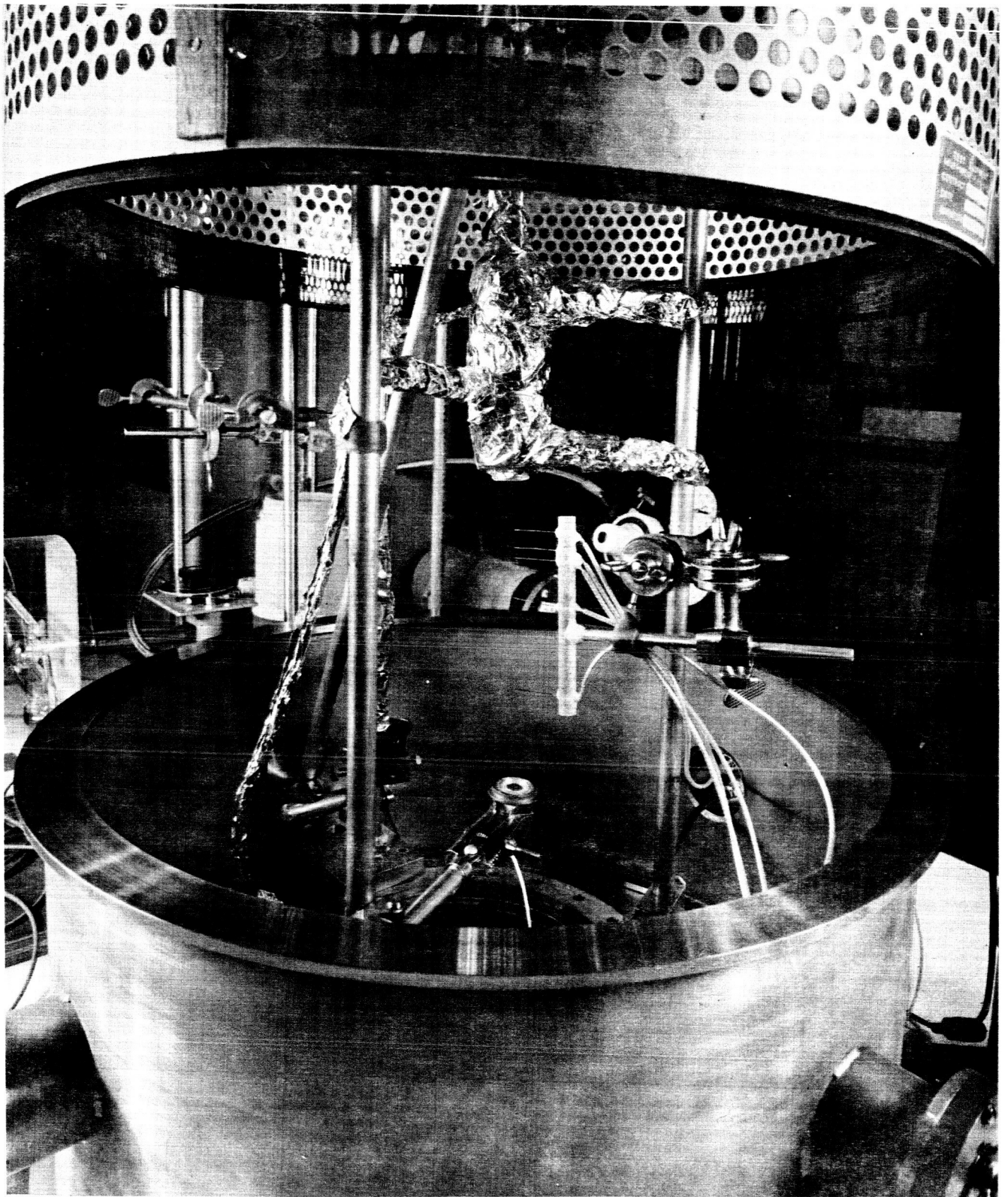


FIG. 45 PLASMA EXPERIMENTAL SETUP TWO

foil shielding was installed to reduce stray signal pickup by the probes. The probes were mounted directly below the UV-tube and centered in the UV beam. The bell jar was pumped to 10^{-6} Torr and then backfilled to the measuring pressure with NO. The NO pressure was measured with a tilting type McLeod gauge, trapped by a dry-ice methanol mixture. A diagram of the system used to measure the probe currents is shown in Fig. 46.

The first set of measurements used the floating double probe arrangement shown in Fig. 44. The probes were spaced 0.5 cm apart. Each probe had a radius of 0.065 cm and was 10 cm. long. The Faraday shield around the probes was 5 cm in diameter and was installed to further reduce stray signal pickup by the probes. With the system pumped to a high vacuum with the UV-tube off, or with the UV beam blocked by a sheet of metal, the probe current was less than 5×10^{-10} amp, the limiting sensitivity of the measuring system. This check was performed not only to check the level of stray signal pickup, but to rule out the possibility that appreciable probe currents could be caused by photoelectric or photoconduction processes.

Data obtained with this probe arrangement for $p = 1$ Torr are shown in Fig. 47. When these data are processed by a straightforward application of the orbital limited, theory of double probes given in Appendix A, the plasma characteristics shown in Table IX were obtained.

Table IX

Probe Results for Plasma Experimental Setup No. 1

($p = 1$ Torr)

Ion density, n_i	$3 \times 10^5 \text{ cm}^{-3}$
Electron Temperature, T_e	27000° K
Sheath Radius	9.3 cm

The data in Table IX cannot be a true measure of the plasma characteristics for the following reasons. From basic energetics of photoionization in NO, the electron temperature cannot exceed 0.95 ev, i.e. 11000° K . From measurements

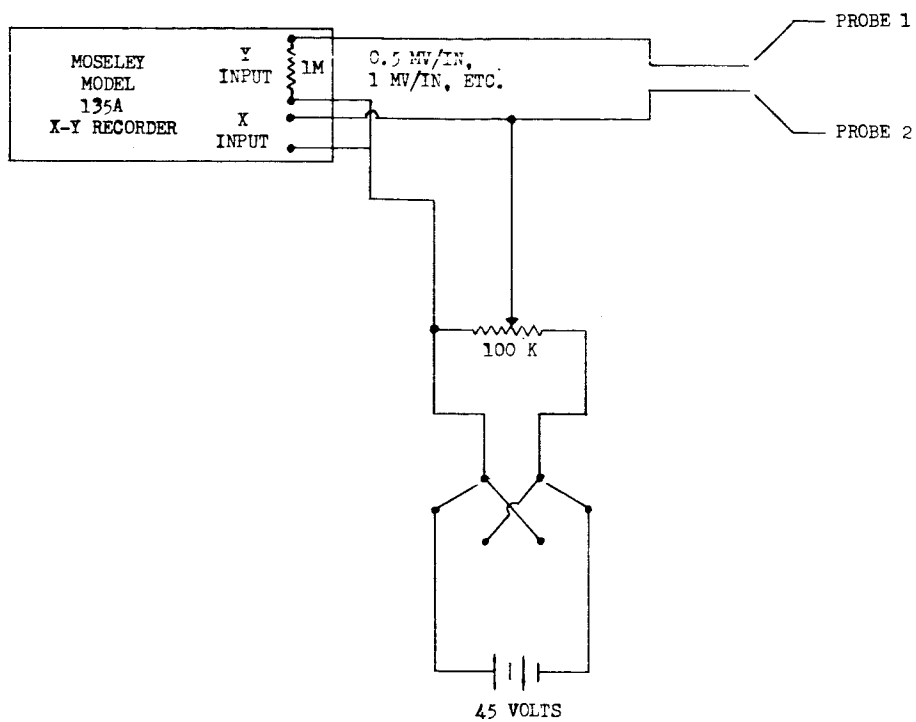


FIG. 46 DOUBLE PROBE CIRCUITRY

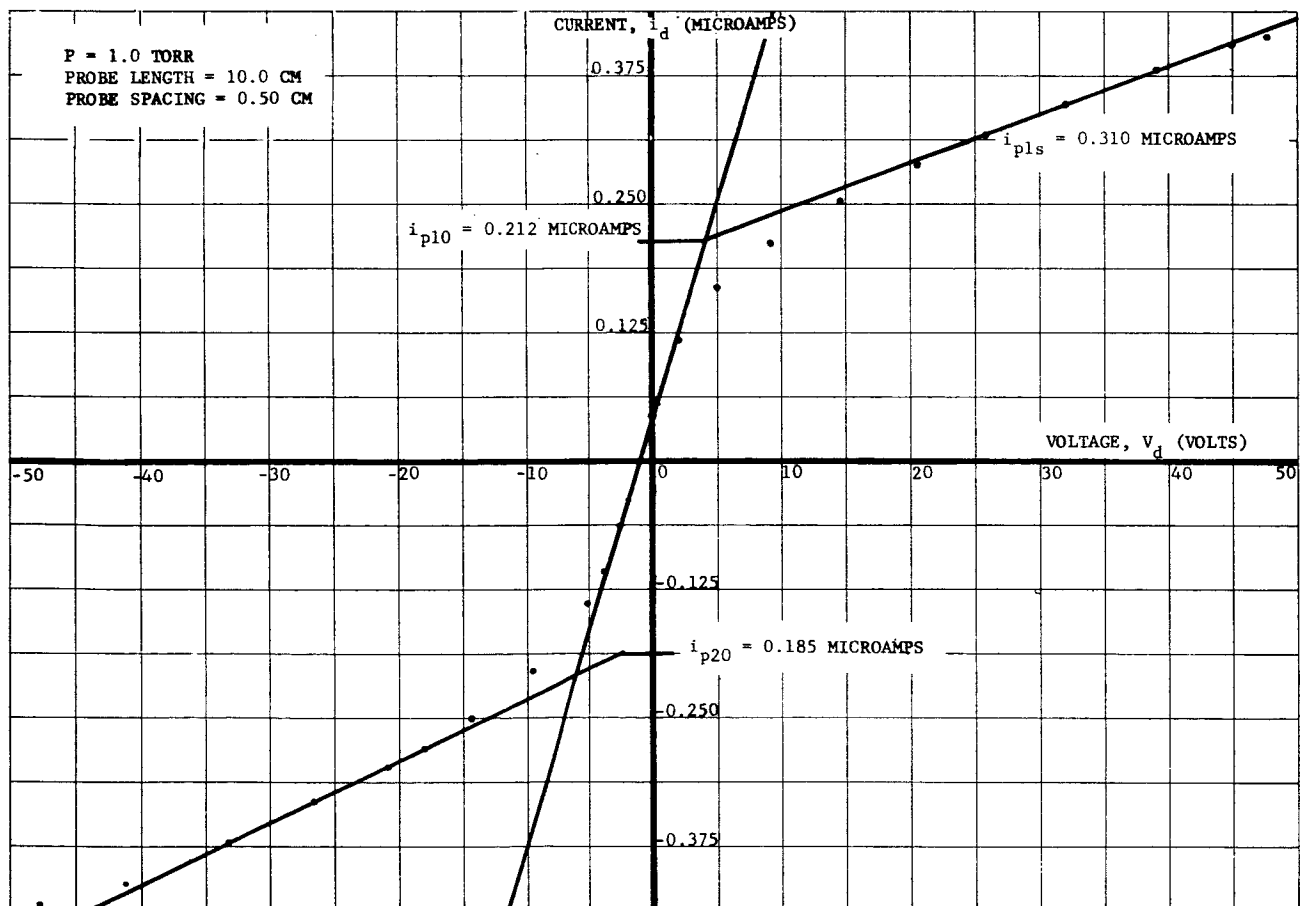


FIG. 47 DOUBLE PROBE I-V CHARACTERISTIC FOR EXPERIMENTAL SETUP NO. 1

of the UV output of the tube and basic physics, the ion density should be between 10^7 and $5 \times 10^8 \text{ cm}^{-3}$ if the plasma is at room temperature. Finally, the theory of the double probe given in Appendix A assumes no overlapping of the sheaths, while the data indicate a sheath radius of 9.3 cm for a probe separation of 0.5 cm.

It was surmised that these difficulties were caused by the probe system collecting too large a percentage of the available electrons and ions. Rough estimates, based upon a measured UV flux at the tube window of about 10^{13} photons- cm^{-2} - sec^{-1} , indicated that the probes were collecting about 20% of the available electrons and 20% of the available ions. Johnson and Malter [16] suggest that 1% is about the maximum that should be collected.

These considerations led to the construction of the double-probe arrangement shown in Fig. 45. This arrangement has five probes, so that measurements can be made at different probe spacings without opening the bell jar. Each probe was 0.0127 cm in radius. Initial measurements were made with an active length of 1 cm. Later measurements were made with an active length of 0.5 cm. Because each probe is at a different distance from the UV-tube, the UV level will be different at each probe, in general. Additionally, the absolute flux level at each probe will be a function of pressure. The flux level at a given distance from the UV-tube should increase with decreasing pressure, due to decreased absorption at the lower pressures. Assuming an inverse square law for intensity with distance, and an exponential dependence upon pressure, the relative flux levels at the two probe pairs used in the experiment is given in Table X for three different pressures.

Table X

Relative UV Intensities at the Probes for Plasma Experimental Setup No. 2

<u>P</u> <u>Torr</u>	<u>Probe 4 relative to Probe 1</u> <u>4.2 cm spacing</u>	<u>Probe 3 relative to Probe 2</u> <u>0.6 cm spacing</u>
1.0	.206	.788
0.4	.254	.813
0.1	.284	.826

Using the second probe arrangement, the plasma characteristics were measured at four pressures (1.0, 0.98, 0.4, and 0.1 Torr), with two probe separations (4.2 and 0.6 cm), and for two active lengths of probes (1.0 and 0.5 cm). The I-V curves obtained under four of these conditions are shown in Fig. 40

By an application of the theory for double probe measurements given in Appendix A, the plasma characteristics given in Table XI were obtained.

Table XI

Same Probe Results for Plasma Experimental Setup No. 2

<u>Run</u>	<u>Probe</u> <u>Separation</u>	<u>Probe</u> <u>Length</u>	<u>Pressure</u>	<u>Ion</u> <u>Density at</u> <u>upper probe</u>	<u>Electron</u> <u>Temp.</u>	<u>Sheath</u> <u>Radius</u>
	<u>(cm)</u>	<u>(cm)</u>	<u>(Torr)</u>	<u>(cm⁻³)</u>	<u>(°K)</u>	<u>(mm)</u>
1	4.2	1.0	0.98	9.8×10^7	5790	0.72
2	0.6	1.0	0.98	2.7×10^7	2520	1.89
3	4.2	0.5	0.40	9.6×10^6	6160	6.07
4	0.6	0.5	0.40	1.2×10^7	5420	5.38

Using the same reasoning as was used to estimate the percentage of ions and electrons collected by the first probe arrangement, it is estimated that the second probe arrangement collected approximately 1% of the ions and electrons.

The data of Table XI indicate a spread of about 2.5:1 in the measured values of electron temperature and about a 10:1 spread in the measured values of ion density. However, aside from Run 2, the spread in electron temperatures reduces to about 1.15:1. Reasons for the deviation of the Run 1 density result from the results for the other three runs is not clear.

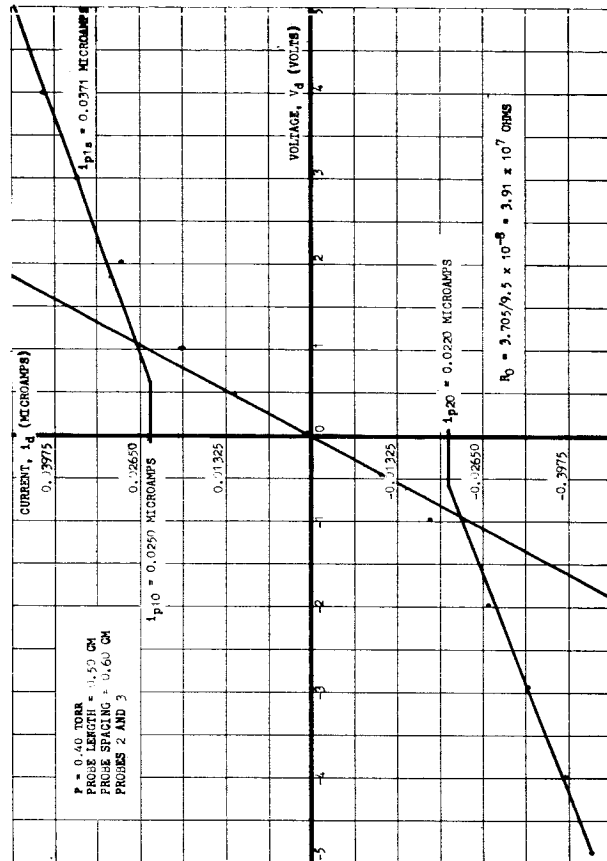
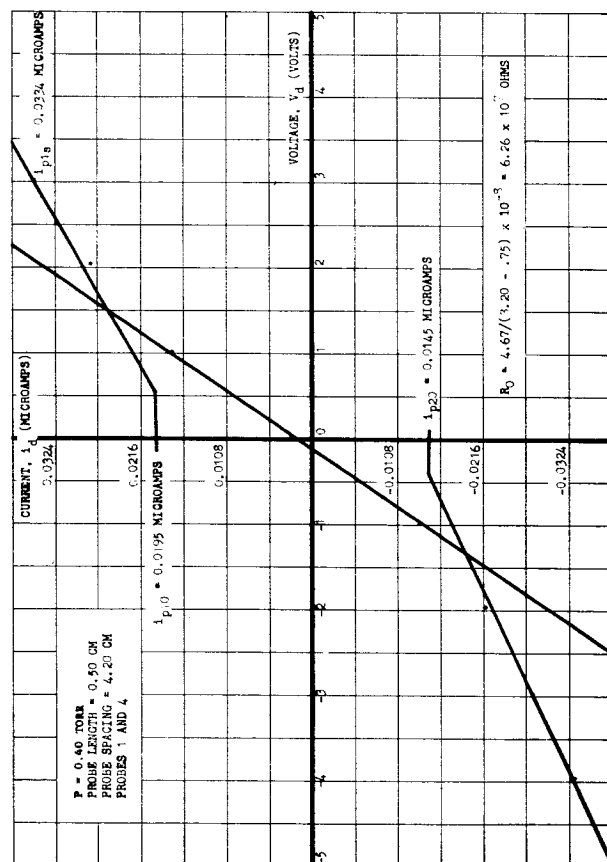
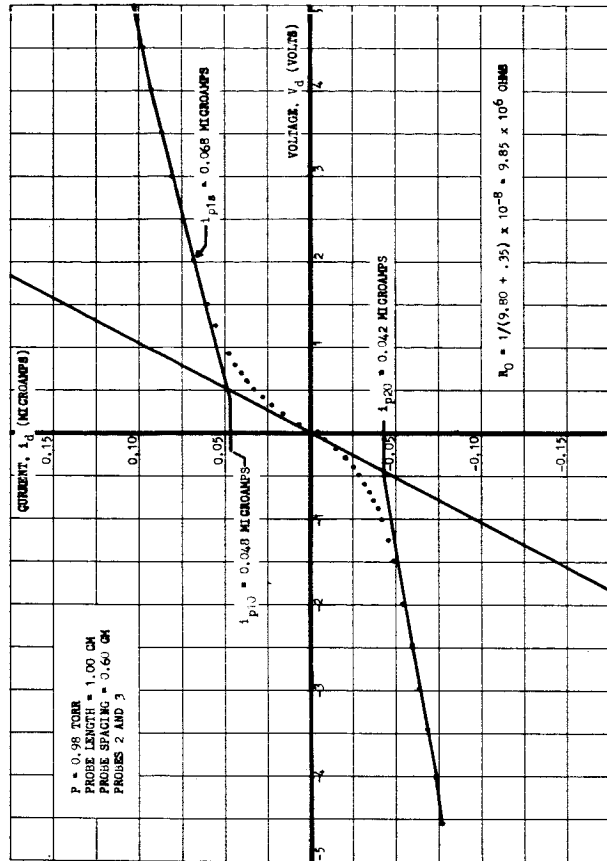
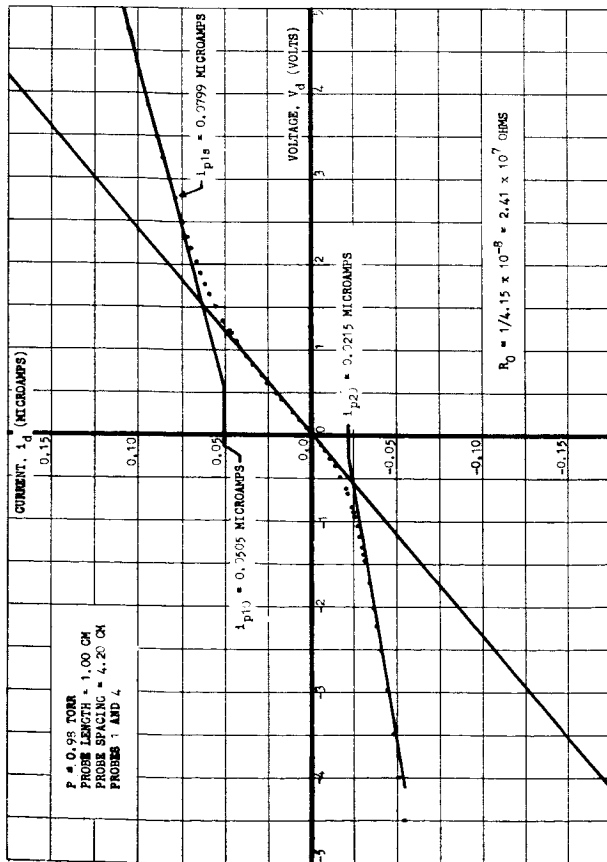


FIG. 48 SOME DOUBLE PROBE I-V CHARACTERISTICS FOR EXPERIMENTAL SETUP NO. TWO

At least part of the reason for the spread of values of electron temperatures and ion densities is a result of judgment in the selection of slopes on the various curves. Overall, however, it is felt that the values in Table XI are all reasonable and fall rather close to expected values. These data indicate that a low-temperature plasma has indeed been created by photoionization of NO.

Work on this problem has emphasized the need for refined techniques for the measurement of the characteristics of low-volume plasmas. These refined techniques include refined theory for the interpretation of probe measurements. The theory of double probes for various conditions is discussed in Appendix A.

3.2.3 Summary and Conclusions of Feasibility Study Program

Photoionization of NO by UV radiation from a hydrogen or krypton discharge tube has been shown to be feasible. The plasma density and temperature lie within the range expected from theoretical considerations. Consequently, the development of a large-volume, low-temperature plasma to simulate the D-region of the ionosphere, using the photoionization of nitric oxide, appears to be feasible.

The theoretical study shows that D-region simulation by this approach requires UV-tubes with photon fluxes of 10^{14} to 10^{16} photons-cm⁻²-sec⁻¹. From practical considerations, these tubes should have efficiencies (ratio of photon flux to d-c power input) in the range 0.01 to 0.1%. Since the electron mean free path should be small compared to the dimensions of the chamber in which the plasma is to be generated, a large chamber is required if plasmas are to be generated at pressures corresponding to the D-region. Using the present chamber, D-region simulation at altitudes of 80 km ($p \sim 10^{-2}$ Torr) is potentially possible.

The experimental work on UV-tube has shown that tubes having the requisite output and efficiency can be constructed. Consequently, it was decided that this technique would be applied to develop a large-volume plasma in the chamber.

Accordingly, a program was drawn up for the development and fabrication of the necessary UV-tubes to produce such a plasma. This program is described in the following section.

3.3 Program to Develop a Large-Volume Low-Temperature Plasma

3.3.1 Scope and Plans

The goal of this program is to produce a large-volume low-temperature plasma in the chamber by UV photoionization of NO. To produce a plasma of large cross section, an extended source of large area is required. This is most readily accomplished by arranging a number of tubes packed fairly closely in a bank. Following the successful demonstration that UV-tubes of the requisite output and efficiency could be built, it remained to choose a design which could be arranged in a geometrical configuration so as to produce a plasma of sufficient density and uniformity to satisfy the requirements. It was then necessary to fabricate a sufficient quantity of these tubes and to demonstrate that adequate output could be achieved and maintained for a reasonable life span. The UV-tubes would then be mounted on the chamber to produce the desired large-volume low-temperature plasma by photoionization of NO in the chamber. Following the successful production of such a plasma, detailed measurements are to be made of its characteristics. A schedule for the program was devised to accomplish this goal within a time of 3 months. In order to prevent bottlenecks, alternative approaches were devised as "backups" should any critical item in the development fail to be solved in the specified time.

Among the various UV-tube configurations which were developed, the type-D and type-B were considered to be the most promising to use. The type-D tube is cylindrical in shape, being a scaled-up version of the commercially available GBL-tube. The type-B tube has a parallel-plate geometry. It gave greater output and efficiency than the type-D. However, considerable additional development was

needed to improve sealing techniques and to increase life before this tube could be considered reliable enough to produce in the quantity required. Furthermore, this geometry did not lend itself to close assembly of a large bank of tubes. Consequently, after careful consideration, a modified type-D geometry was chosen to be the one which could be adapted to the planned program with the least amount of further development. This geometry is easily adaptable to assembly in a bank to produce a large area source, and thus allow the generation of a large volume plasma. Tubes of this design will be designated as Mod-D.

3.3.2 Mod-D Tube Design and Fabrication Program

3.3.2.1 Introduction

In order to generate a fairly large volume plasma of uniform density with the type-D tubes, it is necessary to arrange a number of tubes in a bank. However, the body of the type-D tube is too large, and the window too small, for use in a bank. With the large body-to-window diameter ratio, the "active area" is small compared to the overall diameter of any group of tubes. Accordingly, in the Mod-D tube the body diameter was reduced, the window diameter was increased, and the lead locations were modified.

On the basis of the comparisons between krypton and hydrogen discussed in Sec. 3.2.2.1.6.4, it was decided to use krypton as the filling gas.

The first part of the program was devoted to a series of special tests to obtain information on which to base decisions regarding tube design and assembly. These tests include sealing techniques, life tests and beam angle of the UV radiation. On the basis of these tests, final decisions were made regarding tube design, construction and processing, and the configuration of tubes in the composite tube bank.

3.3.2.2 Window Sealing Tests

The sealing of the lithium fluoride window to the body of the UV-tube is a troublesome process. Ideally, to outgas the source tube it should be baked at, say, about 450°C. However, due to the difference in coefficients of expansion of the glass body of the tube and the lithium fluoride window, this baking cannot be done with the window sealed to the body in the normal manner. Normally this seal is made with an epoxy cement or silver chloride (AgCl). When tubes use this sealing technique and have windows larger than about 0.375-inch diameter, the seal or the tube body will crack when they are baked at elevated temperatures. The best that has been done is to seal a 0.375-inch diameter window to the body with AgCl when the bake is carried to about 450°C.

Indium appeared to be a possible sealing agent, in view of its coefficient of expansion and low melting point. If a seal could be made with indium, then it should be possible to bake the tubes at elevated temperatures. Accordingly, tests of the indium sealing technique were performed.

The edges of a lithium fluoride window were silvered (since indium would not adhere directly to the lithium fluoride), the face of a copper tube was silvered, and an attempt was made to seal the two together using indium. The test setup used is shown in Fig. 49. The indium was flowed onto the sealing surfaces by heating the test setup in an oven flooded with dry nitrogen. Two difficulties were encountered. The indium (99.999% pure) did not wet the sealing surfaces well, and it tended to flow under the window even when a vacuum (< 3 Torr) was pulled on the test setup in an attempt to seat the window tightly against the copper tube. Silver plating the copper seat did not improve the wetting. Grinding the edge surface of the window and the edge of the tube body did not help this situation, although it did allow a better vacuum (0.2 Torr) to be pulled on the test setup.

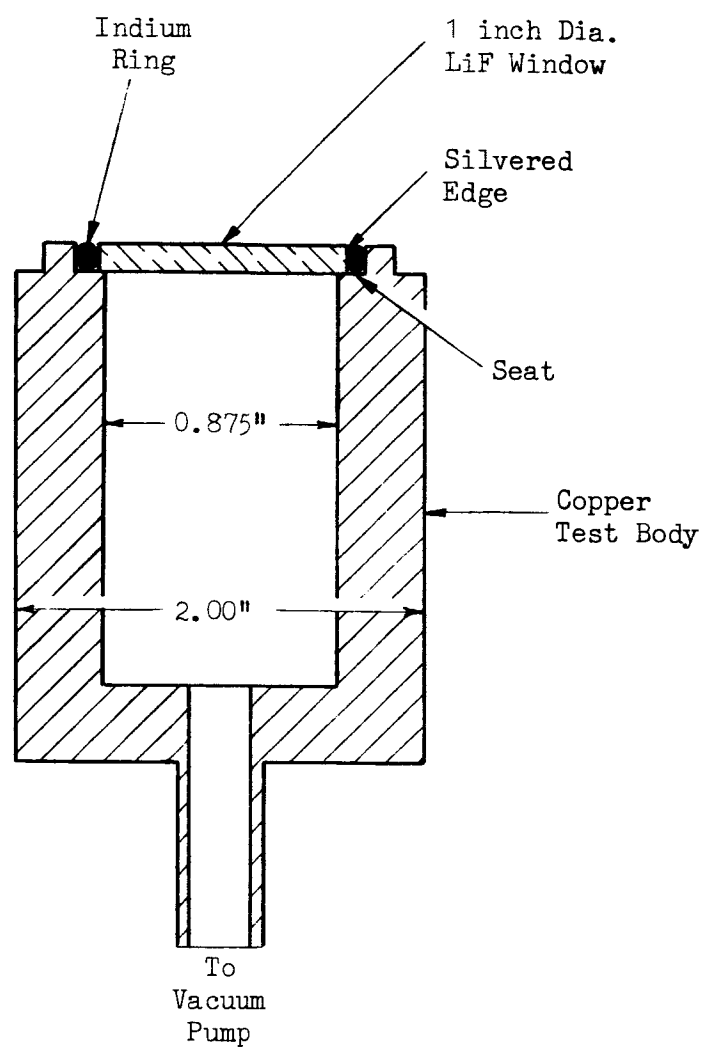


FIG. 49 INDIUM SEAL TEST SETUP

Since the indium sealing technique did not work successfully within the time limit set for this work, it was dropped. Accordingly, it was decided that seals for the large bank of tubes would be made using black wax (Apiezon W). This decision was made in order to maintain the performance schedule.

3.3.2.3 Beam Angle Measurements

When it was decided that a large bank of UV-tubes would be used to generate the large-volume plasma in the chamber, one of the first questions that needed to be resolved was the number of tubes which would be required.

In the first layout of the UV-tubes, they were placed as closely together as was physically possible to completely fill one of the 8-inch diameter ports in the chamber. This arrangement required 31 source tubes. For this number, calculations indicated that the UV flux would be more than needed for ionospheric simulation. This indicated that an arrangement using fewer tubes would be satisfactory from a total flux consideration. However, if a uniform plasma is to be developed, the distance between tubes that can be tolerated depends upon the beam angle of the UV light emerging from the tube.

Consequently, measurements were made to determine the beam angle of the UV radiation emerging from one of the tubes. This was accomplished by moving a UV detector with a 1-mm diameter window laterally across the face of tube D-2. The detector was at a distance of 5 cm from the face, and the intervening path was evacuated to a pressure of 9μ . The beam pattern obtained is shown in Fig. 50. This indicates a half-power beamwidth of 38° .

Using this beamwidth, defining a "uniform" plasma as one in which the density variations do not exceed 2-to-1 at a distance of 5 cm from the UV source, and allowing for some dispersion of the beams, a modified arrangement of the UV-tube was devised. This is shown in Fig. 51. This arrangement uses only 13 tubes,

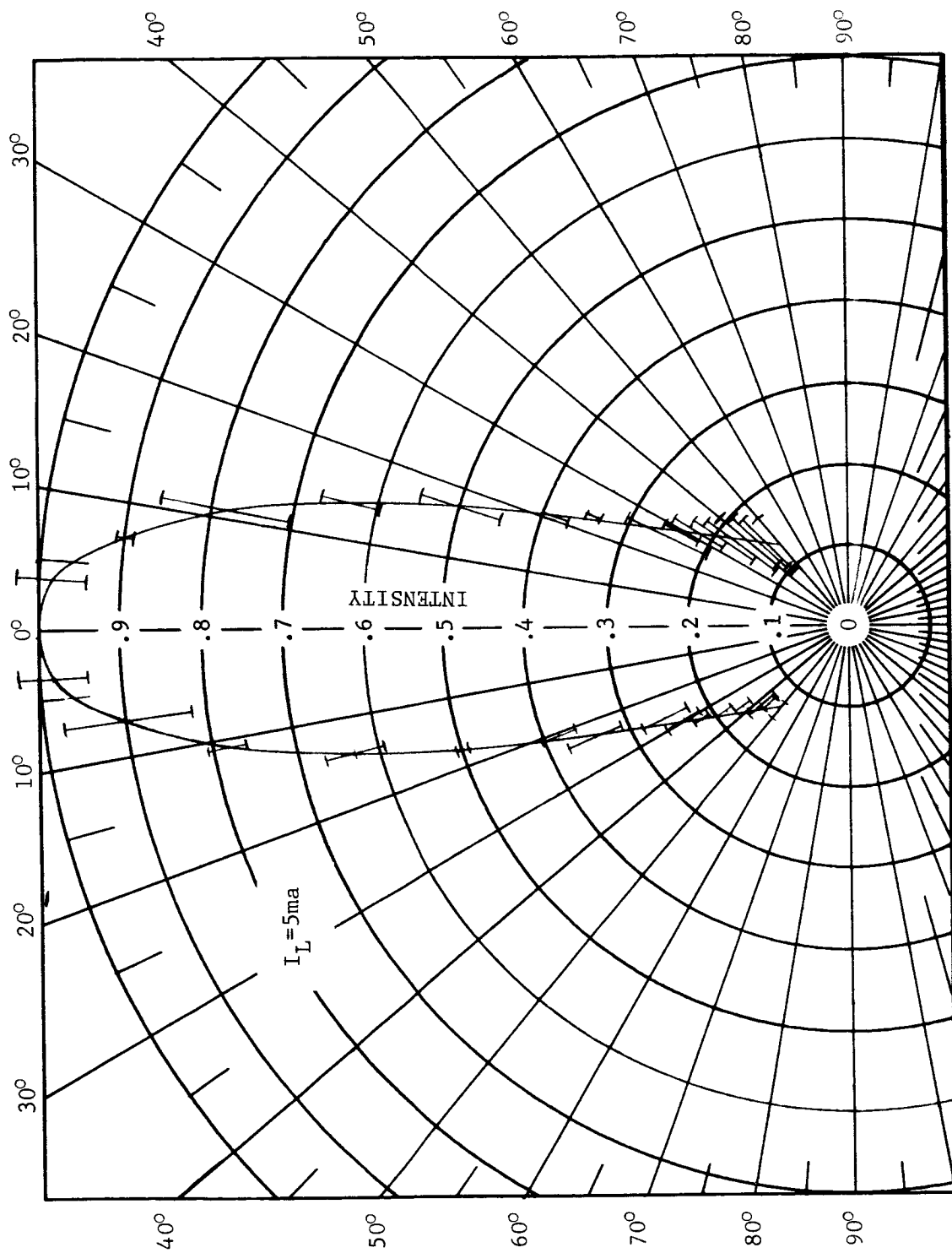
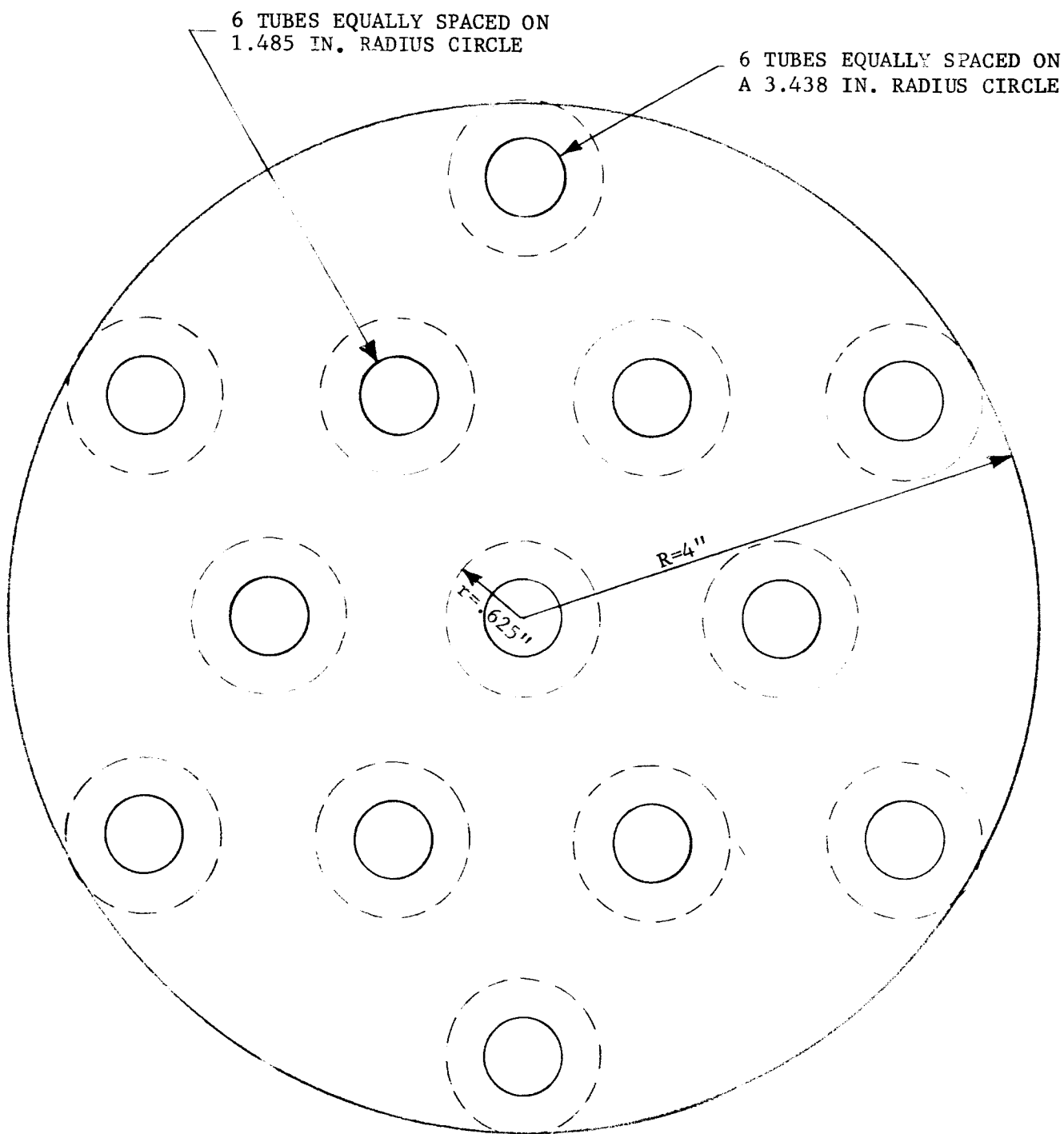


FIG. 50 TUBE D-2 BEAM PATTERN AT 5 CM



DASHED LINE - TUBE SIZE
SOLID LINE - LIF WINDOW SIZE

FIG. 51 TUBE BANK - MODIFIED ARRAY

instead of the 31 tubes in the first layout. Since the ionization density was calculated to be adequate, this arrangement was adopted.

3.3.2.4 Large Detectors

A commercial NO ion chamber detector (developed at NRL and manufactured by GBL) has an effective window diameter of 0.375 inch. The Mod-D tube, selected to develop the large-volume plasma, has an effective window diameter of 0.625 inch. Detectors having an effective window diameter at least as large were required to test these tubes.

Accordingly, three detectors having effective window diameters of 0.875 inch were constructed. A cross-sectional sketch and a photograph of one of these detectors are shown in Fig. 52. The body is larger than that of the GBL detector (11.86-cm effective length, 1.5-inch inside diameter) to prevent the saturation which was noted in previous tests on the standard detector. One of the large detectors (designated as L-1) had an unplated copper body, while the other two (designated as L-2 and L-3) were gold plated in an attempt to reduce the photoelectric current. The NO gas used for filling the tubes was purified by a distillation process described by Stober [17].

The I-V characteristic of detector L-2 was measured when it was evacuated ($p = 4.5 \times 10^{-6}$ Torr) and when it was filled with NO pressures of 0.9, 2.0, and 9.8 Torr. These measurements were made when the detector was irradiated with two different UV levels obtained by operating a type-A UV-tube at currents of 100 μ a and 200 μ a. The results of these tests are shown in Fig. 53. Fig. 53 shows that the plateau for this detector occurs between 10 and 25 volts and that the plateau voltage increases slowly with increasing pressure.

The I-V characteristic of the unplated detector (L-1) was measured when it was evacuated. No significant difference in photoelectric current was noted between the plated and unplated detectors. This was contrary to expectation, and possibly may have been due to poor gold plating.

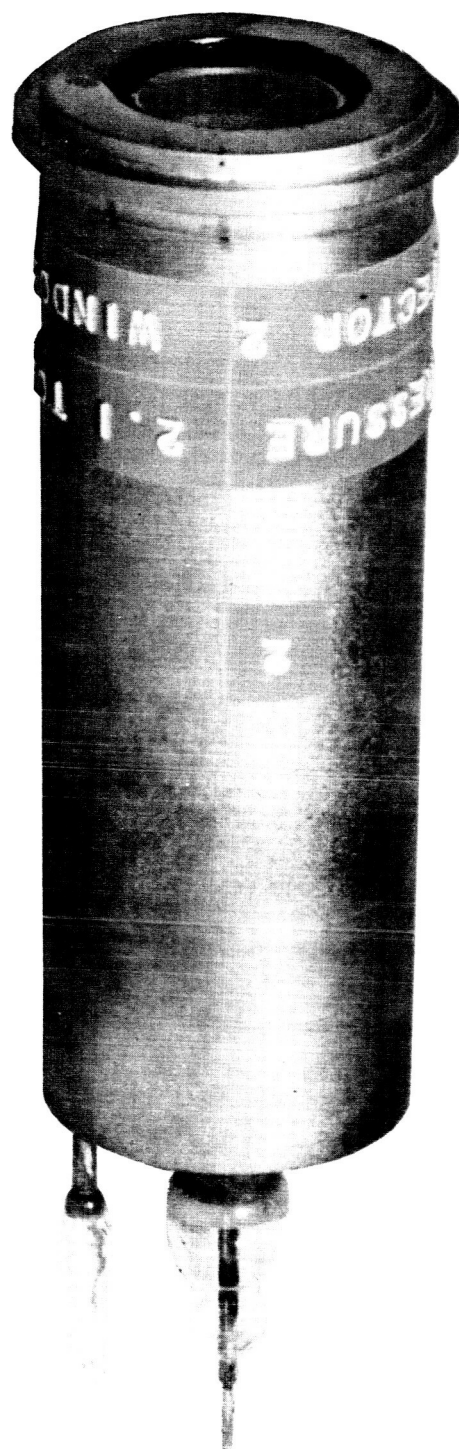
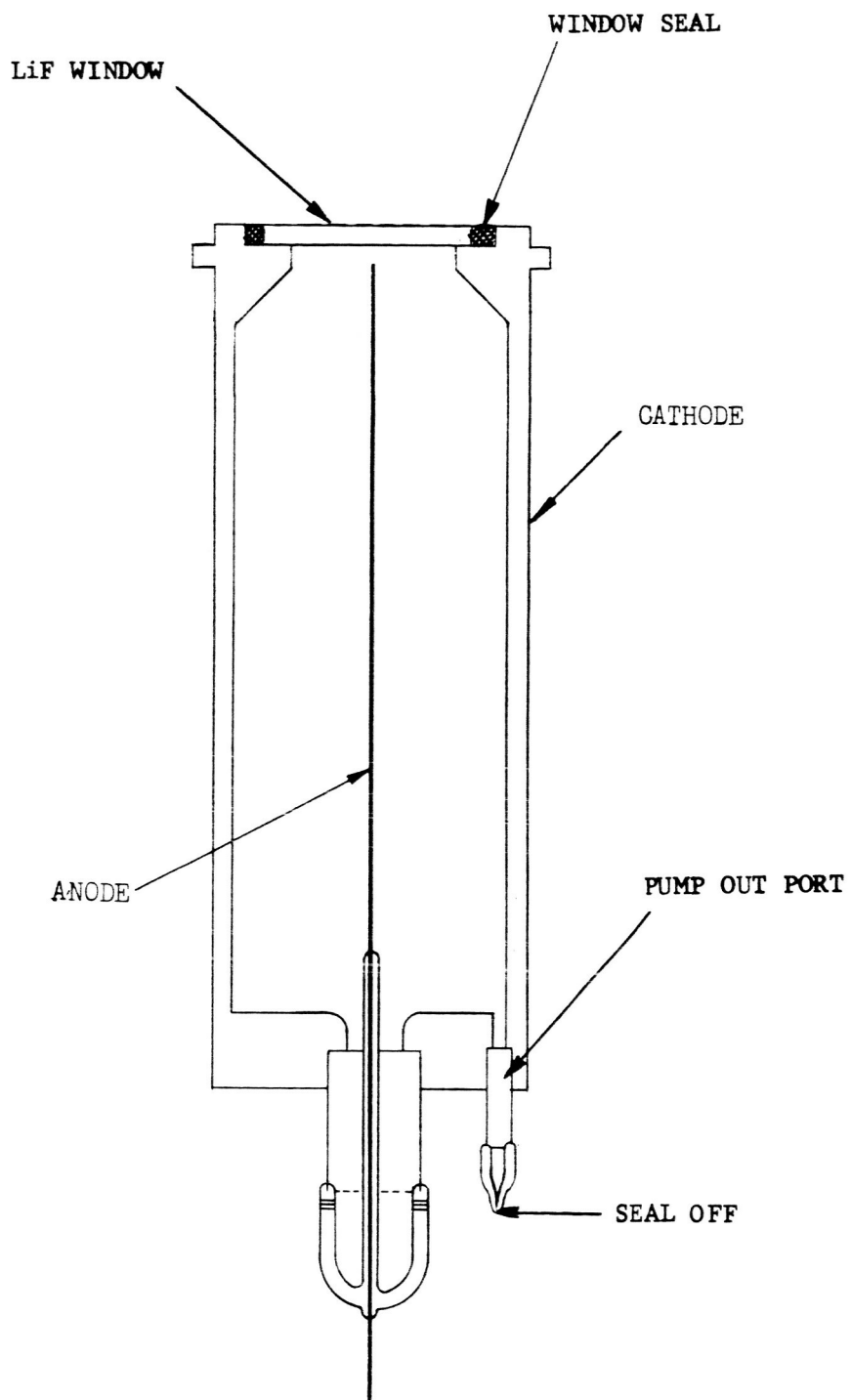


FIG. 52 LARGE DETECTOR CROSS SECTIONAL VIEW AND PICTURE

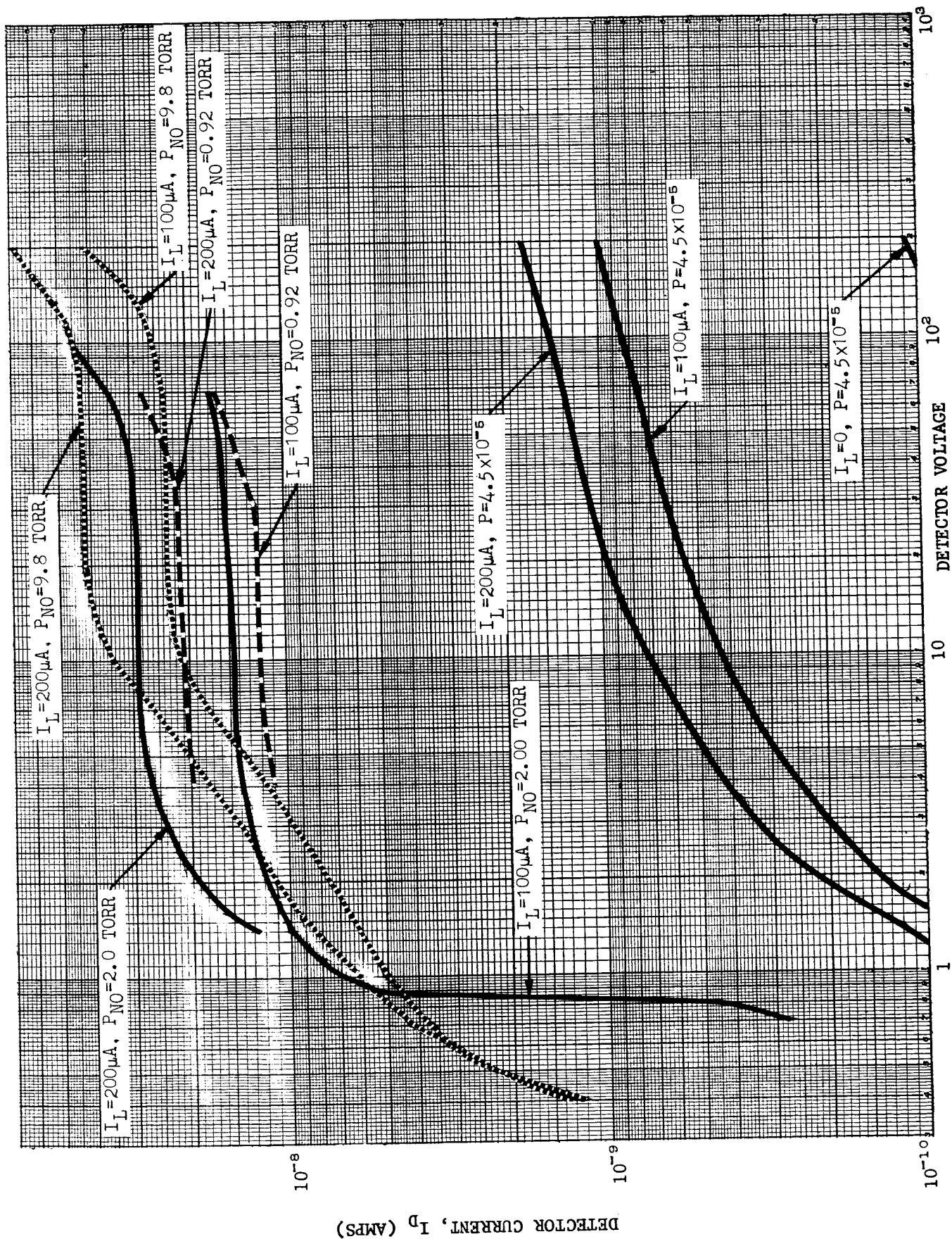


FIG. 53 DETECTOR L-2 CURRENT VS VOLTAGE CHARACTERISTICS

Fig. 54 is a plot of the ratio of the detector current, $I_D(200)$, when irradiated by the type-A tube operating at 200 μA to the detector current, $I_D(100)$, with the type-A tube operating at 100 μA , as a function of detector voltage, V_D , in the plateau regions for NO pressures of 0.92, 2.00, and 9.80 Torr. Within experimental error, pressure does not effect this ratio, which, at a given pressure, appears to be constant over the plateau. These data were obtained to determine the detector efficiency. From theory, at an NO filling pressure of $p = 9.8$ Torr, 99.99% of the photons that enter the detector are absorbed by the NO. The ratio of the photoionization to total absorption cross section at Lyman- α (0.84), multiplied by the window transmission (about 50% at Lyman- α), then defines the absolute efficiency, η_{∞} , of the detector for Lyman- α at $p = 9.8$ Torr. For the detector tested, $\eta_{\infty} = \sim 0.42$ when filled with NO to a pressure of 9.8 Torr.

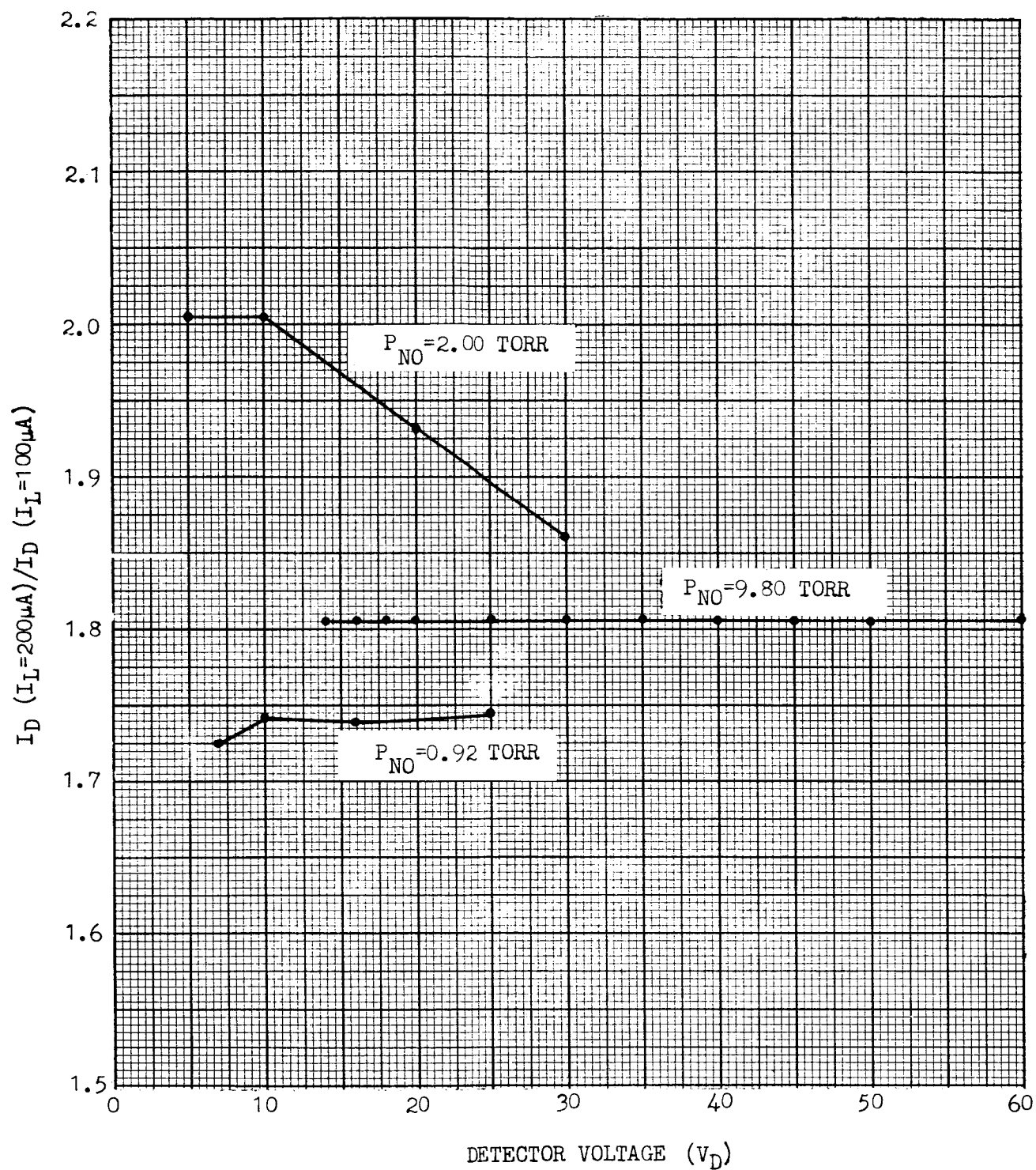
If this value of η_{∞} is multiplied by the ratio of detector currents for the standard commercial detector used in the work described in [18] and the new large detector under the same conditions of Lyman- α irradiation, the efficiency of the standard detector may be estimated. Proceeding in this manner, the efficiency of the GBL detector is about 10%*.

As a further check upon the efficiency of the large detectors, the ratios of the average detector plateau currents for several pressures were determined for two values of UV radiation on the detector. These ratios were then compared with theoretical ratios of the flux absorbed in the detector to the incident photon flux, assuming a total absorption cross section at Lyman- α of $2.4 \times 10^{-18} \text{ cm}^2$ [19]. The theoretical and experimental ratios agree within about 15%.

The large detectors were actually filled to a pressure of 2.0 Torr. Using the ratios just discussed, the efficiencies of the three large detectors were

*

The 10% efficiency of the GBL detector indicates that the photon flux levels given in [18] are low by a factor of ten.



NOTE: EXPERIMENTAL ERROR APPROX. $\pm 10\%$

FIG. 54 RATIO OF DETECTOR CURRENTS FOR TWO UV INPUTS
AS A FUNCTION OF DETECTOR VOLTAGE

determined, and are given in Table XII.

Table XII

Large Detector Efficiencies At Lyman- α

<u>Detector</u>	<u>Efficiency (%)</u>
L-1	23
L-2	29
L-3	24

Taking into account the relative absorption cross sections of NO at 1215.6 \AA and 1235.8 \AA , the efficiency of the detector at the krypton line should be about 0.9 of the efficiency at Lyman- α

3.3.2.5 Mod-D Design

3.3.2.5.1 Construction

The final Mod-D design is shown in Fig. 55. The window has an effective diameter of 0.625 in., and a metal nosepiece anode; the cathode is brought out the rear of the tube in order to allow assembly in a bank. In addition, a getter has been added to keep impurities to a minimum.

Three Mod-D tubes were fabricated for test purposes. The first of these, Mod-D-1, did not have a getter, the spacing between the end of the capillary tube and the window was 1.7 cm, and the cathode area was 2.92 cm². The next two tubes, Mod-D-2 and Mod-D-3, were provided with getters, and cathode areas of 14.6 cm². The spacing between the end of the capillary tube and the window in Mod-D-2 was 1 cm, and 1.7 cm in Mod-D-3. The different spacings for these tubes allowed an investigation of the effect of this spacing on tube output.

3.3.2.5.2 LiF Window Transmission

The transmissions of the LiF windows used on the prototype Mod-D UV-tubes (and also on the detectors discussed in Sec. 3.3.2.4) were determined by measuring the intensity of a standard CBL tube with and without

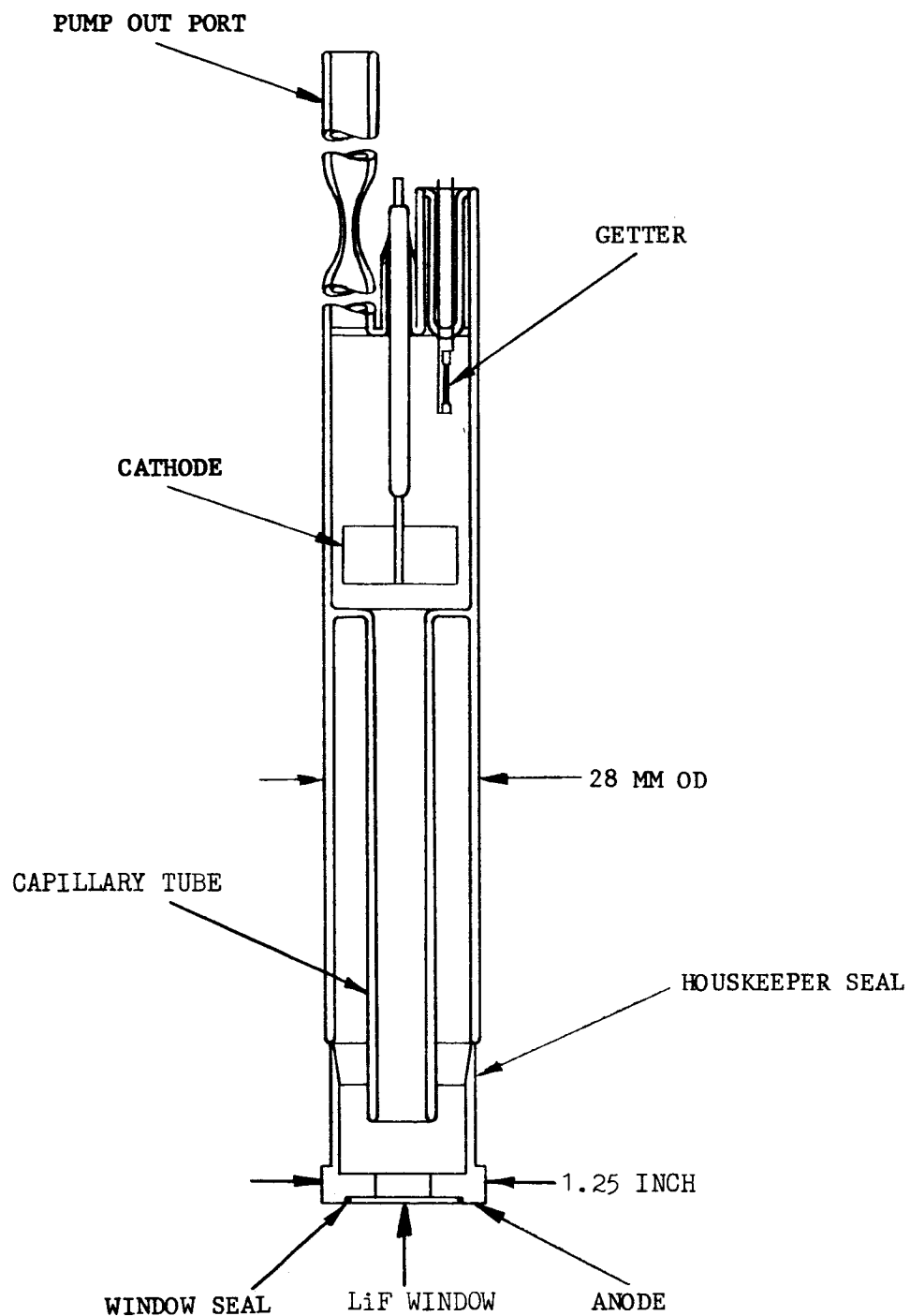


FIG. 55 CROSS SECTIONAL VIEW OF MOD-D TUBE

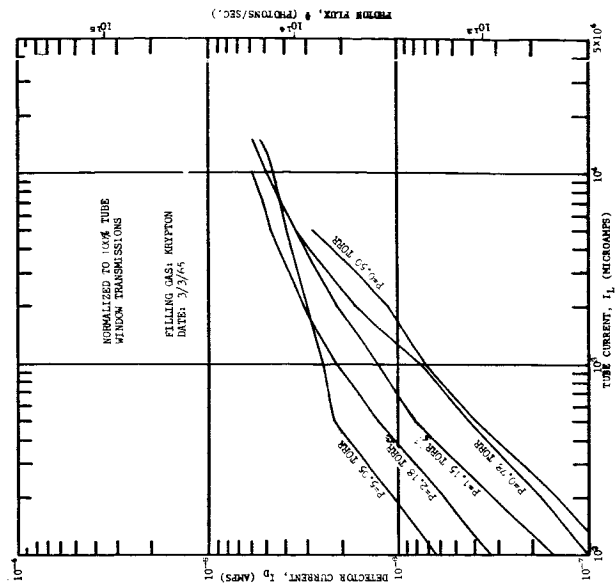
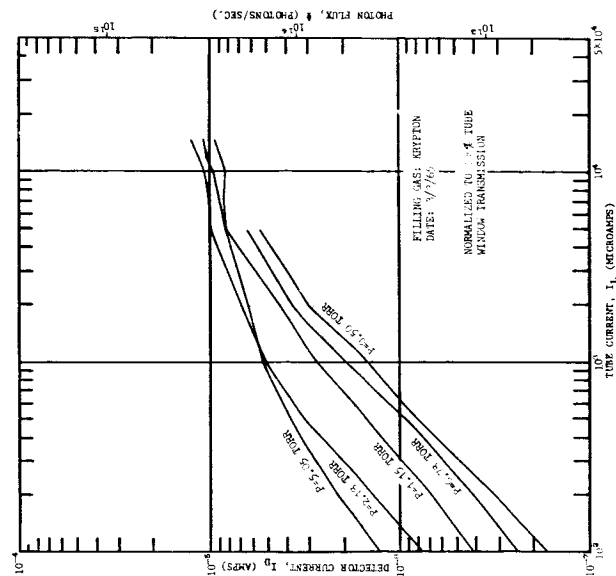
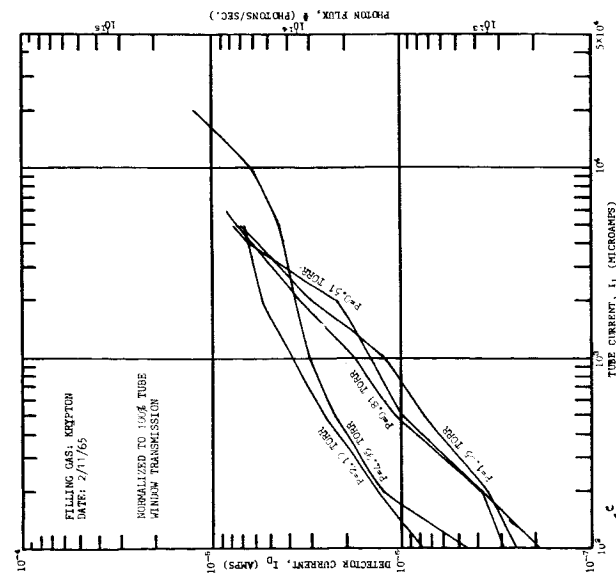
each of the windows in a vacuum transmission path. The measured values of transmission ranged from about 39 to 48%.

For some of these windows, the transmission was also measured using the same experimental setup but with a GEL-type tube filled with krypton as the UV source. The results of these tests show that, within the experimental error, the effective transmissions are the same for the hydrogen and krypton lamps.

3.3.2.5.3 Gas Filling Performance Tests

The outputs of tubes Mod-D-1, Mod-D-2, and Mod-D-3 were measured as a function of discharge current for krypton pressures of 0.51, 0.81, 1.05, 2.10, and 5.05 Torr. The results of these tests are shown in Figs. 56, 57, and 58. These figures show that a pressure of 2 Torr gives the best output over the range of discharge currents, and was thus selected for the filling pressure. The crossovers of the 1.15, 2.18, and 5.05 Torr curves in Figs. 57 and 58 are attributed to self absorption effects, which increase with increasing pressure.

The V-I characteristics of the same three tubes were also measured for the same krypton pressures, and the results for Mod-D-1 are shown in Fig. 59. The quantity $j/p^2 = C_1 = \text{constant}$ for the normal glow region, where j is the cathode current density and p is the pressure. Thus, $I_L/p^2 = C_2 = \text{constant}$ at the transition point between normal and abnormal glow. The transition points and values of C_2 in Table XII were obtained from Fig. 59. The values of C_2 are seen to fall quite close together.



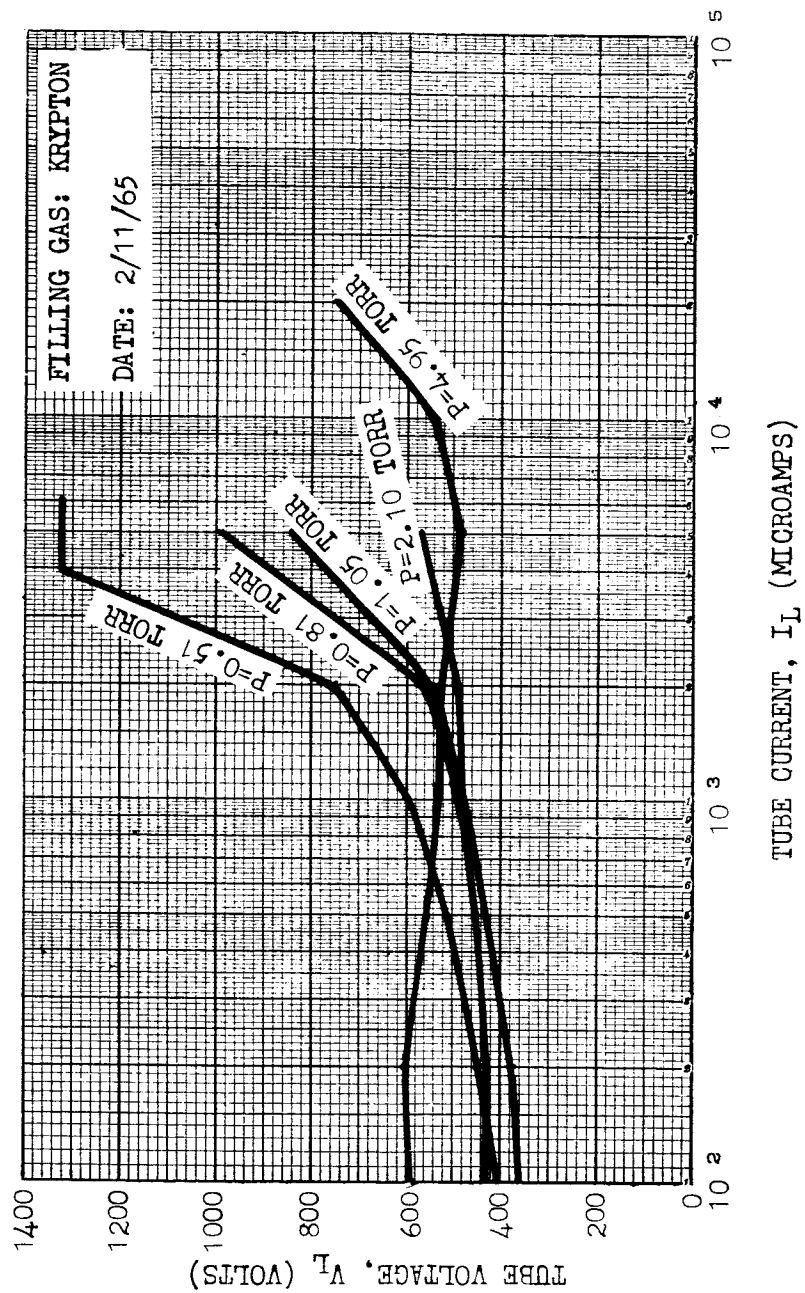


Table XIII

<u>Pressure</u> <u>Torr</u>	<u>Transition</u> <u>Current</u> <u>μa</u>	<u>C_a</u> <u>ma/Torr²</u>
0.5	0.1	0.386
0.81	0.3	0.459
1.05	0.5	0.454
2.10	2	0.454
4.95	10	<u>0.426</u>
	Average	= 0.436

The UV-tube should operate at its maximum power dissipation at the transition point for several reasons: sputtering increases rapidly in the abnormal glow region and shortens tube life; efficiency is less in the abnormal glow region; the widest range of tube operation is obtained; and, at the transition point, the V-I characteristic has a positive slope and thus the tube is a positive resistance so that the operating point will be stable. A reasonable maximum power dissipation for the modified tube is 10 watts (at this point the tube envelope becomes warm-to-hot to the touch). Fig. 59 shows that the tube voltage is approximately 500 volts at the transition point for $p = 2$ Torr. Thus, a tube current of 20 ma is required for the 10-watt maximum power dissipation. Fig. 59 also shows that tube Mod-D-1 operates at about 1 ma at the normal-abnormal transition point. The cathode area should therefore be increased by about ten to provide the necessary tube current.

On the basis of the above tests, the cathode area for the Mod-D tubes to be developed for use on the chamber was chosen to be cm^2 ; this should result in operation at design power input of 10 watts.

3.3.2.5.4 Performance of Mod-D and D-Tube Geometries and Effect of Capillary Window Spacing

Tests run with tubes Mod-D-1 and tube D-3 indicated that they were comparable in output/unit window area. More extensive tests were run with tubes Mod-D-2, Mod-D-3, and D-3 to compare their performance at a number of pressures between 0.5 and 5.05 Torr. The results of these tests are shown in Figs. 60 through 63. (The curves marked with S-2 had a stop introduced in front of the window to reduce the effective window area to that of tube D-3 to allow a direct comparison of effective UV output/unit window area.) It is seen from these figures that Mod-D-2 has greater output than Mod-D-3. It thus appears that the shorter capillary tube-to-window spacing in Mod-D-2 increases tube output. It is also seen that the output/unit window area of tube Mod-D-2 is the same as tube D-3 within experimental error. Thus scaling has not decreased the output/unit window area.

3.3.2.5.5 Beam Angle Measurements

The beam angle tests on tube D-2 have been discussed in Sec. 3.3.3. In addition, similar beam angle measurements were made on tube Mod-D-1. These measurements were carried out in a vacuum for two different UV-tube discharge currents (1 ma and 5 ma), and were repeated several times. There were no appreciable differences between the data obtained on the 1 ma and the 5 ma runs, nor were there appreciable differences on the repeat runs.

The results for Mod-D-1 are shown in Fig. 64. The half-power beamwidth, about 57 degrees, is larger than for tube D-2. The apparent increase in beamwidth seems consistent with the larger window diameter of Mod-D-1.

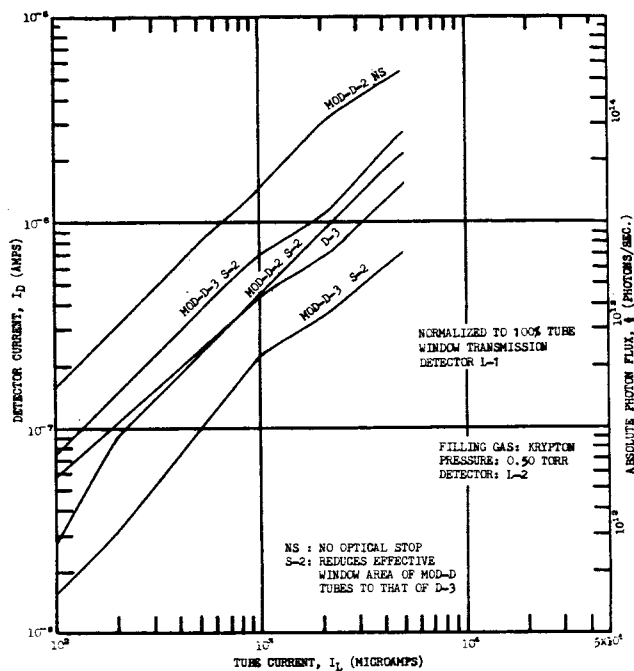


FIG. 60 DETECTOR CURRENT VS CURRENT CHARACTERISTICS OF TUBES MOD-D-2, MOD-D-3, AND D-3 FOR $P=0.50$ TORR OF KRYPTON

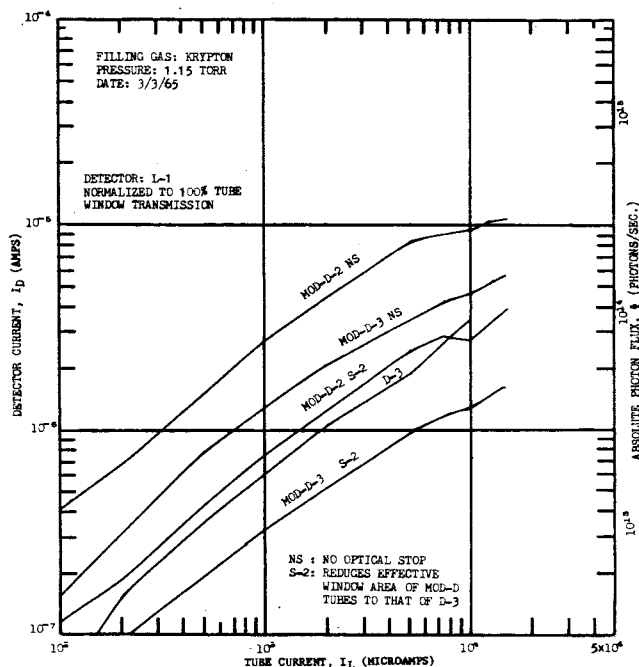


FIG. 61 DETECTOR CURRENT VS CURRENT CHARACTERISTICS OF TUBES MOD-D-2, MOD-D-3, AND D-3 FOR $P=1.15$ TORR OF KRYPTON

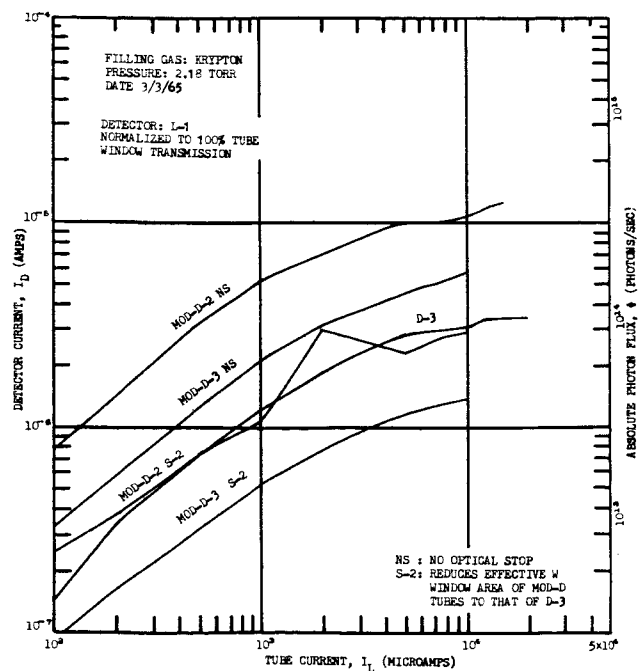


FIG. 62 DETECTOR CURRENT VS CURRENT CHARACTERISTICS OF TUBES MOD-D-2, MOD-D-3, AND D-3 FOR $P=2.18$ TORR OF KRYPTON

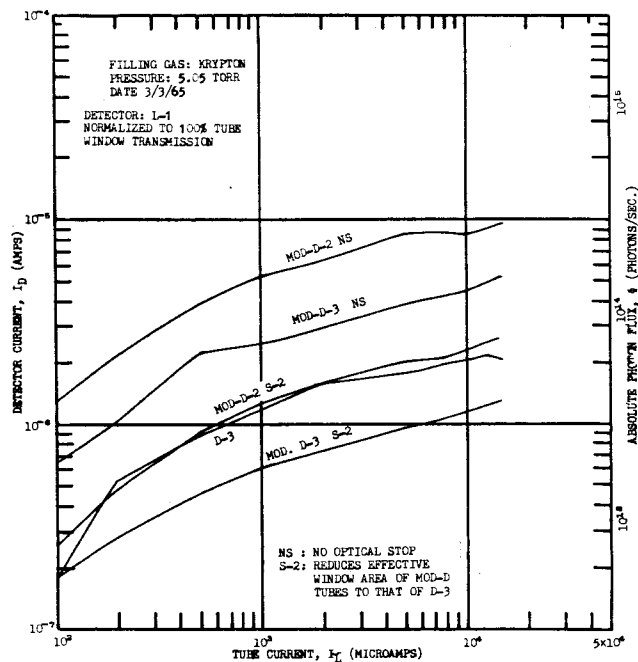


FIG. 63 DETECTOR CURRENT VS CURRENT CHARACTERISTICS OF TUBES MOD-D-2, MOD-D-3, AND D-3 FOR $P=5.05$ TORR OF KRYPTON

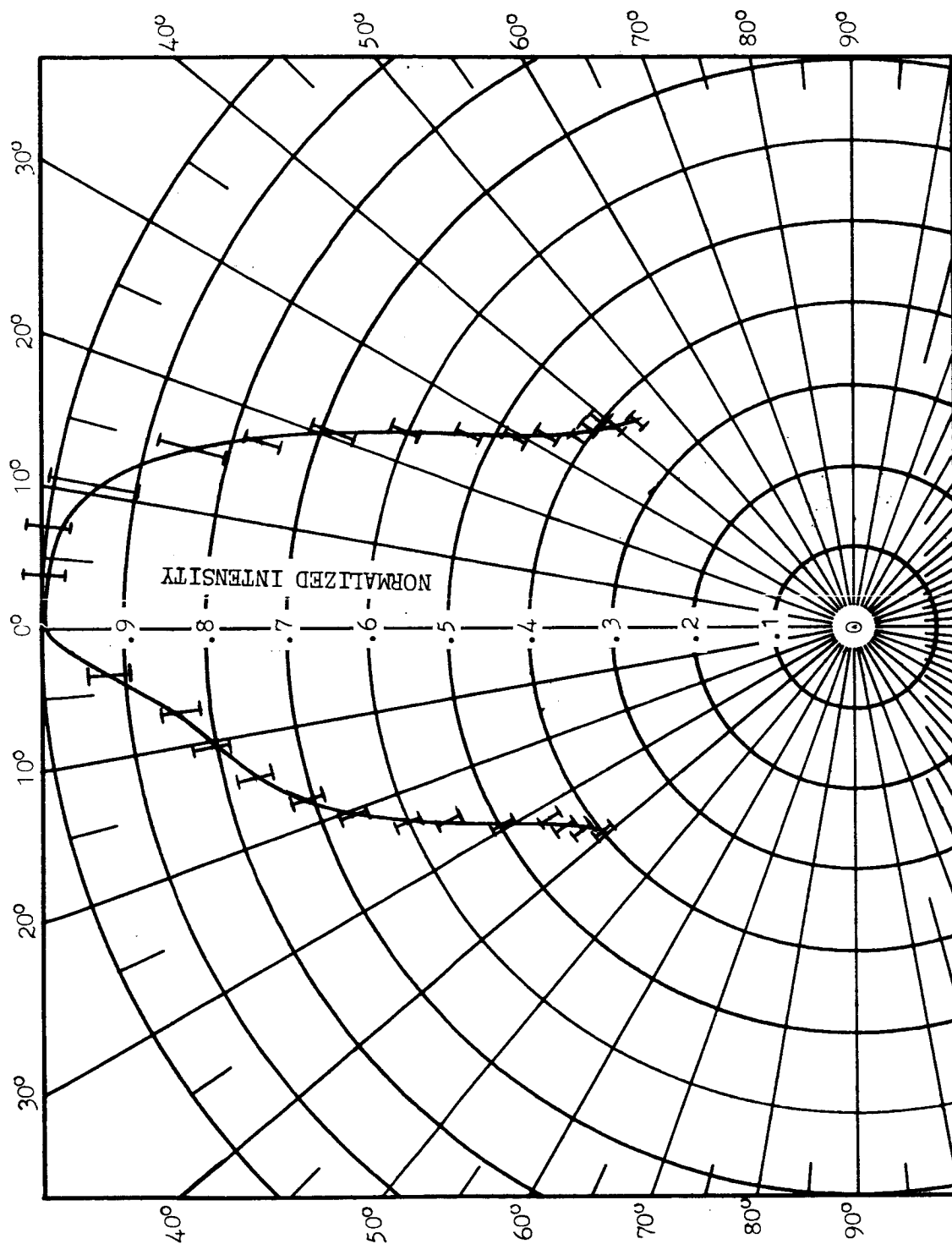


FIG. 64 TUBE MOD-D-1 BEAM PATTERN AT 5 CM.

3.3.2.6 Mod-D Tube Fabrication Program

As a result of the satisfactory performance characteristics obtained from the prototype Mod-D tubes, the fabrication of 25 additional tubes was undertaken. 25 Mod-D tube envelopes were assembled by the glassblower. These were then processed in accordance with stringent specifications and quality control procedures to insure uniformity and long life. The processing was done on a bakeable gas-handling system specially designed and constructed for the purpose. Tests were then made of UV output, output versus time, and spectral density.

3.3.2.6.1 Bakeable Gas-Handling System

The gas-handling system is shown in block diagram form in Fig. 65. It has two sections separated by a vertical divider partition. A heater power of about 12 kw is required to heat the main over to 450° C in 3 hours, and about 4 kw average power is required to hold this temperature. The oven for the molecular sieve trap, which is separate, requires 1.2 kw to heat to 450° C in 3 hours, and 400 watts to hold this temperature. The oven walls are 3-inch thick Marinite-36. The whole system, including the controls, is mounted on a 4 x 7 ft. table. The valves, variable leak, capacitance manometer head, and traps are mounted on the vertical divider in the middle of the table. Photographs of the assembled system with and without the bakeout ovens in place are shown in Fig. 66. With this system, the tubes can be baked at 225° C and the rest of the system at 450° C. A vacuum of less than 5×10^{-8} Torr can be maintained on the system prior to gas filling. The special sieve trap indicated in Fig. 65 uses unsintered Vycor [20] as the active material.

3.3.2.6.2 Tube Processing

The 25 Mod-D tubes were processed in three batches. There were 13 tubes in the first batch, 10 tubes in the second batch, and two tubes in the third batch. Batches nos. 1 and 2 were filled with krypton and batch no. 3

- 1 GRANVILLE PHILLIPS TYPE 10 ℓ /sec BAKEABLE VALVE
- 2 GRANVILLE PHILLIPS TYPE C 1 ℓ /sec BAKEABLE VALVE
- 3 GRANVILLE PHILLIPS TYPE C 1 ℓ /sec BAKEABLE VALVE
- 4 GRANVILLE PHILLIPS BAKEABLE VARIABLE LEAK TYPE 9100
- 5 GRANVILLE PHILLIPS BAKEABLE CAPACITANCE MANOMETER (0-100 TORR HEAD)
- 6 CVC TYPE GM100 McLEOD GAUGE

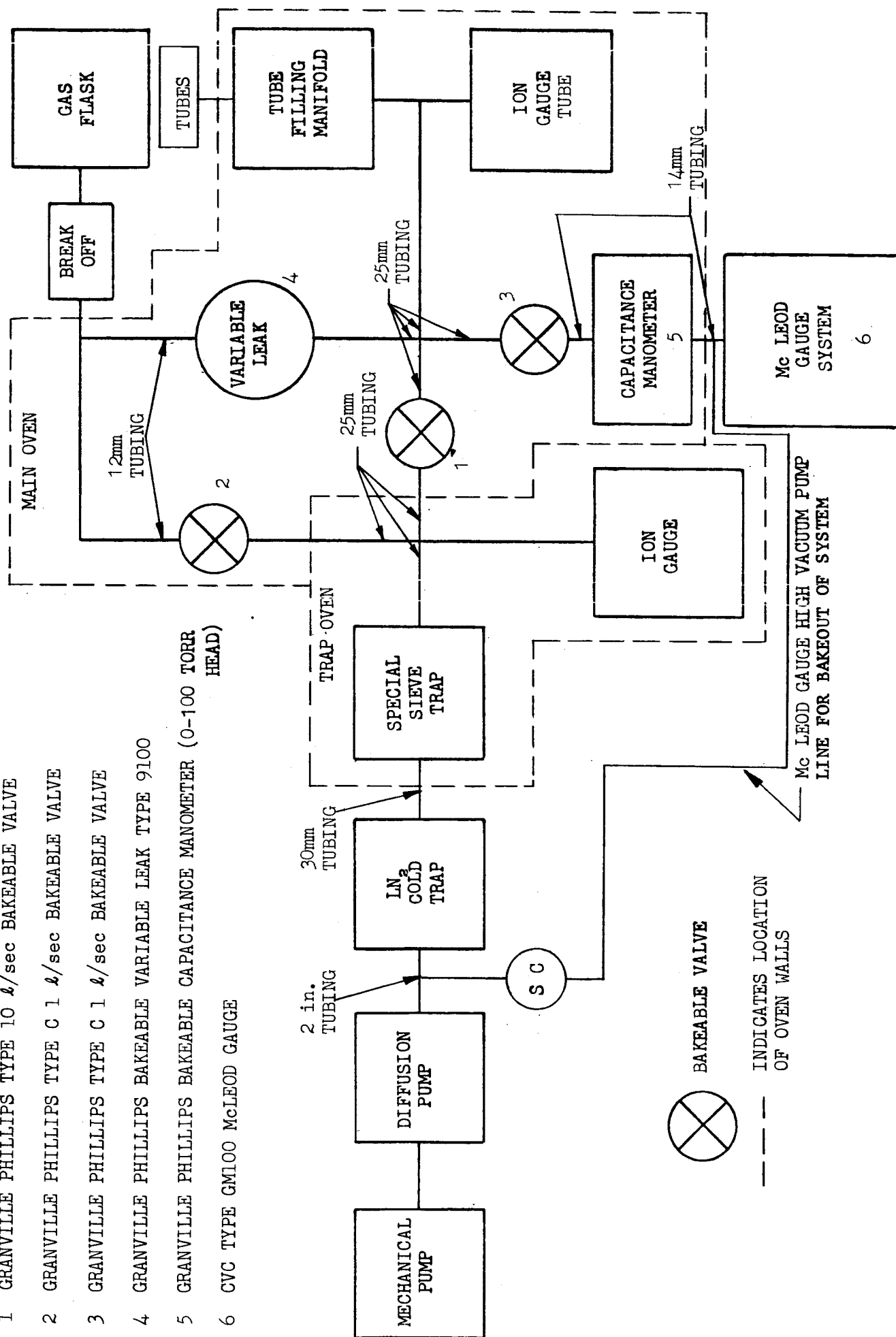
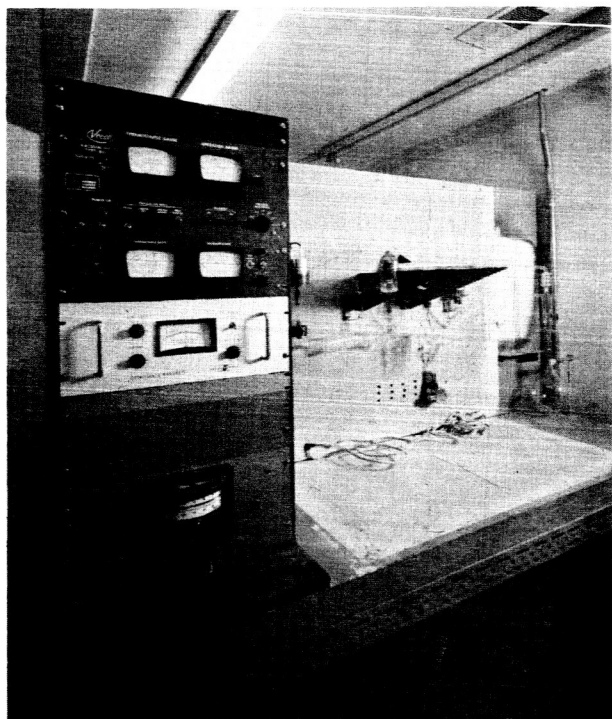
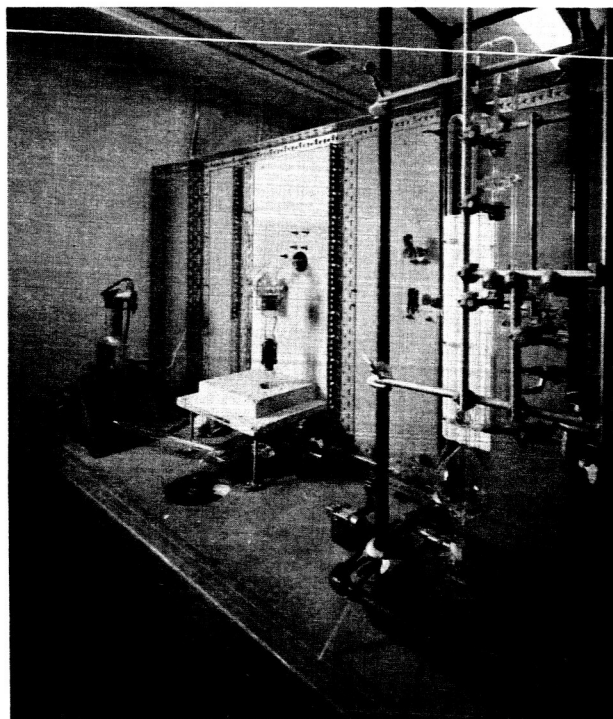


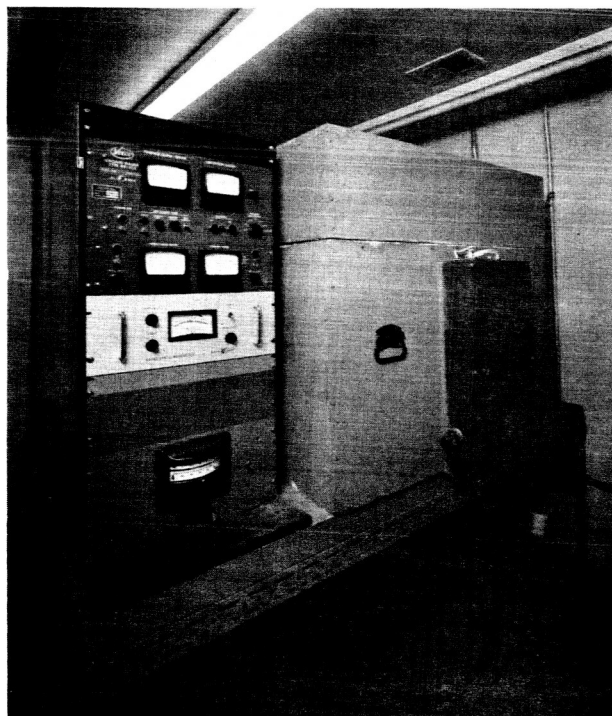
FIG. 65 BAKEABLE GAS HANDLING SYSTEM - BLOCK DIAGRAM



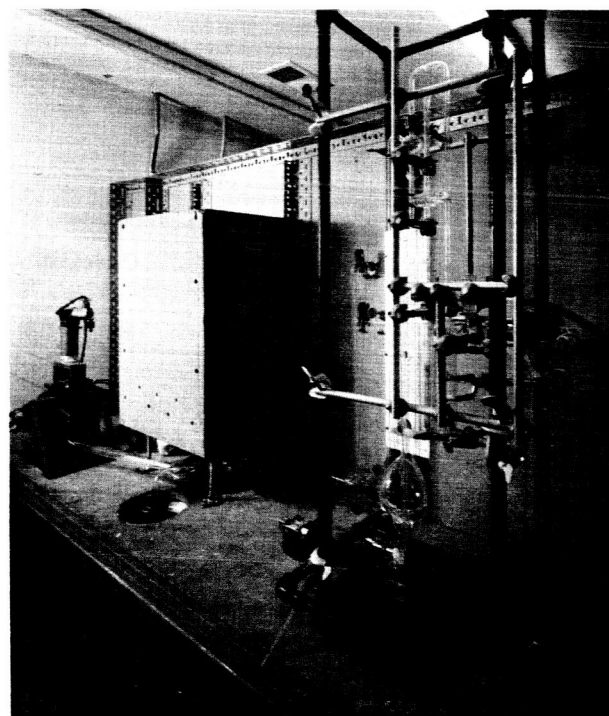
FRONT VIEW



REAR VIEW



FRONT VIEW (WITH OVEN)



REAR VIEW (WITH OVEN)

FIG. 66 BAKEABLE GAS HANDLING SYSTEM

(without getters) with hydrogen. The hydrogen filling for batch no. 3 was chosen to obtain a comparison of the performance and life of hydrogen versus krypton-filled tubes. A photograph of one of the Mod-D tubes is shown in Fig. 67.

3.3.2.6.3 Performance Tests

The performance of each tube was measured immediately after fabrication and again after each tube had been operated for 2 hours. The mean UV output of the 13 tubes in batch 1 and its standard deviation are plotted against the tube currents, before and after the 2-hour run, in Figs. 68 and 69. For currents above 1 ma, the standard deviation is less than 15%. These data have not been adjusted for the variations in window transmission loss, which could explain the observed spread in performance. A comparison of Figs 68 and 69 shows that the mean tube output decreased by about 5% during the 2-hour run.

The I-V characteristics of the 13 tubes in batch 1 were measured immediately after processing and after 2 hours of operation. The mean characteristic and its standard deviation are shown in Figs. 70 and 71. The most noticeable feature of the I-V characteristic is the decrease in the spread of the data after the 2 hours of operation. There was also a slight decrease (less than 10%) in tube voltage and some change in the I-V characteristics at high currents after 2 hours of operation. The thirteen tubes from batch no. 1 were installed on the chamber and have operated successfully for over 110 hours.

Similar data were obtained for batches no. 2 and 3. Qualitatively, the results were the same. Quantitatively, batch no. 2 showed a wider spread in UV output before the 2 hours of operation than batch no. 1. The output of the hydrogen-filled tubes in batch no. 3 dropped more (by a factor of about 2) after the 2 hours of operation than the krypton-filled tubes.

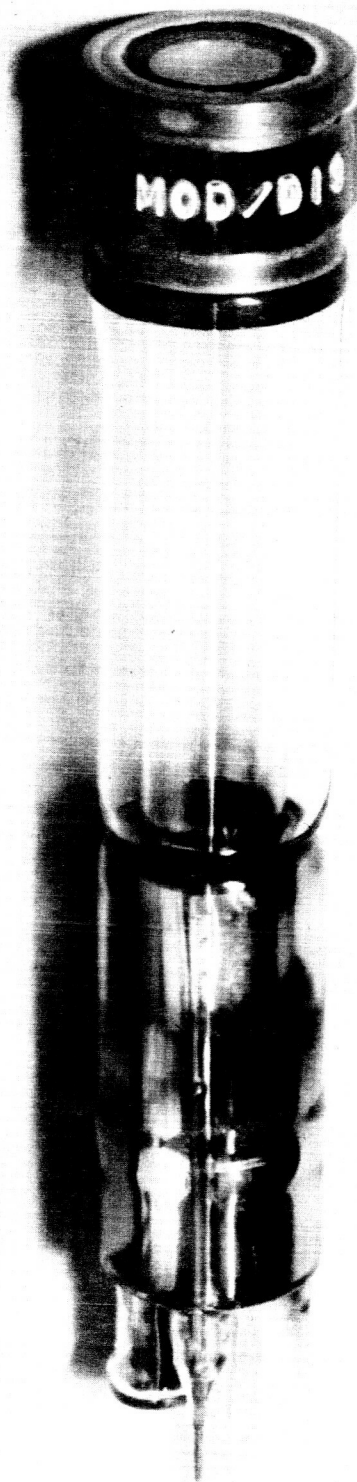


FIG. 67 MOD-D TUBE

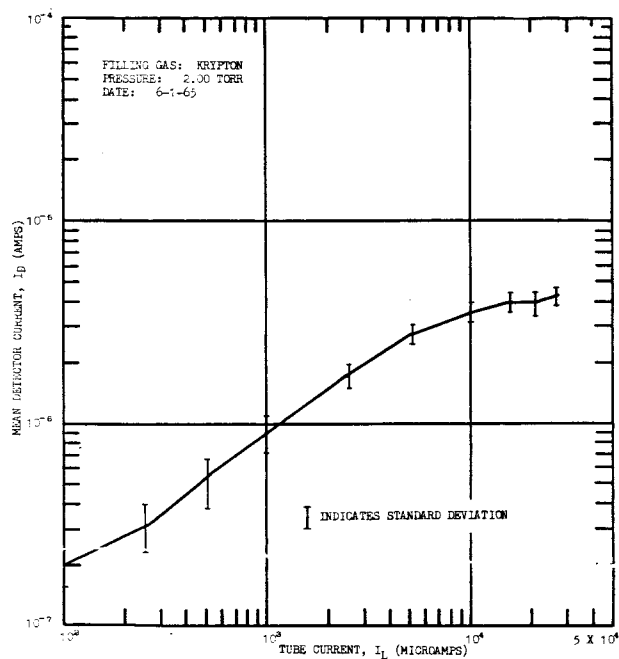


FIG. 68 MEAN DETECTOR CURRENT VS TUBE CURRENT:
BATCH NO. 1, IMMEDIATELY AFTER PROCESSING

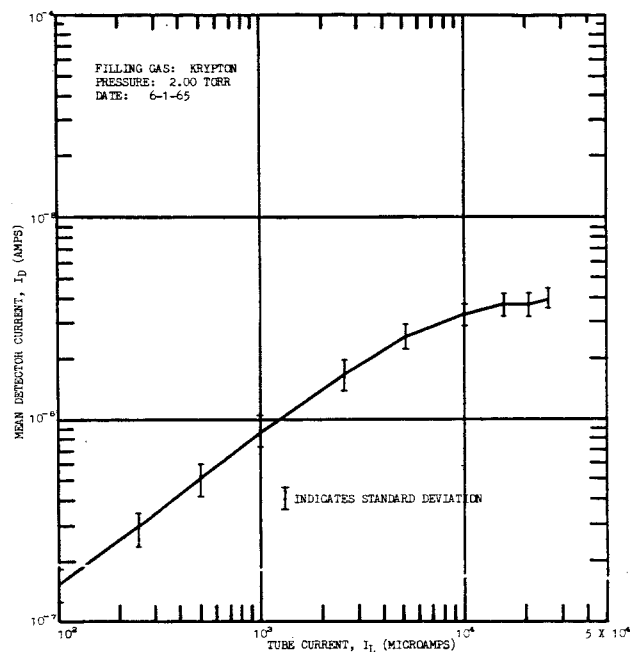


FIG. 69 MEAN DETECTOR CURRENT VS TUBE CURRENT:
AFTER TWO HOURS OF OPERATION

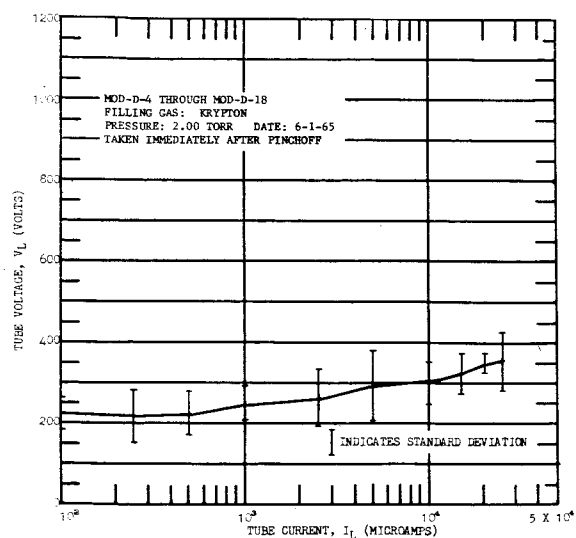


FIG. 70 MEAN TUBE VOLTAGE VS TUBE CURRENT CHARACTERISTICS
BATCH NO. 1, IMMEDIATELY AFTER PINCHOFF

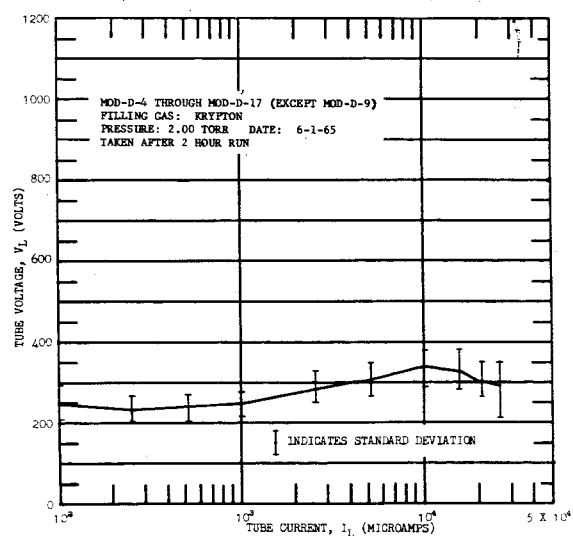


FIG. 71 MEAN TUBE VOLTAGE VS TUBE CURRENT CHARACTERISTICS:
BATCH NO. 1, AFTER TWO HOUR RUN

3.3.2.6.4 Life Tests

After the various performance tests, tubes Mod-D-1, Mod-D-2, and Mod-D-3 were sealed off at a pressure of 2 Torr and life tests were started. The life tests consisted of operating the tubes continuously for 2 hours each day except on those days where other demands on the available power supplies and personnel made this impossible. The performance, in terms of UV output and tube voltage drop versus discharge current, was measured immediately before and after the 2 hours of operation. Tube Mod-D-2 failed immediately after seal-off due to a faulty spot weld of the cathode to the cathode lead. Tube Mod-D-1 was fabricated about a month before tubes Mod-D-2 and Mod-D-3 and therefore had about one more month of life test data.

The results for tube Mod-D-1 for the first 48 days are shown in Figs. 72 and 73. The erratic results in February, and particularly the large drop in output during the period between days 12 to 24 was traced to an oil film that built up on the LiF windows due to inadequate trapping of the mechanical pump used to evacuate the space between the tube and the detector. (This will be discussed in Sec. 3.3.3.6.1) After day 24, both lamp and detector windows were cleaned with methanol just before the output measurements were made. The total accumulated time on tube Mod-D-1 was 68 hours of operation in 48 elapsed days. The output during this time dropped by about 40%. The reason for erratic behavior of the tube voltage drop during the early part of the test may have been due to gas impurities which were absorbed by the getter during the early period of operation.

The results for tube Mod-D-3 are shown in Figs. 74 and 75. A total of 36 hours of operation in 25 elapsed days were accumulated on this tube. During this period the output did not drop significantly. The average tube voltage dropped with time. This, and the erratic behavior of tube voltage, may be

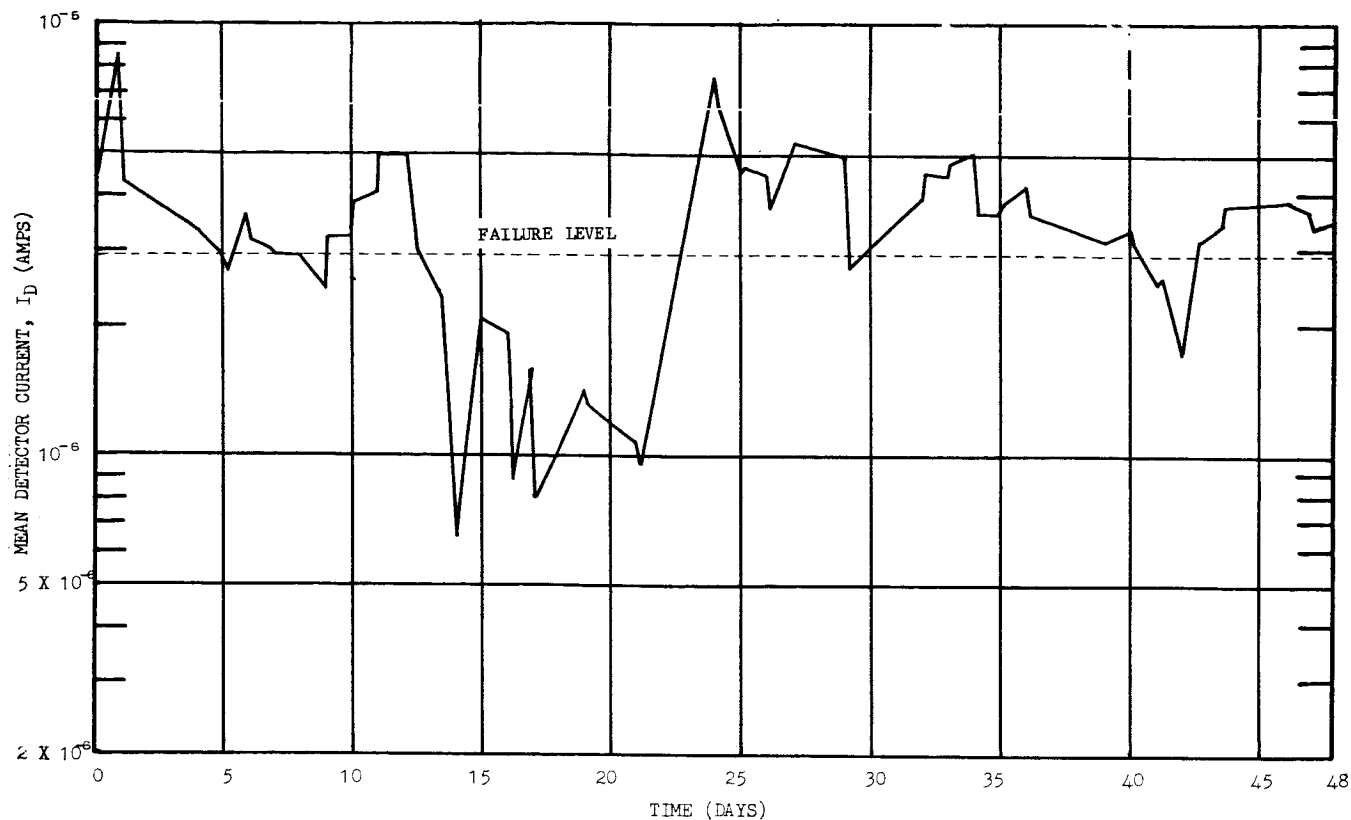


FIG. 72 TUBE MOD-D-1: TUBE OUTPUT VS TIME AT $I_L = 5$ MA.
0-48 DAYS, SEAL-OFF 2-11-65.

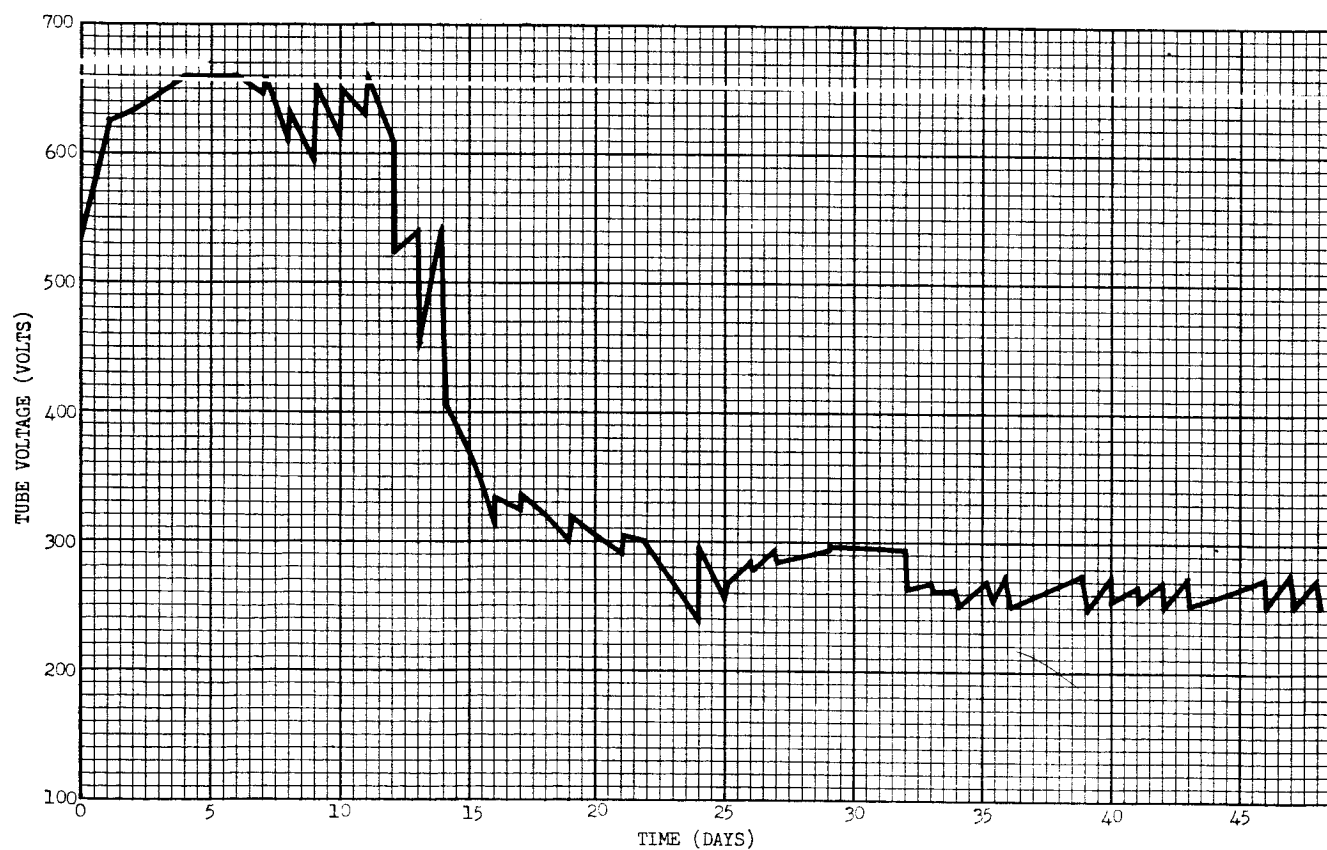


FIG. 73 TUBE MOD-D-1: TUBE VOLTAGE VS TIME AT $I_L = 5$ MA.
0-48 DAYS, SEAL-OFF 2-11-65.

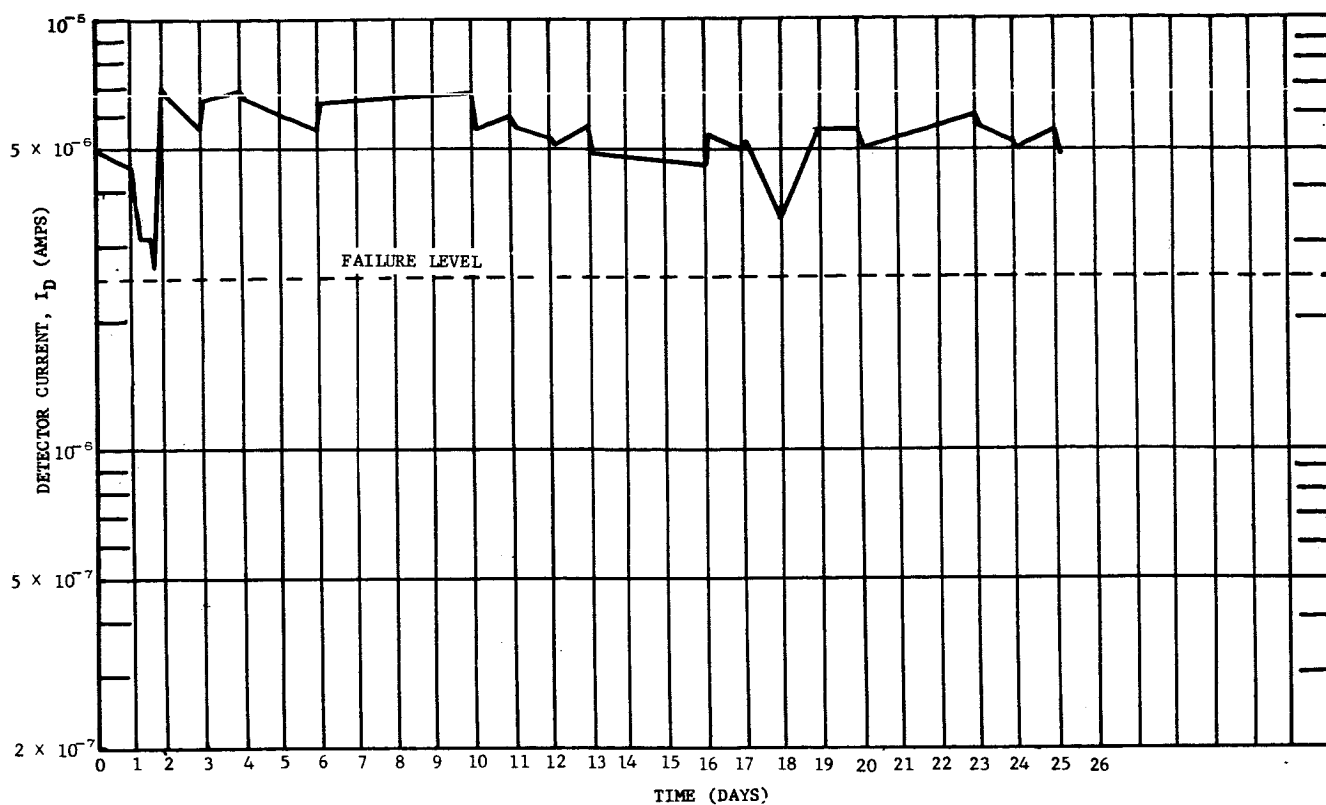


FIG. 74 TUBE MOD-D-3: TUBE OUTPUT VS TIME AT $I_L = 13$ MA.
0-25 DAYS, SEAL-OFF 3-6-65.

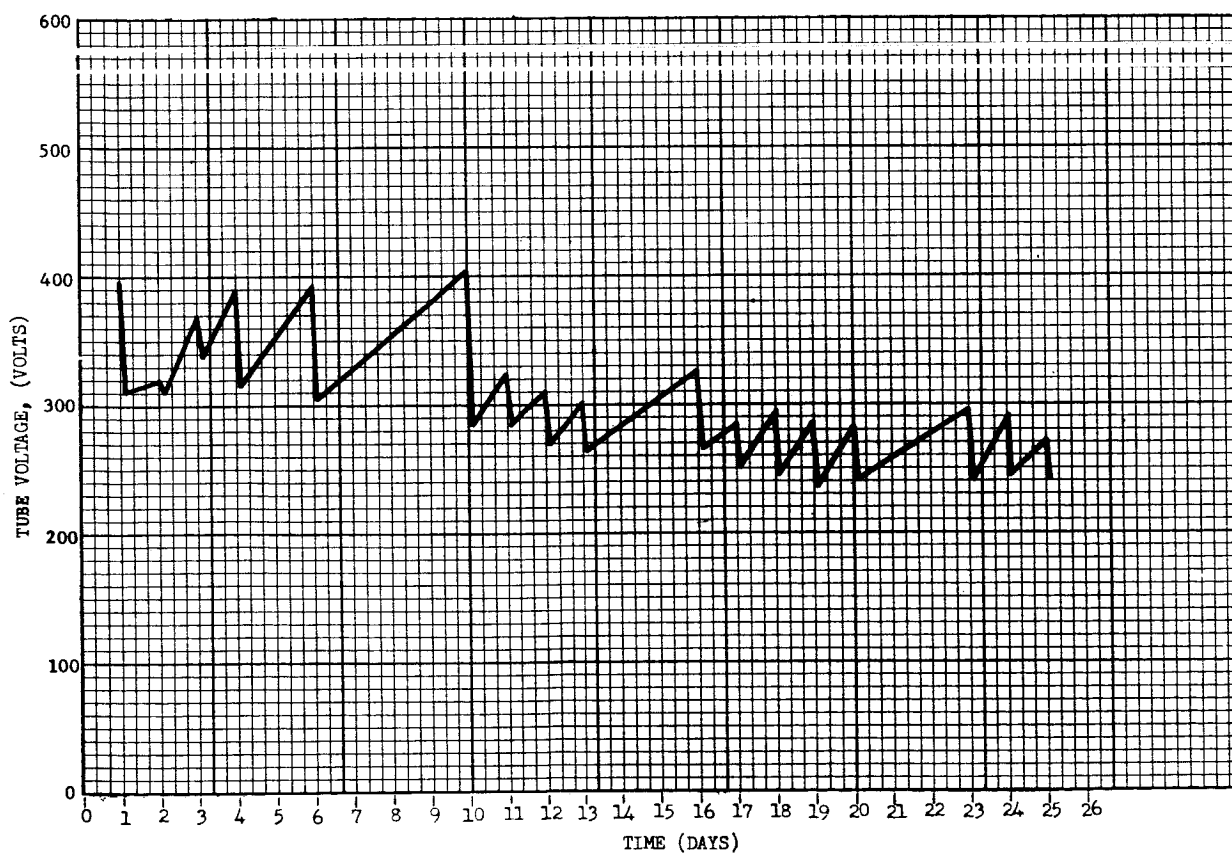


FIG. 75 TUBE MOD-D-3: TUBE VOLTAGE VS TIME AT $I_L = 13$ MA.
0-25 DAYS, SEAL-OFF 3-6-65.

caused by cleanup of minute levels of contamination.

On the basis of these results, it was decided to use sealed off tubes in the bank, thus avoiding the complexity of leaving them connected to a common manifold.

3.3.2.6.5 Spectrums

Spectrums of the outputs of a krypton tube and of a hydrogen tube were obtained* using a McPherson Model 220-f10 1-meter vacuum UV diffraction grating monochromator. The approximate wavelength range of 5500 Å to below 1050 Å was covered. A 600-lines/mm, MgF-coated grating blazed at 1500 Å was used. The intensity of the second-order spectrum of the 1050 Å to 1700 Å region was less than 2% of the intensity of the first-order spectrum. The detector was a sodium-salicylate-coated EMI 6255 photomultiplier.

The vacuum UV spectrum (1050 Å to 1375 Å) of a krypton-filled tube operating at 10 ma current is shown in Fig. 76. Spectrums taken at 25 ma tube current show the same general features, but with some changes in relative line intensities.

The corresponding spectrum of the hydrogen-filled tube is shown in Fig. 77. This spectrum has many lines besides the dominant Lyman- α line. These are part of the molecular spectrum of hydrogen. However, the relative intensities of these lines are considerably different from other UV sources, and many molecular lines are either missing or too weak to be detected.

The noteworthy feature of the spectrum of the krypton-filled tube is the lack of lines other than the krypton resonance lines at 1235 Å and 1165 Å. This is in contrast to the spectrum of the hydrogen-filled tube.

* These spectrums were obtained through the generous cooperation of A. Stober and D. V. Wright, Jr., of the Astrophysics Branch, Space Sciences Division of NASA-GSFC.

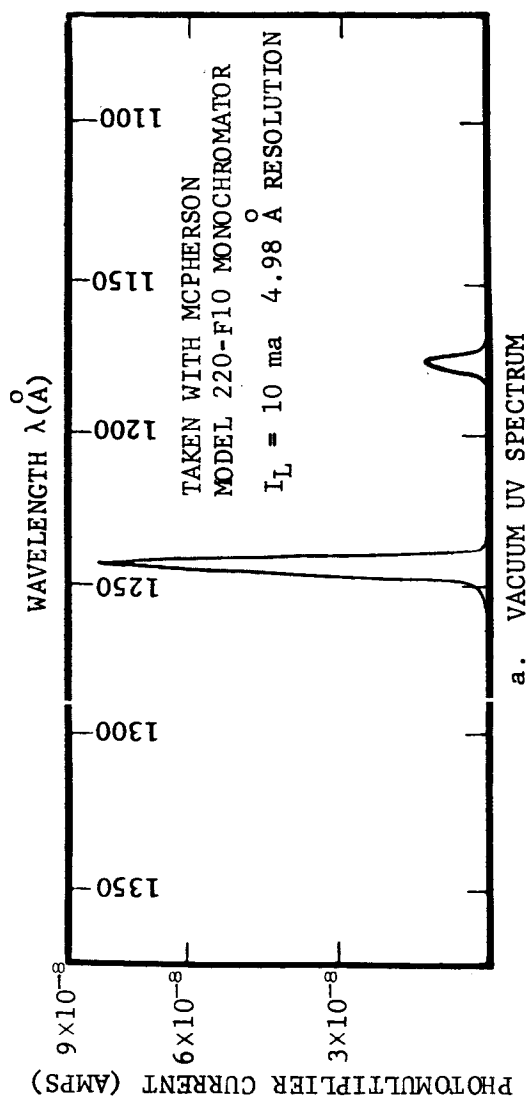


FIG. 76 MOD-D-25 KRYPTON FILLED LAMP VACUUM UV SPECTRUM ($I_L = 10$ ma)

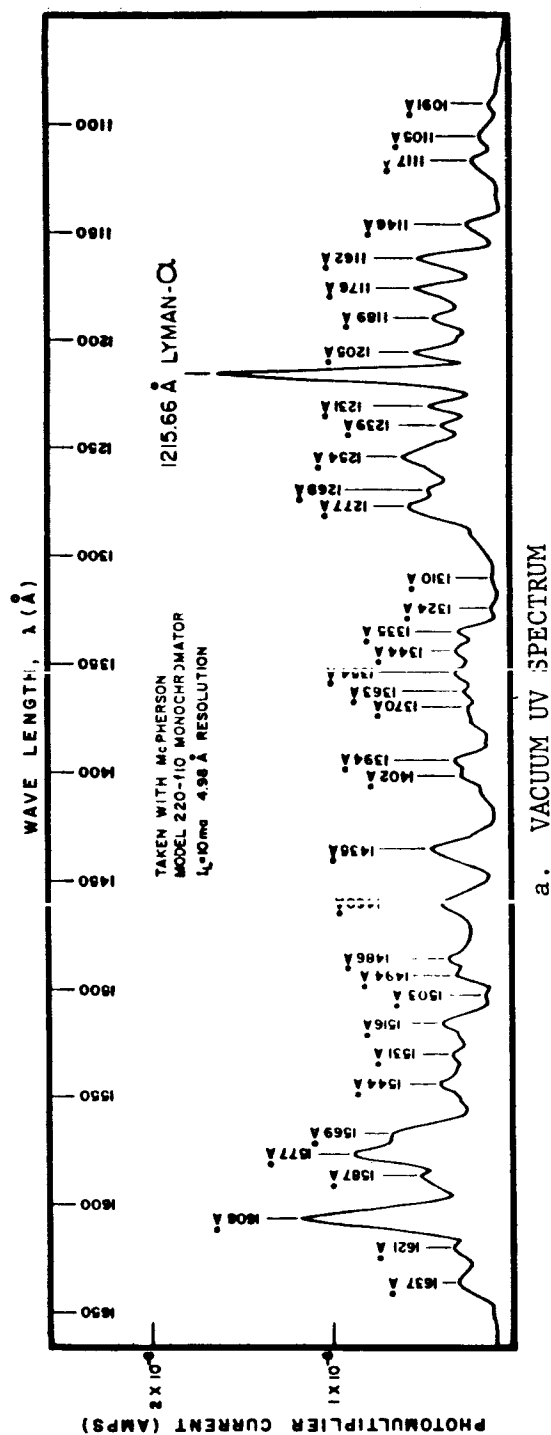


FIG. 77 MOD-D-29 HYDROGEN FILLED LAMP VACUUM UV SPECTRUM ($I_L = 10$ ma)

3.3.2.7 Conclusions

The Mod-D tube design and fabrication program has resulted in highly reliable UV-tubes which adequately meet the requirements for producing a large-volume plasma by photoionization of NO. The Mod-D is a sealed tube which produces a UV flux level of up to 10^{16} photons-sec⁻¹. The tube geometry lends itself to close packing in a bank of tubes to increase the area of the UV beam. From beamwidth measurements, it was determined that a bank of 13 tubes would produce a beam of adequate uniformity across an 8-inch diameter port of the chamber. The tubes have been proved to be of exceptional stability and reliability, and have been operated successfully for over 110 hours with no significant drop in UV output. Furthermore, the UV spectrum of the tube is exceptionally clean, only the 1235 Å and 1165 Å resonance lines being present, the former being predominant in the ratio 6:1.

3.3.3 Large-Volume Plasma Production

3.3.3.1 Objectives

The Mod-D tube fabrication program described in Sec. 3.3.2.6 led to the production of UV-tubes which produced sufficient output over a large enough area so that a bank of these tubes could be utilized for plasma production in the chamber. The last phase of the program, therefore, was to mount a bank of these tubes on the chamber, to produce a plasma therein by photoionization of NO, and to probe its characteristics.

In order to do this, several ancillary items of equipment and instrumentation were required. These included a tube bank mount to allow the composite UV-source to be attached as a unit to the chamber, a power supply for energizing and controlling each of the UV-tubes in the bank, and a gas-handling system for admitting purified NO into the chamber at the desired operating pressure and discharging the toxic NO harmlessly to the atmosphere outside the building. In addition, in order

to provide for mass analysis of the gas within the chamber during the measurements, a differential pumping system was developed toward the end of the program for the mass spectrometer attached to the chamber. These ancillary items will be described first, after which the various probe measurements that were made on the plasma will be discussed. The analysis and interpretation of the measurements will then be presented. This will be followed by a discussion of the mass analyses that were made during the last stages of the probe measurement program.

3.3.3.2 Tube Bank Mount

The chamber has an 8-inch diameter port on each end. The beam angle tests described in Sec. 3.3.2.3 led to an arrangement of 13 UV-tubes as shown in Fig. 51. To limit down time in case of tube failure, and to provide a means of adjustment of UV beam intensity, the tubes were mounted with an evacuated space between them and the chamber. To do this, an 8-inch port cover was drilled for thirteen 1-inch diameter LiF windows. Then a 0.250-inch thick spacer ring was sealed to the port cover with O-rings and to the plate on which the UV-tubes were mounted. The UV tubes were sealed to their plate with O-rings. A photograph of the tube bank in place on the chamber is shown in Fig. 78.

The space between the tube windows and the 1-inch windows on the port cover can be pumped, or back-filled with an absorbing gas to control UV intensity. Filling this space with NO at a pressure of 100 Torr would attenuate the UV by 1000:1. This range of variation, combined with the 50-to-1 variation in UV output available by varying the source tube current, gives a capability for large variations of UV intensity. The design allows UV-tubes to be replaced without bringing the chamber to atmospheric pressure. Thus, a time consuming and expensive operation is avoided.

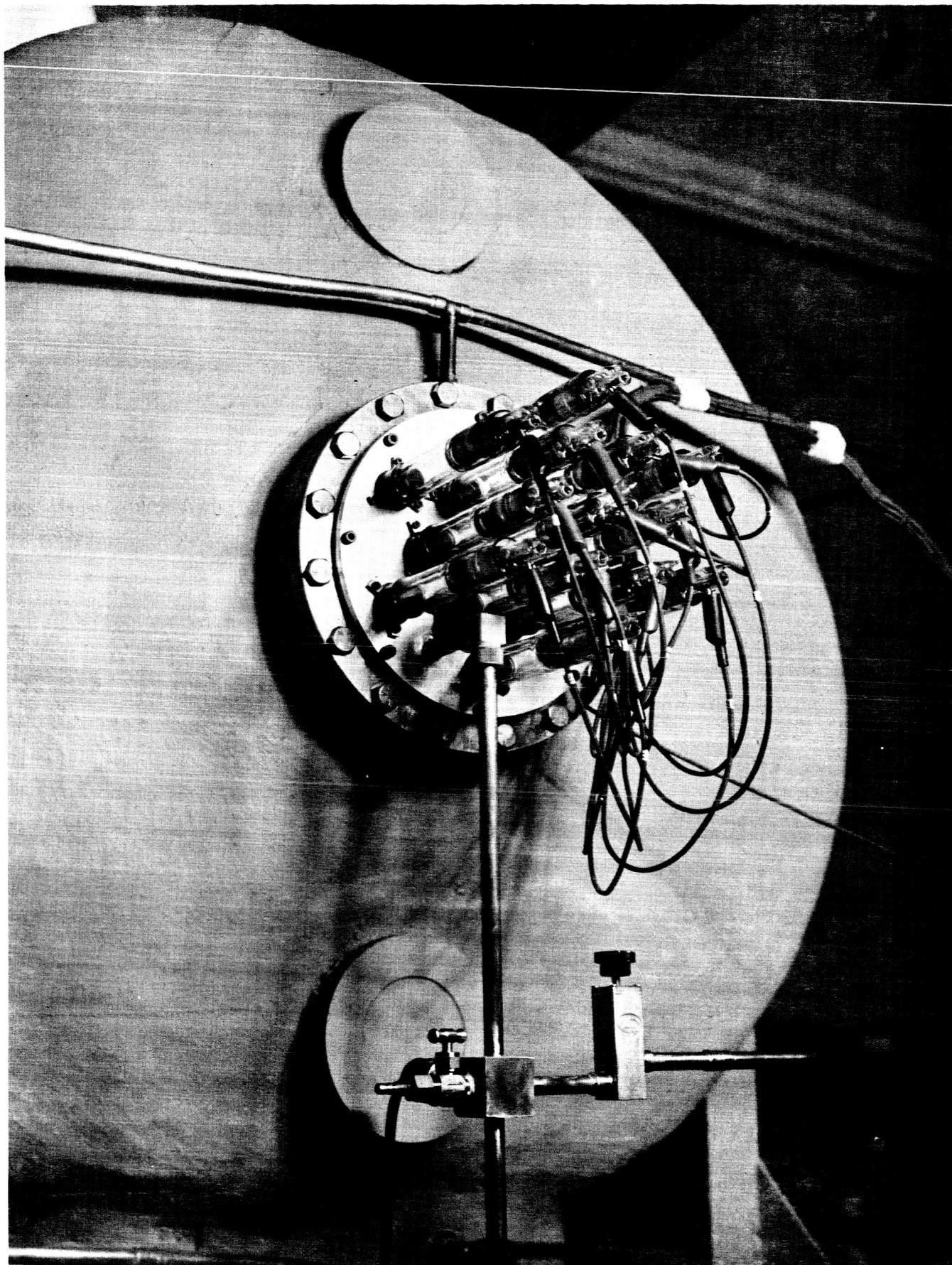


FIG. 78 TUBE BANK

3.3.3.3 Tube Bank Power Supply

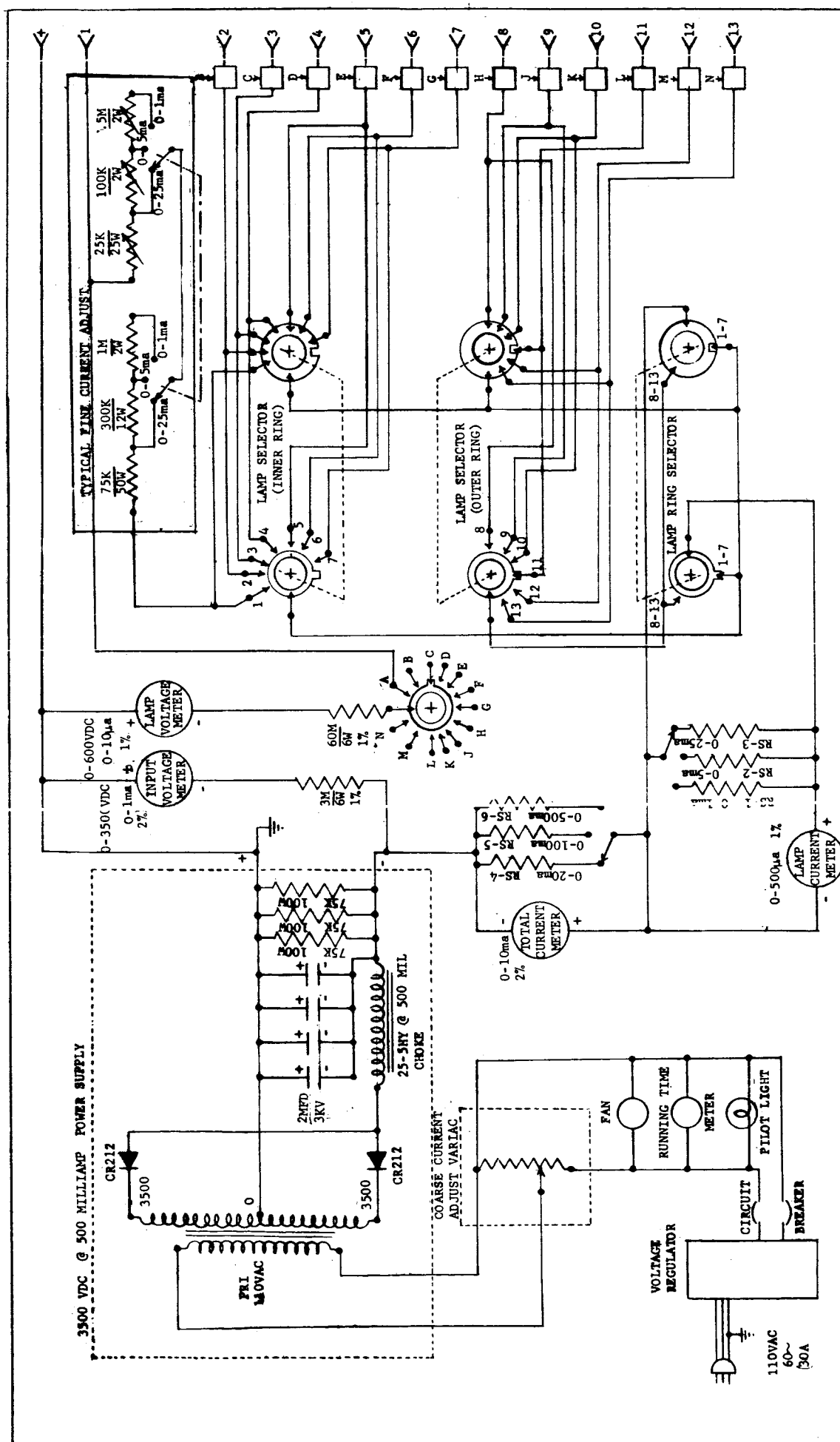
A power supply for the bank of UV-tubes was designed and built to supply each of the 13 tubes in the bank through separate series resistor chains. Each chain has a set of variable resistors to allow the current to each tube to be varied by $\pm 12\%$ from its average value. The power supply voltage may be varied from 0 to 3 kv with a Variac, and the maximum current available is 400 ma. The UV-tube current may be varied from 0.5 to 25 ma for a tube voltage drop of 500 volts. The current and voltage for any single tube can be monitored individually by switching of metering circuits. The output voltage of the power supply and the total current to the tube bank are monitored continuously. The power supply ripple is less than 2.5%. The supply, controls, and meters occupy most of a 7-foot relay rack. The circuit diagram for the power supply is shown in Fig. 79 and photographs of the completed supply are shown in Fig. 80.

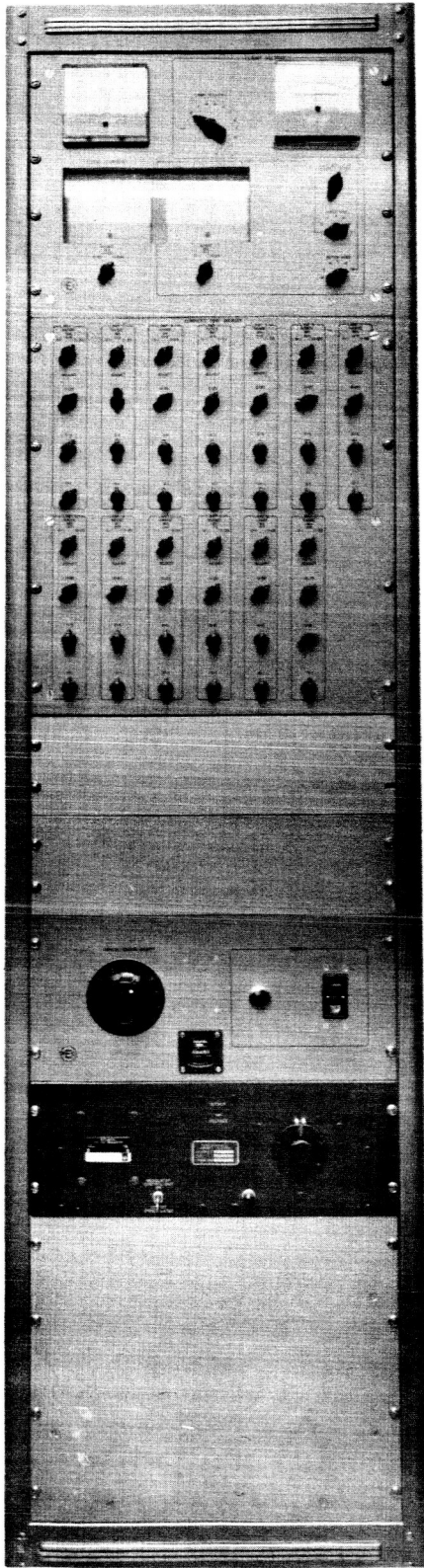
3.3.3.4 NO Gas-Handling System

A gas-handling system was designed and constructed to fill the chamber with NO to the desired pressure. A block diagram of this system is shown in Fig. 81.

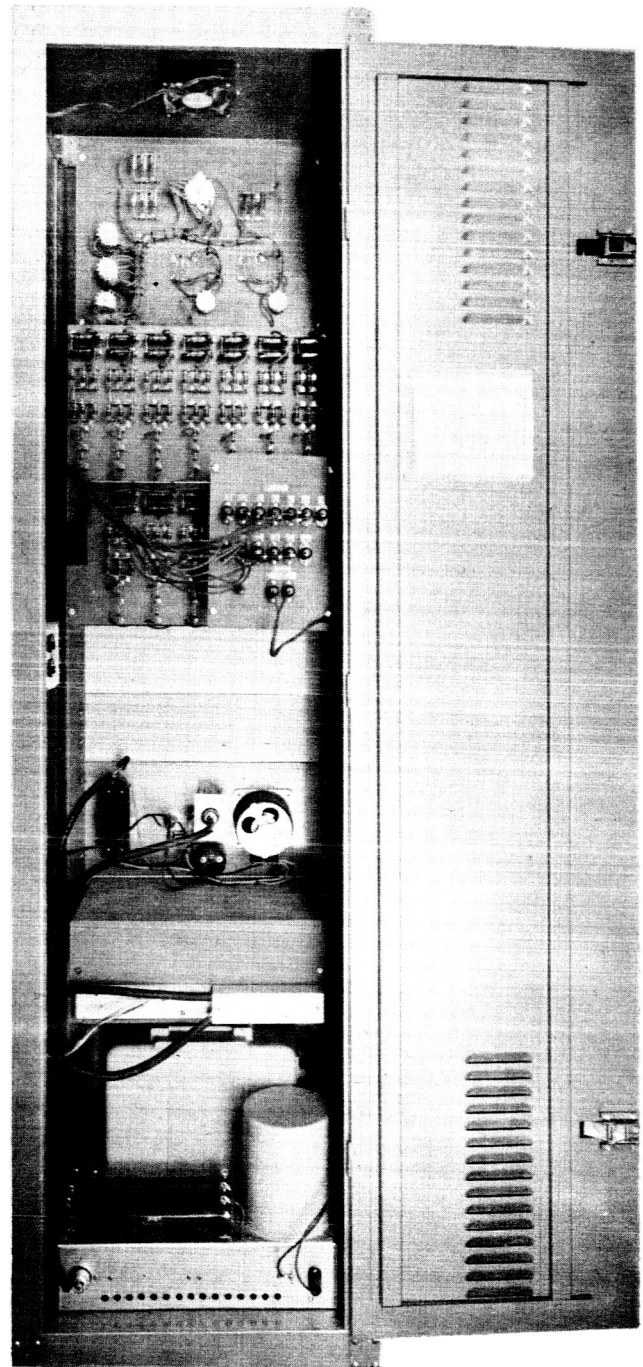
Items such as thermocouple gauges, air release valves and valves which allow pumping of specific areas in the system have been omitted for the sake of clarity. The system provides for the following functions:

- 1) Admission of NO to the chamber after a partial distillation of the NO to improve its purity.
- 2) Pumping the space between the UV-tubes and port windows.
- 3) Filling the space between the UV-tubes and port windows with NO.
- 4) Measurement of NO pressure in the chamber, and in the space between UV-tubes and port windows.





a. FRONT VIEW



b. REAR VIEW

FIG. 80 TUBE BANK POWER SUPPLY

- 5) Pumping the various filling and pressure measuring lines.
- 6) Simultaneous handling and filling of the chamber with a second or "buffer" gas.

These various functions are carried out by opening and closing appropriate valves. The partial distillation process is carried out by passing the NO through a dry-ice methanol trap before admission to the system. A molecular sieve trap is provided in the main pumping line to prevent back streaming of oil vapors from the mechanical pump, and to provide a better vacuum than that achievable with the mechanical pump alone.

3.3.3.5 Differential Pumping System for the Mass Spectrometer

After a number of probe measurements had been made of the plasma produced in the chamber, questions arose regarding the purity of the NO in the chamber. In order to throw some light on this important problem, it was desirable to make mass spectrometer measurements of the NO in the chamber while measurements of the plasma characteristics were in progress. Since the NO pressure during the plasma tests ranged from 10^{-3} to 5×10^{-1} Torr, while the maximum operating pressure of the mass spectrometer (a Veeco Model GA-3 UHV Residual Gas Analyzer) is 10^{-6} Torr, it was necessary to construct a differential pumping system for the mass spectrometer. To maximize the sensitivity of the mass spectrometer to impurities in the chamber, it was necessary to minimize the impurities and background contributed by the differential pumping system. This meant that the differential pumping system had to be capable of achieving an ultrahigh vacuum (10^{-6} Torr or less) when sealed from the chamber. To accomplish this, it was designed to be bakeable, and ultra-high vacuum techniques were utilized throughout. In using the differential pumping system, certain modifications to the mass spectrometer were found to be desirable. In the following sub-sections, the differential pumping system and the modifications to the mass spectrometer will be discussed.

3.3.3.5.1 Differential Pumping System

A block diagram of the system, bakeable to 400° C, is shown in Fig. 82. A photograph of the system is shown in Fig. 83. A high-vacuum pumping system is connected to a manifold. The manifold is connected to the mass spectrometer, to a nude ionization gauge, and, through a differential pumping aperture and a bakeable valve, to the chamber. The pumping system is composed of a mechanical pump, a 2-inch air-cooled diffusion pump using DC-705 pump fluid, and a 2-inch Granville-Phillips Cryosorb LN₂ cold trap. A bakeable valve bypassing the differential pumping aperture facilitates pumping the region between the aperture and the valve to the chamber during initial pumpdown and bakeout.

Calculations show that when the chamber is filled to 0.5 Torr of NO and the differentially pumped region is at 10⁻⁴ Torr, an 0.008-inch aperture in a 1/32-inch aperture plate would be required. In practice, however, the bakeable valve was used in place of the aperture. Experience with this valve indicates that a variable aperture is more suitable than a fixed aperture.

After a 14 hour bake at 400° C, pressures of 6×10^{-10} Torr were achieved without the mass spectrometer filament on. A spectrum of the residual gases in the differential pumping system was obtained after baking and pumping. This spectrum, shown in Fig. 84, indicates that the total system is quite clean. With the mass spectrometer filament on, pressures of less than 2×10^{-9} Torr were achieved. From a cold start with mass spectrometer filament on, about 20 hours of pumping are required to reach 2×10^{-9} Torr.

3.3.3.5.2 Modifications to Mass Spectrometer

Several modifications were made to the mass spectrometer to obtain better and more reproducible data. These modifications were as follows:

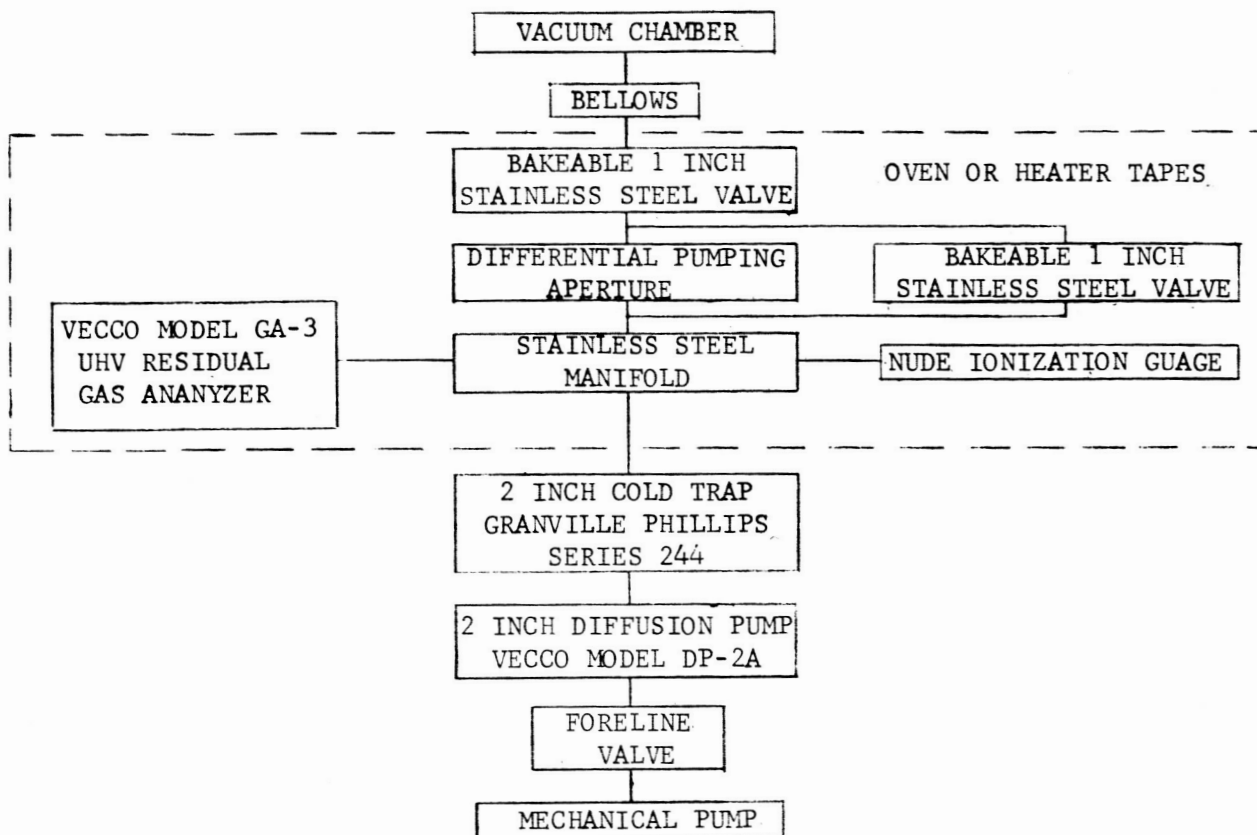


FIG.82 MASS SPECTROMETER DIFFERENTIAL PUMPING SYSTEM, BLOCK DIAGRAM

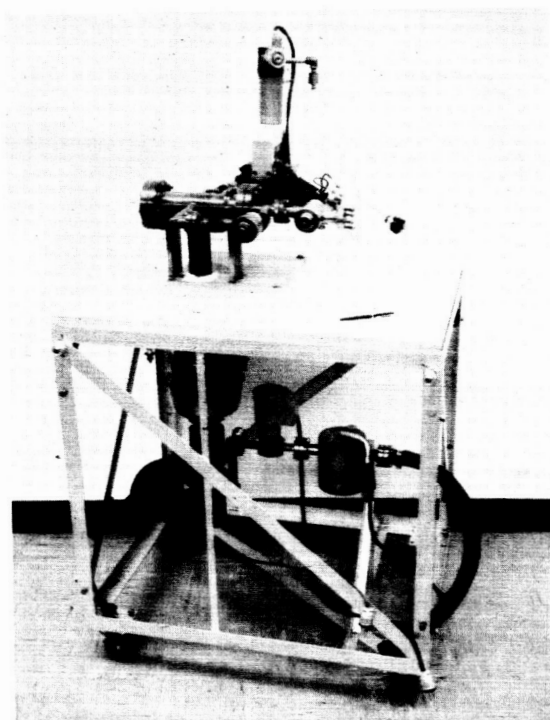


FIG. 83 MASS SPECTROMETER DIFFERENTIAL PUMPING SYSTEM

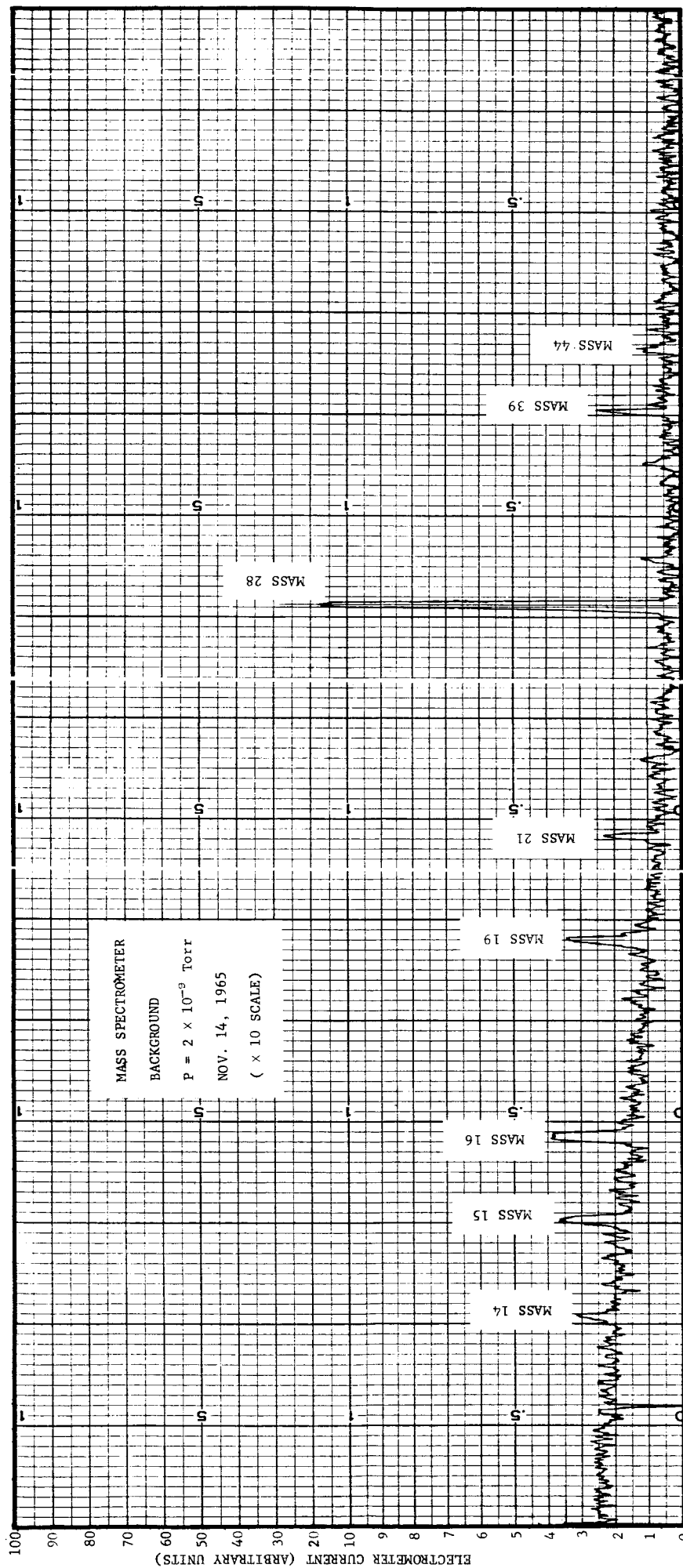


FIG. 84 MASS SPECTROMETER DIFFERENTIAL PUMPING SYSTEM
BACKGROUND MASS SPECTRUM (12 - 100 AMU)

- 1) The range of the repeller voltage adjustment was changed from 32 to 8 volts.
- 2) The voltage across the repeller voltage potentiometer was regulated with a zener diode.
- 3) The 2-inch emission current meter was replaced with a 4-inch 1% mirror-scale meter.
- 4) The repeller voltage and the high voltages were brought out to test points so that they could be monitored with a digital voltmeter. This allowed corrections to be made for the inadequate linearity of the sweep potentiometer ($\frac{1}{2}\%$). The high voltage output was measured as a function of potentiometer dial setting for mass 28 to mass 100 using these test points. These data were then used to determine the mass number of peaks above mass 28. The resultant circuit of the spectrometer source power supply is shown in Fig. 85.

3.3.3.6 Film Build-Up on Windows of UV-Tubes

During the measurements made with the tube bank installed on the chamber (to be discussed in Sec. 3.3.3.7), it was noticed that the UV output appeared to decrease fairly rapidly with time. It was discovered, however, that the output was restored after the outside surfaces of the windows were wiped with methanol.

A test was conducted to investigate this phenomenon further. A Mod-D tube was operated for two hours. Its output was measured before and after this period with a detector mounted about 1 cm away, the intervening space being evacuated by a mechanical pump. The windows of both the lamp and detector were then cleaned with methanol and the tube output was measured again. Next, the lamp was operated for another two hours, after which the system was pumped continuously for another 8 hours with the tube current off. The results of these tests are shown in Fig. 86.

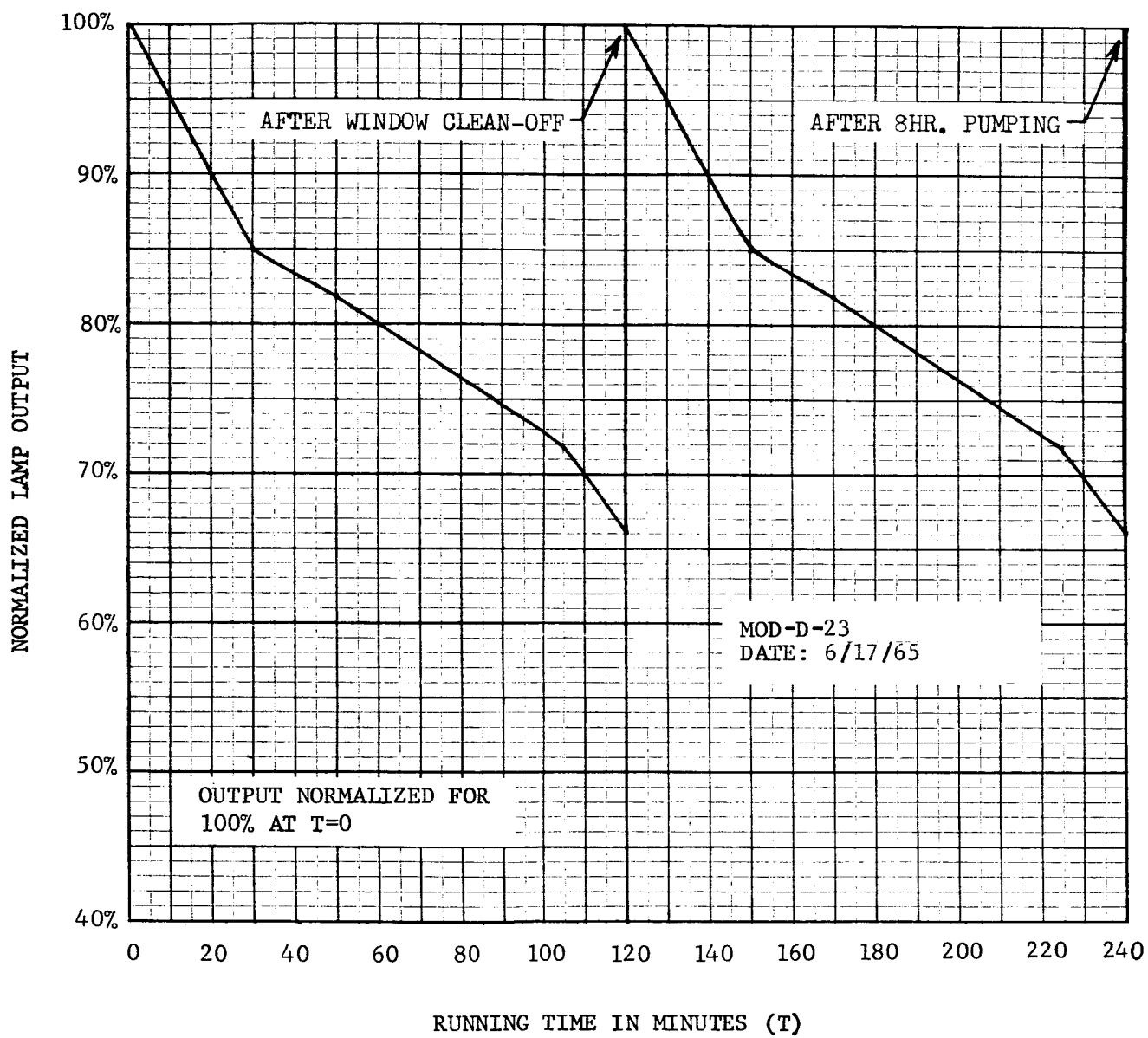


FIG. 86 HYDROCARBON FILM BUILD-UP TEST

Clearly the output decreased with tube operating time in a reproducible fashion, and the agent causing the decrease in output could be removed by either cleaning the window with methanol or by pumping. Similar tests with an air path between source tube and detector showed no similar decrease in output with time. It is thus concluded that the loss of output is a result of the build-up of a UV-absorbing hydrocarbon film on the windows. This film presumably is developed by photolysis of the residual oil vapors from the mechanical pump.

3.3.3.7 Probe Measurements

3.3.3.7.1 Introduction

After completion of the instrumentation of the chamber as described above, except for the differential pumping system for the mass spectrometer, a series of probe measurements was carried out in the chamber, using probes of several different types. These measurements gave probe curves which were completely anomalous, and in no way resembled the results obtained in the bell jar which were discussed in Sec. 3.2.2.2. After thorough checking to insure that no spurious instrumentation problems were responsible, it was decided to repeat the measurements in the bell jar. The repeat measurements, however, gave anomalous probe curves similar to those obtained in the chamber, and thus did not reproduce the earlier bell jar results.

In running down the cause of this non-reproducibility, attention was drawn to the source of NO used in the measurements. The NO bottle used in the first series of bell jar measurements had developed a leaky valve, so that it was exchanged for another bottle from the same supplier. Persistent inquiries to the supplier finally elicited the information that the second bottle of NO was manufactured by a completely different process from the first.

The probe curves suggested that a highly active electron attaching agent, present as an impurity in the NO, might be the cause of the anomalous results.

In order to identify such an impurity, arrangements were made for mass analysis of the gas during a final set of probe measurements in the chamber. The mass analysis program, which will be discussed in detail in Sec. 3.3.3.8, showed that such an impurity, namely N_2O , was indeed present.

In this section, the instrumentation for making the probe measurements will be described first. This will be followed by a presentation and discussion of typical probe curves obtained with various probe arrangements. The interpretation of these results, aided by the hindsight gained through the later identification of an electron attaching impurity, will be presented along with the results.

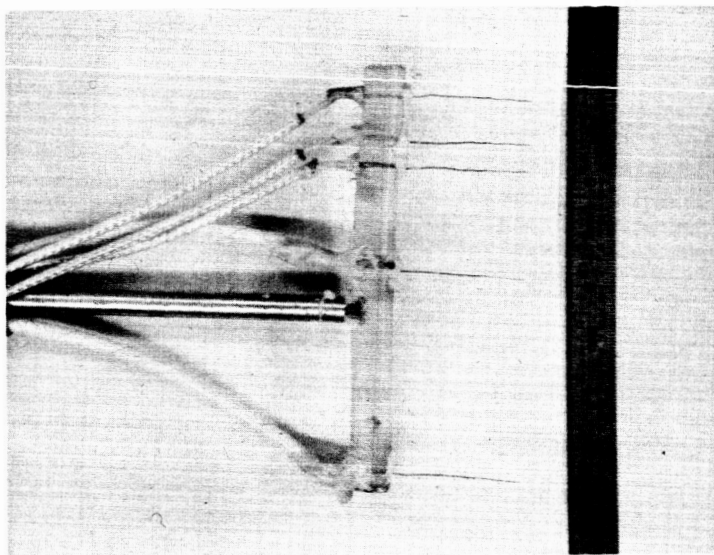
3.3.3.7.2 Probes for Measurement of Plasma Characteristics

To measure the characteristics of the plasma developed in the chamber with the bank of 13 Mod-D tubes, measurements were made with two different sets of double probes (denoted as "small" and "large", respectively), a Langmuir probe, and a Gerdian condenser probe. Photographs of the double probes and the Gerdian condenser probe are shown in Fig. 87. The dimensions of these probes are given in Table XIV. In the case of the Gerdian condenser, the first number refers to the inner conductor, and the second to the outer conductor.

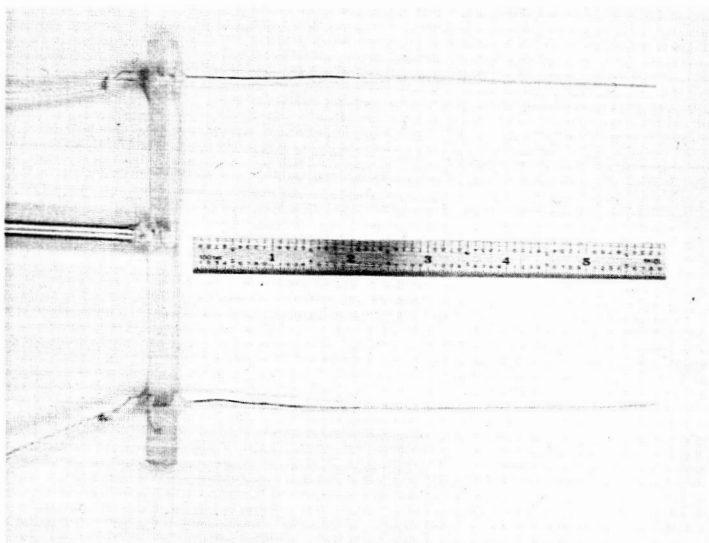
Table XIV

Probe Dimensions

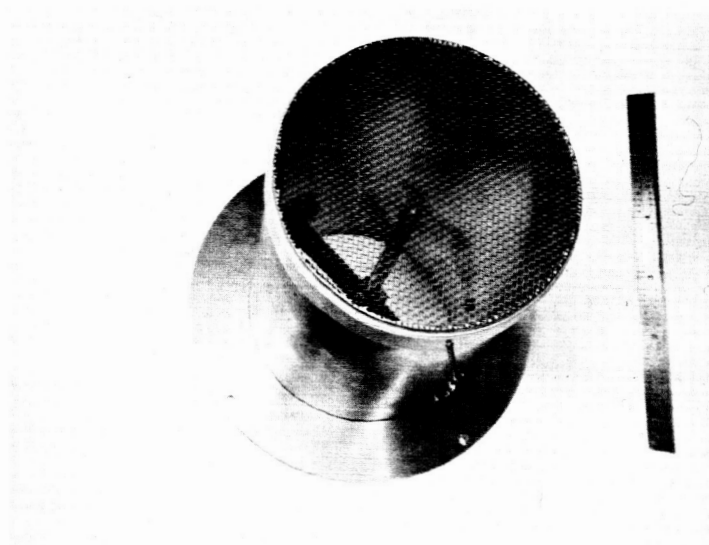
<u>Probe Type</u>	<u>Length (cm)</u>	<u>Radius (cm)</u>	<u>Surface Area (cm²)</u>	<u>Separation (cm) From</u> <u>Probe No. 1 to Probe</u>				
				<u>Nos. 2,</u>	<u>3,</u>	<u>4,</u>	<u>5</u>	
Double (small)	1	0.10	0.06	1	2	4.2	9.2	
Double (large)	10	0.03	1.92	10				
Langmuir	10	0.03	1.92	-				
Gerdian	9.93/17.78	0.317/4.91	19.81/548	-				



SMALL DOUBLE PROBE



LARGE DOUBLE PROBE



GERDIAN CONDENSER

FIG. 87 PROBES

It is seen that the small double probe actually consisted of 5 probes separated so that probe pairs had the separations listed in Table XIV. The Langmuir probe was actually one of the probes of the large double probe, and used the chamber as the return lead.

The location of the small double probe, in relation to the port on which the UV-tubes were mounted and to an NO detector mounted within the chamber to monitor UV output, is sketched in Fig. 88. Measurements were taken with the Gerdian condenser in two different orientations. These orientations are sketched in Fig. 89.

The instrumentation to apply probe voltages and to measure the probe currents is shown in the block diagram of Fig. 90. The probe voltage may be controlled from 0 to ± 45 volts with potentiometer R-1 and polarity reversal switch SW-1. Probe current is determined by measuring the voltage drop across precision resistor R-2 with the Dymec 2401C Digital Voltmeter (DVM) after the voltage drop has been amplified (10 X) in the Dymec 2411A amplifier. All probe connections were made through coaxial cables. With a one-second averaging time in the DVM and with $R-2 = 10^7$ ohms, a minimum current of 3×10^{-12} ampere could be measured.

3.3.3.7.3 Probe Data

3.3.3.7.3.1 Chamber Measurements (Series II)

In the first series of measurements on the plasma in the chamber, which will be referred to as Series II, all four types of probes described in Sec. 3.3.3.7.2 were used under varying conditions of pressure and other operating conditions. These conditions are summarized in Table XV. The results obtained with each type of probe will now be discussed in turn.

3.3.3.7.3.1.1 Small Double Probe

A typical I-V characteristic for the small double probe in the chamber is shown in Fig. 91. The striking feature of

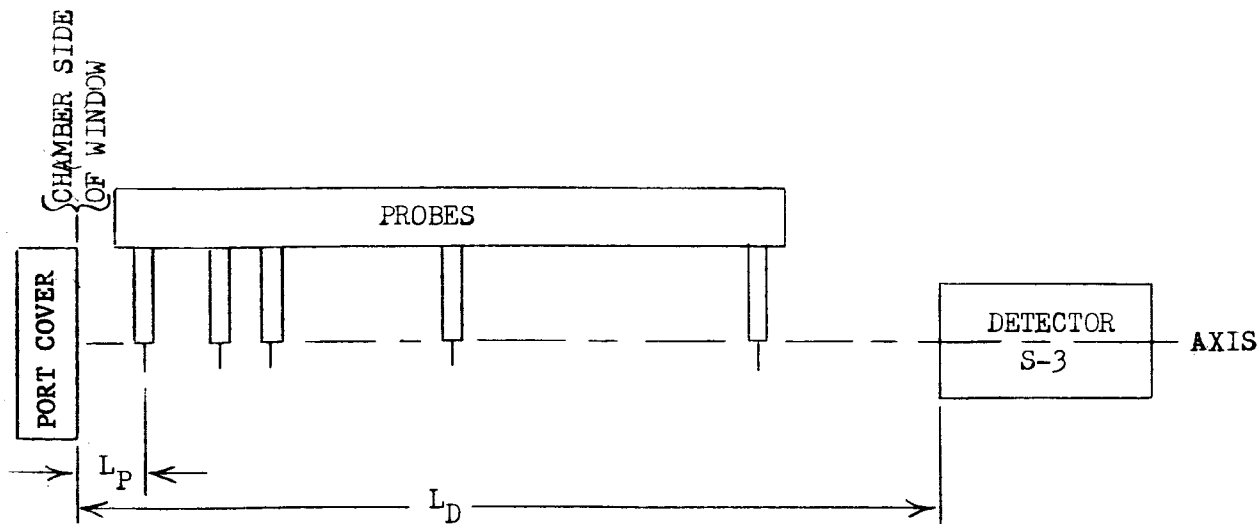
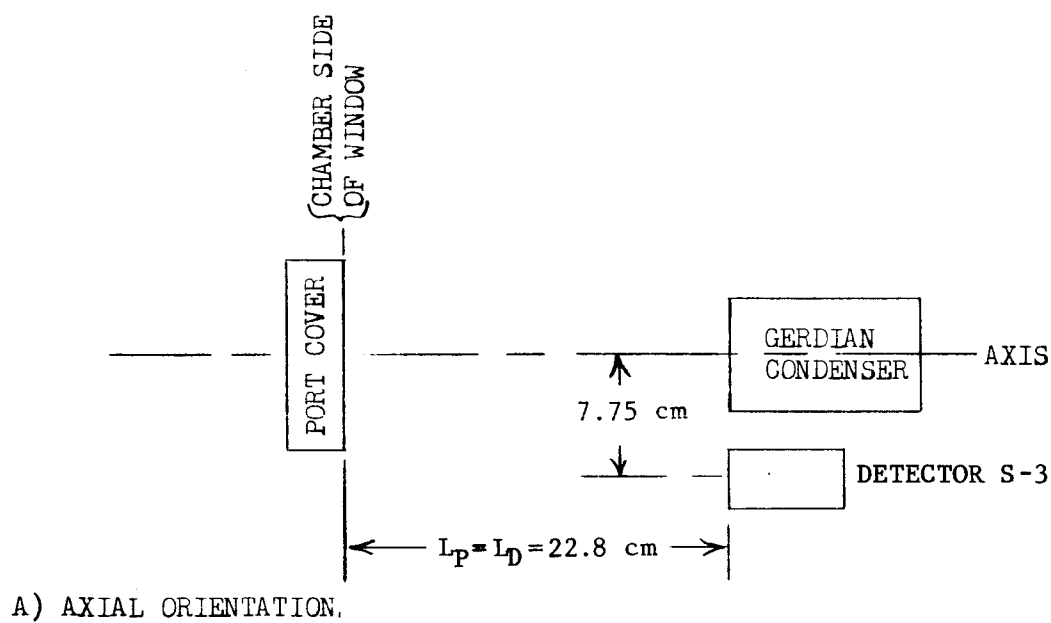
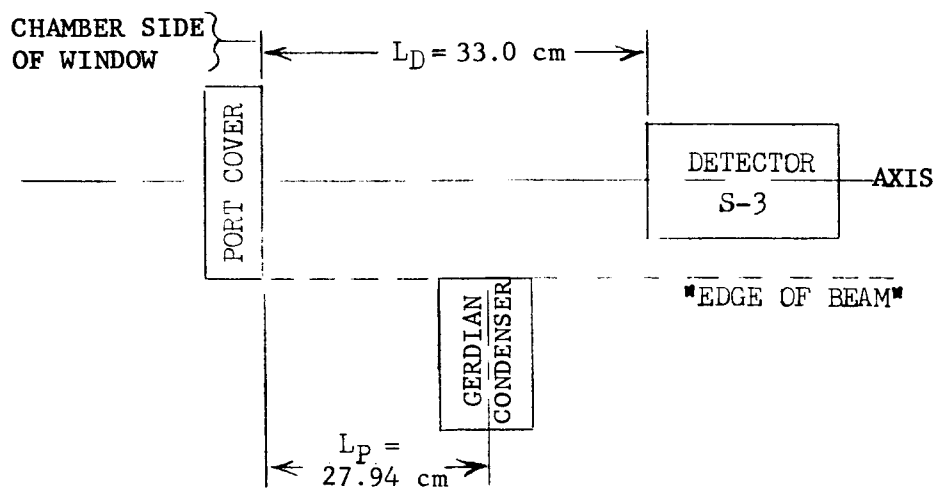


FIG. 88 LOCATION OF DOUBLE PROBES AND DETECTOR IN LARGE SCALE PLASMA GENERATION TEST

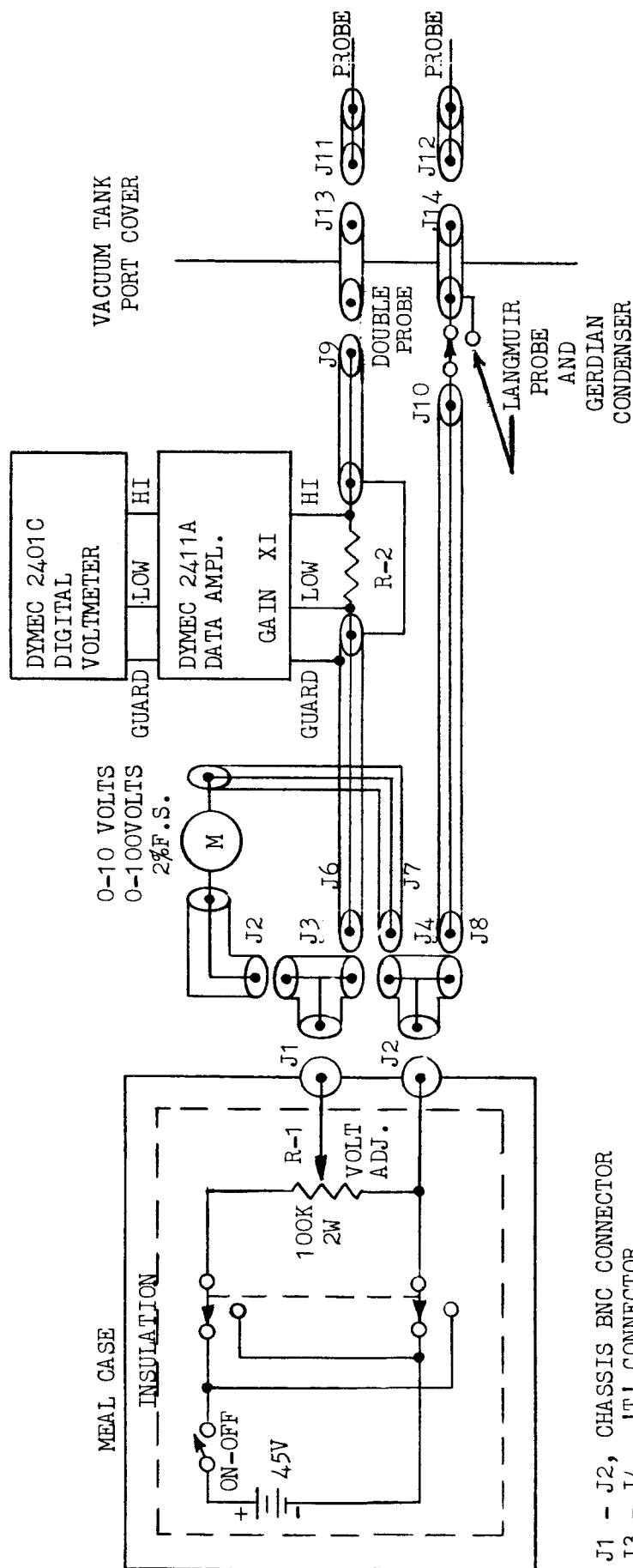


A) AXIAL ORIENTATION.



B) RIGHT ANGLE ORIENTATION

FIG. 89. GERDIAN CONDENSER AND DETECTOR LOCATION FOR LARGE CHAMBER PLASMA MEASUREMENTS



- J1 - J2, CHASSIS BNC CONNECTOR
- J3 - J4, 'T' CONNECTOR
- J5 - J12, MALE CABLE BNC CONNECTOR
- J13 - J14, BULKHEAD VACUUM SEAL FEEDTHRU BNC CONNECTOR

FIG. 90 PROBE ELECTRONICS

TABLE XV
SUMMARY OF CONDITIONS OF PROBE MEASUREMENTS IN CHAMBER (SERIES II)

RUN NO.	DATE	TIME	NITRIC OXIDE PRESSURE (TORR)	CONDITIONS	FOOT-NOTES	FLUX AT DETECTOR, Φ_D (PHOTONS-CM ⁻² -SEC ⁻¹)	PROBE TYPE	PROBE NO'S	PROBE ORIENTATION	VOLTAGE RANGE	
										UPPER (VOLTS)	LOWER (VOLTS)
1	5/6/65	1600	0.200	Sealed Chamber	1,2 & 4	1.07×10^{11}	Small Double Probe	1 and 4	See Fig. 88	+47.3	-47.25
2	5/7/65	0900	0.500	"	1,2 & 4	9.6×10^{10}	"	1 and 4	"	+47.4	-44.94
3	5/7/65	1445	0.500	"	1,2 & 4	8.74×10^9	"	1 and 5	"	+47.5	-47.48
4	5/7/65	1600	0.200	"	1,2 & 4	1.14×10^{10}	"	1 and 5	"	+46.9	-46.9
5	5/10/65	1025	0.500	"	1,2 & 4	6.1×10^{10}	"	1 and 5	"	+47.4	-47.4
6	5/10/65	1235	0.200	"	1,2 & 4	1.4×10^{11}	"	1 and 5	"	+47.4	-47.5
7	6/8/65	1220	0	Pumped Chamber - Mech. Pump Only	2 & 4	1.05×10^{13}	"	1 and 2	"	+44.9	-45.9
8	6/8/65	1510	0.100	Sealed Chamber	2 & 4	4.0×10^{12}	"	1 and 4	"	+44.8	+1.8
9	6/9/65	-	0.500	"	2 & 4	9.6×10^{11}	"	1 and 4	"	+44.3	-44.7
10	6/9/65	1615	1.00	"	2 & 4	4.5×10^{11}	"	1 and 4	"	+44.8	-13.2
11	6/10/65	1010	0.500	"	2 & 4	8.7×10^{11}	"	1 and 4	"	+44.8	-1.0
12	6/20/65	1720	0	Pumped Chamber With Diffusion Pump	2 & 4	5.1×10^{12}	"	1 and 2	"	+9.9	-9.9
13	6/21/65	-	0	Pumped Chamber - Mech. Pump Only	2 & 4	4.5×10^{12}	"	1 and 2	"	+10	-10
14	6/21/65	1400	0.110	Sealed Chamber	2 & 4	3.6×10^{12}	"	1 and 2	"	+9.5	-3.9
15	6/21/65	1610	0.095	Sealed Chamber	2 & 4	3.5×10^{12}	"	1 and 2	"	+6	-6.6
16	6/21/65	1700	0.095	Sealed Chamber	2 & 4	3.6×10^{12}	"	4 and 5	"	+6.4	-3.3
17	6/21/65	1830	0.095	"	2 & 4	3.3×10^{12}	"	1 and 2	"	+5.9	-5.5
18	6/22/65	0930	0.500	Sealed Chamber	2 & 4	1.48×10^{12}	"	1 and 2	"	+6.9	-24.6
19	6/22/65	1130	0.500	Sealed Chamber With LCO ₂ In Cold Trap	2 & 4	1.57×10^{12}	"	1 and 2	"	+24.8	-24.8
20	6/22/65	1400	0.065	Continuous Flow of NO With LN ₂ In Cold Trap	2 & 4	2.62×10^{12}	"	1 and 2	"	+9.9	-9.9
21	6/22/65	1540	0.065	Continuous Flow of NO With LN ₂ In Cold Trap	2 & 4	3.1×10^{12}	"	1 and 2	"	+10	-10
22	7/2/65	-	0	Pumped Chamber With Diffusion Pump	2 & 4	1.3×10^{13}	"	1 and 2	"	+29.9	-29.9
23	7/2/65	-	0	Pumped Chamber - Mech. Pump Only	2 & 4	1.2×10^{13}	"	1 and 2	"	+29.4	-29.4
24	7/2/65	-	0.010	Sealed Chamber	2 & 4	8.7×10^{12}	"	1 and 2	"	+28.3	-28.6
25	7/2/65	-	0.065	Continuous Flow of NO	2 & 4	6.1×10^{12}	"	1 and 2	"	+29.2	-29.3
26	7/2/65	2027	0.065	Sealed Chamber	2 & 4	5.4×10^{12}	"	1 and 2	"	+29.5	-5.5
27	7/2/65	2357	0.065	Sealed Chamber	2 & 4	5.1×10^{12}	"	1 and 2	"	+43.1	-44.3
28	7/19/65	1345	0.100	Sealed Chamber	2 & 5	3.0×10^{12}	"	DNA	Axial See Fig. 89	+43.1	-44.3
29	7/19/65	1400	0	Pumped Chamber - Mech. Pump Only	2 & 5	5.2×10^{12}	"	DNA	"	+44.6	-44.9
30	7/20/65	-	0.010	Sealed Chamber	2 & 5	2.8×10^{12}	"	DNA	"	+44.6	-44.8
31	7/20/65	-	0.200	Sealed Chamber	2 & 5	1.75×10^{12}	"	DNA	"	+43.2	-44.3
32	7/23/65	1530	0	Pumped Chamber - Mech. Pump Only	3 & 6	7.2×10^{12}	"	DNA	Right Angles " 89	+44.9	-44.9
33	7/26/65	1245	0.010	Sealed Chamber	3 & 6	2.3×10^{12}	"	DNA	"	+43.5	-44.5
34	7/27/65	0830	0.100	Sealed Chamber	3 & 6	1.6×10^{12}	"	DNA	"	+43.0	-44.4
35	7/27/65	1250	0.200	"	3 & 6	1.05×10^{12}	"	DNA	"	+42.5	-44.6
36	7/29/65	0915	0	Pumped Chamber With Diffusion Pump	3 & 6	1.4×10^{12}	"	DNA	"	+44.8	-40
37	7/30/65	1325	0	Pumped Chamber - Mech. Pump Only	3 & 7	1.9×10^{12}	Large Double Probe	DNA	Axial See Fig. 88	+44.9	-44.9
38	8/2/65	1530	0.010	Sealed Chamber	3 & 7	1.05×10^{12}	"	DNA	"	+42.7	-43.1
39	8/3/65	0800	0	Pumped Chamber With Diffusion Pump	3 & 7	7.8×10^{11}	"	DNA	"	+44.8	-44.9
40	8/3/65	1300	0.10	Sealed Chamber	3 & 7	5.0×10^{11}	"	DNA	"	+40.3	-40.3
41	8/4/65	0830	0.200	"	3 & 7	4.4×10^{11}	"	DNA	"	+41.1	-40.9
42	8/4/65	1430	0	Pumped Chamber - Mech. Pump Only	3 & 7	5.7×10^{11}	Langmuir Probe	DNA	Normal See Fig. 88	+44.0	-44.8
43	8/10/65	0900	0.010	Sealed Chamber	3 & 7	3.6×10^{11}	"	DNA	"	+42.5	-44.1
44	8/13/65	1600	0.200	"	3 & 7	5.0×10^{11}	"	DNA	"	+38.8	-39.6
45	8/13/65	1330	0.100	"	3 & 7	9.2×10^{11}	"	DNA	"	+39.6	-39.1

Footnotes: 1. Only Two Lamps - 3.8 and 12.5 MA
2. Detector to Source Distance 24.7 CM
3. Detector to Source Distance 34.6 CM
4. Closest Probe to Source Distance 12 CM
5. Closest Probe to Source Distance 24.7 CM
6. Closest Probe to Source Distance 29.6 CM
7. Closest Probe to Source Distance 19.4 CM

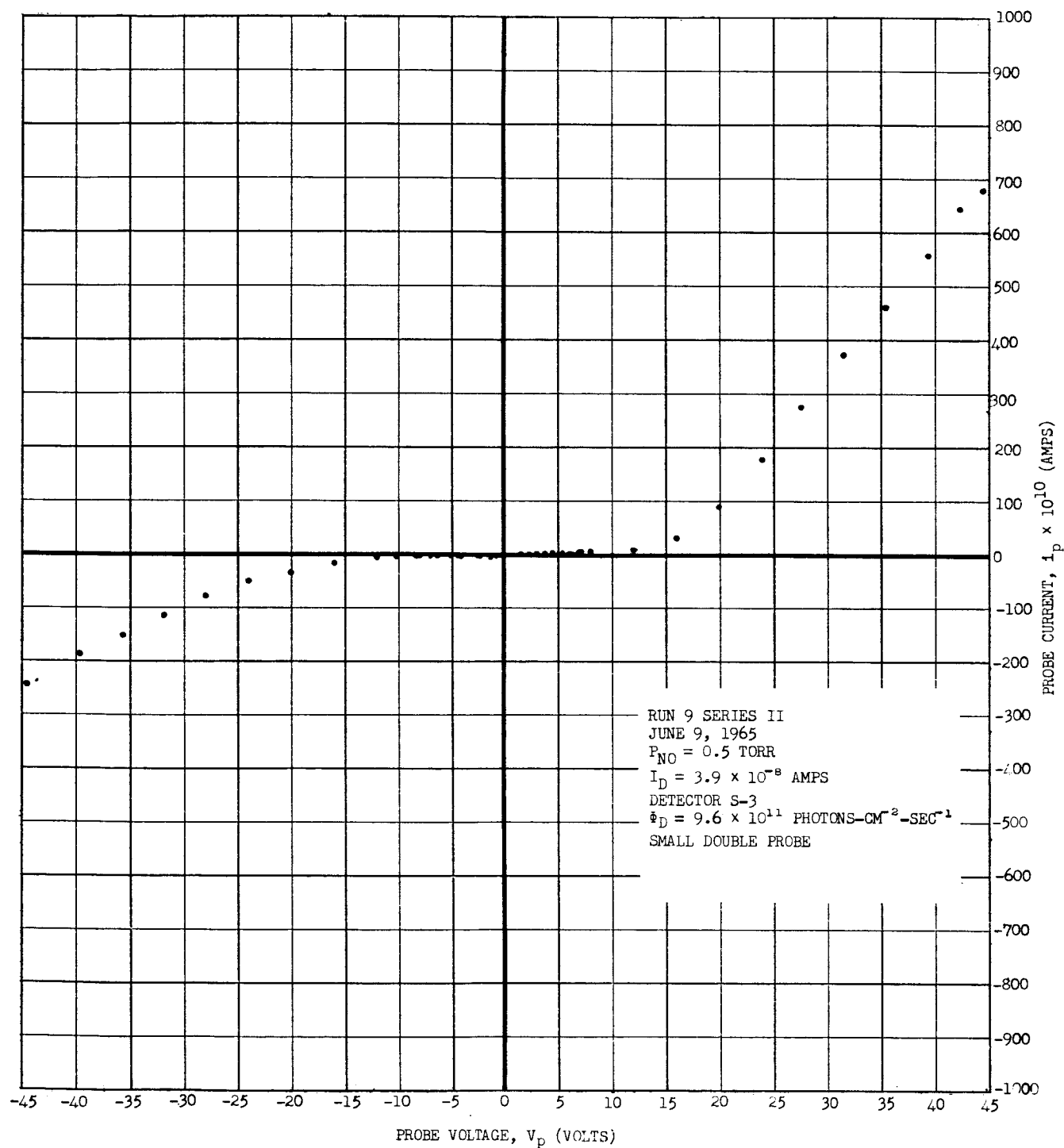


FIG. 91 TYPICAL SMALL DOUBLE I-V CURVE (SERIES II)

this curve is that it in no way resembles the curves obtained earlier in the bell jar (which will be referred to hereafter as Series I). In particular, there is no saturation region over the range 0-45 volts; the shape is concave with an extended plateau straddling the origin, while a double probe curve for a Maxwellian plasma should be convex. This is all the more surprising because the earlier bell jar measurements, using the same probe, gave typical double probe curves which were in reasonable agreement with the theory.

In view of the absence of a saturation region in the curves obtained with the small double probe, no information regarding plasma properties can be obtained from these curves.

3.3.3.7.3.1.2 Gerdian Condenser

Next, a Gerdian condenser [21, 22] was tried to see if something might be learned from its I-V characteristic, as well as to see how an actual flight probe responded in this plasma. These measurements were made at a pressure of 0.2 Torr.

The I-V characteristic for the condenser located coaxial with the beam is shown in Fig. 92, and a log-log plot of the same data is shown in Fig. 93. The I-V characteristic for the Gerdian condenser with its axis at 90° to the UV beam and its aperture located at the edge of the beam is shown in Fig. 94; a log-log plot of the same data is shown in Fig. 95. It can be seen that the same type of "kink" (i.e., concave region) occurs near the origin in both curves, as first observed in the data taken with the small double probe. However, it is not as pronounced, and, in fact, is almost nonexistent in Fig. 94.

In the first quadrant, the curve for the axial orientation (Fig. 92) looks suspiciously like that for an ion chamber. (See, for example, the NO detector curves of Figs. 20 and 53.) However, the current at the plateau represents a drain of only 9.4×10^{11} electrons-sec⁻¹, while the value calculated from the

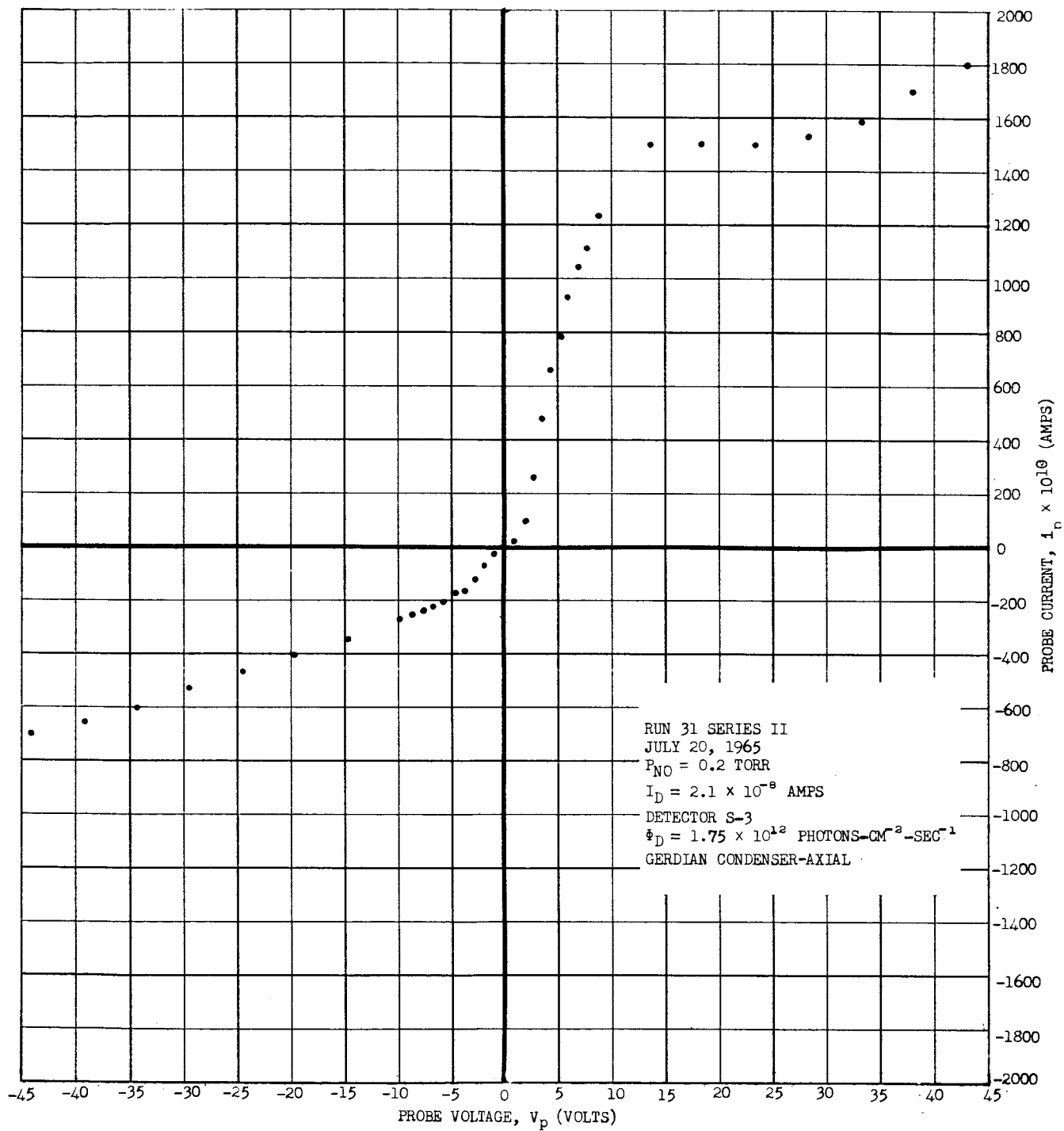
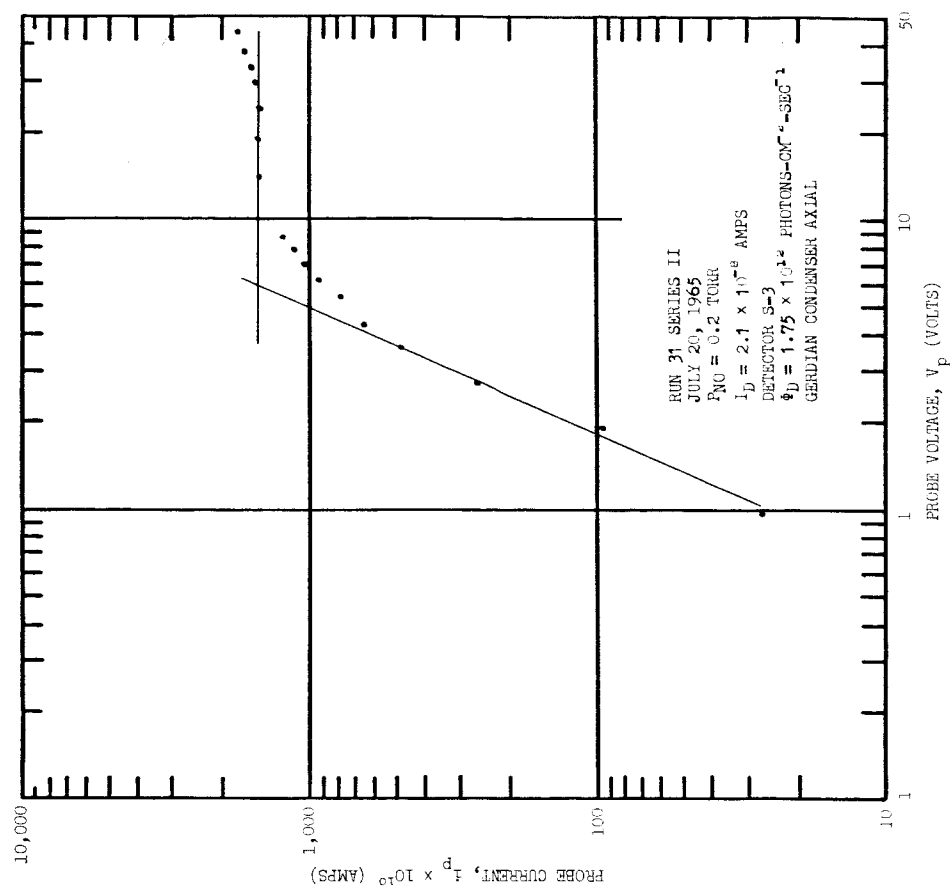
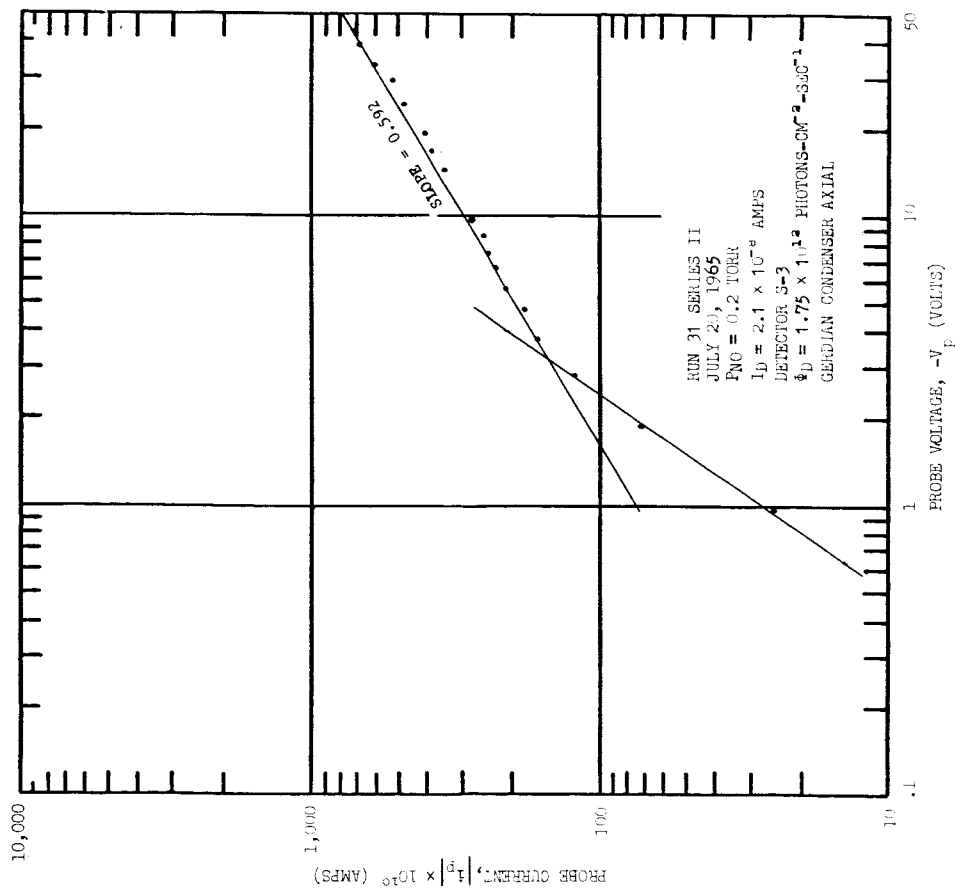


FIG. 92 TYPICAL GERDIAN CONDENSER I-V CURVE AXIAL ORIENTATION (SERIES II)



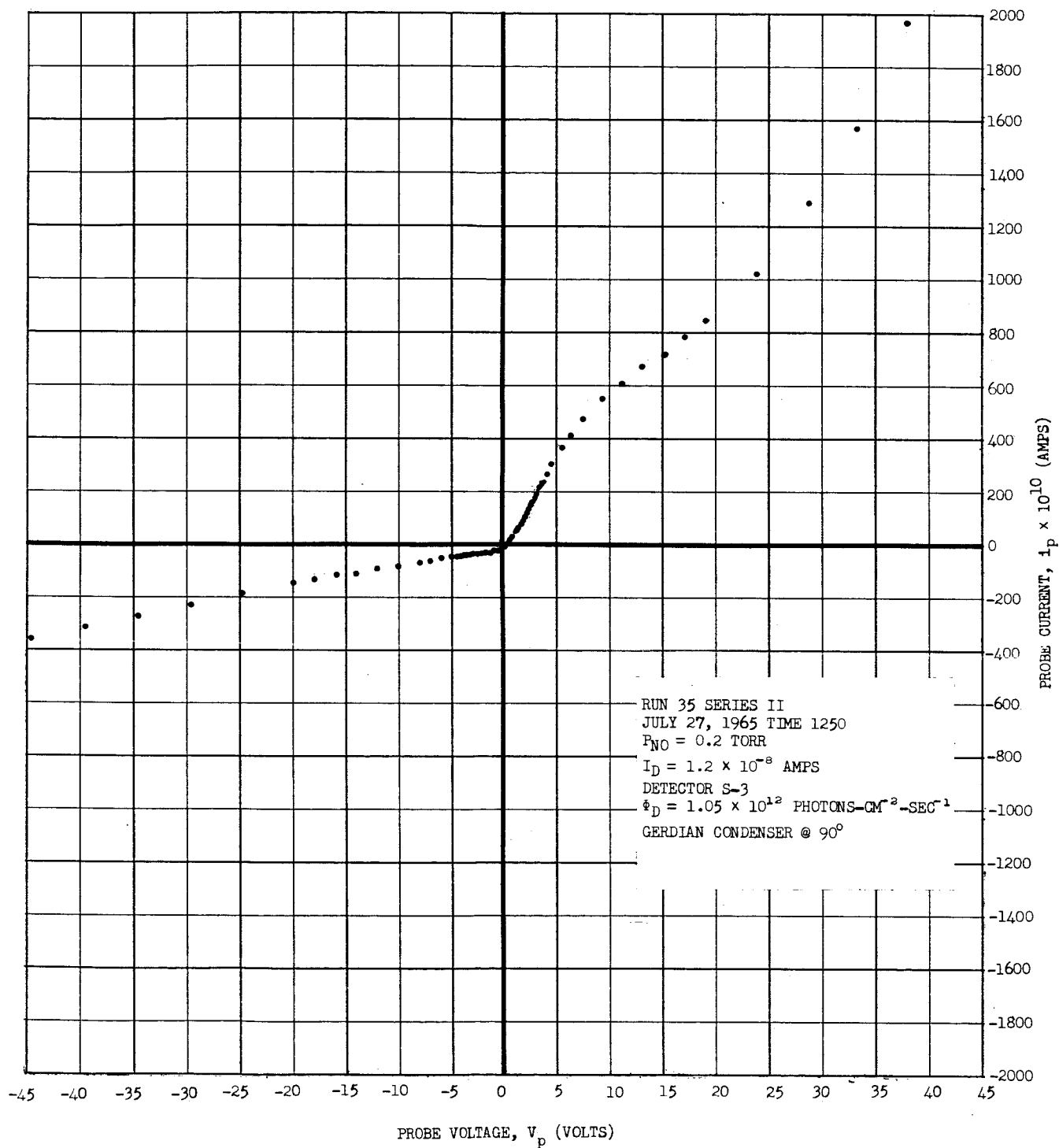


FIG. 94 TYPICAL GERDIAN CONDENSER I-V CURVE RIGHT ANGLE ORIENTATION (SERIES II)

FIG. 93 LOG-LOG PLOT OF TYPICAL GERDIAN CONDENSER I-V CURVE
AXIAL ORIENTATION (SERIES II)

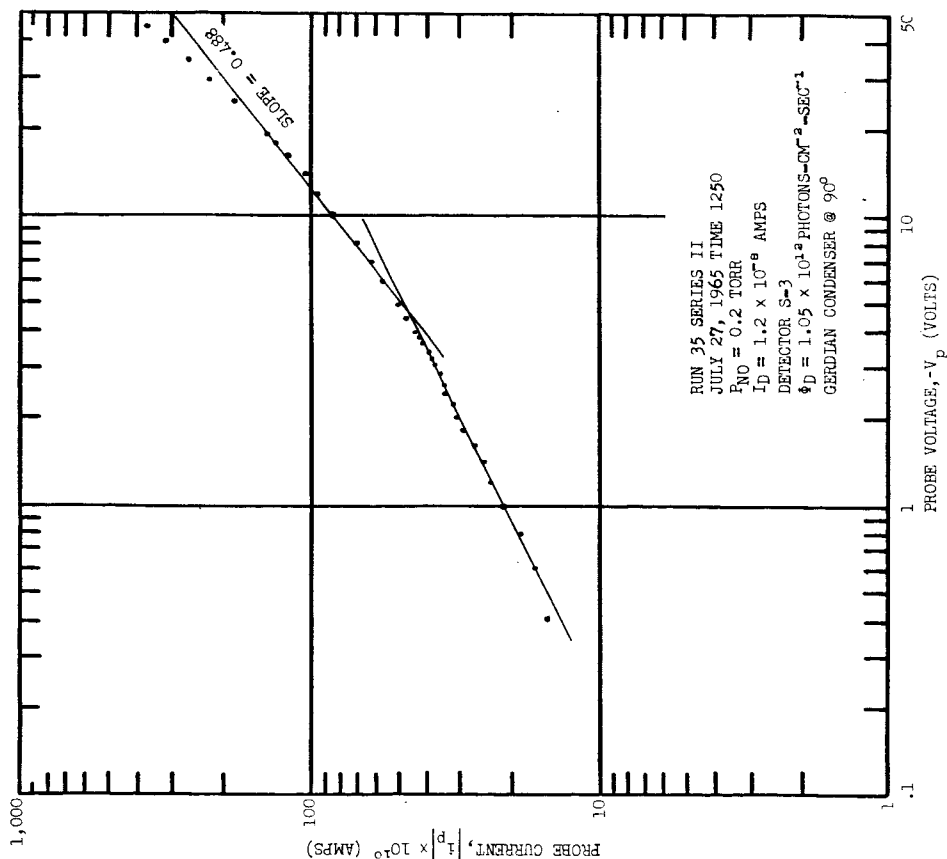
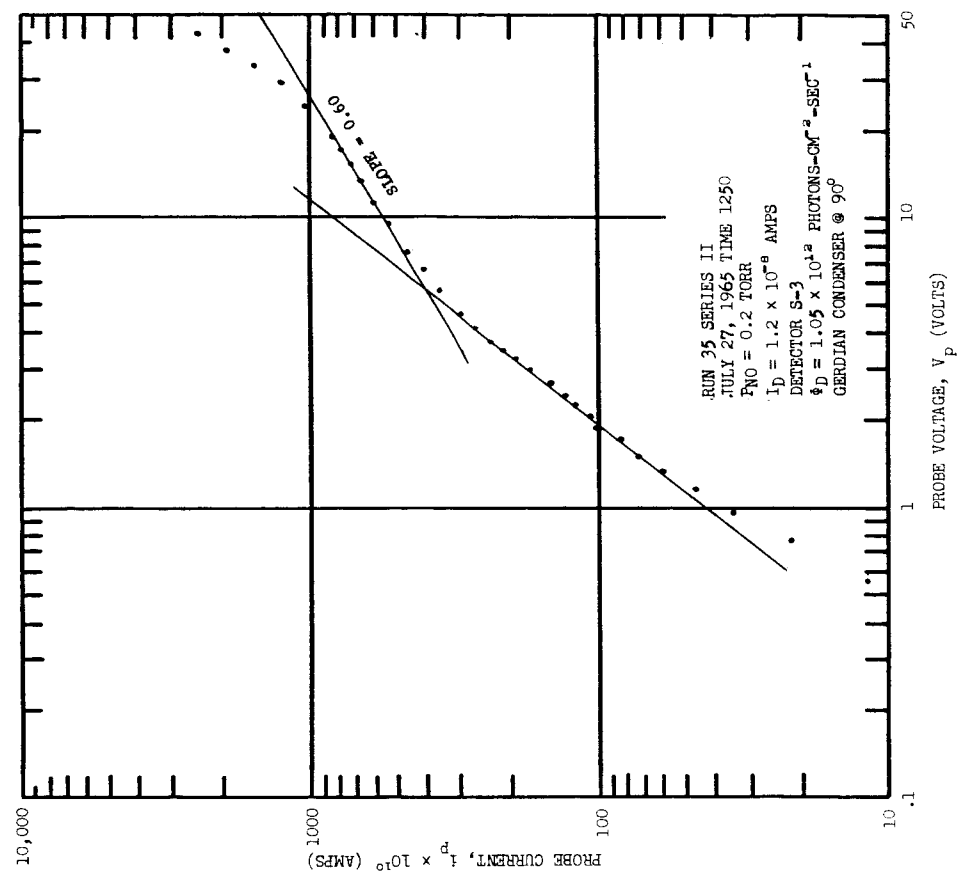


FIG. 95 LOG-LOG PLOT OF GERDIAN CONDENSER I-V CURVE
RIGHT ANGLE ORIENTATION (SERIES II)

measured photon flux is over three orders of magnitude greater. This fact eliminated the possibility that the Gerdian condenser is acting like an ion chamber.

Under the conditions of the experiment, the Gerdian condenser should behave as though the center electrode were a thick Langmuir probe, with the outer cylinder and chamber walls acting as a ground return. In other words, under these conditions the Gerdian condenser is nothing but a highly asymmetric double probe (Appendix A2.4). Assuming this to be the case, and that there are only electrons and positive ions present, the following upper limits for the electron and ion densities are obtained:

$$n_e \leq 2 \times 10^4 \text{ cm}^{-3}$$

$$n_p \leq 4 \times 10^4 \text{ cm}^{-3}.$$

These estimates are obtained using the theory of Appendix A2.1.1.1, assuming electron and positive ion temperatures of 300° K . If the electron temperature were higher than 300° K , the upper limit on the electron density would be decreased. On the other hand, if the negative particle saturation region (the flat portion in the first quadrant of Fig. 92) is assumed to be due entirely to negative ions, rather than electrons, one obtains an upper limit on the negative ion concentration of $n_n \leq 4 \times 10^5 \text{ cm}^{-3}$. Since the upper limit on the positive ion density is one-tenth of this value, and by charge conservation there can be no more negative than positive particles, it follows from Appendix A2.2 that most of the current variation in the transition region of the probe curve is due to electrons, so that there can be no more than twice as many negative ions as electrons.

On the other hand, the theory of Sec. 3.2.1.4 predicts an electron density of about 10^9 cm^{-3} . Thus, the upper limit on the actual positive ion density obtained above is about 3 orders of magnitude lower than that predicted by the theory. This is consistent with the presence of an electron attacher in an amount

sufficient to provide an attachment rate between 400 and 4000 times that of NO.

Finally, the slope of the log-log plot of the positive ion saturation region gives 0.59 for the exponent on the voltage, compared to 0.57 predicted by probe theory (Appendix A2.1.2.2) for many collisions in the sheath. But from Sec. 3.2.1.5, $\lambda_p \approx 2.5 \times 10^{-2}$ cm, while a sheath size of approximately 1 cm is obtained from the charge densities deduced above. Thus it follows that many collisions occur in the sheath, in fairly good agreement with the experimental slope.

As already pointed out, the negative particle saturation portion of the curve is quite flat. From Table VI in Sec. 3.2.1.5, the electron mean free path should lie between 0.25 and 3.2 cm, depending on electron energy. These values bracket the sheath radius of 1 cm, so that there should be at most a few electron collisions in the sheath. Thus, from the probe theory of Appendix A, one would indeed expect the electron saturation portion of the probe curve to be fairly flat under these conditions. This is in agreement with the observations.

One cannot obtain an electron temperature because of the "kink". However, the high breakpoint voltage for the ion saturation region indicates a number of epithermal electrons of considerable (few volts) energy.

A similar analysis applied to the data for the 90° orientation yields densities about one-fourth of those for the axial geometry. It would be expected that the densities would be lower for this case. However, the negative particle saturation portion is no longer a flat plateau, but has a slope of 0.6. This indicates the existence of a few electron collisions in the sheath. This is consistent with the decreased electron density, and hence larger sheath size.

3.3.3.7.3.1.3 Large Double Probe Results

Next, a large double probe was tried.

A typical I-V curve is shown in Fig. 96, and a log-log plot of the same curve is

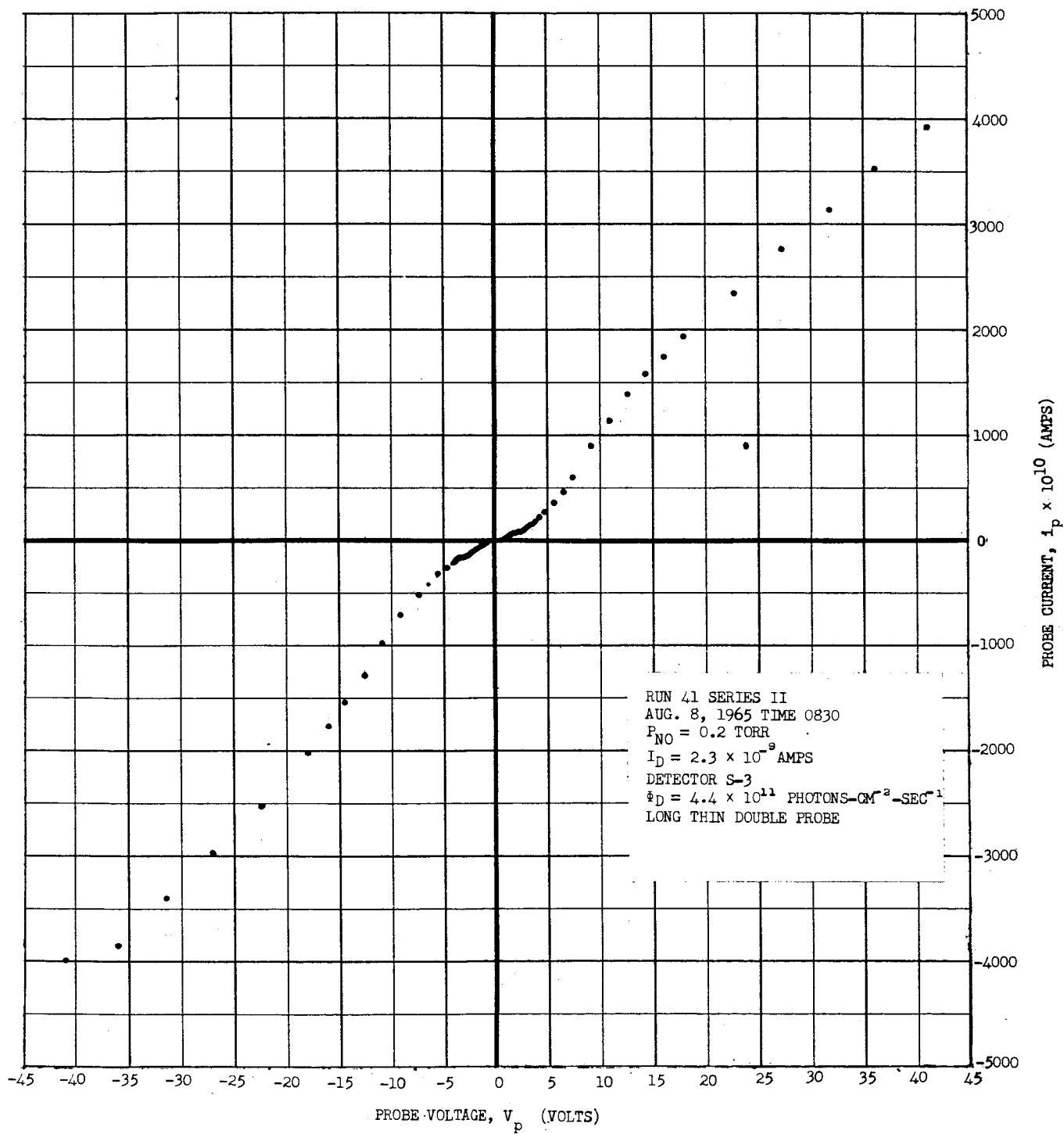


FIG. 96 TYPICAL LARGE DOUBLE PROBE I-V CURVE (SERIES II)

given in Fig. 97. Applying analysis similar to that for the Gerdian condenser yields an upper limit of $n_p \leq 1.9 \times 10^8 \text{ cm}^{-3}$ for the positive ion density. This is a factor of about 30 below the calculated value of $6 \times 10^7 \text{ cm}^{-3}$ from Sec.

3.2.1.4. Again the same "kink" or concave portion appears in the curve near the origin.

The slope of 0.83 in the "saturation" region does not fit any of the probe theory developed in Appendix A. Hence this isolated discrepancy is unexplained. Finally, the fact that all of the large probes, which are 10 times longer than the small double probes, show saturation, while the small double probe is possibly attributable to end effects existing for the small double probe. The measured densities imply sheath sizes from about 0.25 cm up to about 2 cm, which are large compared to the length of the small probes.

3.3.3.7.3.1.4 Langmuir Probe Results

Finally, a Langmuir probe was tried to see if it produced any different results. A typical Langmuir probe curve is shown in Fig. 98, and a log-log plot of the same data is given in Fig. 99. Again it is noted that the same "kink" is present near the origin as before. Assuming that the temperatures are 300° K , a similar analysis to that for the Gerdian condenser yields the following upper estimates of the densities:

$$n_p \leq 2.4 \times 10^5 \text{ cm}^{-3}$$

$$n_n \leq 10^6 \text{ cm}^{-3}$$

$$n_e \leq 4.4 \times 10^4 \text{ cm}^{-3}.$$

On the other hand, the predicted ion density is $6 \times 10^7 \text{ cm}^{-3}$, or about 200 times the upper experimental estimate. Finally, both of the measured slopes in the saturation region are a little higher than that predicted by the probe theory for a few collisions in the sheath, which is the applicable case here.

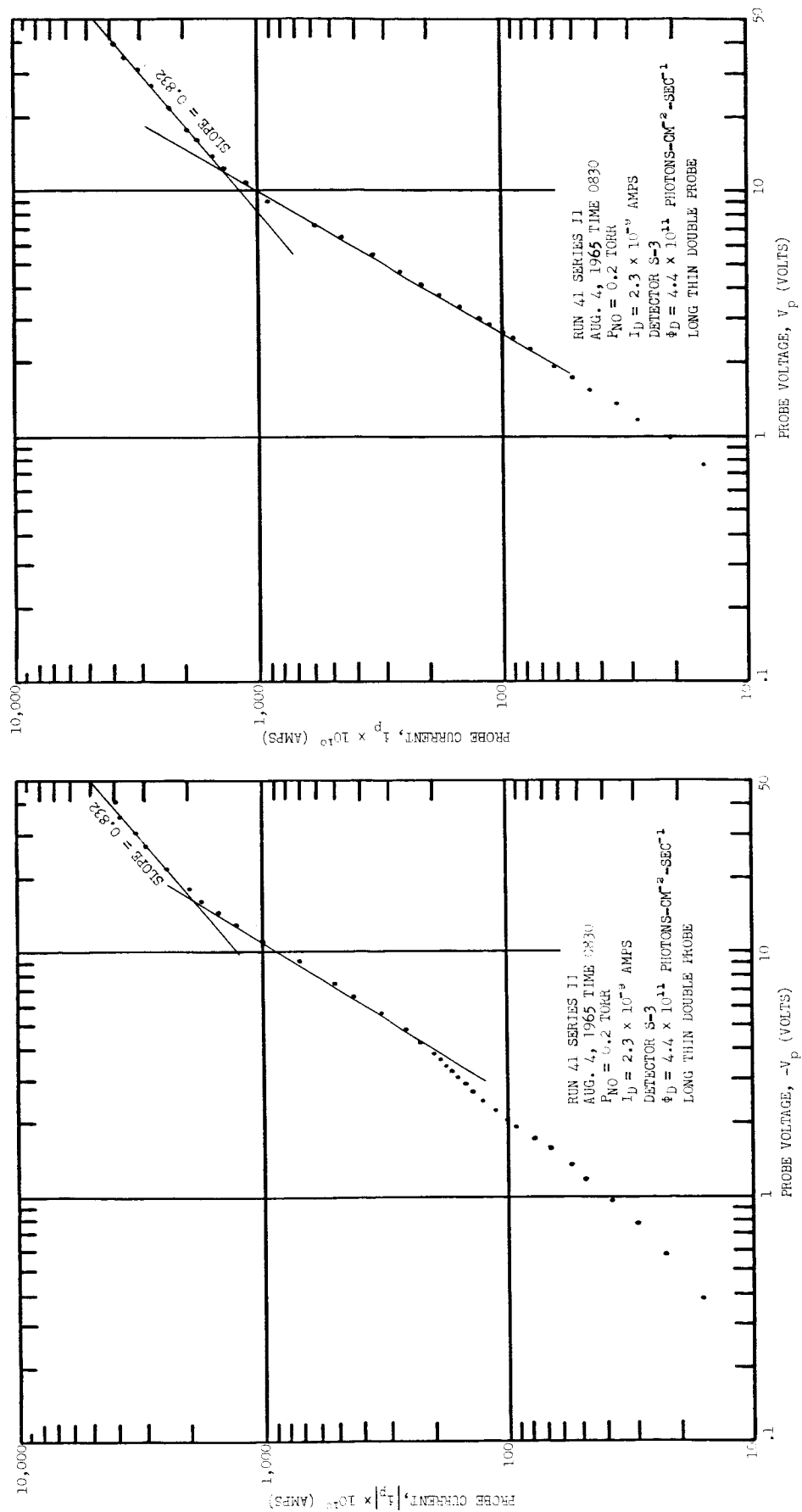


FIG. 97 LOG-LOG PLOT OF TYPICAL LARGE DOUBLE PROBE I-V CURVE (SERIES 11)

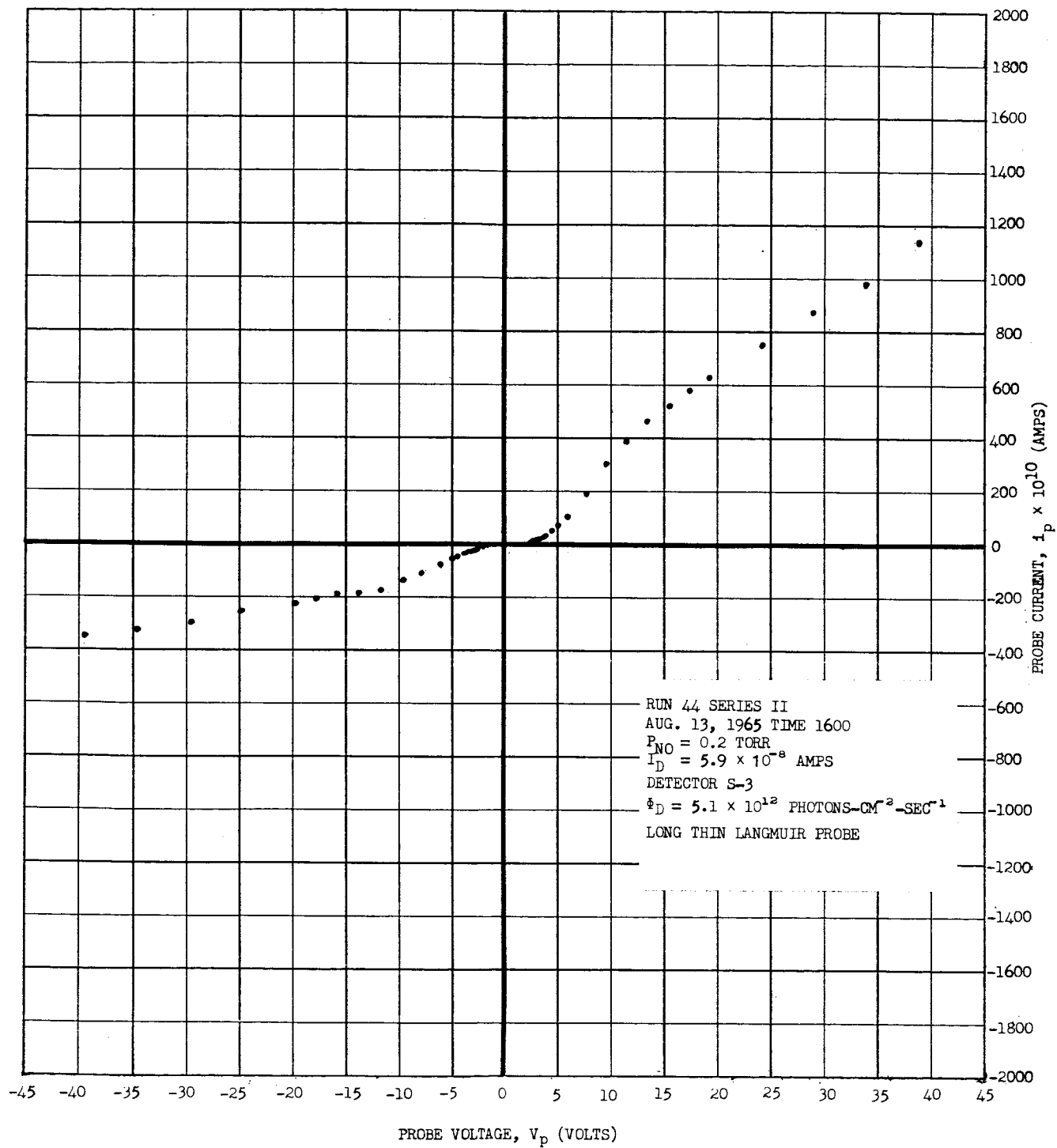


FIG. 98 TYPICAL LANGMUIR PROBE I-V CURVE (SERIES II)

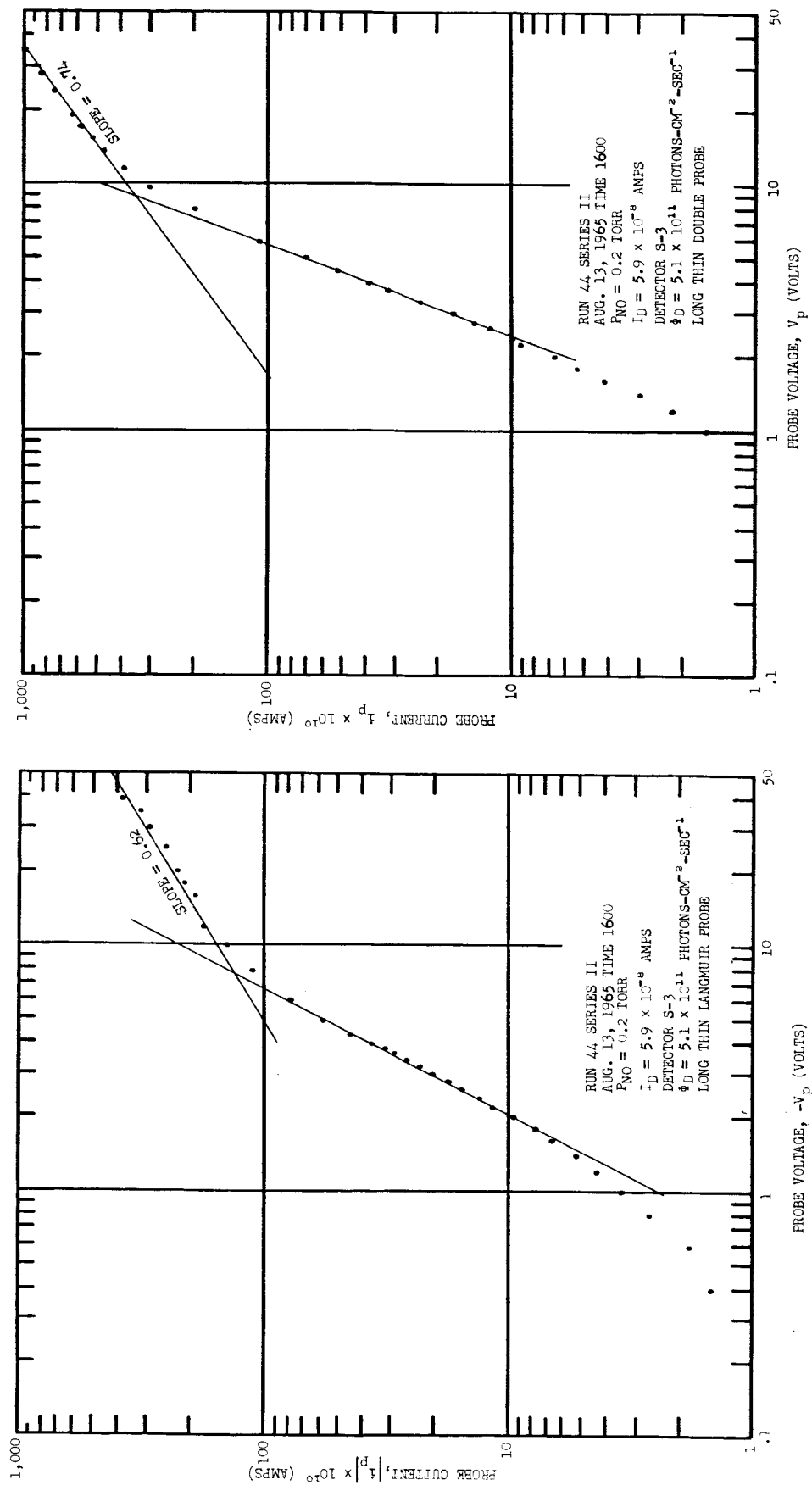


FIG. 99 LOG-LOG PLOT OF TYPICAL LANGMUIR PROBE I-V CURVE (SERIES II)

3.3.3.7.3.1.5 Summary of Series II Measurements

All of the curves of the Series II measurements, regardless of the probe used, show the same "kink" or concave shape near the origin. Second, they all show positive ion densities lying between $1/40$ and $1/2500$ of the predicted densities for pure NO. Finally, the electron densities, where they can be deduced, lie between $1/2$ and $1/10$ of the positive ion densities. These results are quite different from those obtained in Series I. At the time, they seemed quite unexplainable, since it was thought that there should be no significant difference between the gas samples used in the two series.

3.3.3.7.3.2 Repeat of Bell Jar Measurements (Series III)

On the basis of the above results, it was decided to return to the bell jar to see if the results of Series I could be reproduced. In this series of tests, to be referred to as Series III, two different gas supplies were used: the Matheson Co. NO used in Series II and a sample of NO supplied by Air Products and Chemical Co. In addition, an attempt was made to further purify the Air Products NO by passing it through silica gel at dry-ice temperature and then sublimating it at LN₂ temperatures. Also, both a krypton and a hydrogen filled lamp were used to see if, possibly, UV spectrum had anything to do with the kink. The various conditions under which these measurements were made are summarized in Table XVI. A small double probe was used for all of these measurements.

A typical probe I-V characteristic for Series III is shown in Fig. 100. It is seen to be essentially the same as that obtained in the chamber. Since all the other curves for this series are similar in shape, one is forced to the conclusion that the "kink" is a result of differences in the gas used between Series I and Series II and III. It was at this point that a check was made with the gas manufacturers to see what impurities might be present in their gas samples.

TABLE XVI

Summary of Conditions of Probe Measurements

Series III, Bell Jar

(Small Double Probes, $L_p = 2.5$ CM, Probes 1 and 4, $L_D = 14.5$ CM)

RUN NO.	DATE	TIME (TORR)	NITRIC OXIDE PRESSURE	CONDITIONS	GAS MANUF.	FLUX AT DETECTOR, Φ_D (PHOTONS-CM ⁻² -SEC ⁻¹)	VOLTAGE RANGE (VOLTS) (VOLTS)	
							UPPER	LOWER
1	8/20/65	1300	0.100	Sealed Chamber, Straight Gas, Kr Lamp Matheson	"	5.9×10^{12}	+40	-40
2	9/8/65	0900	1.15	"	"	1.4×10^{12}	+40	-40
3	9/9/65	1000	1.00	"	"	Air Products 1.87×10^{12}	+40	-40
4	9/17/65	0900	1.00	"	"	H ₂ Lamp 4.5×10^{12}	+40	-40
5	9/21/65	1100	1.00	"	"	Different 4.2×10^{12}	+40	-40
Air Products								
6	9/22/65	1000	1.00	"	"	8.15×10^{12}	+40	-40
7	9/23/65	1015	1.010	"	"	5.9×10^{12}	+38	-38
Cleaned Bell Jar								
8	9/23/65	1605	1.05	Sealed Chamber, Straight Gas, H ₂ Lamp	"	5.3×10^{12}	+40	-38
Placed Pump Oil on Walls								
9	9/24/65	0810	1.10	"	"	4.2×10^{12}	+40	-40
10	9/30/65	1530	1.00	Sealed Chamber, Purified Gas, H ₂ Lamp	"	3.42×10^{12}	+35	-10
Cleaned Bell Jar								
11	10/1/65	1500	0.900	Sealed Chamber, Purified Gas, H ₂ Lamp	"	3.48×10^{12}	+35	-10
Cleaned Bell Jar								

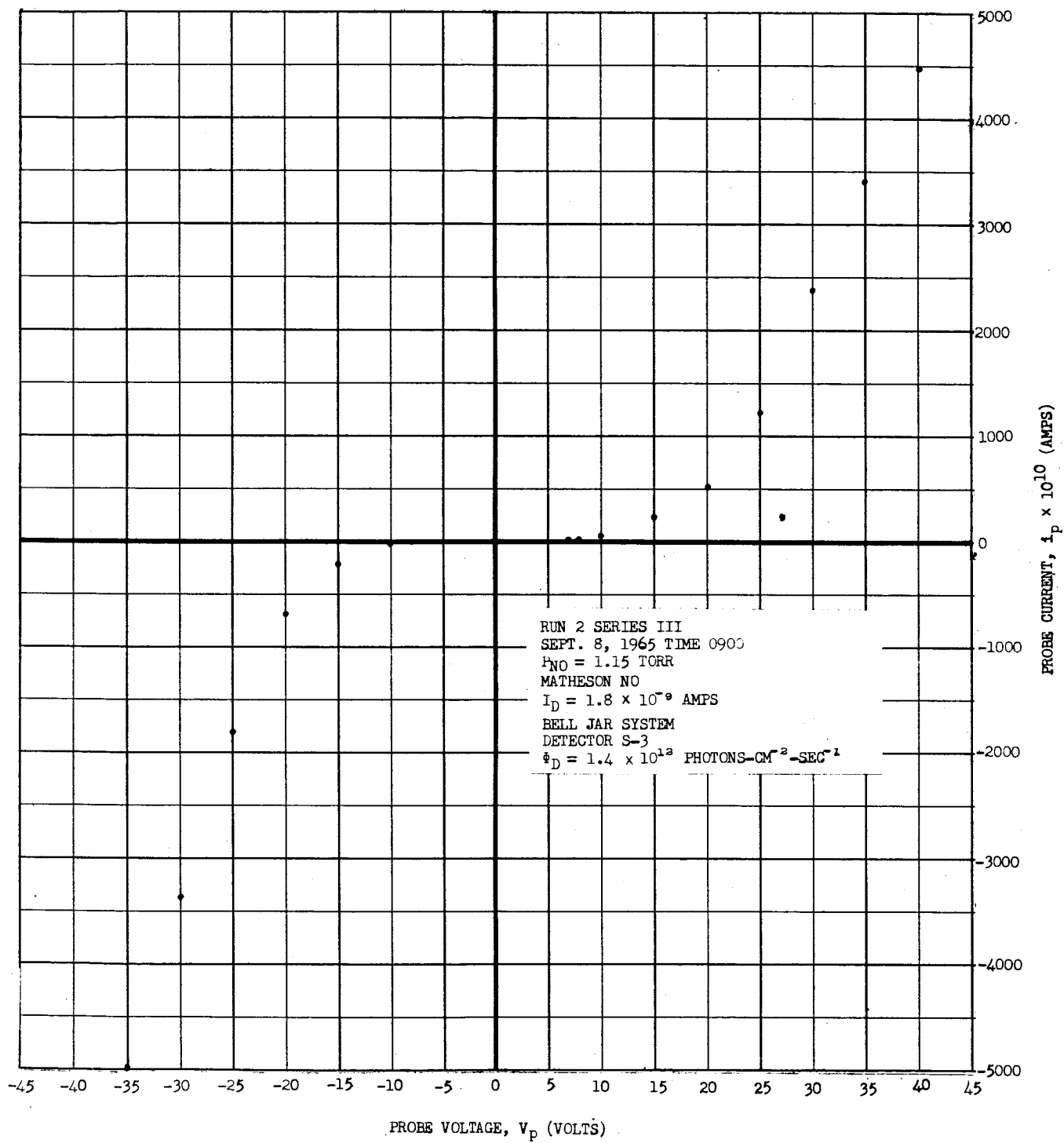


FIG. 100 TYPICAL PROBE I-V CURVE FOR BELL JAR (SERIES III)

This check revealed that there had been a change in manufacturing processes between the two bottles of Matheson NO, and that the second Matheson bottle and the Air Products gas had N_2O as a common impurity which was not present in the first Matheson bottle (see Sec. 3.3.3.7 for full details). However, the possibility of N_2O being the attaching impurity was not given much weight at the time, since the work of Rapp and Briglia [23] on the attachment cross section of N_2O had not yet been published.

3.3.3.7.3.3 Final Chamber Measurements (Series IV)

At this juncture it was suggested that perhaps a film buildup on the probes, together with changes in this film with applied voltage, might be responsible for the behavior observed above (e.g., see Refs. [24], and [25]). It has been known since the early days of Langmuir probes that they are subject to such surface effects, and that changes in work function due to probe contamination could produce erroneous results. However, double probes are supposed to be relatively free from such effects [16]. Such a film buildup and changes therein might also account for the long time constants observed.

All of the data of Series I to III were taken under so-called "steady-state" conditions. That is, the voltage was applied to the probe and then the technician waited approximately two minutes, for the current to stabilize, before reading and recording the probe current. To check the film buildup and change hypothesis and effects, a different method (called the "semi-swept" method) of taking the data was devised. In this method, the voltage to be applied to the probe was set; then the battery on-off switch of Fig. 90 was turned off, so that the probe voltage was zero. Next, two minutes were allowed to elapse, the voltage was applied to the probe, and the current at 3 sec after the application of the voltage to the probe was read and recorded. By following this procedure it was hoped to keep any film on the probe at its value at zero voltage.

Some 13 probe curves or portions of probe curves were taken using both the steady-state and semi-swept methods. Every attempt was made to keep the plasma conditions the same while taking the I-V characteristics, so that the curves resulting from the two methods could be compared directly. The conditions for the various measurements are summarized in Table XVII. These experiments were performed in the chamber, using both the Langmuir and the large double probe. Mass analysis of the contents of the chamber was carried out simultaneously with the taking of the probe data.

3.3.3.7.3.3.1 Langmuir Probe

In Fig. 101 are shown two of the semi-swept Langmuir probe curves taken in close succession. One is immediately struck by the total lack of reproducibility. Similar results were obtained for the other Langmuir probe curves. Thus, the data obtained from any Langmuir probe curve measured in the program are felt to be totally unreliable. The other feature of note is that all of the semi-swept Langmuir probe curves still possessed the "kink".

3.3.3.7.3.3.2 Double Probe

Large double probe curves were taken in both a straight NO atmosphere and in a NO-He mixture. These results are discussed separately below.

For the chamber filled with NO at 0.2 Torr, typical results for the large double probe, using both data taking methods, are shown in Fig. 102 for the voltage range -5 to +5 volts. Points taken by the steady-state method are indicated by dots (•), and by the semi-swept method by (+). Also shown in this figure are some reproducibility check points (⊠) and a curve (⊙) derived from the steady-state curve by a process to be described.

TABLE XVII

Summary of Conditions of Probe Measurements, Series IV, Large Chamber

 $(L_p = 17.8 \text{ CM}, L_D = 32.7 \text{ CM}, \text{ See Fig. 88})$

RUN NO.	DATE	TIME	GAS MIXTURE PRESSURE (TORR)	CONDITIONS	FLUX AT DETECTOR, ϕ_D (PHOTONS- $\text{CM}^{-2} \text{ SEC}^{-1}$)	PROBE TYPE	METHOD	PROBE VOLTAGE RANGE (VOLTS)	
								UPPER	LOWER
1	11/17/65	1053	0.020	Straight NO Gas	5.94×10^{12}	Large Double Probe	Steady State	+45	-3.5
2	11/17/65	1530	0.200	"	1.96×10^{12}	"	Semi-Swept	-45	-45
3a	11/18/65	0930	0.200	"	1.96×10^{12}	"	Steady State	+5	+5
3b	11/18/65	1100	0.200	"	1.96×10^{12}	"	Semi-Swept	+5	+5
3c	11/18/65	1355	0.200	"	1.96×10^{12}	"	Semi-Swept	+5	+5
4	11/18/65	"	0.200	"	1.84×10^{12}	"	Steady State	+5	+5
5a	11/18/65	1515	0.200	"	1.18×10^{12}	Langmuir Probe	Semi-Swept	45	0
5b	11/18/65	1700	0.200	"	1.18×10^{12}	"	"	45	0
6	11/19/65	1045	0.200	"	1.01×10^{12}	"	Steady State	45	-45
7	11/19/65	1400	0.200	"	1.01×10^{12}	"	Semi-Swept	45	-45
8	11/22/65	1030	0.200	"	1.01×10^{12}	"	"	45	-45
9	11/23/65	1245	0.200	"	7.84×10^{11}	"	"	45	-45
10a	11/24/65	1000	1.20	10 Torr NO + 1.99 Torr He	"	Large Double Probe	"	0	+5
10b	11/24/65	"	1.20	"	"	"	"	+5	0
10c	11/24/65	"	1.20	"	"	"	"	0	-45
10d	11/24/65	"	1.20	"	"	"	"	0	-45
10e	11/24/65	"	1.20	"	"	"	"	+5	-45
11	11/24/65	1430	1.20	"	"	"	"	45	-45
12a	11/24/65	1600	1.20	"	"	"	"	+3	-2
12b	11/24/65	1643	1.20	"	"	"	"	2	-2
12c	11/24/65	"	1.20	"	"	"	"	2	-2
13a	11/24/65	1730	1.20	Reverse Connections	"	"	"	+2	-2
13b	11/24/65	1800	1.20	"	"	Langmuir Probe	"	+45	0
				"	"	"	Steady State	+45	0

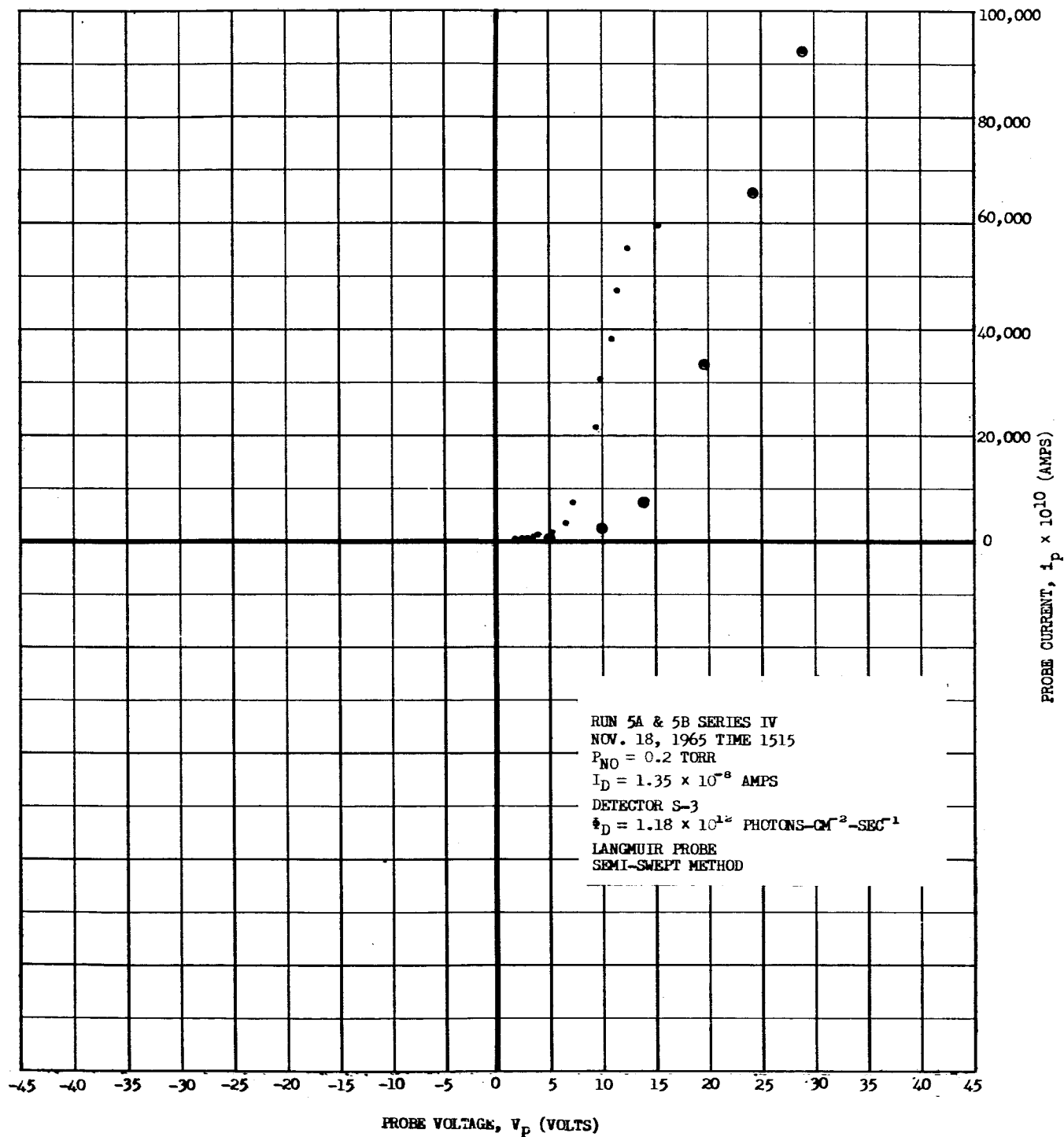


FIG. 101 COMPARISON OF LANGMUIR PROBE I-V CURVE FOR STEADY-STATE AND SEMI-SWEPT METHOD (SERIES 11)

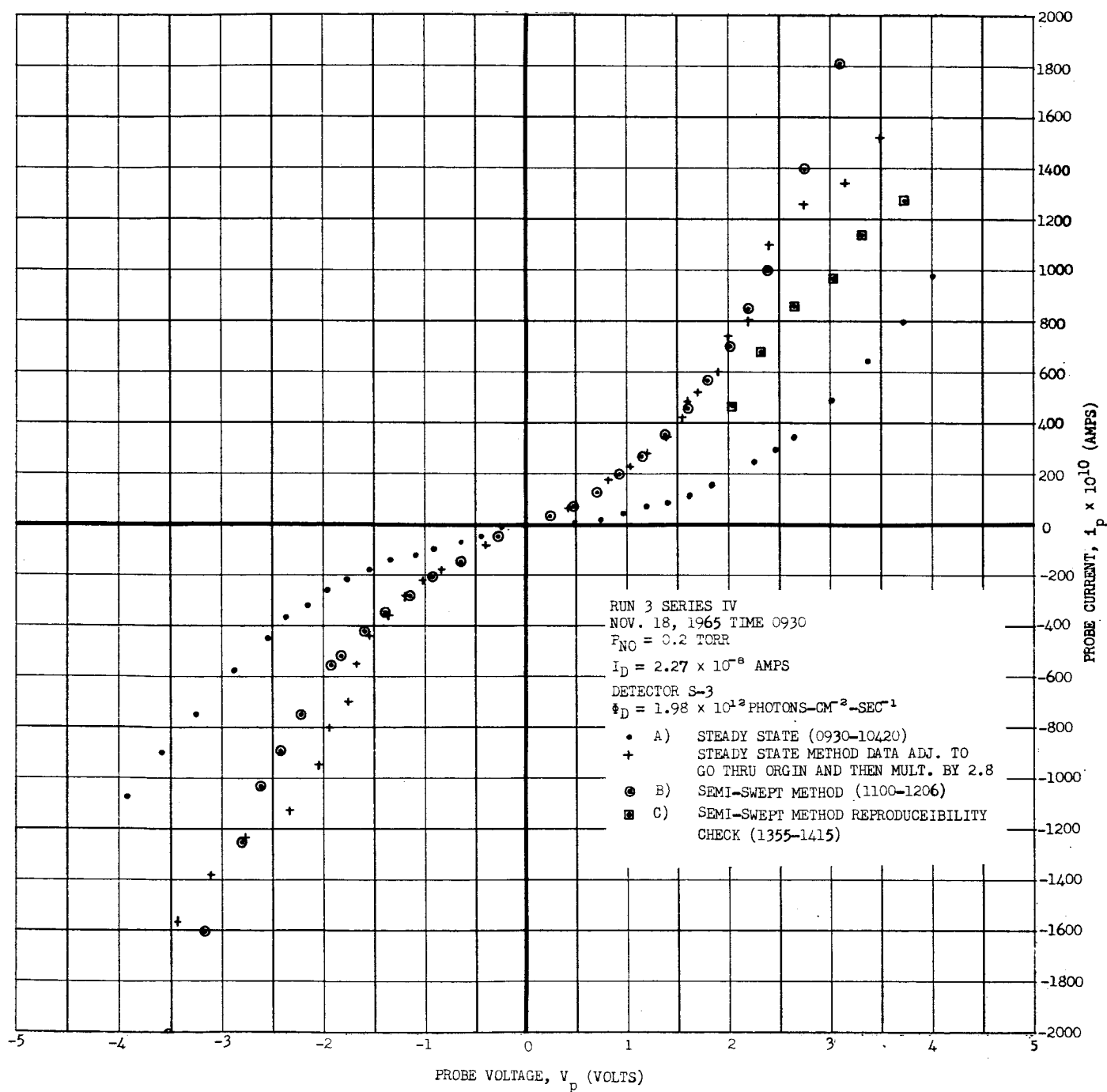


FIG. 102 COMPARISON OF LARGE DOUBLE PROBE I-V CURVE FOR STEADY-STATE AND SEMI-SWEPT METHOD (SERIES IV)

The first point worthy of note is that the data are reasonably reproducible. The next point is illustrated by the curve (⊙) derived from the steady-state data (○). This curve was obtained by shifting the steady-state curve horizontally so that it has the same value of i_d at $V_d = 0$ as the semi-swept curve, and then multiplying the curve by 2.8. The curve so derived is seen to coincide with the semi-swept curve (+) in the region -2.5 to +2.5 volts. Thus it is seen that the functional form for the steady-state and semi-swept curves is the same, so that the "kink" is present in both. Next, it follows that the main effect of the film is to raise any temperature obtained by the equivalent resistance method from steady-state measurements, since it decreases the slope, in this case by a factor 2.8. It thus appears that the electron temperatures obtained during the first series of ball jar measurements (Series I) may be too high by a factor of about 3.

A full double probe curve taken by the semi-swept technique is shown in Fig. 103, and a log-log plot of the same data is shown in Fig. 104. Using the same type of approach as in the analysis of the Series II data, an upper limit for the positive ion density of

$$n_p \leq 5 \times 10^8 \text{ cm}^{-3}$$

is obtained. On the other hand, the theoretically predicted value is 2×10^9 , which is higher by a factor of 40 or more. One of the slopes in the saturation regions matches the probe theory well, while the other seems high.

After the straight NO measurements, a set of data was taken for a mixture of 0.84% NO - 99.16% He. This was done to see if lowering the concentration of the suspected attaching species with respect to the main scattering species could have any significant effect on curve shape or other plasma properties. A double probe semi-swept curve for this situation is shown in Fig. 105, and a log-log plot of the same data is shown in Fig. 106. The "kink" is still seen to be present.

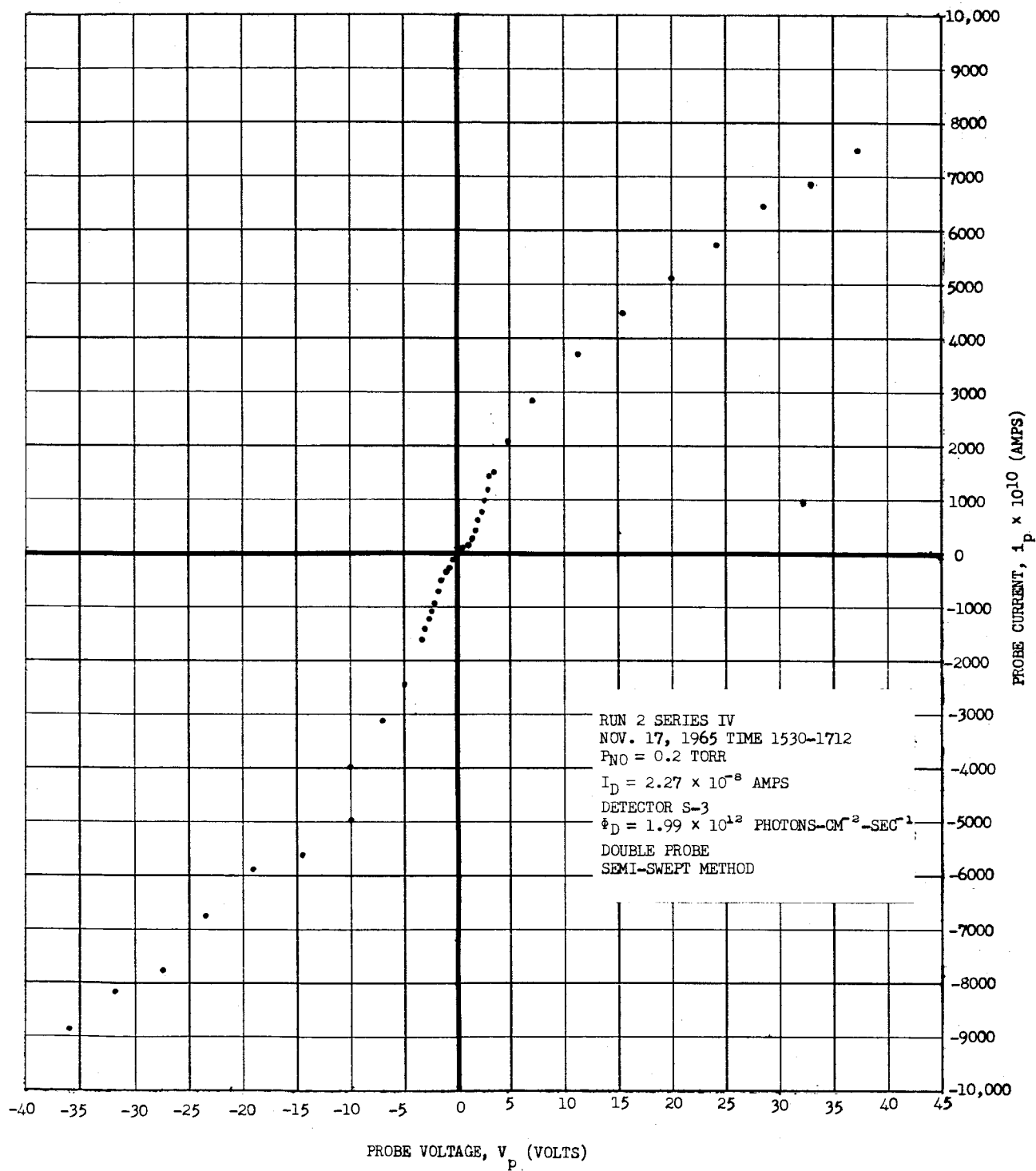


FIG. 103 TYPICAL LARGE DOUBLE PROBE I-V CURVE, STRAIGHT NO., SEMI-SWEPT METHOD (SERIES IV)

FIG. 106 LOG-LOG PLOT OF TYPICAL LARGE DOUBLE PROBE I-V CURVE,
NO-H₂ MIXTURE, SEMI-SWEPT METHOD (SERIES IV)

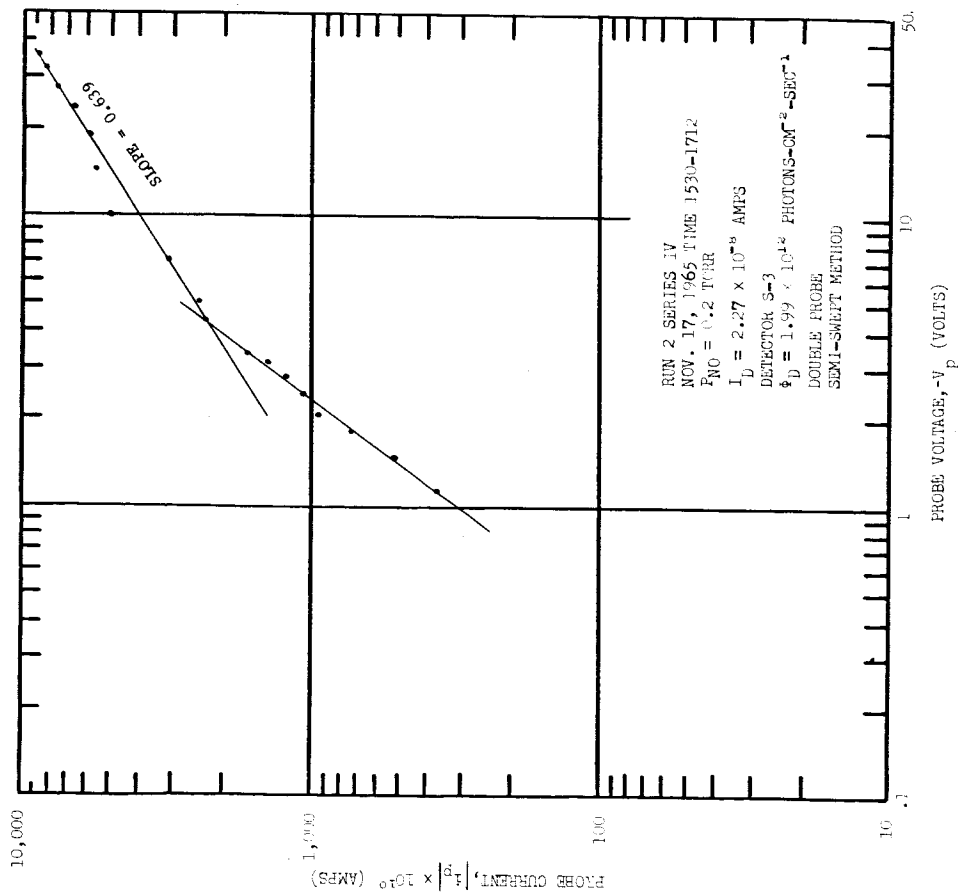
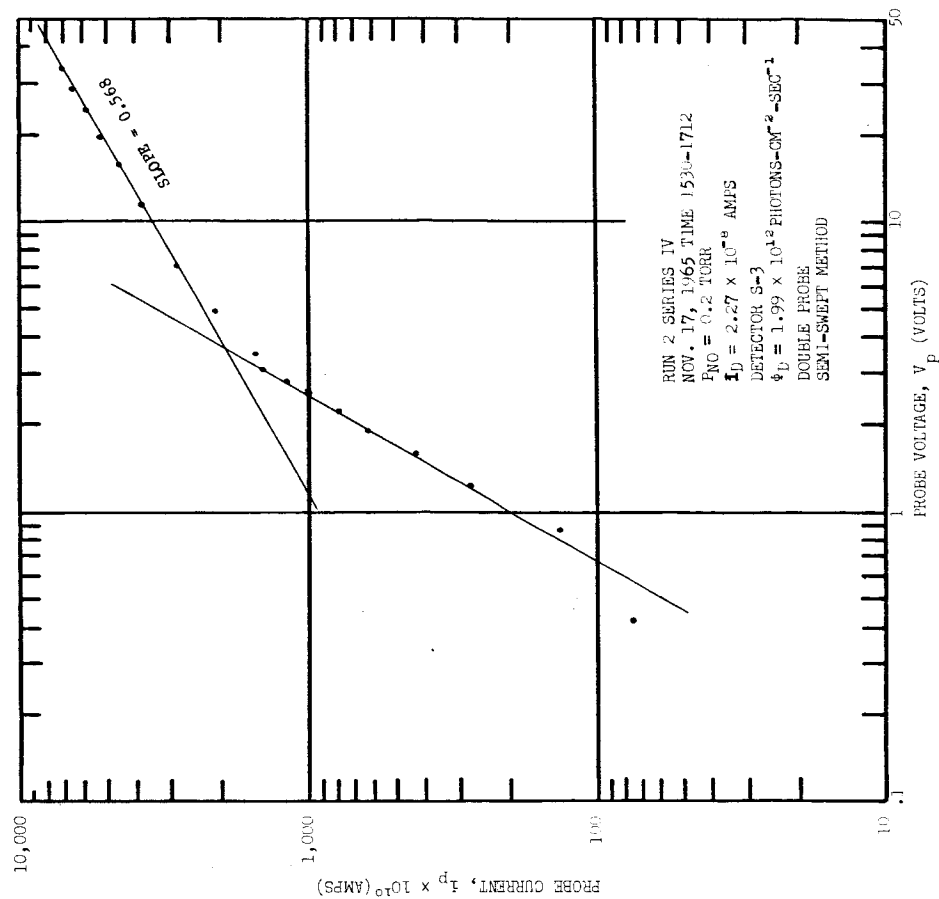


FIG. 104 LOG-LOG PLOT OF TYPICAL LARGE DOUBLE PROBE I-V CURVE,
STRAIGHT NO₂, SEMI-SWEPT METHOD (SERIES IV)

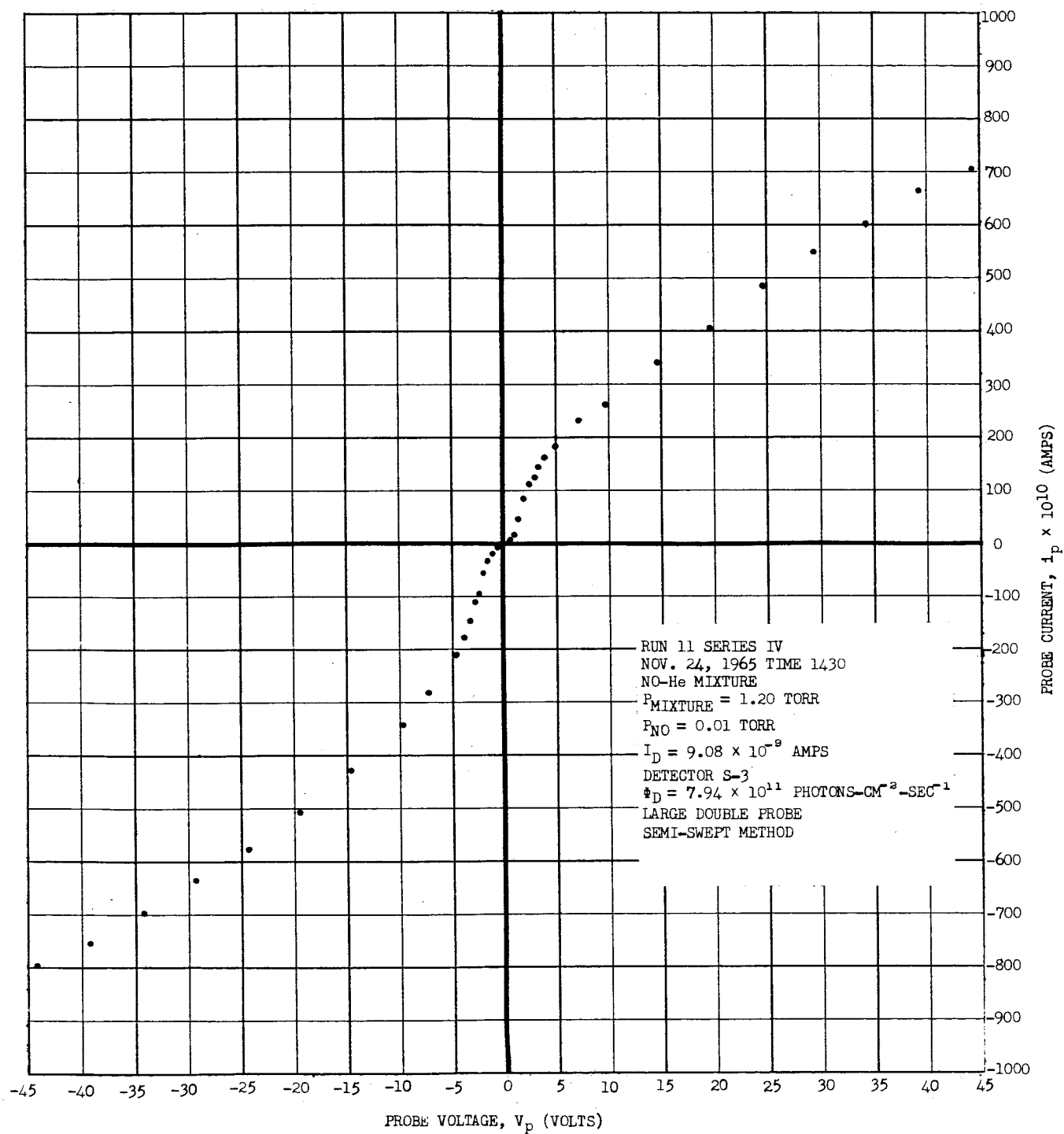
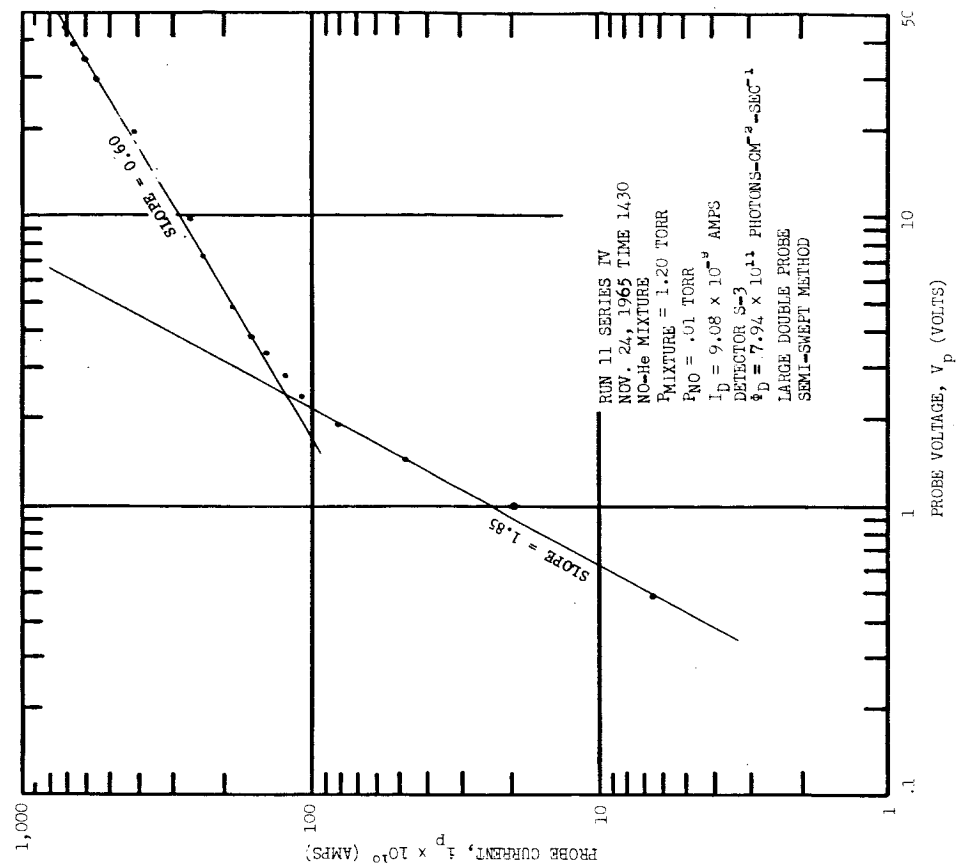
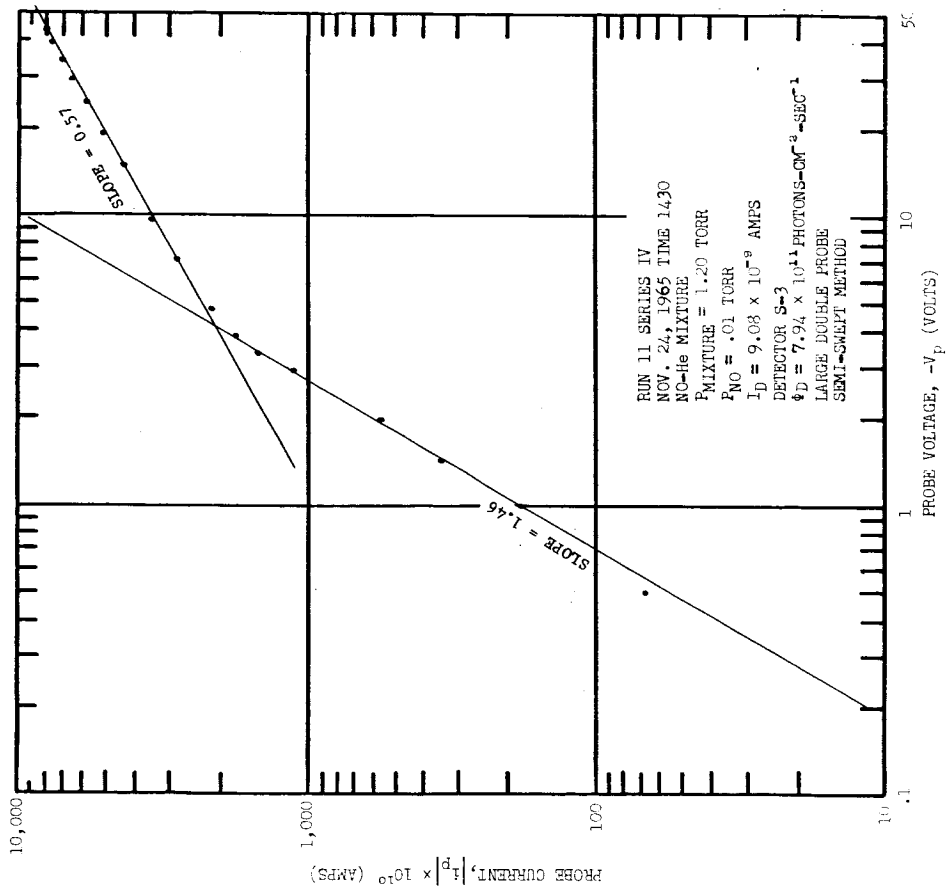


FIG. 105 TYPICAL LARGE DOUBLE PROBE I-V CURVE, NO-He MIXTURE, SEMI-SWEPT METHOD (SERIES IV)



Further, from the ion current at the break point it can be reasonably surmised that the positive ion density, and, hence, ion-electron pair production rate is down in direct proportion to the decrease in NO pressure. This experiment apparently had no effect on the central problem of the "kink". This is exactly what one would expect for a dissociative attachment type of electron removal process.

3.3.3.7.3.4 Summary and Conclusions

The probe results show that a large volume plasma has been produced in the chamber with positive ion densities, n_p , ranging between 4×10^4 and $2 \times 10^5 \text{ cm}^{-3}$, and electron densities lying between about n_p and $n_p/10$. The measured densities are two to three orders of magnitude below those predicted for pure NO. The low densities, and electron densities below those of positive ions, suggest the existence of a highly active electron attaching agent which combines quickly with the electrons produced by photoionization. Such a process also would distort the probe curves at low voltages so as to give the observed initial concave portion, or "kink", in the I-V characteristic.

The distortion of the I-V curve does not allow electron temperatures to be deduced in the presence of the electron attaching agent. It was found that the probe currents at low probe voltages were depressed by a constant factor of about 3 due to surface changes taking place on the probes with varying voltage, presumably due to a film of pump oil vapor. This effect leads to apparent electron temperatures which are too high by this factor when the probe characteristic is taken slowly point by point. Consequently, the electron temperatures deduced from the measurements discussed in Sec. 3.2.2.2.2 (in a "clean" NO atmosphere) should be divided by a factor of about 3.

3.3.3.8 Mass Analysis

The chamber probe measurements discussed in Sec. 3.3.3.7 suggest the presence of an electron attaching agent in the NO which was not present in the sample of NO used for the feasibility study tests in the bell jar (Sec. 3.2.2.2). The NO for the above two sets of measurements came from different bottles, manufactured at different times by different processes, but from the same supplier. To help determine the origin and quantity of this attaching agent, the differential pumping system for the Veeco GA-3 gas analyzer described in Sec. 3.3.3.5.1 was constructed. This system permits sampling of the gas in the chamber. In the following, the various mass analysis experiments are described, and the results presented and analyzed. The results indicate that N_2O is probably the suspected electron attaching agent.

3.3.3.8.1 Cracking Pattern Measurements

Prior to installing the mass spectrometer on the differential pumping system, it originally was planned to study the "cracking pattern" of the oxides of nitrogen and carbon, using the bakeable gas handling system. The electron beam energies in the ion source of the mass spectrometer are high enough to dissociate or "crack" the molecules of the gas (principally NO) used in the plasma experiments, so that chemical reactions [26] can occur in the ion source. Thus, a mass analysis of the gas used in the plasma experiment will show mass lines due to the cracking, in addition to the line representing the parent gas molecule. If P_M is the peak height at mass M,

$$P_M = \sum_{N=1} h_{MN} P_N$$

where P_N is the partial pressure of gas N and the "cracking coefficients," h_{MN} , are a function of the particular mass spectrometer and its operating conditions. It is thus necessary to determine these cracking coefficients for the mass spectrometer under the conditions to be used in the plasma experiment, and for the gases of particular interest in the program.

The cracking pattern experiments were carried out on the bakeable gas-handling system described in Sec. 3.3.2.6.1. The mass spectrometer head was mounted inside the oven and connected to the tube manifold section. A bakeable glass thermocouple gauge was added to the gas-filling flask section to insure that the pressure was kept below atmospheric when using high-pressure gas bottles.

The cracking pattern studies were delayed because of the necessity of replacing a defective magnet on the mass spectrometer, and in the limited time remaining a preliminary examination of the NO used in the chamber plasma studies was made.

3.3.3.8.1.1 Preliminary Studies of NO

The high pressure NO bottle, regulator, and needle valve were sealed to the gas-handling system through a glass to metal seal and the entire system pumped out. The mass spectrometer and gas-handling system, with the exception of the NO bottle, regulator and tubing joining the regulator to the system, were baked at 425° C for 8 hours. The pressure after bakeout was 1.3×10^{-7} Torr, which indicated that a considerable gas load was still present due to the regulator and connecting tubing. It was discovered after the bakeout that the pressure regulating diaphragm on the NO tank was defective, so that, upon opening the valve, the entire regulator came up to tank pressure. For safety reasons, it was decided that, rather than pressurize the gas flask side of the system and admit NO to the spectrometer through the variable leak, NO would be admitted to the system while the system was pumping. This was done by opening the type "C" valve between gas flask and vacuum system and allowing the NO to diffuse back through the 1" valve to the spectrometer, the pressure in the system being adjusted using the needle valve on the NO regulator.

Prior to admitting NO to the system, a background mass scan was taken on two sensitivity ranges of the mass spectrometer. The first range included the entire mass spectrums, and the second scan, at a factor of 30 greater in sensitivity, was taken to obtain the detail of the smaller mass peaks, during which the larger mass peaks were allowed to go off-scale. The NO was then admitted to the system and the pressure allowed to stabilize to 2.6×10^{-8} Torr, after which two additional mass scans were taken.

The results of the background mass scans and those with NO in the system are given in Table XVIII. The peak heights indicated are the mean values of the two scans, the mean being taken for those peaks which could be accurately determined on both scans. Those peaks which were off scale or quite small are single values only. The agreement between scans was found to be quite good, and the values are within $\pm 4\%$ in almost every case.

The third column in Table XVIII represents the difference when the peak heights due to the background scan are subtracted from those with NO in the system. Thus the difference in peaks should represent the contribution of NO and its impurities to the system. It will be noted that among the different peaks there are those which are negative. This indicates that there has been a change in the residual gas in the system during the time required for pressure stabilization of the system. These changes, in general, are rather small and do not hamper the analysis.

From Table XVIII the most prominent peak is seen to be mass 28, with a second significant peak at mass 14. This is contrary to what one would expect, since the system has been pressurized with NO (mass 30). The mass 28 peak is primarily due to N_2 , with possibly some small contribution by CO. It is believed that the prominence of the N_2 peak over the NO peak is caused by the fact that the gas was injected into the system at a point close to the pumping system and

TABLE XVIII

NO Mass Analysis and Peak Height Data(Gas Handling System Test)

MASS (A.M.U.)	MEAN BACKGROUND PEAK HEIGHT	MEAN PEAK HEIGHT WITH NO	DIFFERENCE PEAK HEIGHT
12	310.1	298.5	11.6
13	15.9	7.9	8.0
14	482.0	2439.0	1957.0
14.5	-	9.7	9.7
15	168.0	140.0	28.0
16	381.0	374.8	6.2
17	741.0	793.0	52.0
17.5	34.6	-	34.6
18	2638.0	2510.0	128.0
19	30.3	10.9	19.4
20	14.5	13.3	1.2
22	10.2	16.4	6.2
28	9511.0	24650.0	15139.0
29	107.4	225.3	117.9
30	19.4	1092.0	1072.6
32	52.7	92.7	40.0
34	2.5	-	2.5
35.3	2.6	-	2.6
36	11.0	-	11.0
37.4	12.1	-	12.1
38	9.9	-	9.9
40	32.2	33.4	1.2
44	162.1	283.7	121.6
55.5	12.7	6.1	6.6
76.5	1.7	-	1.7

allowed to diffuse back to the spectrometer. The relative pumping speed for N_2 is restricted to that provided by the diffusion pump, while the NO pumping speed is greater because of the liquid nitrogen cold trap, which freezes out the NO and has little or no effect on the N_2 . The result of this difference in pumping speed is that, in a system being continually fed a mixture of N_2 and NO, the N_2 will buildup in the system until the N_2 pumping speed is equal to that of NO. Thus a deceptively high N_2 concentration will result.

A second interesting feature of this mass scan is the presence of mass 44. The origin of this peak most probably is due to N_2O . The absence of any NO_2 ($M = 46$) may appear unusual, since NO_2 is known to be a common contaminant found in NO from the manufacturer of this sample. However, NO_2 has a lower vapor pressure than NO at LN₂ temperature, so that its pumping speed is even higher than that of NO.

It was found during data analysis that the resolution of the mass analyzer was rather poor. Steps were then taken to improve the resolution by carefully adjusting the various grid potentials in the ion source. Considerable trouble was encountered in accurately determining the mass of each of the peaks. This led to the modifications of the spectrometer discussed in Sec. 3.3.3.5. A detailed explanation of the mass determination problem is given in Sec. 3.3.3.7.1.2 below.

From the above, it is concluded that cracking pattern measurements should be done on the differential pumping system concurrent with pumping speed tests for each gas. It is important that these measurements be performed with carefully purified gas.

3.3.3.8.1.2 Improved Accuracy of Mass Determination

Preliminary studies with the mass spectrometer discussed above in Sec. 3.3.3.8.1.1 indicated that there were certain problems in the evaluation of the mass number for each peak. The solution of the equations of

motion of a charged particle of mass M accelerated by a voltage V and deflected by a fixed magnetic field give the solution

$$MV = K \quad (51)$$

where K is a constant. In order to evaluate the constant K , the first and most straightforward method is to assume that the accelerating voltage varies linearly with chart distance, as stated by the manufacturer. Using this assumption and two easily identifiable peaks on the mass scan (for example mass 14 and 28), K can be computed by solving two simultaneous equations $MV = K$ which give

$$V(14) - V(28) = K \left(\frac{1}{14} - \frac{1}{28} \right) \quad (52)$$

The difference voltage $V(14) - V(28)$ could be obtained by measuring the distance from mass 14 to mass 28 and using the manufacturer's calibration of 40 volts per inch. Having determined the value of K , it is then possible to compute the value of $V(28)$. The value of $V(28)$ provides a reference point from which the voltage of the other peaks, and thus the mass, can be determined.

Efforts to use this method for evaluating the value of K indicated that there were large errors present when determining the value of M for $M > 40$.

The voltage linearity of the mass spectrometer was then measured using a digital voltmeter (accuracy $\pm .001\%$). Using the dial indicator on the high voltage sweep potentiometer, the voltage was measured from 110 to 600 volts in 1 dial-division (approximately .8-volt) steps and from 600 volts to 1800 volts in 50-dial-division (approximately 40 volt) steps. Evaluation of these data shows the average voltage variation rate to be $40.81 \pm .254$ volts per inch.

Using the results of this voltage linearity check, a detailed error analysis was undertaken. The results of this analysis show that at mass 50 the error in M is $\pm .69$ and for mass 100 the error is ± 2.84 . This error, as can be seen above, still remains unacceptably large.

In order to avoid the relatively large errors involved in determining M by either of the above methods, an alternate approach was adopted. The spectrometer was modified to allow direct measurement of the accelerating voltage by means of an accurately constructed voltage divider and the digital voltmeter. The value of the accelerating voltage for mass 28 and mass 14 were measured and the constant K determined using (52). The dial setting of the high voltage potentiometer was also determined for each of these two mass peaks.

The voltage of peaks other than mass 28 were determined by measuring the distance from the unknown peak to the mass 28 peak, this distance was then converted to the number of dial units from the mass 28 peak, and the voltage determined from the data taken during the linearity test. This method allows determination of mass to within 1/2% for $M = 100$, and more accurately for lower mass numbers. In most cases it was found that the mass actually determined during data analysis was far more accurate than this. For this reason the values of M quoted below will be given in integral values only, except where large discrepancies occur.

3.3.3.8.2 Chamber Mass Spectrums

During the final series of probe curves (series IV), the gas in the chamber was subjected to mass analysis. Mass analysis was performed at both the start and end of each probe curve. Spectrometer and chamber background scans were also taken. In all cases, NO was admitted to the chamber through a dry ice/methanol cold trap, which helped reduce the contamination level in the NO.

Each mass analysis consisted of two scans, taken concurrently with the probe curve. The first scan, taken on the lowest sensitivity range of the spectrometer, shows the major mass peaks. The second scan, taken with a factor of 100 gain over the first scan, shows the fine detail of the mass spectrum, the larger peaks being off-scale. The results of one pair of these scans have been compiled into

a single table, Table XIX, giving the mass and peak heights. Adjustments to the data given in Table XIX have been made for pressure drift during the mass scan, and for some consistent discrepancy in peak height between the two scans. In order to facilitate examination of the data, the major constituents of the gas (greater than .1%) have been placed in a separate column and listed in percent of the total concentration. The minor constituents of the gas have been placed in a second column and are quoted in parts-per-million (PPM).

An examination of Table XIX shows that, as would be expected, the major constituent of the gas has a mass of 30 (NO). Extensive analysis of the data, however, is not possible since detailed "cracking pattern" data for purified NO, etc., are not available at this time. From an empirical point of view, one would expect that for pure NO ($M=30$) the spectrometer would yield the major peak at mass 30, with additional peaks at $M=16$ (O) and at $M=14$ (N) caused by cracking of the NO molecule. The presence of free N and O atoms and ions would also give rise to reactions with NO which produce NO_2 ($M=46$) and N_2O ($M=44$). These chemical or ion-induced reactions should, however, be second order effects. There also exists the possibility of finding the peaks of doubly ionized NO, NO_2 , and N_2O , which would appear at apparent mass numbers of 15, 23, and 22, respectively.

An examination of the data in Table XIX shows a relatively large concentration of mass 14 (6.38%). This probably is due principally to nitrogen arising from "cracked" NO, with some additional N arising from N_2 present as a contaminant in the NO, and from doubly ionized N_2 or doubly ionized CO (a common residual gas of mass 28). The mass 15 peak (doubly ionized NO) is also seen to be large (7.12%). The major contribution to this peak is probably due to doubly ionized NO.

The rather small O ($M=16$) peak (.72%) indicates that, if oxygen is being produced by cracking of NO, then it must be involved rather strongly in the

TABLE XIX**Chamber Mass Spectrum (Series IV Run 20, 21)**

MASS (A.M.U.)	PEAK HEIGHT	PERCENT CONCENTRATION	P.P.M. CONCENTRATION
12	120.7	.122	
13	5.70		57
14	6329.0	6.38	
15	7063.0	7.12	
15.46	25.82		260
16	714.8	.721	
17	95.0		958
18	301.9	.304	
19	5.58		56
20	11.76		119
22	33.62		339
23	4.00		40
24	2.12		21
25	5.33		54
26	24.36		246
27	38.0		383
28	9477.0	9.56	
29	96.36		971
30	73590.0	74.2	
31	266.7	.269	
32	339.9	.342	
33	2.00		20
33.46	1.58		16
34	2.12		21
35	2.12		21
37	1.76		18
38	1.70		17
39	4.55		46
40	24.36		246
41	5.15		52
42	6.00		60
43	2.91		29
44	578.2	.583	
45	7.03		71
46	2.66		27
52	2.73		27
60	1.64		16
71.37	1.52		15
77.38	1.52		15
78.42	3.15		32
79.25	1.64		16

reaction $\text{NO} + \text{O} \rightarrow \text{NO}_2$. If this were true, then a large NO_2 concentration should be seen. This is not found in the data ($\text{NO}_2 \approx 27\text{PPM}$). This implies that, assuming M=46 is the primary peak due to NO_2 , there is very little cracking of NO , or some other effect is removing the oxygen.

The large size (9.55%) of the mass 28 peak, which indicates the presence of an appreciable quantity of N_2 or CO (both M=28), is rather more difficult to understand. This same effect was also noted in the preliminary examination of NO performed on the gas-handling system, where the N_2 peak was by far the most prominent peak in the mass spectrum. It is suspected that a significant variation in pumping speed for NO and N_2 could give rise to this effect. This was discussed in Sec. 3.3.3.8.1.1.

Mass peak 31 is probably caused by NO with an isotope of nitrogen (N_{15}) or oxygen (O_{17}), while the mass 32 peak is primarily due to molecular oxygen. The size of the mass 44 peak (.58%) indicates rather large quantities of N_2O , while the mass 46 peak (27 PPM) indicates almost no NO_2 .

Approximately sixty mass scans were taken during probe measurements in the chamber. All of these scans were examined, and it was found that the scans with NO present showed no marked deviation from the typical result given in Table XIX. The background level of "cracked" hydrocarbon contaminants due to both mechanical pump oil and diffusion pump oil remained at a low level ($< 100\text{ ppm}$) and in approximately the same proportions to NO . A mass peak due to SO_2 (M=64) was looked for, since this is a possible contaminant arising from the production of the NO , as discussed in Sec. 3.3.3.7.3. A number of the mass scans showed a peak at M=64, but the height of the peak generally was very small and of the same order of magnitude as the noise level. This peak for one scan was definitely above the noise level ($\text{S/N} \sim 3$), but had the same height relative to the NO peak as those

where $S/N \sim 1$. From this it is felt that SO_2 was present in a concentration of not more than about 15 ppm.

3.3.3.8.3 Chemical Analysis of NO

The first bottle of NO, which was used in the bell jar feasibility tests (3.3.2.2), was purchased from the Matheson Company. It was produced using $NaNO_2 + H_2SO_4$, with $FeSO_4$ acting as a catalyst. This process gives rise to NO_2 and N_2 as contaminants. It is important to note that no N_2O or SO_2 are given off as contaminants in this process. The batch analysis for this specific bottle was not available from the Matheson company. The Matheson company reports that typical batch analysis of this gas shows no N_2O or SO_2 contamination. The sensitivity of their analysis is 1000 ppm.

The second bottle of NO purchased from the Matheson company was produced by a different process. This process involves the reaction of HNO_3 with SO_2 . At the end of the experimental program, this bottle of NO was returned to the Matheson company for analysis. Table XX gives the contamination found.

Table XX

<u>Contaminants in Matheson NO</u>	
N_2O	.54%
CO_2	.29%
NO_2	.62%
N_2	.65%
O_2	< 100 ppm
CO	< 100 ppm
SO_2	< 65 ppm

Comparison of these data with that taken with the mass spectrometer on the gas in the chamber shows that the NO_2 and CO_2 concentrations in the chamber are small compared to the concentration in the NO gas bottle. However, both NO_2 and CO_2 have a low vapor pressure at the dry ice/methanol trap temperature, so that they must have been frozen out before the gas reached the chamber. (The temperature of the dry ice/methanol mixture is at a temperature below the sublimation point of CO_2 alone). The N_2O concentration given by the mass spectrometer data (.58%) is in very close agreement with that found in the Matheson analysis (.54%). The vapor pressure of N_2O is in the order of 100 Torr at the trap temperature, and thus very little, if any, of the N_2O should be removed by the dry ice/methanol trap. The relatively large concentration (.65%) of N_2 given by the Matheson analysis could give rise to the large N_2 peak (9.55%) found by the mass analysis if there were a factor of 15 difference in the pumping speed for N_2 and NO due to the liquid nitrogen trap. This does not seem to be a completely unreasonable difference in pumping speed, since NO vapor is highly condensible at liquid nitrogen temperature.

The gas from the second bottle of Matheson NO was used in all of the probe measurements in the chamber, and also in the bell jar measurements reported in Sec. 3.3.3.7.3.2.

The NO manufactured by Air Products and Chemical Company was produced by reacting N_2O_4 with H_2O . A typical batch analysis of this gas made by Air Products shows the contamination given in Table XXI.

Table XXI

Contaminants in Air Products NO

A	60 ppm
N_2	.32%
N_2O	600 ppm
N_2O_4	trace (< 10 ppm)

NO_2 was not present in detectable quantities, and there should be no SO_2 impurity in this gas.

However, Matheson reports that Air Products has been buying large quantities of NO from them. This raises some question about whose NO gas is really present in the Air Products bottle used. Unfortunately, it has not been possible to obtain what can be regarded as a fully satisfactory answer on this point from Air Products.

3.3.3.8.4 Summary and Conclusions

Both the mass analysis and chemical analysis of the NO gas have indicated that N_2O is the most prominent contaminant in the chamber which is likely to act as a strong electron attacher.

The earliest probe data taken in the bell jar, using the first batch of NO supplied by the Matheson company, did not indicate the presence of a strong electron attaching agent. The process used to produce this NO does not give rise to N_2O or SO_2 , and within the sensitivity of the Matheson chemical analysis no N_2O was even found.

The second batch of NO supplied by the Matheson company, and that manufactured by Air Products and Chemical Company, both contained relatively large quantities of N_2O (.54% and 600 ppm respectively). All probe data taken using these gases show the effects of a strong electron attacher, as described in Sec. 3.3.3.7.

Further, N_2O is the only contaminant common to the second Matheson and Air Products gases but not present in the original Matheson NO.

The use of LiCO_2 or LiN_3 in the chamber cold trap (Sec. 3.3.3.7.3.3) did not change the nature of the probe data. But with LiCO_2 in the chamber cold trap there should be little NO_2 in the chamber, and with LiN_3 in the chamber cold trap both NO_2 and CO_2 should be reduced to negligible levels. Further, the mass spectrum data indicate that the dry ice/methanol trap in the NO-handling

system reduces the NO_2 concentration to the order of 10 ppm. However, none of these would have had much effect on the N_2O contamination levels. The N_2O level can only be reduced by very carefully controlled multiple distillation at about 85°K . Even then, the N_2O level would still be about 10 ppm.

Finally, SO_2 is present in such small quantities ($\approx 15 \text{ ppm}$) that it is doubtful that it is the culprit. It is thus concluded from the mass and chemical analyses that N_2O must be the attaching agent responsible for the anomalous probe curves.

A preferable procedure to purification of the NO by the distillation process mentioned above would be to obtain NO manufactured by the process used in producing the first sample used in the bell jar experiments discussed in Sec. 3.2.2.2. Efforts to obtain such a sample from the manufacturer have been unsuccessful, however.

3.3.3.9 Summary and Conclusions

A large volume plasma has been produced in the chamber by photoionization of nitric oxide. The probe results show that this plasma has positive ion densities, n_p , ranging between 4×10^4 and $2 \times 10^5 \text{ cm}^{-3}$ and electron densities lying between n_p and $n_p/10$. These measured densities are two to three orders of magnitude less than those predicted for pure NO by the theory of Sec. 3.2.1. The low positive ion densities, and electron densities below the positive ion density, suggest the presence of an electron attaching impurity which gives rise to negative ions. Both the mass and chemical analysis data show the presence of such an impurity in the form of N_2O in a concentration of 0.5%. The theory of Appendix B shows that the presence of N_2O in this concentration can quantitatively account for the observed decreased densities. N_2O was not present in the NO sample used in the first bell jar experiments (Series I), described in Sec. 3.2.2.2), which accounts for the difference between the data for Series I measurements and the rest of the probe data, and the agreement of the Series I data with the predictions of the theory of Sec. 3.2.1.

The probe curves taken with the N_2O impurity present show an anomalous behavior in the form of a "kink" near the origin. From Appendix B, the presence of N_2O changes the electron energy distribution to a two-peak non-Maxwellian form. From the probe theory of Sec. A2.3 of Appendix A, this accounts qualitatively for the observed anomalous behavior of the probe curves. The anomalous probe curves due to the N_2O contaminant preclude the determination of an electron temperature.

The Series I measurements gave apparent electron temperatures in the order of 5500°K . The comparison of the steady-state against the semi-swept methods of taking probe curves, as discussed in Sec. 3.3.3.7.3.3.2, indicates that the former method leads to apparent temperatures which are too high by a factor of about three. Hence, the Series I temperatures actually were in the order of 1800°K .

Thus the photoionization method of plasma production does indeed result in a rather cool plasma, as predicted theoretically.

Finally, some serious inadequacies of the experimental techniques employed have become apparent. These are the NO supply, pump oil vapor contamination, and the technique for taking probe curves. Foremost of these of course, is the contaminated NO supplied by the manufacturer. Further purification of the NO to reduce the N_2O concentration is mandatory before a realistic plasma can be produced and meaningful measurements made therein. Preferably, a manufacturing process should be employed which does not give rise to N_2O or SO_2 , such as the process used in the production of the first sample.

In addition to an improved NO supply, trapping should be installed in the mechanical pump line. Finally, a fast sweep technique should be employed in taking probe curves in order to prevent perturbations due to slow changes of the probe surfaces which take place as a function of the probe voltage.

4. MISCELLANEOUS VACUUM SERVICES

Under this topic, a number of miscellaneous services have been performed, such as the redesign and refurbishing of vacuum systems and components, tests of instruments and components in the high vacuum chamber, and design and construction of special types of discharge tubes. These are described and discussed below.

4.1 Portable 4-Inch Vacuum System

A portable high vacuum system was constructed and delivered to GSFC. This vacuum system consists of the following: A 4" oil diffusion pump, containing a water-cooled cold trap to decrease back-streaming, mounts to a 4" vacuum gate valve. The output side of the gate valve is bolted to an adaptor plate to which the bell jar and its adaptor will be mounted. The bell jar adaptor which was supplied by GSFC consists of a circular assembly 18" in diameter and 8" high. The lower portion of this adaptor mounts on the adaptor plate, while the bell jar sits on the upper edge. The vertical section contains 4 ports to which various feed-throughs may be attached.

The fore pump is a Welch mechanical pump. A thermocouple gauge and an ionization gauge and their controls are an integral part of the system. The thermocouple gauge is mounted directly below the bell jar adaptor and the ionization gauge mounts in one of the ports in the bell jar adaptor. A water-flow control shuts down the system in the event there is loss of water pressure. The system has pumped down to 3×10^{-6} Torr without the bell jar or its adaptor in place.

4.2 Vac-Ion System

The portable pumping system described above had originally been built for use in the low-temperature plasma studies. In order to allow these studies to continue, GSFC delivered to ERC a bell jar pumping system. The following work was necessary to recondition this system:

(a) The system was extremely dirty, with pools of diffusion pump oil collected in the lower portions of the system. Because of this, the total system was completely disassembled and thoroughly cleaned.

(b) Since the system contained no trap to prevent back-streaming of diffusion pump oil throughout the system, and since cleaning of the entire system is a large chore due to the complicated manifolding, ERC recommended to GSFC that the system be reassembled with a Vac-Ion pump instead of the oil diffusion pump. GSFC was agreeable to this procedure.

(c) The original system contained an ion generator, two ionization gauges, three thermocouple gauges and a 2" air-cooled oil diffusion pump (for the ion generator). The system was reassembled with only one ionization gauge and one thermocouple gauge.

(d) The motor for the bell jar lift system was inoperative and required a new armature.

(e) The roughing pump oil was extremely dirty. The pump was thoroughly cleaned and rebuilt by GSFC.

(f) The power supply for the Vac-Ion pump gave considerable difficulty. Upon several occasions while the system was pumping, for apparently no reason one leg of the bridge rectifier (solid state diodes) would fail. This occurred even after a current overload circuit was installed in the output line of the power supply. It appeared that the power transformer would intermittently short to its frame, putting double voltage on one leg of the bridge rectifier. No difficulty has been experienced since the transformer frame was insulated from ground. A Variac to control the voltage to the power supply was installed in the system. This allows control of pumping current and is helpful when the pump is first started and pumping currents are high.

When the system was completely reassembled with the bell jar on a bell jar

adaptor as described in the previous section, the system pumped down to a pressure of 5×10^{-6} Torr. The roughing pump was connected into the system as in the original arrangement. This places its foreline valve at the end of about 4 feet of 2-inch Sylphon tubing. With this arrangement, the Sylphon tubing remains in the high-vacuum portion of the system. The system was later altered so as to have the foreline valve mounted as close to the high vacuum portion of the system as possible. At this time a molecular sieve trap was added between the foreline valve and the mechanical pump. This trap prevents back diffusion of oil and water vapor from the mechanical pump and thus eliminates a troublesome source of contamination for both the ion gauge and the Vac-Ion pump. Vacuums of 2×10^{-6} Torr and better have since been produced.

After prolonged use of the vacuum system, the Vac-Ion pump began to develop short circuits in several of its pumping elements. These shorts are typical of ion pumps and are due to the formation of "whiskers" of sputtered titanium, or are due to the formation of scales of oxidized titanium. The pump was removed from the system and both the pump body and the elements were chemically cleaned in a hot potassium hydroxide solution followed by a hydrofluoric acid dip. After reassembly of the pumping system, there has been no reoccurrence of the shorting problem.

4.3 Portable 2- and 4-Inch Vacuum Systems

The vacuum system delivered to ERC by GSFC contained both a 2-inch and a 4-inch diffusion pump. These pumps were intended to become the nucleus of two portable pumping systems. The 2-inch pumping system, with its associated manifold valve, manifold, connectors, gauges, has been completed and tested. It was discovered during test that the manifold valve was defective and had to be returned to the manufacturer for replacement. The pumping system, without valve, finally was incorporated in the differential pumping system for the mass spectrometer

described in Sec. 3.3.3.5. Work on the 4-inch pumping system was deferred in favor of the plasma program, so that the components were returned to GSFC.

4.4 Outgassing Rate of a Fiberglass Rocket Body

The outgassing rate of a segment of a rocket body to be used in an experiment by GSFC was measured in the chamber at the request of the Technical Director. The sample was mounted in the chamber, and the system allowed to pump down to an equilibrium pressure of 1.4×10^{-6} Torr. The temperature of the chamber was then raised to 232°C . During the heating period there was a tremendous pressure rise, which required that the bake and diffusion pumps be turned off and the chamber cooled. The bake was again started and controlled at 125°C . The temperature then was slowly increased to 232°C . The equilibrium pressure at 232°C was 1×10^{-6} Torr. The bake was then turned off, and the chamber cooled.

The sample was removed from the chamber, and a second run was started with only the bare chamber. The pumping and baking schedule of the chamber was maintained the same as that used during the sample run.

A second sample run was made in order to see if the initial burst of gas in the first run was due to some initial surface condition of the sample, and whether it is possible to permanently outgas the sample. The results of this run indicate that there was no large gas burst upon initiation of the bake, and it was possible to increase the temperature steadily to 232°C , in contrast to the step-wise increase necessary in the first run. There was also an obvious decrease in the outgassing rate of the sample at 232°C .

Using the results of both the bare chamber run and the sample run it is possible to compute the outgassing rate of the sample.

The differential equation which governs pressure as a function of time is given by

$$-V(dp/dt) = Sp - \sum_1 A_1 Q_1$$

where V is the volume of the chamber in liters, $p = p(t, T)$ is the pressure in Torr, S is the pumping speed at the chamber in liters-sec⁻¹, A_i is the area in cm² of the i^{th} surface which outgasses at a rate $Q_i = Q_i(t, T)$ in Torr-liters-sec⁻¹-cm⁻².

This equation can be integrated and has the form

$$p = p_0 e^{-St/V} + V^{-1} e^{-St/V} \sum_i A_i \int_0^t e^{St/V} Q_i dt.$$

If it is assumed that the bare chamber pressure, p_B , is known as a function of time and temperature, then, substituting this into the previous equation, the equation for the pressure p_S for the chamber plus the sample, as a function of (t, T) , becomes

$$p_S = p_B + V^{-1} e^{-St/V} \int_0^t e^{St/V} Q_S(t, T) dt.$$

Thus, if some reasonable time dependence for Q_S is assumed, this equation can be integrated. Assuming that $Q_S = Q_S(t, T) = Q'_S(T) e^{-\mu t}$, where μ is some constant and $Q'_S(T)$ contains the temperature dependence of Q_S , this yields upon integration

$$p = p_B + [A_S Q'_S(T) (e^{-\mu t} - e^{-St/V}) / (S - \mu V)].$$

The pumping speed, S , at the chamber is given by

$$(1/S) = (1/G) + (1/S_p)$$

where S_p is the pumping speed at the pump (10,500 l/sec) and G is the conductance of the water and the liquid nitrogen baffles (5700 l/sec each)

$$1/G = (1/G_{\text{water}}) + (1/G_{\text{LN}_2}).$$

This gives $S = 2435$ l/sec. The volume of the chamber is 1000 liters so that the term $S/V = 2.435$ sec⁻¹, which is quite large. Thus the terms involving $e^{-St/V}$ approach zero very rapidly and may be dropped. Thus p_S is given by

$$p = p_B + [A_S Q'_S(T) e^{-\mu t} / (S - \mu V)].$$

In the case where $\mu t \ll 1$, this reduces to

$$p_s = p_B + [A_s Q'(T)/S]$$

and solving for $Q'(T)$,

$$Q'(T) = S(p_s - p_B)/A_s$$

Using the above equations, the peak outgassing rate of the sample as a function of temperature was computed from the data. The results are given in Table XXII.

Table XXII

Peak Outgassing Rate of Fiberglas Rocket Section as a Function of Temperature

<u>Torr-liters-sec⁻¹-cm⁻²</u>	<u>T °C</u>
4.86×10^{-7}	25
8.7×10^{-6}	125
1.73×10^{-5}	150
3.41×10^{-5}	175
3.84×10^{-5}	200
5.41×10^{-5}	232
3.52×10^{-7} upon return to	25

The outgassing rates for the rocket section given in Table XXII can be compared with those for typical metals in Table XXIII, taken from Das [33].

Table XXIII

Peak Outgassing Rates for Some Typical Metals

(Torr-liters-sec⁻¹-cm⁻²)

<u>Metal</u>	<u>25° C</u>	<u>200° C</u>	<u>Return to 25° C</u>
1020 mild steel	1.7×10^{-9}	7.0×10^{-7}	4.5×10^{-11}
6061-T6 aluminum	2.8×10^{-9}	2.0×10^{-8}	4.4×10^{-10}
304 stainless steel	5.3×10^{-10}	3.3×10^{-8}	1.7×10^{-10}

The sample was allowed to remain at 232°C for an extended length of time, and at this temperature the outgassing rate has the form of a very slowly varying exponential

$$Q = Q_0 e^{-\mu t}$$

where μ was found to be $1.02 \times 10^{-4} \text{ sec}^{-1}$.

A comparison of the outgassing rate measurements for Runs 1 and 2 is shown in Table XXIV. This shows a reduction in the outgassing at 232°C , by a factor of 2.8 during the second run. The second run was made after the rocket section had been exposed to the atmosphere for 10 days. It was found that the tremendous pressure rise in the first run during the initial heating (where the outgassing rate was in excess of $5.41 \times 10^{-4} \text{ Torr-liters-sec}^{-1}\text{-cm}^2$), was not found in the second run. These results indicate the outgassing rate of the fiberglass can be permanently reduced by a factor of more than 10 by pumping and heating. This is due to removal of grease and water vapor which has been absorbed by the surface during manufacture and handling. The overall reduction of the outgassing rate after this initial cleamp is not considered to be significant, since subsequent baking and pumping yield very little additional reduction in Q_0 .

Table XXIV

Comparison of Outgassing Rates of Fiberglass Rocket
Section Between Runs 1 and 2 (ten day exposure)

(Torr-liters-sec $^{-1}$ -cm 2)

$Q_0 \rightarrow$	<u>at 25°C</u>	<u>at 232°C</u>	<u>Return to 25°C</u>
Run 1	4.86×10^{-7}	5.41×10^{-5}	3.52×10^{-7}
Run 2	2.08×10^{-8}	1.95×10^{-5}	2.27×10^{-7}

The mass spectrometer was used before and after each bake on both the bare chamber and the fiberglass rocket body sample. The mass scans on the bare chamber were subtracted from the mass scans on the sample to remove the contribution from the chamber. Significant differences were chosen as those whose heights were more than 0.5% of the total of all the differences. These differences, which are roughly proportional to the partial pressure of a given gas component contributed by the sample, have been plotted versus mass number in Fig. 107.

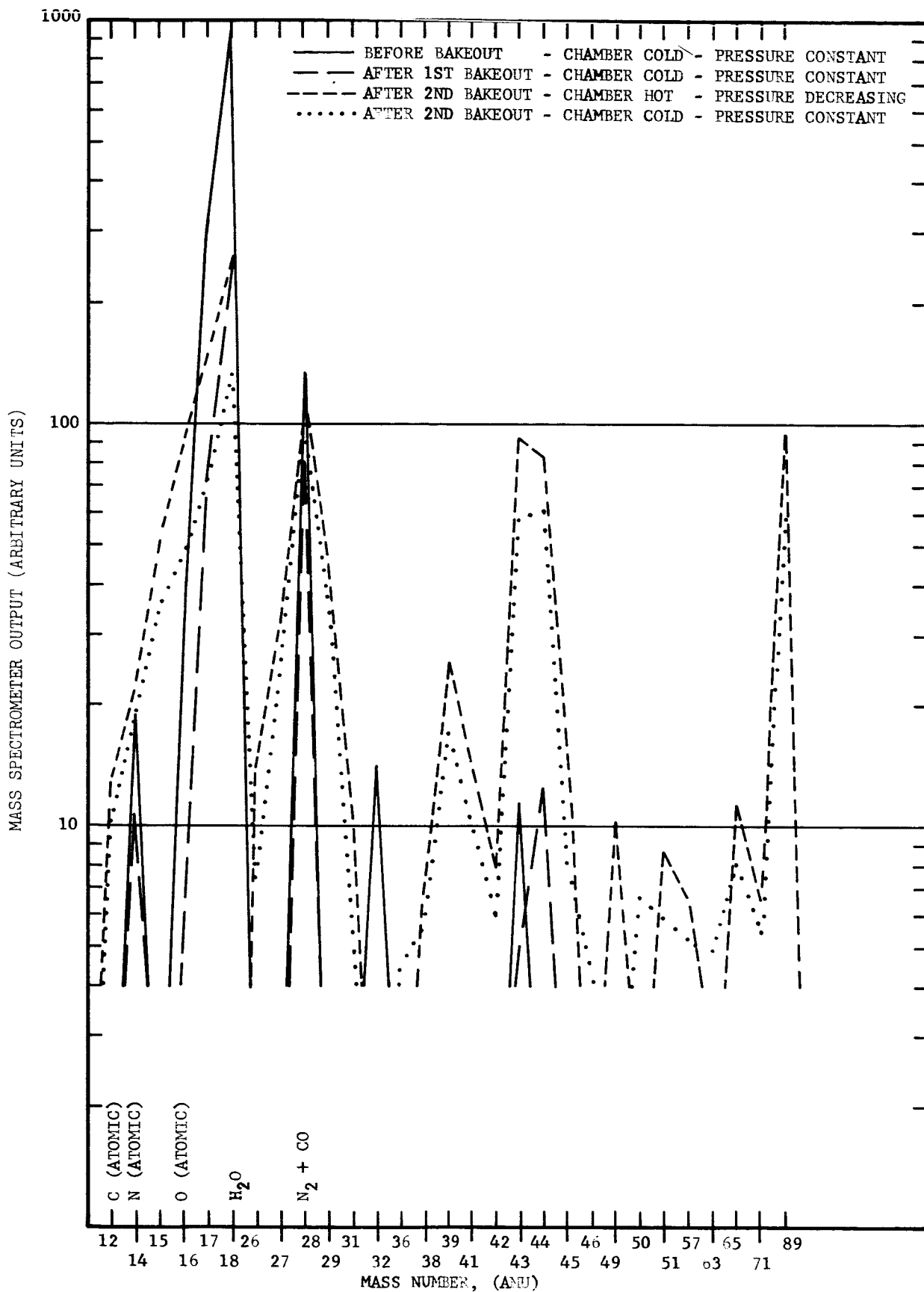


FIG. 107 PARTIAL PRESSURE VS MASS NUMBER DUE TO FIBERGLAS MISSILE SECTION OUTGASSING

It can be seen that the largest peak before bakeout occurs at mass 18, the water vapor peak. The large peak at mass 28 represents the sum of N_2 and CO. The peak at mass 14 represents atomic nitrogen, while those at 12 and 16 indicate the presence of atomic carbon and atomic oxygen respectively. The exact amount of masses 12, 14, and 16 depends upon the cracking pattern of N_2 and CO. There may be a contribution at these peaks due to fragments of large organic molecules which have been decomposed by the hot tungsten filaments in the mass spectrometer and the ion gauge. The evidence of cracking of large organic molecules can be seen in the mass spectrum after the bake, where there are a large number of peaks in the mass range above mass 30. This is indicative of a decomposition of large "organic" molecules. The large peak at mass 89 may be the parent molecule of many of those mass peaks found in the lower mass range, or may be due to cracking of a molecule whose mass exceeds 100, the upper limit of the spectrometer.

The occurrence of the large mass peaks after bakeout is indicative of a slight chemical breakdown of either the fiberglass or the epoxy used to seal the fiberglass to the aluminum rings. Examination of the sample before and after bake showed that there was a very slight color change in the fiberglass. The epoxy used to seal the fiberglass to the aluminum ring changed in color from white to brown. This change in color may indicate the origin of the large mass molecules observed after bake.

The percentage concentration of the residual gas after each step is shown in Fig. 108. Here, again, it is obvious that large mass number molecules are more numerous after bake, while water vapor, which before bake was the most dominant of the residual gases, shows a marked decrease in concentration.

4.5 Ion Trap Test

At the request of GSFC, vacuum services were provided for the calibration of an ion-electron source and sensor assembly built for a rocket experiment. The apparatus was attached to the small portable 4-inch vacuum system by a glass

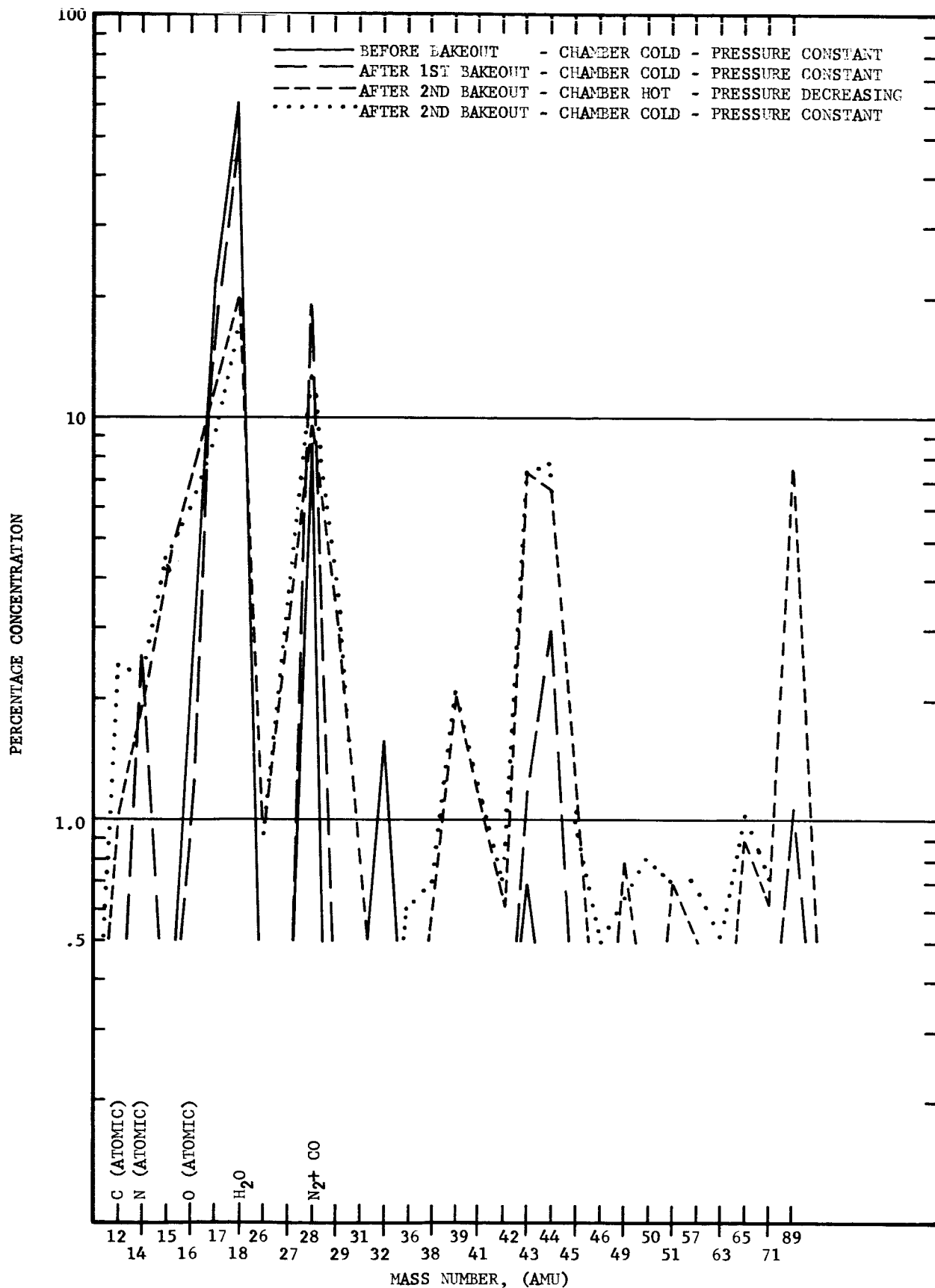


FIG. 108 PERCENTAGE CONCENTRATION VS MASS NUMBER DUE TO FIBERGLAS MISSILE SECTION OUTGASSING

tubulation. An initial pumpdown leveled off at 5×10^{-6} Torr. By the use of acetone, it was found that the ion trap had several leaks. Consequently, it was decided to transfer the experiment to the large vacuum chamber so that the entire instrument could be immersed in a low-pressure medium. The chamber was evacuated to 2×10^{-7} Torr, and calibration measurements were performed. After the necessary measurements at 2×10^{-7} Torr were completed, the pressure was raised to 1×10^{-6} Torr by admitting helium to the chamber, and the series of measurements was repeated at this pressure.

4.6 Bell Jar Lift System

A motor-driven bell jar lift system was installed on a vacuum system for GSFC. The system consisted of a high-vacuum pumping station in which the evacuation chamber was an 18-inch bell jar. The necessary mechanical design was made, the required modifications to the station were installed, and the completed system was returned to GSFC.

4.7 Tube Fabrication Services

Two special Mercury discharge tubes were designed for GSFC on a priority basis. Both tubes were completed and delivered. The second tube was an improved and somewhat more elaborate version of the first.

5. SUMMARY, CONCLUSIONS AND RECOMMENDATIONS

5.1 Summary and Conclusions

An experimental investigation of the behavior of an r-f capacitance probe has shown that the expected decrease in capacitance upon immersion in a plasma may not always be found. Due to the formation of ion sheaths around the electrodes and the effective conductivity due to collisions at higher pressures, the effective separation between the plates may decrease in a plasma, with a resulting increase in capacitance. Consequently, in the use of this type of probe, compensation or allowance for the effects of sheath formation is required.

A program for D-region simulation in the large high-vacuum chamber installed at ERC has been carried out. For this purpose, the process of ultraviolet (UV) photoionization of ND around the Lyman- α line was studied both theoretically and experimentally, with the goal of producing a low-temperature plasma in the chamber.

Before proceeding with the simulation program on a large scale, a feasibility study program was carried out. It consisted first of a theoretical study, in which the required photon flux was calculated, taking into account the various loss processes which are operative. This showed that a photon flux of 10^{14} to 10^{15} photons-cm⁻²-sec⁻¹ is sufficient to generate electron densities suitable for D-region simulation, and that the electron temperature should be that of the gas for pressures of 10^{-1} Torr or greater. Furthermore, it was shown that a somewhat lower electron temperature should be obtainable with a krypton UV-tube than with a hydrogen tube.

The theoretical study was followed by an experimental feasibility study to demonstrate that UV sources with large enough efficiency and photon flux to meet the requirements could be produced. Several tubes of new design were built and the effects of tube geometry and gas filling were investigated. Krypton was found to yield a higher efficiency and output than hydrogen or hydrogen-neon combinations

for the gas filling. UV outputs one to two orders of magnitude higher than the output of a commercially available UV tube were obtained. Output and efficiency were well above the minimum values determined from the theoretical study.

Finally, a plasma of approximately the desired characteristics was generated by photoionization of ND in a bell jar, and ionization densities and electron temperatures of the expected order were obtained, using double probes to measure the plasma characteristics. Electron densities around 10^7 cm^{-3} and electron temperatures around 1800° K were obtained. Thus the photoionization method of plasma production does result in a rather cool plasma, as predicted theoretically.

Following the successful demonstration that UV-tubes of the requisite output and efficiency could be built, a program to develop a large-volume low-temperature plasma in the chamber was undertaken. From the various basic tube designs investigated in the feasibility study program, a design was chosen which would allow a number of tubes to be packed fairly closely in a bank mounted on the chamber. A number of these tubes were constructed and their characteristics measured. This program resulted in UV-tubes which adequately meet the requirements for producing a large-volume plasma, yielding flux levels up to 10^{15} photons sec^{-1} per tube. The tube geometry is compact, lending itself to close packing in a bank of tubes to increase the UV beam area. The tubes were proved by life tests and subsequent operation to have exceptional stability and reliability, and long life. In addition, large photon detectors for these tubes were constructed.

The final part of the program was devoted to the development of a large-volume plasma in the chamber, using the tubes developed under the program. Unexpectedly, the probe curves obtained were of unusual shape, being wholly unlike those obtained in the bell jar during the feasibility study program. A repeat of the measurements in the bell jar also gave anomalous probe curves. This was finally traced to the fact that in the later measurements a different sample of ND was used, which was

manufactured by a completely different process from the first sample, although obtained from the same manufacturer. Mass analysis of the second sample in the chamber, using a differential pumping system which was assembled as an adjunct to the chamber mass spectrometer, showed N_2O as an impurity, with a concentration of 0.5%. Analysis shows that N_2O acts as a very effective electron attaching agent, producing negative ions, as well as distorting the electron energy distribution. As a result, positive ion and electron densities obtained are two to three orders of magnitude below those expected, and obtained in the bell jar measurements with the first (uncontaminated) sample of NO. Also, the distortion of the probe curves due to the distorted electron energy distribution resulting from the N_2O contamination precludes the determination of an electron temperature. Thus this type of impurity must be kept to a very low level.

During the experimental program, some inadequacies of the experimental techniques employed became apparent. It was found that a film was produced on the lithium fluoride windows as a result of photolysis of residual pump vapors by the radiation from the UV-tubes. This film could be removed either by wiping with methanol, or by overnight pumping with the UV-beam turned off.

In addition, it was found that taking probe curves by the point-by-point method was subject to error due to slow changes of the probe surfaces (presumably the formation of surface layers) as a function of probe voltage. This results in probe I-V curves of reduced slope, and apparent increased electron temperatures as a result thereof.

5.2 Recommendations

As a result of the difficulties encountered in the program, certain improvements should be made in the experimental techniques. These are in the NO supply, pump oil vapor contamination, and the technique for taking probe curves. The most important item requiring improvement is the contaminated NO

supplied by the manufacturer. Further purification of the NO to reduce the N_2O concentration is mandatory before a desired type of plasma can be produced and meaningful measurements made therein. Preferably, a manufacturing process should be employed which does not give rise to N_2O or SO_2 , such as the process used in the production of the first sample of NO.

In addition to an improved NO supply, trapping should be installed in the mechanical pump line. Finally, a fast sweep technique should be employed in taking probe curves in order to prevent perturbations due to slow changes of the probe surfaces which take place as a function of the probe voltage.

APPENDIX A

PROBE THEORY

A1. INTRODUCTION

In this Appendix, theoretical relations are presented for the current-voltage characteristics of the types of probes employed in the measurement program. Thus, cylindrical probes are considered exclusively. An attempt has been made to extend the usual probe theory to a wider variety of conditions and situations than normally considered. This includes the effect of collisions, negative ions, and a non-Maxwellian distribution of electron velocities.

A2. DOUBLE PROBE THEORY

A generalized theory for the double probe that will cover all of the conditions encountered experimentally is needed. To obtain the basis for such a theory, consider the basic double-probe circuit shown in Fig. A1. The probe system is isolated; thus, probes 1 and 2 are at some potential, $-V_1$ and $-V_2$, respectively, with respect to the plasma. Potential V_c accounts for contact potentials and a possible difference in potential between the plasma immediately surrounding the two probes; V_d is the potential applied between the probes. Probe 1 has a positive ion current, i_{p1} , and an electron current, i_{e1} , flowing to it from the plasma. Similarly, a positive ion current, i_{p2} , and an electron current, i_{e2} , flow to probe 2. Then, with the sign convention indicated in Fig. A1,

$$i_d = i_{p1} - i_{e1} = i_{e2} - i_{p2} \quad (A1)$$

$$V_d = V_1 + V_c - V_2. \quad (A2)$$

It is implicitly assumed here that the probes are sufficiently far apart to prevent their sheaths from overlapping.

A relationship between the observed I-V characteristic of the probes and the plasma properties is needed for the conditions of interest. This requires the development of relationships for i_{p1} , i_{p2} , i_{e1} , and i_{e2} in terms of V_d and the plasma properties. Substitution of these relationships into (A1) and (A2) then will allow plasma densities and temperatures to be determined from the observed probe I-V characteristics. However, these relationships are dependent on a number of parameters and conditions of the plasma. Thus it will be necessary to consider separately the various factors which influence the results.

A2.1 Maxwellian Velocity Distribution and NO Negative Ions

The theory is considerably simplified if the plasma consists solely of electrons and positive ions, each of which has a Maxwellian distribution of velocities. Using the term "ion" to denote a (singly) charged particle of either

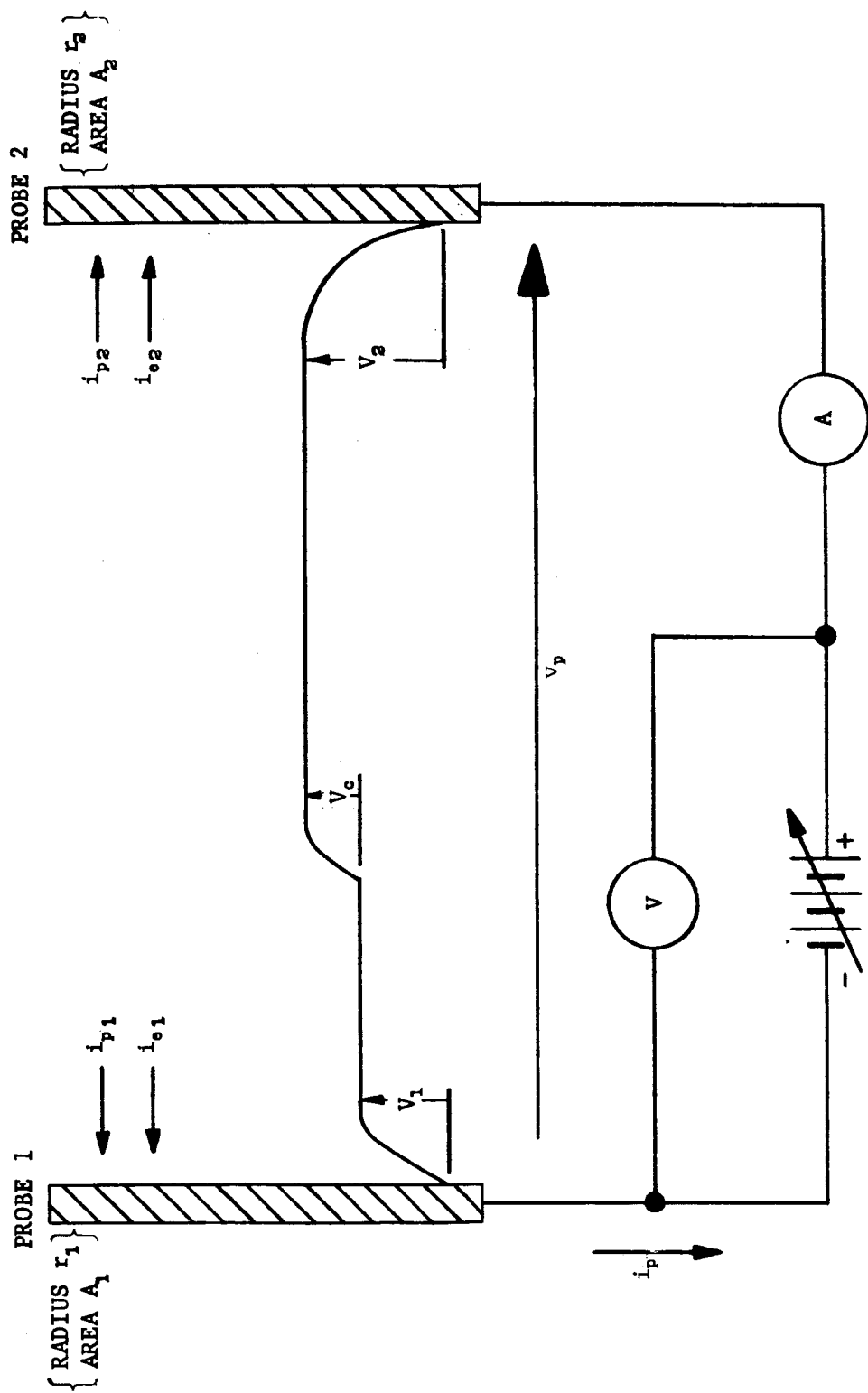


FIG. A1 BASIC DOUBLE PROBE CIRCUIT

species, the random ion current density in a field-free region then is given by [27]

$$j_0 = \frac{1}{4} n \bar{v} e = e \sqrt{\frac{kT}{2\pi m}} n \quad (A3)$$

where, for a particular species, n is the ion density, \bar{v} is the average velocity, e is the charge, m is the mass, and T is the temperature in $^{\circ}\text{K}$. Langmuir and Mott-Smith (LMS) [27], [28] further show that, in a retarding field where the potential is V , the random current density is

$$j = j_0 e^{-\frac{eV}{kT}} \quad (A4)$$

(Note that for electrons, for which e is negative, a negative potential V is required for a retarding field; conversely, for positive charges a positive potential is required for retardation.) The ion current to a body charged to a retarding potential then is

$$i = A j_0 \quad (A5)$$

where A is the surface area of the body, and j is given by (A4).

From (A3), the random electron current density is greater than the random positive ion current density by the factor

$$\sqrt{\frac{m_p T_e}{m_e T_p}} \frac{m_e}{m_p} \quad (A6)$$

where the subscripts e and p refer to electrons and positive ions, respectively. Thus, from (A4) and (A6), an isolated body in a plasma will become sufficiently negatively charged to floating potential, V_f , with respect to the plasma to reduce the random electron current to a value equal to the random ion current, by forming a positive ion sheath about the body. Hence, if $V_d = 0$, the electrodes are at potentials $-V_1$ and $-V_2$, respectively, with respect to the plasma.

To find the magnitude of floating potential V_f , it is noted that the floating potential represents an attractive field for the positive ions. Its presence will increase the random ion current by some factor, f , over the value, Aj_{0p} , for the

random ion current to the body without the field. The factor, f , in general, will be a function of the potential V_f , its relative range a/r (where a is the sheath radius and r the probe radius), and the ion temperature, T_p . Thus, the random ion current in an attractive field to a body at potential V with respect to its surroundings is

$$i_p = j_{op} A f(a/r, V, T_p). \quad (A7)$$

Equating electron and ion currents as given by (A3), (A4), (A5), and (A7) gives

$$V_f = -[kT_e/2e] \ln \{ (m_e T_p / m_p T_e) f^2 \}. \quad (A8)$$

Since f , in general, is a function of V_f , (A8), in general, is a transcendental equation for V_f . However, if the body is a plane surface, or if a/r is sufficiently close to unity, $f = 1$ and (A8) reduces to the usual simple expression for V_f .

(A3), (A4), (A5), and (A7) give the desired expressions for i_{p1} , i_{p2} , i_{e1} , and i_{e2} , if neither V_1 or V_2 becomes negative. In this case, combining (A1), (A3), (A4), (A5), and (A7) gives

$$i_d = j_{op1} A f_{1p} - j_{oe1} A_1 e^{-\eta_{1e}} \quad (A9)$$

and

$$i_d = j_{oe2} A_2 e^{-\eta_{2e}} - j_{op2} A_2 f_{2p} \quad (A10)$$

where

$$\eta = \phi V \quad (A11)$$

$$\phi = \frac{e}{kT}. \quad (A12)$$

If f is an increasing function of V , and if V_1 (or V_2) is sufficiently large, the electron current to that electrode becomes small enough that it may be neglected relative to the ion current and

$$i_d \approx j_{op1} A_1 f_{1p}, \quad V_1 \gg |V_{p1}| \quad (A13)$$

$$i_d \approx -j_{op2} A_2 f_{2p}, \quad V_2 \gg |V_{p2}| \quad (A14)$$

These are the desired general equations for the behavior of the I-V characteristic in the saturation regions.

The behavior of V_2 for saturation current to probe 1 and the behavior of V_1 for saturation current to probe 2 will now be investigated. For saturation current to probe 1, (A13) and (A10) are combined with the result:

$$\exp[-\phi_{2e} V_2] = (j_{0e2} / j_{0e1}) f_{2p} + (A_1 / A_2) (j_{0p1} / j_{0e2}) f_{1p}, \quad V_1 \gg |V_{p1}|. \quad (A15)$$

Similarly, for saturation current to probe 2, (A14) and (A9) are combined:

$$\exp[-\phi_{1e} V_1] = (j_{0p1} / j_{0e1}) f_{1p} + (A_2 / A_1) (j_{0p2} / j_{0e1}) f_{2p}, \quad V_2 \gg |V_{p2}|. \quad (A16)$$

From (A15) and (A2), if f_{1p} and f_{2p} are slowly varying functions of V_1 and V_2 , then for saturation current to probe 1, V_2 is a constant to terms of first order for a small range of variation of V_1 , and V_1 is a linear function of V_d . For large enough V_d , V_1 is essentially equal to V_d . Similarly, for saturation current to probe 2, V_1 is a constant to terms of first order for a small range of variation of V_2 , V_2 is a linear function of V_d , and for large enough V_d , V_2 is essentially equal to V_d . Further, examination of (A15) shows that, if the properties of the plasma in the regions of the two probes are similar, and if f_{1p} and f_{2p} are nearly unity,* then A_1/A_2 must be greater than 40 (235 for NO) for V_2 to become negative (probe 2 positive with respect to the plasma). If $A_1 = A_2$, the ratio of the plasma densities at the two probes must be 40 or more for V_2 to become negative (probe 1 positive with respect to the plasma). Since, in a double probe, A_1 is of the same order of magnitude as A_2 , and the densities at the probes generally are about the same, neither of the probes should go positive with respect to the plasma.

To proceed farther, it is necessary to investigate the nature of the function f .

*

An investigation of the detailed nature of f shows that it will indeed lie between 1 and 10 for most cases of interest.

The theory of double probes developed by Johnson and Malter (JM) [16], the inventors of this type of probe, assumes that the probe current in the saturation regions of the I-V characteristic is space charge limited, and that all ions crossing the sheath are captured. Thus, the saturation current is independent of probe voltage and equal to the random ion current density in the plasma multiplied by the sheath area. This is equivalent to assuming that $a/r \sim 1$, where a is the sheath radius and r is the probe radius.

When the plasma is weakly ionized (the case of interest in the present program), it is not necessarily true that $a/r \sim 1$. In fact, generally $a/r \gg 1$, and some ions crossing the sheath in an attractive field are not captured by the probe [27, 28]. Many ions undergo hyperbolic orbits if their impact parameter, s , and/or their energy is large enough. This situation is depicted in Fig. A2.

Further, in this situation three conditions may be distinguished:

- 1) $\lambda_p \gg a$
- 2) $\lambda_p \sim a$
- 3) $\lambda_p \ll a$

where λ_p is the mean free path of the positive ions in the sheath.

A2.1.1 No Collisions in the Sheath ($\lambda_p \gg a$)

For no collisions in the sheath, IMS integrate over the momentums that allow particles to have orbits that result in capture. They find for a cylinder:

$$f = \left(\frac{a}{r}\right) \operatorname{erf}(\sqrt{\xi}) + e^{\eta} [1 - \operatorname{erf}(\sqrt{\eta + \xi})] \quad (\text{A17})$$

where

$$\xi = [r^2/(a^2 - r^2)]\eta = s^2\beta^2\eta, \quad (\text{A18})$$

$$\eta + \xi = [a^2/(a^2 - r^2)]\eta = \beta^2\eta, \quad (\text{A19})$$

$$s = r/a, \quad (\text{A20})$$

$$\beta = [1 - (r/a)^2]^{-1/2}, \quad (\text{A21})$$

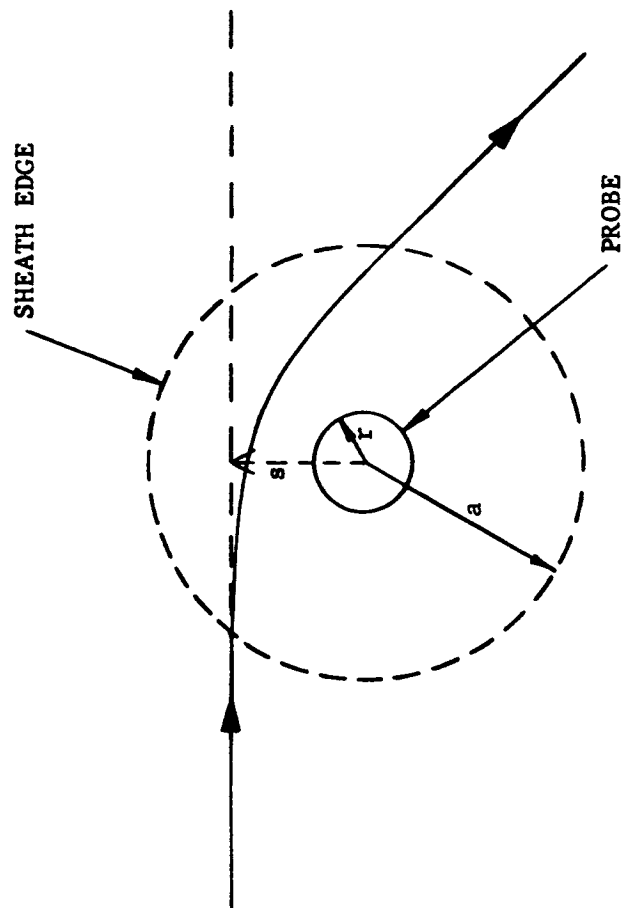


FIG. A2 THE PATH OF A CHARGED PARTICLE PASSING THROUGH A SHEATH SURROUNDING
A CYLINDER OR SPHERE (ATTRACTIVE POTENTIAL, PARABOLIC ORBIT)

$$\begin{aligned} \operatorname{erf}(x) &= \frac{2}{\sqrt{\pi}} \int_0^x e^{-y^2} dy \\ &= \frac{2}{\sqrt{\pi}} \sum_{k=0}^{\infty} (-1)^k \frac{x^{2k+1}}{k!(2k+1)}. \end{aligned} \quad (\text{A22})$$

Although LMS have investigated the behavior of (A17) under various limiting conditions, it is necessary to reproduce much of their work to obtain needed expressions.

There are two limiting cases of (A17). These are:

- 1) $a/r \sim 1$,
- 2) $a/r \gg 1$.

When $a/r \sim 1$, ξ is large, and LMS show that for large η

$$f \rightarrow \frac{a}{r} \rightarrow 1$$

and

$$L = A_s f_0 \rightarrow A f_0$$

where A_s is the surface area of the sheath. Then, except for second order sheath growth effects, i_{p1} and i_{p2} are sensibly constant and the double probe theory of JM applies.

When $a/r \gg 1$, the following procedure may be used: The asymptotic expansion of $\operatorname{erf}(x)$ for large x is

$$[1 - \operatorname{erf}(x)] = \frac{2}{\sqrt{\pi}} \left(\frac{e^{-x^2}}{2x} \right) \sum_{k=0}^s (-1)^k \frac{(2k)!}{2^k k!} (2x^2)^{-k} \quad (\text{A23})$$

where $s + 1$ is the number of useful terms in the asymptotic expansion. The asymptotic expansion of (A23) is good to 10% for $X = 2$ and $1\frac{1}{2}\%$ for $X = 2.5$.

Substitution of the series expansion (A22) for $\operatorname{erf} \sqrt{\xi}$ and the asymptotic expansion (A23) for $1 - \operatorname{erf} \sqrt{\eta + \xi}$ into (A17) then gives

$$f = \frac{2}{\sqrt{\pi}} \beta \sqrt{\eta} \left\{ 1 + (\alpha^2 \beta^2 \eta / \xi) + O[(\alpha^4 \beta^4 \eta)^2] + [1 - \alpha^2 \beta^2 \eta + O[(\alpha^2 \beta^2 \eta)^2]] [(2\beta^2 \eta)^{-1} + O[(2\beta^2 \eta)^{-2}]] \right\}. \quad (\text{A24})$$

For $a/r \gg 1$, i.e. $\alpha^2 = O(10^{-2})$, and $\alpha = O(\eta^{-1})$, which imply that $\eta^{-2} \ll 1$, $(\alpha^2 \eta)^2 = O(\alpha^2)$, and $\beta = 1$, (A24) reduces to

$$f = \frac{2}{\sqrt{\pi}} \beta \sqrt{\eta} \left\{ 1 + \frac{1}{2\eta} - \frac{1}{3} \alpha^2 \eta + O[\alpha^2] \right\} \quad (\text{A25})$$

which is the fundamental result for the limiting case at hand.

It is now noted that the first three terms in $\{ \}$ in (A25) are identical with the first three terms of the expansion of $\sqrt{1+x}$ with $x = (1/\eta) = (r/a)^2 \eta$. Thus, for η sufficiently large that terms of order η^{-2} may be neglected, and if $(r/a)^2$ is small enough that terms of order $[(r/a)^2 \eta]^2$ may be neglected, then (A25) reduces to

$$f = \frac{2}{\sqrt{\pi}} \sqrt{1+\eta - \frac{2}{3} \left(\frac{r}{a}\right)^2 \eta^2}, \quad (\text{A26})$$

This is the same as (32) in LMS. At this point LMS assume that the term involving $(r/a)^2 \eta^2$ may be neglected with respect to $(1+\eta)$ if $(a/r)^2$ is sufficiently large. However, as will be seen, this leads to an erroneous result in some important circumstances.

Instead, it is noted that there exist three possible and fundamentally different cases for (A26) as a result of the fact that the sheath dimensions may be voltage dependent. These are:

- 1) (r/a) independent of η : then sheath dimensions are voltage independent.
- 2) $r/a \propto \eta^{-1/2}$; then $(r/a)^2 \eta^2 = \text{constant}$.
- 3) $(r/a) \propto \eta^{-1/2}$; then $(r/a)^2 \eta^2 = \text{constant } \eta$.

A2.1.1.1 (r/a) Independent of η

For (r/a) independent of η , the arguments of LMS are valid. If (a/r) is sufficiently large, (A26) reduces to

$$f = \left(\frac{2}{\sqrt{\pi}}\right) \sqrt{1+\eta}; \quad \begin{cases} \eta \text{ large} \\ (r/a)^2 \eta^2 \ll \eta \\ (r/a) \text{ independent of } \eta \end{cases} \quad (\text{A27})$$

Inserting (A27) into (A13) and (A14),

$$I_d = f_{0P_1} A_1 (2/\sqrt{\pi}) \sqrt{1+\eta_{P_1}} \quad (A28)$$

$$I_d = -f_{0P_2} A_2 (2/\sqrt{\pi}) \sqrt{1+\eta_{P_2}} \quad (A29)$$

These both have the form

$$I_d^2 = B + S V$$

where,

$$S_{1,2} = (4 A_{1,2}^2 f_{0P_{1,2}}^2 e) / (\pi k T_{P_{1,2}}) \quad (A30)$$

$$B_{1,2} = 4 f_{0P_{1,2}}^2 A_{1,2}^2 / \pi \quad (A31)$$

Over some portion of the saturation regions, plots of the square of the observed current against the potential (V_1 or V_2) relative to the plasma are straight lines, with slopes S_1 and S_2 , respectively, as given by (A30). The intercepts of these straight lines with the V axis occur at

$$V_{1,2} = -(\frac{1}{2} \phi_{P_{1,2}}) = -T_{P_{1,2}} / 11,600 \text{ volts} . \quad (A32)$$

Making use of (A3) and solving (A30) for $n_{P_{1,2}}$ gives

$$\eta_{P_{1,2}} = \frac{\pi}{\sqrt{2e/m_p}} \frac{\sqrt{S_{1,2}}}{A_{1,2}e} = 3.32 \times 10^4 (\sqrt{S_{1,2}} / A) \sqrt{m_p/m_e} \quad (A33)$$

where \sqrt{S} is expressed in amp-volt $^{-1/2}$.

But, it is V_d , and not V_1 or V_2 , which is known. However, since, from (A27), f is a rather slowly varying function of η , and hence of V_1 or V_2 , the earlier argument that V_2 is a constant (with value V_{2s}), to first order, for saturation of probe 1 is valid. Thus,

$$V_1 = (V_{2s} - V_c) + V_d \text{ (saturation of probe 1)} \quad (A34)$$

and

$$V_s = (V_{1s} + V_c) - V_d \text{ (saturation to probe 2)}$$

Hence, where the quantities in parentheses may be regarded as constants, to first order in the saturation regions, i_d^2 vs. V_d yields straight lines with the same slopes as plots of i_d^2 vs. V_1 or V_2 . The intercepts of the i_d^2 vs. V_d plots, however, will be shifted to

$$V_{d1,2} = \mp (1/\phi_{p1,2}) \mp V_c \mp V_{2,1s} \quad (A35)$$

Since V_{1s} and V_{2s} are not known, the ion temperature cannot be found from the intercepts (in contrast to the situation of LMS). However, if the ion densities and temperatures are the same in the regions near both of the probes, $V_{1s} = V_{2s}$ and the contact potential, V_c , can be found by adding V_{d1} and V_{d2} in (A35).

It should be noted that each intercept occurs on the opposite side of the i_d^2 axis from the saturation region whose slope is being extrapolated.

$$\begin{aligned} \text{A2.1.1.2 } (r/a) &\propto \pi^{-1} \\ \text{For } (r/a) &\propto \pi^{-1}, \\ 2/3 (r/a)^2 \pi^2 &= C \end{aligned}$$

so that (A26) becomes

$$f = (2/\sqrt{\pi}) \sqrt{1-C+\eta} \quad (A36)$$

Inserting (A36) into (A13) and (A14),

$$i_d = j_{op1} A_1 (2/\sqrt{\pi}) \sqrt{1-C_1+\eta_{f1}} \quad (A37)$$

and

$$i_d = -j_{op2} A_2 (2/\sqrt{\pi}) \sqrt{1-C_2+\eta_{f2}} \quad (A38)$$

Over some portion of the saturation regions, plots of the square of the observed current, i_d , against the potentials V_1 and V_2 , are straight lines with slopes S_1 and S_2 given by (A30). Similarly, the ion densities are given by (A33). However, the intercepts of these straight lines with the V axis now occur at

$$V_{i,2} = (C_{i,2} - 1) / \phi_{P_{i,2}} , \quad (A39)$$

or, in terms of V_d , at

$$V_{d,i,2} = \pm [(C_{i,2} - 1) / \phi_{P_{i,2}}] + V_c \mp V_{2,i} \quad (40)$$

If the constants C_1 and C_2 are positive and sufficiently large, the intercepts are on the same side of the i_{d1}^2 axis as the saturation portion of the curve. This is very different from the behavior of case 1 treated in A2.1.1.1. This feature, which has been noted in experimental data, leads to consideration of the present case 2. A typical curve will be presented and discussed at a later point.

The effect of the assumed dependence of (r/a) on η on the approximations leading to (A26) need to be investigated to insure that the approximations are not invalidated. It is found that as long as $(3/2) C = O(1)$, the approximations leading to (A25) and (A26), and thence to (36) are valid and consistent.

$$A2.1.1.3 \quad \underline{(r/a) \propto \eta^{-1/2}}$$

$$\text{For } (r/a) \propto \eta^{-1/2},$$

$$(2/3) (r/a)^2 \eta^2 = F\eta$$

so that (A26) becomes

$$f = (2/\sqrt{\pi}) \sqrt{1 + (1-F)\eta} . \quad (A41)$$

Inserting (A41) into (A13) and (A14),

$$i_d = j_{OP} A_1 (2/\sqrt{\pi}) \sqrt{1 + (1-f_i)\eta_{P_1}} , \quad V_1 \gg V_{f_1} \quad (A42)$$

and

$$i_d = -j_{0P_2} A_2 (2/\sqrt{\pi}) \sqrt{1 + (1 - F_2) \eta_{P_2,1}} \quad V_2 \gg V_{P_2} \quad (A43)$$

Again, as in case 1, over some portion of the saturation regions plots of the square of the observed current, i_d , against the potential, V_1 or V_2 , will be straight lines. The slopes S_1 and S_2 , however, are now given by

$$S_{1,2} = 4j_{0P_{1,2}}^2 A_{1,2}^2 (1 - F_{1,2}) / \pi \quad (A44)$$

and the intercepts with the V axis now at

$$V_{1,2} = -1 / [(1 - F_{1,2}) \phi_{P_{1,2}}] \quad (A45)$$

Since the arguments leading to (A34) and (A35) are still valid, the intercepts of

$$V_{d,1,2} = \mp \frac{1}{(1 - F_{1,2}) \phi_{P_{1,2}}} + V_c \mp V_{1,2} \quad (A46)$$

If $F_{1,2} > 1$, then the intercepts could also occur on the same side of the i_d^2 axis as the saturation region (as for case 2). However, from (A44) it is clear that (A33) no longer gives the ion densities.

A2.1.1.4 Dependence of Sheath Size on Potential

The next problem to be investigated is the possible dependence of sheath size on potential. From LMS, to some undefined approximation, the space charge limited current for a cylindrical diode, including the effect of initial velocities, is

$$i = \frac{2\sqrt{2}}{9} \sqrt{\frac{e}{m}} \frac{V^{\frac{3}{2}}}{r\beta^2} \quad (A47)$$

where

$$V = 1 + \frac{2.66}{\sqrt{\eta}} \quad (A48)$$

$$\beta = \gamma - 0.4\gamma^2 + 0.09167\gamma^3 - 0.01424\gamma^4 + 0.00168\gamma^5 + \dots, \quad (\text{A49})$$

$$\gamma = \ln(r/a). \quad (\text{A50})$$

When η is sufficiently large (large V or low temperature), $v \sim 1$ and is a slowly varying function of V . For $a/r \gg 1$, Langmuir and Blodgett [29] have shown that

$$\beta^2 = 4.6712(a/r) [\log_{10}(a/r) - 0.1505]^{3/2}. \quad (\text{A51})$$

(A51) is good to 1% if $a/r = 10$, and to 0.01% if $a/r = 80$. The term in square brackets in (A51) is a slowly varying function of a/r for large a/r , so that, for large V and a/r , the saturation current, to terms of first order in a/r and V , is

$$i = \frac{2\sqrt{2}}{q} \sqrt{e/m} \phi^{-3/2} r^{-1} \eta^{3/2} [\text{const}(a/r)] \quad (\text{A52})$$

However, the current to the probe is space charge limited, where a , instead of being the cathode radius, is now the sheath radius. Hence, the current as determined by the orbital limited theory must be equal to that given by (A52). For all the preceding cases, for η_p sufficiently large, $i \propto \sqrt{\eta_p}$, and thus from (A52), $(A/r) \propto \eta_p$ (case 2). Thus from (A24) and (A52) for η_p and a/r sufficiently large,

$$j_{OP} A(2/\sqrt{\pi}) = \frac{2\sqrt{2}}{q} \sqrt{e/m_p} \phi_p^{-3/2} r^{-1} \eta_p [\text{const}(a/r)]$$

or

$$\begin{aligned} a/r &= [\log_{10}(a/r) - 0.1505]^{-3/2} \times \\ & \left[\frac{\sqrt{2\pi}}{q} (4.6712)^{-1} \sqrt{e/m_p} j_{OP}^{-1} A_i^{-1} \phi_p^{-3/2} r^{-1} \right] \eta_p \\ &= \sqrt{3/2} C^{-1/2} \eta_p \end{aligned} \quad (\text{A53})$$

where the term on the right-hand side involving a/r is sensibly constant for small variations in a/r , and hence, limited variations of η_p . Thus, it has been shown that for a limited variation of η_p , $s^2 \approx 0(10^{-2})$ and $s = 0(\eta_p^{-1})$, $a/r \propto \eta_p$.

On the other hand, Shultz and Brown (SB [30] have shown that over a wider range, when (A53) is combined with (A17), (A13) and (A14)

$$i_d \propto V_d^{0.55} \eta_p^{0.8} \quad (A54)$$

A2.1.1.5 Comparison with Experimental Data

A plot of i_d^2 vs. V_d for a double probe measurement made in the bell jar (described in Sec. 3.2.2.2.2) is shown in Fig. A3. It is seen that over a reasonable range of V_d , i_d^2 vs. V_d is a straight line, and that the intercepts occur on the same side of the i_d^2 axis as the saturation region, as expected if $(a/r) \propto \eta_p$. The electron densities obtained by applying (A33) to the data of Sec. 3.2.2.2.2 are in reasonable agreement with expected densities, as pointed out there.

A2.1.2 The Effect of Collisions in the Sheath

A2.1.2.1 The Sheath Edge and the Effect of a Net Field

In the theoretical treatment given above, it has been assumed that the probe-plasma system is made up of two well defined regions, the plasma and the sheath. It was further implicitly assumed that in the plasma $n_p = n_e$ and that there were no net electric fields, while in the sheath it was assumed that no collisions occurred and that $n_p \gg n_e$, so that the Langmuir-Child space charge law could be applied. In practice, there must be a transition region between the plasma and the edge of the sheath where $n_p \gtrsim n_e$ but where there exists a net field. This net field will impart a drift velocity to the positive ions, and this drift velocity can be of the order of or greater than the random ion velocity. If this is the case, this drift velocity and the corresponding increase in particle current across the sheath edge must be taken into account.

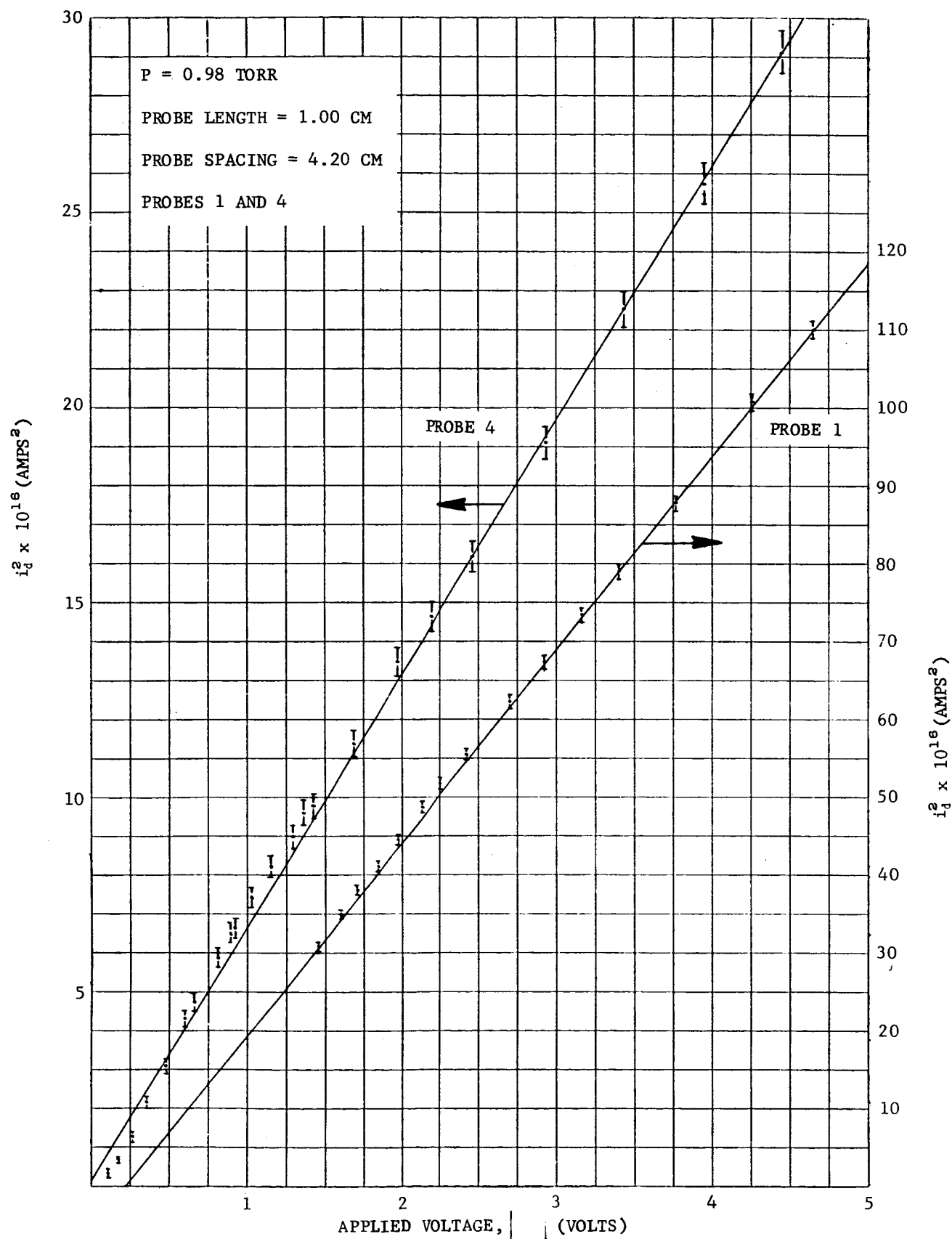


FIG. A3 TYPICAL EXPERIMENTAL i_d VS. v_d PLOT FOR A DOUBLE PROBE IN THE ORBITAL LIMITED CASE: MAXWELLIAN DISTRIBUTION, $\lambda \gg a$, AND NO NEGATIVE IONS

This problem has been treated by Shultz and Brown [30] and in more detail by Boyd [31] and Allen, Boyd and Reynolds [32], as well as others. These treatments show that the drift velocity results in an increase of the positive ion current, and that this current becomes strongly dependent on the electron temperature.

Further, these treatments show that if there is a sufficient number of collisions in the transition region, then the drift velocity imparted by the electric fields in the transition region will be small enough compared to the ion thermal velocity that it can be neglected. Since the transition region may be several sheath thicknesses in size, it follows that if there are many collisions in the sheath there will be enough collisions in the transition region to severely limit the drift velocity, so that the sheath edge effect can be neglected. Similarly, if there is more than one collision in the sheath, one would expect that the effect can also be neglected. However, between an ion mean free path of a few sheath thicknesses and one collision in the sheath the sheath edge effect will become important.

In this section the functional dependence of i_d on V_d is investigated when collisions occur in the sheath. First the case of many collisions, and then the case of a few collisions in the sheath is treated.

A2.1.2.2 Many Collisions ($\lambda_p \ll a$)

The case where $\lambda_p \ll a$, and hence where there are many (nonionizing) collisions in the sheath, corresponds to relatively high gas pressures, so that the ion velocity is controlled by mobility. This case has been treated by Schultz and Brown (SB) [30] for moderate fields where the mobility is constant, so that the drift velocity, v_d , is given by

$$v_d = \mu_p (E/p) \quad (A55)$$

where E is the electric field and μ_p is the positive ion mobility. SB then obtain for the positive ion saturation region

$$i_d \propto V^{0.572} \quad (A56)$$

For values of E/p larger than a certain limit, the mobility as defined by (A55) no longer remains constant. The limiting value of E/p beyond which (A55) no longer holds depends on the particular ion and the neutral gas with which it collides. To illustrate the effect of an altered mobility at high fields, the I - V relation in strong fields will be given for the drift velocity relationship given by von Engel [7, p. 100], namely,

$$v_d = C_p (E/p)^{1/2} \quad (A57)$$

The SB derivation is then modified by replacing (A55) by (A57). The relation obtained between V and i_d then is

$$V = K \alpha^{-1} i_d^{2/3} \left\{ \frac{1}{\sqrt{3}} \left(\tan^{-1} \frac{2u+1}{\sqrt{3}} - \tan^{-1} \frac{1}{\sqrt{3}} \right) + \frac{-u^2}{2} - \frac{1}{6} \log \frac{1-u^3}{(1-u)^3} \right\} \quad (A58)$$

where

$$u = (1 - \alpha^{3/2})^{1/3}$$

and, as before,

$$\alpha = r/a$$

For very small α (i.e., a thick sheath), (A58) reduces to

$$V = K \alpha^{-1} i_d^{2/3} \left[.253 - \frac{1}{2} \log \alpha^{-1} \right] \quad (A59)$$

For very small α , the term in $\{ \}$ in (A59) is sensibly constant for small variations in α so that (A59) is of the form

$$V \propto \alpha^{-1} i_d^{2/3} \quad (A60)$$

But the random ion current is also proportional to the sheath area, so that

$$i_d \propto a^{-1} \quad (A61)$$

The combination of (A60) and (A61) leads to

$$i_d \propto V^{0.6} \quad (A62)$$

This is the high field equivalent of (A56). The voltage dependence of the probe ion current, for thick sheaths, thus is virtually the same at low and high fields.

A2.1.2.3 A Few Collisions ($\lambda_p \sim a$)

This is the case of one to ten collisions in the sheath.

For this case, SB [30] have shown that for the orbital limited case

$$i_d = 0.6 j_p V^{0.63} / N^{0.424} \quad (A63)$$

where

$$N = (e/\epsilon_0) m_p^{1/2} j_p r^2 (kT_p)^{-3/2} \quad (A64)$$

Thus

$$i_d \propto V^{0.63} \quad (A65)$$

For one collision in the sheath, j_p is the ion current at the sheath edge; for 2 to 10 collisions in the sheath

$$j_p = (j_{op}/2) [3 - \exp(-Sp)] / (1+Sp) \quad (A66)$$

where j_{op} is the random ion current at the sheath edge and

$$S = v_c \tau / p \quad (A67)$$

where v_c is the collision frequency for positive ions, τ the time spent by an unscattered ion in the sheath, and p the neutral gas pressure.

A2.1.3 Determination of Electron Temperature

One approach (the equivalent resistance method) [16] used in determining the electron temperature distribution when $r/a \sim 1$ is to equate (A9) and (A10), with the result

$$\sum i_p = \sum_1^2 j_{opK} A_K f_{PK} = A_1 j_{oe1} e^{-\phi_1 V_1} + A_2 j_{oe2} e^{-\phi_2 V_2}$$

or, if $\phi_1 = \phi_2$,

$$\sum i_p = i_{e2} (1 + \sigma e^{-\phi V_d}) \quad (A68)$$

or

$$i_{e2} = (1 + \sigma e^{-\phi V_d})^{-1} \sum i_p \quad (A69)$$

where

$$\sigma = (A_1 j_{oe1} / A_2 j_{oe2}) e^{\phi V_c} \quad (A70)$$

Since $a/r \sim 1$, $\sum i_p$ is essentially a constant, so that (A68) may be differentiated with respect to V_d to yield

$$\left[d i_{e2} / d V_d \right]_{V_d=0} = \phi \sum i_p [\sigma / (\sigma + 1)^2] \quad (A71)$$

But an examination of (A10) shows that in this case $[d i_{e2} / d V_d] = [d i_d / d V_d]$. Using this fact and solving (A71) for T_e , we have

$$T_e = 11,600 [\sigma / (1 + \sigma)^2] \sum i_d / \left[d V_d / d i_d \right]_{V_d=0} \quad (A72)$$

Hence, the steeper the probe I-V characteristic at the origin, the lower the temperature.

This approach will also work even when $\sum i_p$ is not a constant, provided only that i_{p1} and i_{p2} vary slowly compared to i_{e2} or i_{e1} , which, for a Maxwellian distribution, is generally the case even if $a \gg r$. However, it is necessary to

obtain the quantity Σi_p evaluated at $V_p = 0$. To do this, it is necessary to make use of (A7), (A8), (A17), and (A53) along with the experimental data in the saturation region, in an iterative process, to extrapolate back to $V_p = 0$.

A2.2 Negative Ions

The direct effect of the presence of negative ions on the probe theory is twofold. First, it can have some effect upon the value of the positive ion current arriving at the sheath edge by changing the charge distribution in the transition region. Second, their presence can have a major effect upon the form of the negative charge current contribution to the probe current, and hence upon any negative particle temperature derived from the probe curves. It is these latter effects which will be examined here.

With negative ions present, i_{e1} and i_{e2} in (A1) are replaced by $i_{n1} + i_{e1}$ and $i_{n2} + i_{e2}$, respectively. Further, under conditions of a neutral plasma, $n_p = n_n + n_e$. The i_n , by the same arguments as given in Sect. A2.1, will have, for a Maxwellian distribution, the same functional form as the i_e 's. Thus,

$$i_n = j_{on} A e^{-eV/kT_n} \quad (A73)$$

where j_{on} is given by (A3). Hence

$$i_n + i_e = i_e \left\{ 1 + \sqrt{m_e T_n / (m_n T_e)} n_n / n_e \exp \left[-\frac{eV}{k} (T_n^{-1} - T_e^{-1}) \right] \right\} \quad (A74)$$

Several important conclusions may be drawn from (A74). First, for $V = 0$, the relative importance of negative ions compared to electrons is given by the factor

$$\sqrt{m_e T_n / (m_n T_e)} n_n / n_e$$

By virtue of the large value of $\sqrt{m_n T_e / m_e T_n}$ ($\sim 300-1000$ for N_2O , for example), negative ions will have an appreciable effect (at $V = 0$) only if n_n / n_e is large

enough to equal or overweigh this factor. Thus, at $eV = 0$ as well as $eV < 0$ (i.e., retarding field), the effect of negative ions is appreciable only if

$$\rho \equiv n_n/n_e \geq \sqrt{m_n T_e / (m_e T_n)} \equiv \rho_0 \quad (A75)$$

Second, even for $\rho \geq \rho_0$, the effect of negative ions in the saturation region ($|V|$ large) will be negligible under the usual conditions where $T_e \gg T_n$.

It is clear from the above considerations, therefore, that a relatively large concentration of negative ions ($\rho \geq \rho_0$) will affect the probe I-V characteristic chiefly near the origin.

The above qualitative deductions will be made more quantitative by considering two specific special cases.

(a) $n_n \sim n_e \sim \frac{1}{2} n_p$. This corresponds to a reasonably large number of negative ions, but still the second term in the braces of (A74) can be neglected. Then, if the plasma properties are the same at both probes and if i_p varies slowly compared to i_e at $V_d = 0$, the slope of the I-V characteristic at $V_d = 0$ is the same as if no negative ions were present. Thus, the equivalent resistance method for evaluating electron temperature is not affected under these conditions.

However, the floating potential is decreased. For example, for NO ions, if $T_p = T_n = 300^\circ \text{ K}$, $T_e = 3000^\circ \text{ K}$, going from no negative ions to $n_n/n_e = 10$ drops V_f by a factor of about 2 from 1.18 volts to 0.655 volt. This latter value of V_f starts to call into question the assumption that $n_p \gg 1$, which makes valid by (A26) the assumption that i_p varies slowly compared to i_e at $V_d = 0$ in the orbital limited case.

The situation is much worse for lower temperatures; for example, for $n_p = n_e$, $n_n = 0$, and $T_e = 300^\circ \text{ K}$, $V_f \sim .11$ volt and n_p no longer is $\gg 1$. Hence in this case the equivalent resistance method is not applicable even with no negative ions present. Of course, with negative ions present, V_f is even smaller.

As a result of the depression of the floating potential by negative ions, borderline situations where, in the absence of negative ions, the equivalent resistance method is just applicable may be changed by the presence of negative ions so that it no longer is possible to use the equivalent resistance method.

(b) $\rho \gg \rho_0$. In this case the electrons can be neglected, since, by assumption, their contribution to the negative particle current to the probe is small. Now, if the negative and positive ions have the same mass and temperature, and $V_f = 0$, there is no sheath at $V_d = 0$, and one or the other of the probes will be positive with respect to the plasma for $V_d \neq 0$. It follows that all of the theory given above becomes totally useless anywhere near the origin. One further is forced to solve the Boltzman equation simultaneously with Poisson's equation to determine the I-V characteristic in the non-saturation region, since in this region the sheath criterion that $n_p \gg n_n$ cannot be satisfied with the negative ions the dominant negative charge. In the saturation region, however, where $i_d = i_p$, $n_p \gg n_n$ in the sheath, the solutions will be the same as for no negative ions.

A2.3 Non-Maxwellian Electron Energy Distribution

The presence of a non-Maxwellian electron energy distribution will have a considerable effect on the shape of the double probe I-V curves between the saturation regions. In what follows, a number of examples of non-Maxwellian electron distributions and their effects on the double probe I-V characteristics are considered. The energy distribution of positive and negative ions will still be assumed to be Maxwellian, however. The derivations given are only strictly valid for planar sheaths. However, it has been assumed (as was done implicitly for (A4)) that they are directly applicable to cylindrical probes by using the cylindrical probe area in place of the planar area.

A2.3.1 Monoenergetic Isotropic Distribution

We first consider the case of a monoenergetic isotropic electron velocity distribution. In this case, only those electrons with approach velocities great enough to overcome the potential increase across the sheath can penetrate to the probe. Thus, the current drawn by the probe will be

$$i_e = A n_e e (4\pi v_0^2)^{-1} \int_{v_z = \sqrt{2eV/m}}^{\infty} \int_0^{\infty} \int_0^{\infty} v_z \delta(v - v_0) dv_x dv_y dv_z \quad (A76)$$

Changing to polar coordinates, (A76) comes

$$i_e = -n_e e (2v_0^2)^{-1} \int_0^{\infty} \int_0^{\cos^{-1} \frac{1}{2} \sqrt{2eV/m}} v^3 \delta(v - v_0) \cos \phi d(\cos \phi) dv$$

Carrying out the remaining integrations yields the result

$$i_e = \begin{cases} \frac{1}{4} A n_e e v_0 [1 - (eV/E_0)] & E_0 \geq eV \\ 0 & E_0 < eV \end{cases} \quad (A77)$$

where

$$E_0 = \frac{1}{2} m v_0^2. \quad (A78)$$

There are a number of points to be noted about the delta function energy distribution. First, according to (A77) the electron current varies linearly with potential across the sheath. Second, electron current becomes zero for sheath potentials greater than E_0/e . Next, the random electron current (i.e., at $V_d = 0$) is that of a Maxwellian distribution with $\bar{v} = v_0$. The double probe curve for this situation is shown in Fig. A4.

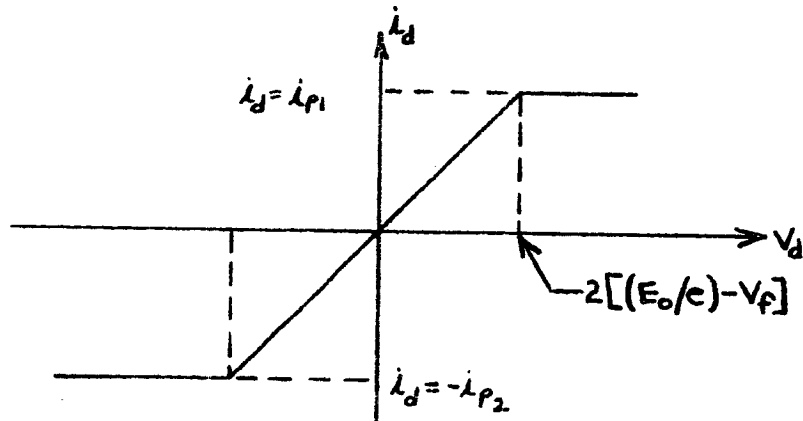


Fig. A4 Monoenergetic Isotropic Electron Energy Distribution
Double Probe I-V Characteristic

The floating potential is now given by

$$V_f = (E_0/e) \left\{ 1 - \left[\sqrt{8/\pi} \sqrt{m_e/m_p} \sqrt{kT_p/E_0} (n_p/n_e) f \right] \right\} \quad (A79)$$

which, for $n_p/n_e \leq 10$ and $kT_p \ll E_0$ becomes (since $f = c \pi \alpha$)

$$V_f \approx (E_0/e) \left\{ 1 - c \sqrt{8/\pi} \sqrt{m_e/m_p} (n_p/n_e) (E_0/kT_p)^{\alpha-1/2} \right\} \quad (A80)$$

Thus for $n_p/n_e \leq 10$, $kT_p \leq E_0$, $V_f \approx E_0/e = V_0$ within a few percent.

Finally, carrying out arguments similar to those used in discussing the case of negative ions with $n_e \geq 0.1 n_i$, one can show that, if the probes are symmetrical and the plasma properties are the same at the two probes,

$$d i_d / d V_d \big|_{V_d=0} = i_{oe} (e/E_0)^{1/2} \quad (A81)$$

where

$$i_{oe} = \frac{1}{4} n_e e v_0 \quad (A82)$$

This is a factor of $\exp[eV_f/kT_e]$ greater than for a Maxwellian distribution of temperature $T_e = \pi/4 E_0/k$, where here V_f is the floating potential for a Maxwellian distribution. Thus the application of the equivalent resistance method, e.g. (A72) would yield a lower value of temperature than that equivalent to the actual mean energy E_0 of the delta function distribution.

A2.3.2 Rectangular Isotropic Energy Distribution

Next we consider a rectangular isotropic energy distribution; that is, the electrons have equal probability of having any energy between E_0 and E_1 :

$$f(E) = \begin{cases} 0 & 0 \leq E < E_0 \\ B & E_0 \leq E \leq E_1 \\ 0 & E_1 < E \end{cases} \quad (\text{A83})$$

Applying the normalization condition that $\int_0^{\infty} f(E)dE = 1$, it follows immediately that

$$B = E_1^{-1}(1-\gamma)^{-1} \quad (\text{A84})$$

where

$$\gamma = E_0/E_1 \leq 1. \quad (\text{A85})$$

The corresponding velocity distribution $f(\vec{v})$ is

$$f(\vec{v}) = \begin{cases} 0 & 0 \leq v < v_0 \\ m_e B/4\pi v & v_0 \leq v \leq v_1 \\ 0 & v_1 < v \end{cases} \quad (\text{A86})$$

where the v_k 's are the velocities associated with the corresponding energies.

Calculation of the electron current arriving at a probe at repelling potential V with respect to the plasma by integrating over all those electrons with directed energies greater than the potential hill, yields the result

$$i_e = \begin{cases} j_{re} \Lambda \{1-3(eV/E_1)[(1-\gamma^{1/2})/(1-\gamma^{3/2})]\} & 0 \leq V < E_0/e & (A87) \\ j_{re} \Lambda (1-\gamma^{3/2})^{-1} \{1-3(eV/E_1)[1-(\frac{2}{3}eV/E_1)^{-1/2}]\} & E_0/e \leq V \leq E_1/e & (A88) \\ 0 & E_1/e < V & (A89) \end{cases}$$

where j_{re} is the random electron current for the distribution (A83), and is given by

$$j_{re} = \frac{1}{4} ne\bar{v} = (\frac{1}{6} ne n_i) \{ [1-\gamma^{3/2}] / (1-\gamma) \}. \quad (A90)$$

Here \bar{v} is the average electron speed for the distribution (A83) and is given by

$$\bar{v} = (4n_i/6) [(1-\gamma^{3/2}) / (1-\gamma)] \quad (A91)$$

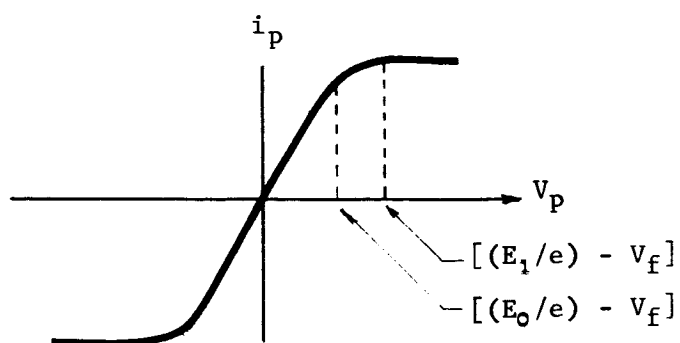
From (A87), (A88) and (A89), one notes that the electron current decreases linearly with sheath potential until $eV = E_0/e = V_0$; then, as will be exhibited more clearly below, it varies with a slope which decreases in magnitude with increasing sheath potential until $V = E_1/e = V_1$, at which point the electron current is zero.

The floating potential $V_f \leq V_0$ is given by

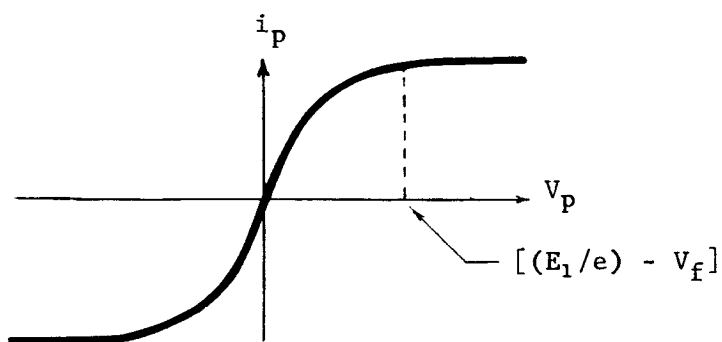
$$V_f = (E_1/3e) [(1-\gamma^{3/2}) / (1-\gamma^{1/2})] [1 - (j_{op}/j_{re})f] \quad (A92)$$

and, therefore, is equal to E_0/e when γ (the distribution width parameter) satisfies the cubic in $\gamma^{1/2}$

$$(3G-1)(\gamma^{1/2})^3 - 3G(\gamma^{1/2})^2 + 1 = 0 \quad (A93)$$



(a) $\gamma > \gamma_0$



(b) $\gamma < \gamma_0$

FIG. A5 DOUBLE PROBE I-V CURVES FOR RECTANGULAR ENERGY DISTRIBUTION

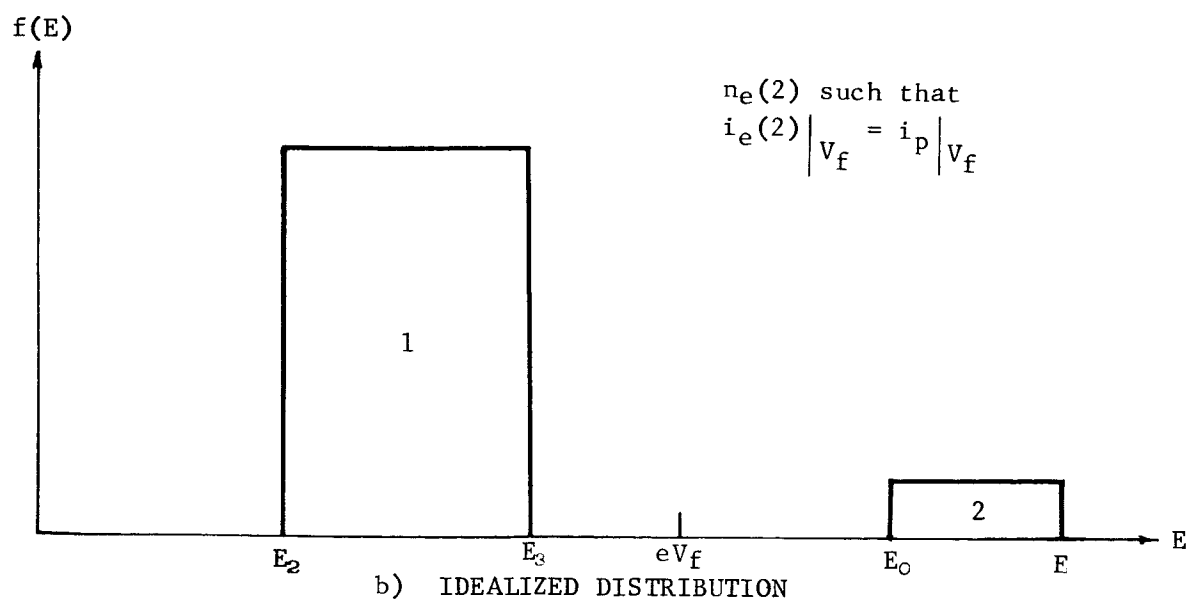
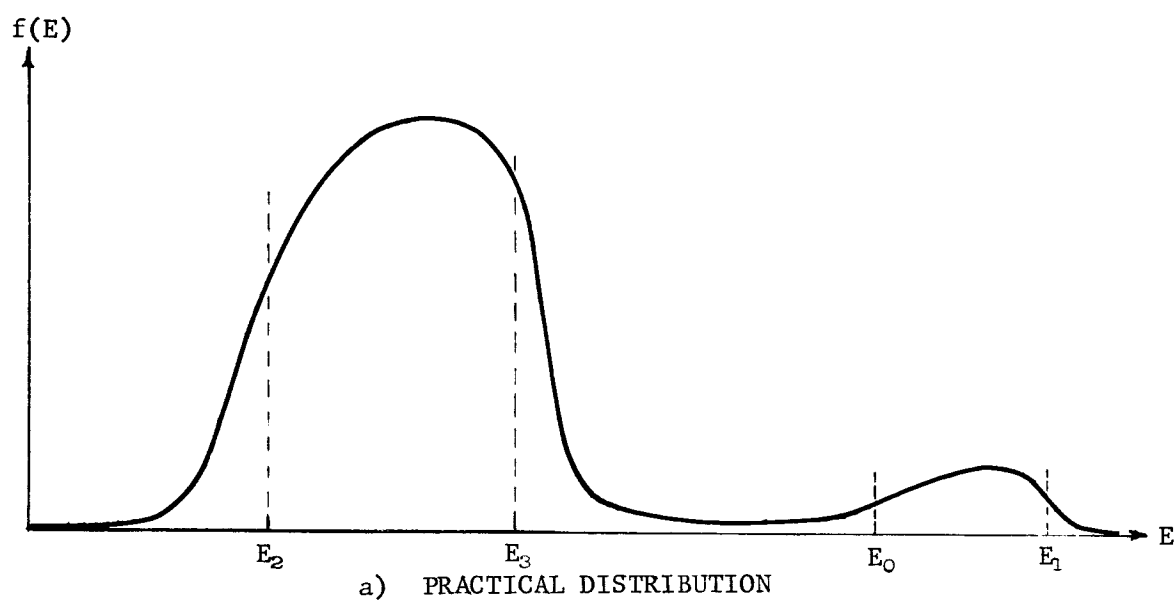


FIG. A6 TWO PEAK ELECTRON ENERGY DISTRIBUTIONS

where

$$G = [1 - (j_{0P}/j_{re})f] \quad (A94)$$

The value γ_0 of the width parameter γ which satisfies (A93) is the dividing line between two different cases with different probe curves.

Differentiation of (A87), (A88) and (A89) now yields

$$(di_e/dV) = \begin{cases} -(3j_{re} A/E_1)[(1-\gamma^{1/2})/(1-\gamma^{3/2})] & V < E_0/e \\ -(3j_{re} A/E_1)(1-\gamma^{3/2})^{-1}[1-\gamma(eV/E_1)^{1/2}] & E_0/e \leq V \leq E_1/e \\ 0 & E_1/e < V \end{cases} \quad (A95)$$

(A95), (A96) and (A97) illustrate clearly the point, previously made, that the slope of the i_e - V curve is constant up to $V = E_0/e$, and then decreases monotonically to zero at $V = E_1/e$. Further, since $j_{re} \propto \sqrt{E_1}$, di_e/dV is proportional to $(E_1)^{-1/2}$. Thus, if $a/r \sim 1$, so that the positive ion current may be assumed constant, the double probe I-V curves for a rectangular energy distribution have the shapes shown in Fig. A5a, b, depending on whether $\gamma \gtrless \gamma_0$, respectively. The case where $a/r \gg 1$, so that the positive ion current may not be sensibly constant compared to the electron current variation, will result in greater slopes, particularly near the origin.

A2.3.3 Two-Peak Distribution

An even more interesting situation is that depicted in Fig. A6a. This is a distribution having two energy peaks, which may be a fair representation of the situation actually existing in both the chamber and, perhaps, the ionosphere. Normally, the number of electrons in the higher energy hump will represent a small fraction of the random electron current. However, it is this tail which is sampled by the double probe, and any change from a Maxwellian electron distribution could

have a pronounced effect upon the double probe curve in the region between the saturation regions.

To illustrate this point more clearly, consider the idealized situation of Fig. A6b. Further, assume that at $V_D = 0$ the electron current to the probe due to the higher energy peak when $V_1 = V_f$ is just equal to the positive ion current to the probe, where eV_f is greater than E_s , but less than $\frac{1}{2} E_0$. Then, initially, $\Delta V_1 = -\Delta V_2 = V_p/2$ so that the i_d-V_D curve has an initial slope one-half that given by (A95). However, once V_D is large enough that V_2 is significantly less than E_s/e , it will take only a small change in V_2 to compensate for any change in i_{e1} , so that ΔV_1 becomes proportional to V_D . Hence the i_d-V_D curve now has twice the slope it had initially. The resultant double probe I-V curve is shown in Fig. A7 for the case $a/r \sim 1$, so that i_p is sensibly constant. This curve is similar in character to those observed experimentally in the chamber with the contaminated NO, as discussed in Sec. 3.3.3.7.3. Thus it has been demonstrated that a non-Maxwellian distribution of two distinct energy groups will give rise to the type of I-V curves observed. The actual distribution clearly is more complicated than the idealized one used here. In particular, the upper energy group must have a more complicated shape, since the slope ratio is more than 2:1. In fact, the second segment definitely is not a straight line.

A2.4 Highly Asymmetrical Double Probes

If the double probe is made highly asymmetrical ($A_2/A_1 > 40$ for H and 235 for NO), then the smaller probe (no. 1) can be driven positive with respect to the plasma. We then have essentially a Langmuir probe. For the probe (no. 1 under our assumption $A_1/A_2 > 40$) which is positive with respect to the plasma, the roles of electrons and positive ions are interchanged. That is, the positive ions are now in a repelling field, and the electrons are in an attractive field. Thus the positive ion current now is given by (A4) and (A5), and the electron

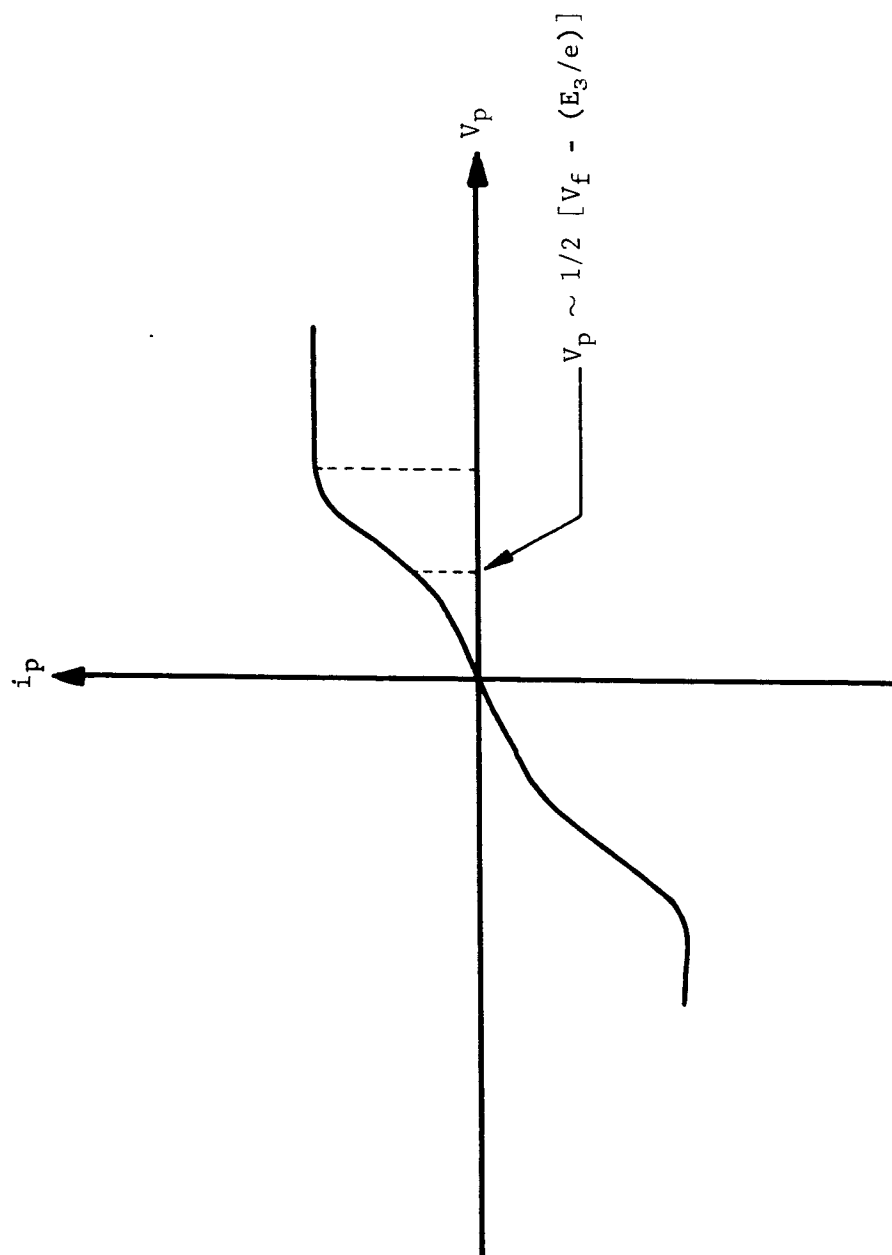


FIG. A7 DOUBLE PROBE I-V CURVE FOR THE IDEALIZED TWO ENERGY GROUP DISTRIBUTION OF FIG. A6(b)

current by (A7), with the subscript p replaced by e. Similarly, the expressions for f are those for the positive ions with the subscripts p replaced by e. The various conditions analogously become:

1) $\lambda_e \gg a$

2) $\lambda_e \ll a$

3) $\lambda_e \sim a$

Finally, it follows that there exists an electron saturation region (provided $A_2/A_1 \gg 40, 235$ for ND) whose log-log plot will have different slopes according to which of 1), 2), or 3) are valid. Clearly, the Gerdian condenser is only an asymmetric double probe.

A3. SUMMARY AND CONCLUSIONS

It has been shown that the I-V characteristic of a double probe consists of three regions:

- 1) ion saturation to probe 1 $V_p \gg 0$
- 2) a transition region $V_p \sim 0$
- 3) ion saturation to probe 2 $V_p \ll 0$

In the ion saturation regions, the electron current to the probe that is saturated is essentially zero, so that the circuit current is equal to the ion saturation current. In this saturation region, it follows that the circuit current is a function of the positive ion temperature, the positive ion density, the ratio a/r , and the applied voltage V_d . The functional form of the dependence on V_d , in turn, is dependent on whether there are no, a few, or many collisions in the sheath, and on the value of a/r .

On the other hand, if electrons comprise 10% or more of the negative particles and are Maxwellian distributed, the current in the region between the saturation regions is an exponential function of voltage, with a slope (of a log-linear plot) at the origin which is dependent on the electron temperature. If the probes are reasonably symmetrical, only those electrons (the tail of the distribution) with energies greater than the floating potential will be sampled. Finally, the effect of negative ions for $n_n < 10n_e$ has been shown to be primarily a slight decrease in the minimum energy of the electrons sampled, without much effect on the electron temperature as determined by the equivalent resistance method. On the other hand, if $n_n > 10n_e$ the presence of the negative ions has a significant effect on the transition region and the theory becomes extremely complicated.

Next, it has been shown that any deviation from a Maxwellian distribution in the tail of the distribution can have a strong effect upon the functional form of the transition region. For example, a delta function or rectangular energy

distribution changes the dependence from exponential to linear near the origin. Finally, and most importantly, it has been shown that a two-energy-group distribution can give a two segment transition region, i.e., a "kink" in the I-V characteristic near the origin.

Finally, the Langmuir probe has been shown to be simply a highly asymmetric double probe, and the Gerdien condenser an asymmetric double probe. As a result, the I-V characteristic of a Langmuir probe consists of

- 1) a positive ion saturation region $V_p \ll 0$
- 2) a transition region $V_p \sim 0$
- 3) an electron saturation region $V_p \gg 0$

The shape of the transition region is extremely sensitive to the electron energy distribution and, for $n_n > 10n_e$, to the presence of negative ions. The electron saturation region (similar to the ion saturation region) is dependent on the electron temperature, the electron density, the applied voltage, and whether the electrons undergo no, a few, or many collisions in the sheath.

APPENDIX B

THE EFFECT OF ELECTRON ATTACHMENT

In Sec. 3.2.1 a theory for plasma production by photoionization is worked out and applied to the production of such a plasma in the chamber. There are some related effects which were not considered in that treatment which now require examination in view of the nature of the experimental probe curves which were obtained. These are the effects of energy dependence of cross sections for the various processes which remove free electrons, and the effects of attachment and detachment processes on electron energy distribution and electron density. These will now be examined briefly.

B1. ENERGY DEPENDENCE OF ELECTRON REMOVAL CROSS SECTIONS

The magnitude and energy dependence of the electron removal cross sections relative to the collision cross section can have a profound effect on the electron energy distribution in the plasma. For example, using age theory (see Sec. 3.2.1.6), one finds that it takes about 10^5 collisions to slow down from a birth energy of 0.75 ev to a room temperature energy of 0.025 ev, while in an attaching gas it can take less than 10^4 collisions for the electron to attach. Thus, in this case there would be few free electrons with energy less than about 0.2 ev.

To illustrate this and several other points more forcibly, consider the following situation. Electrons are all born initially at some energy E_0 . If $\sigma_a \gg \sigma_c$ at E_0 , where σ_a is the electron removal cross section and σ_c the collision cross section, then only electrons of energy E_0 will be present in appreciable quantity, as shown in Fig. B1(a). If the cross sections are independent of energy, and $\sigma_a \sim \sigma_c$, then the energy distribution will have a narrow bell-shaped spread about energy E_0 , as illustrated in Fig. B1(b). If $\sigma_a \sim \sigma_c/N_t$ (where N_t is the

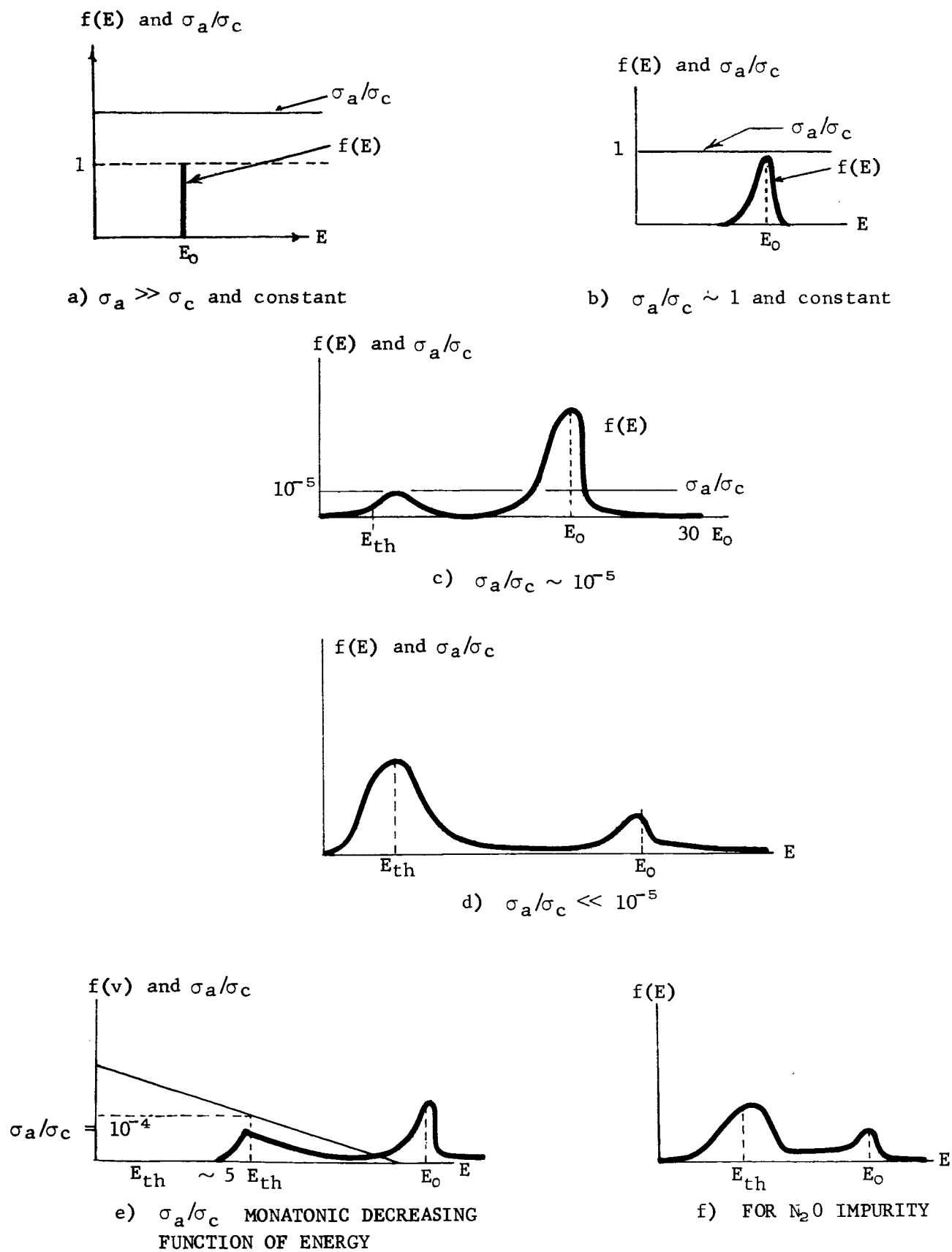


FIG. B1 RELATIONSHIPS BETWEEN σ_a/σ_c AND ELECTRON ENERGY DISTRIBUTION.

number of collisions to thermalize), but is independent of energy, the distribution will extend down to thermal energies, as well as upwards with a small tail. There will be few thermal electrons and the high energy tail will have a practical finite cutoff. These features are indicated in Fig. B1(c). Only when $\sigma_a \ll \sigma_c/N_t$ will the energy distribution resemble the Maxwellian. However, even in this case there will be an energy peak at E_0 , as shown in Fig. B1(d).

If σ_a increases monotonically with decreasing energy, and if it reaches a value of $\sigma_a \sim 10\sigma_c/N_t$ for some energy E_1 above the thermal energy, the distribution will be highly epithermal (i.e., above thermal), extending upward from an energy somewhat less than E_1 , as in Fig. B1(e). The energy cutoff of the distribution will depend on how rapidly σ_a increases. If σ_a increases monotonically with increasing energy, the high energy tail will be missing from the distribution, resulting, among other effects, in a decrease in the floating potential. Finally, if the electron removal cross section is bell-shaped and of finite width, there will be a hole in the distribution, so that the double-peaked character of the basic distribution will be accentuated further. In fact, if the peak value of σ_a is large enough and lies below E_0 , the distribution will become like that shown in Fig. B1(c).

B2. ATTACHMENT AND DETACHMENT

B2.1 General

Electron attachment to neutral particles will give rise to negative ions. From Figs. 7 and 8 in Sec. 3.2.1.3, attachment should be the dominant loss mechanism for electron densities below about 10^6 to 10^7 cm^{-3} . The negative ion density depends on the loss rate of negative ions due to ion-ion recombination and to photodetachment, versus the production rate due to attachment. Assuming a 3-body attachment process, we have

$$\beta_3 n_e N^2 = \gamma n_p n_n + \sigma_{pd} n_n \Phi \quad (\text{B1})$$

where β_3 is the 3-body attachment coefficient, N is the neutral particle density, γ the ion-ion recombination coefficient, σ_{pd} the microscopic photodetachment cross section, and Φ the photon flux.

For nitric oxide at 0.2 Torr, $\beta_3 N^2 n_e < 43.5 n_e$ ($n_e < 10^7$ cm^{-3}). For an average photon flux in the chamber of about 10^{18} $\text{cm}^{-2}\text{-sec}^{-1}$ and a detachment cross section of 10^{-18} cm^2 , $\sigma_{pd} \Phi n_n \sim 10^{-6} n_n$. On the other hand, the electron-ion pair production rate, for the same conditions, is about 10^{10} cm^{-3} . This implies $n_e \sim 2.3 \times 10^6$ cm^{-3} . Thus the rate of production of detached electrons cannot exceed about 230 sec^{-1} . This implies that the perturbation in the electron energy distribution due to detached electrons generally cannot be very significant, and that $\gamma n_n < 43.5$ sec^{-1} .

B2.2 Attachment with N_2O Present

From Sec. 3.3.3.8, N_2O is the only known attaching impurity in the NO gas which is present in the chamber in sufficiently significant concentration to cause a perturbation in the electron energy distribution. Now pure N_2O has a threshold energy for dissociative attachment slightly less than 0.3 eV [23,8], with a peak microscopic cross section of 8.59×10^{-18} cm^2 at 2.2 eV [23]. However,

there exist data [8] showing that when N_2O is mixed with other gases (e.g., N_2 or A) the threshold energy is decreased considerably. However, we have not found any data indicating the presence of a 3-body attachment process.

Using the peak value of the dissociative cross section for N_2O given above, a dissociative rate constant of $7.56 \times 10^{-10} \text{ cm}^3$ at an energy of 2.2 ev is obtained. This is 7.6×10^5 -times the same rate constant for NO. From Sec. 3.2.1.3.2, dissociative attachment dominates the 3-body recombination in NO at 0.2 Torr. Thus, at 0.2 Torr, a concentration of 0.5% of N_2O would lead to an attachment rate 3800-times that of pure NO at 2.2 ev. From [23], the ratio is about 100-times at 0.4 ev. Hence, since $E_0 = 0.75 \text{ ev}$, the electron concentration with 0.5% N_2O present should be in the order of one-hundredth that for pure NO. This illustrates the strong effect of N_2O as an attaching impurity in NO, and its energy dependence.

Proceeding further, it is found that the ratio σ_a/σ_c has the values 4×10^{-8} at 0.4 ev, 1.7×10^{-5} at 0.7 ev, and increases still further with continuing increase in energy up to 2.2 ev, at which point it starts to decrease. Since from age theory it takes about 1.7×10^4 collisions to get to 0.4 ev and 5.6×10^4 collisions to get to 0.1 ev while the above ratios of σ_a/σ_c imply about 2.5×10^5 collisions to thermalize more than 80% of the electrons will make it energies less than 0.1 ev. Thus, from the discussion of Sec. B1, one surmises that the electron energy distribution with N_2O present consists of a thermal group of decreased strength (but not Maxwellian in shape), a group centered on $E_0 = 0.75 \text{ ev}$, a very weak high energy tail, and fewer electrons in the range between about 0.1 ev and E_0 than for pure NO. This is illustrated in Fig. B1(f).

From Sec. A2.3.4 of Appendix A, a two-peak energy distribution of this type will give a double probe curve with a "kink" near the origin. Further, again from Sec. A2.3.4, for this "kink" to exist it is additionally required that only a few

(less than 0.5%) of the electrons have energies greater than a few times E_{th} if $n_e \lesssim n_p/10$. Thus, most of the electrons must of necessity be relatively "cold", i.e., have energies less than 0.1 ev (850°K).

B3. SUMMARY AND CONCLUSIONS

It has been shown that the magnitude of the ratio of the electron removal cross section to the collision cross section, σ_a/σ_c , relative to the inverse of the number of collisions to thermalize, N_t^{-1} , and the energy dependence of σ_a/σ_c can have a very appreciable effect on the electron energy distribution for the situation of a single electron birth energy. In particular, it has been shown that only if $\sigma_a/\sigma_c \ll N_t^{-1}$ will the distribution resemble a Maxwellian. Next, it has been shown that photodetachment will have only a small effect on the energy distribution.

Finally, it has been shown that the presence of N_2O as an impurity in a concentration of 0.5% can lead to electron densities in the order 1/100 of those that would otherwise exist. In addition, it has been shown that the energy dependence of the dissociative attachment cross section of N_2O , combined with the magnitude of this cross section relative to the collision cross section in NO , is such as to give rise to a two-peak electron energy distribution: one peak at thermal energies, and the other peak at E_0 , with heavily reduced electron concentration in between and a weak high energy tail. In turn, this type of distribution will give a double probe curve with a "kink" near the origin if most of the electrons are "cold". These facts correlate strongly both qualitatively and quantitatively with the experimental results of Secs. 3.3.3.7 and 3.3.3.8 and the results of the probe theory of Sec. A2.3.4 for a two-peak electron energy distribution.

BIBLIOGRAPHY

- [1] M. Nicolet and A. C. Aikin, "The Formation of the D-Region of the Ionosphere", J. Geophys. Research 65, 1469-1483 (1960).
- [2] P. J. Nawrocki and R. Papa, "Atmospheric Processes", Geophysics Corp. of America, GCA No. 61-37-A (1961).
- [3] K. Watanabe, "Photoionization and Total Absorption Cross Section of Gases. I. Ionization Potentials of Several Molecules. Cross Sections of NH_3 and NO ", J. Chem. Phys. 22, 1564 (1954).
- [4] Robert C. Ganton and Edward C. Y. Inn, "Rates of Electron Removal by Recombination, Attachment, and Ambipolar Diffusion in Nitric Oxide", J. Chem. Phys. 35, 1896 (1961).
- [5] John P. Doering and Bruce H. Mahan, "Photoionization of Nitric Oxide", J. Chem. Phys. 36, 669 (1961).
- [6] W. B. Kunkel and A. L. Gardner, "Free Electrons in Active Nitrogen", J. Chem. Phys. 27, 1785 (1962).
- [7] A. Von Engel, "Ionized Gases", Oxford, London, 1955.
- [8] Sanborn C. Brown, "Basic Data of Plasma Physics", MIT, Cambridge, 1959.
- [9] Francis F. Chen, "Electrostatic Probes and Sheaths. A Survey", an unpublished report.
- [10] L. B. Loeb, "Fundamental Processes of Electrical Discharges in Gases", John Wiley and Sons, Inc., New York, Second Edition, Revised, 1955.
- [11] I. Langmuir, "Studies of Electric Discharges in Gases at Low Pressures - Part I", General Electric Review, XXVIII, 449 (1924).
- [12] S. Glasstone and M. C. Edlund, "The Elements of Nuclear Reactor Theory", D. Van Nostrand Company, Inc., New York, 177, 1952.

- [13] J. Nervitsky, "A Seal for Lithium Fluoride Windows", reprint obtained from Harshaw Chemical Co.
- [14] M. H. Greenblatt, "Sealing A Calcium Fluoride Window to Glass", Rev. Sci. Instr. 29, 738 (1958).
- [15] P. G. Wilkinson, NRL, private communication.
- [16] E. O. Johnson and L. Malter, "A Floating Double Probe Method for Measurements in Gas Discharges", Phys. Rev. 30, 58 (1950).
- [17] Alfred K. Stober, "Ceramic Vacuum Ultraviolet Ion Chambers", NASA TN D-1180.
- [18] M. Katzin, et. al., "Experimental Investigations Related to Ionospheric Probing", Scientific Report No. 2 on contract NASw-835 (September 30, 1964).
- [19] K. Watanabe, "Ultraviolet Absorption Processes in the Upper Atmosphere", in "Advances of Geophysics", Vol. 5, Ed. H. E. Landsberg and J. Van Mieghen, Academic Press, New York (1958).
- [20] F. B. Haller, "All Glass Sorption Vacuum Trap", Rev. Sci. Instr., 35, No. 10, 1356 (1964).
- [21] H. Gerdian, "Absolute Determination of Electrical Conductivity and Specific Velocity of the Ions in the Atmosphere" Phys. Zeitschr., 4, 632-635 (1903).
- [22] Elden C. Whipple, Jr., "Electricity in the Atmosphere Above the Exchange Layer", NASA TN D-2092 (1964).
- [23] Donald Rapp and Donald P. Briglia, "Total Cross Sections for Ionization and Attachment in Gases by Electron Impact-II. Negative Ion Formation", J. Chem. Phys. 43, No. 5, 1480-1489 (1965).
- [24] G. V. Jorgenson and G. K. Wehner, "Sputtering Studies of Insulators by Means of Langmuir Probe", J. Appl. Phys. 36, No. 9 2672-2674 (1965).
- [25] Yu M. Kagan and V. I. Perel, "Probe Methods in Plasma Research", Soviet Physics USPEKHI 81, No. 3 and 4, 767-793 (1964).

- [26] G. P. Barnard, "Modern Mass Spectrometry", The Institute of Physics, London, 1953, pp 214-230.
- [27] I. Langmuir and H. Mott-Smith, Jr. "Studies of Electric Discharge in Gases at Low Pressures: Part I", General Electric Review, Vol. XXVII, No. 7, p 449-455 (1924).
- [28] H. Mott-Smith and I. Langmuir, "The Theory of Collectors in Gaseous Discharges", The Physical Review, Vol. 28, No. 10, pp 727-763 (1926).
- [29] I. Langmuir and K. B. Blodgett, "Currents Limited by Space Charge Between Coaxial Cylinders", The Physical Review, Vol. 22, pp 347-365 (1923).
- [30] George J. Schultz and Sanborn C. Brown, "Microwave Study of Positive Ion Collection by Probes", Phys. Rev. 98, No. 6, 1642-1649 (1955).
- [31] R. L. F. Boyd, "The Mechanism of Positive Ion Collection by A Spherical Probe in A Dense Gas" Proc. Phys. Soc. (London) B64 795 (1951).
- [32] J. E. Allen, R. L. F. Boyd and P. Reynolds, "The Collection of Positive Ions by a Probe Immersed in a Plasma", Proc. Phys. Soc. (London) B-70, No. 3-B 297-304 (1957).
- [33] D. K. Das, "Outgassing Characteristics of Various Materials in an Ultra High Vacuum Environment", National Research Corporation, Technical Documentary Report No. AEDC-TDR-62-19.